

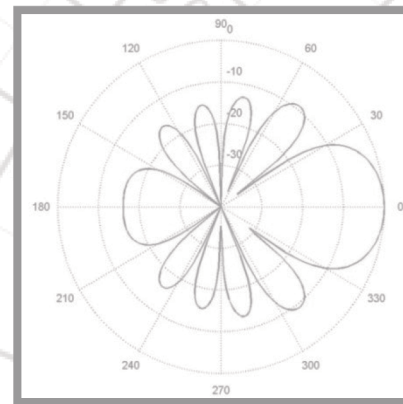
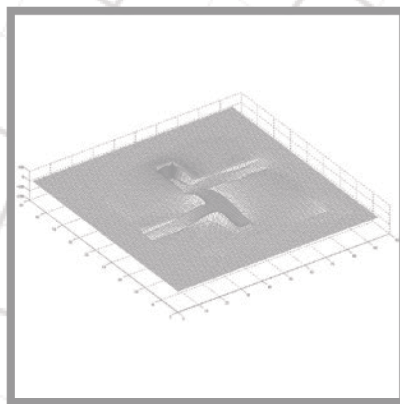
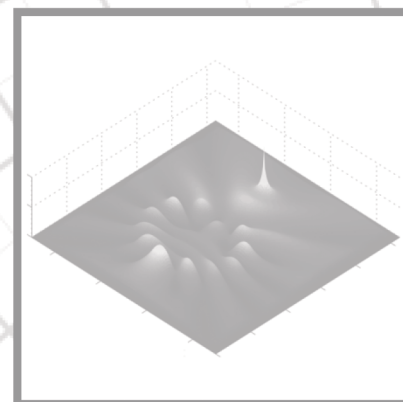
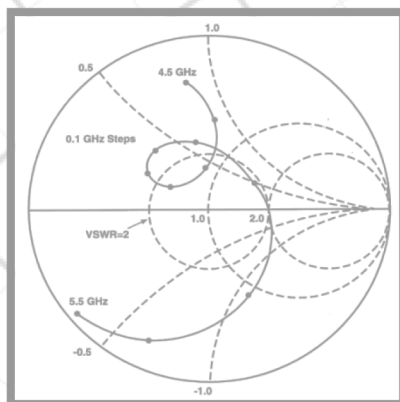
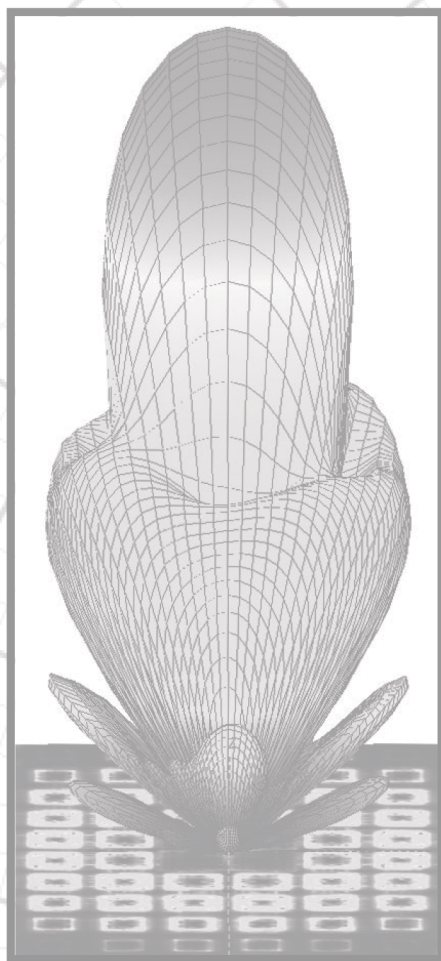
Applied Computational Electromagnetics Society

Journal



November 2013

Vol. 28 No. 11



ISSN 1054-4887

GENERAL PURPOSE AND SCOPE: The Applied Computational Electromagnetics Society (*ACES*) Journal hereinafter known as the *ACES Journal* is devoted to the exchange of information in computational electromagnetics, to the advancement of the state-of-the art, and the promotion of related technical activities. The primary objective of the information exchange is to inform the scientific community on the developments of new computational electromagnetics tools and their use in electrical engineering, physics, or related areas. The technical activities promoted by this publication include code validation, performance analysis, and input/output standardization; code or technique optimization and error minimization; innovations in solution technique or in data input/output; identification of new applications for electromagnetics modeling codes and techniques; integration of computational electromagnetics techniques with new computer architectures; and correlation of computational parameters with physical mechanisms.

SUBMISSIONS: The *ACES Journal* welcomes original, previously unpublished papers, relating to applied computational electromagnetics. Typical papers will represent the computational electromagnetics aspects of research in electrical engineering, physics, or related disciplines. However, papers which represent research in applied computational electromagnetics itself are equally acceptable.

Manuscripts are to be submitted through the upload system of *ACES* web site <http://www.aces-society.org> See “Information for Authors” on inside of back cover and at *ACES* web site. For additional information contact the Editor-in-Chief:

Dr. Atef Elsherbeni
Electrical Engineering and Computer Science Department
Colorado School of Mines
310D Brown Building
1610 Illinois Street
Golden, CO 80401
Phone: (303) 273-3667
Email: aelsherb@mines.edu

SUBSCRIPTIONS: All members of the Applied Computational Electromagnetics Society are entitled to access and download the *ACES Journal* any published journal article available at <http://www.aces-society.org>. Printed issues of the *ACES Journal* are delivered to institutional members. Each author of published papers receives a printed issue of the *ACES Journal* in which the paper is published.

Back issues, when available, are \$50 each. Subscription to *ACES* is through the web site. Orders for back issues of the *ACES Journal* and change of address requests should be sent directly to *ACES* office at:

Hank Ducey - ACES 13A
Electrical Engineering Department
The University of Mississippi
University, MS 386377 USA

Allow four weeks advance notice for change of address. Claims for missing issues will not be honored because of insufficient notice, or address change, or loss in the mail unless the *ACES* office is notified within 60 days for USA and Canadian subscribers, or 90 days for subscribers in other countries, from the last day of the month of publication. For information regarding reprints of individual papers or other materials, see “Information for Authors”.

LIABILITY. Neither *ACES*, nor the *ACES Journal* editors, are responsible for any consequence of misinformation or claims, express or implied, in any published material in an *ACES Journal* issue. This also applies to advertising, for which only camera-ready copies are accepted. Authors are responsible for information contained in their papers. If any material submitted for publication includes material which has already been published elsewhere, it is the author’s responsibility to obtain written permission to reproduce such material.

**APPLIED
COMPUTATIONAL
ELECTROMAGNETICS
SOCIETY
JOURNAL**

November 2013
Vol. 28 No. 11
ISSN 1054-4887

The ACES Journal is abstracted in INSPEC, in Engineering Index, DTIC, Science Citation Index Expanded, the Research Alert, and to Current Contents/Engineering, Computing & Technology.

The illustrations on the front cover have been obtained from the research groups at the Department of Electrical Engineering, The University of Mississippi.

THE APPLIED COMPUTATIONAL ELECTROMAGNETICS SOCIETY

<http://www.aces-society.org>

EDITOR-IN-CHIEF

Atef Elsherbeni

Colorado School of Mines, EECS Department
Golden, CO 80401, USA

ASSOCIATE EDITORS-IN-CHIEF

Sami Barmada

University of Pisa, EE Dept.
Pisa, Italy, 56126

Fan Yang

Microwave and Antenna Institute
Tsinghua University, Beijing, China

Mohamed Bakr

McMaster University, ECE Dept.
Hamilton, ON, L8S 4K1, Canada

Yasushi Kanai

Niigata Inst. of Technology
Kashiwazaki, Japan

Mohammed Hadi

Kuwait University, EE Dept.
Safat, Kuwait

Mohamed Abouzahra

MIT Lincoln Laboratory
Lexington, MA, USA

Ozlem Kilic

Catholic University of America
Washington DC, 20064, USA

Alistair Duffy

De Montfort University
Leicester, UK

Levent Gurel

Bilkent University
Ankara, Turkey

EDITORIAL ASSISTANTS

Matthew J. Inman

University of Mississippi, EE Dept.
University, MS 38677, USA

Mohamed Al Sharkawy

Arab Academy for Science and
Technology, ECE Dept. Alexandria,
Egypt

EMERITUS EDITORS-IN-CHIEF

Duncan C. Baker

EE Dept. U. of Pretoria
0002 Pretoria, South Africa

Allen Glisson

University of Mississippi, EE Dept.
University, MS 38677, USA

David E. Stein

USAF Scientific Advisory Board
Washington, DC 20330, USA

Robert M. Bevensee

Box 812
Alamo, CA 94507-0516, USA

Ahmed Kishk

University of Mississippi, EE Dept.
University, MS 38677, USA

EMERITUS ASSOCIATE EDITORS-IN-CHIEF

Alexander Yakovlev

University of Mississippi, EE Dept.
University, MS 38677, USA

Erdem Topsakal

Mississippi State University, EE Dept.
Mississippi State, MS 39762, USA

EMERITUS EDITORIAL ASSISTANTS

Khaled ElMaghoub

University of Mississippi, EE Dept.
University, MS 38677, USA

Anne Graham

University of Mississippi, EE Dept.
University, MS 38677, USA

Christina Bonnington

University of Mississippi, EE Dept.
University, MS 38677, USA

NOVEMBER 2013 REVIEWERS

**Ahmed Abdelrahman
Aghogho Atemu
Abdul Ali Babar
Mohamed Bakr
Ming Chen
Mario Cvetkovic
Vijay Devabhaktuni
Park Hyun Ho
Darko Kajfez
Zulfiqar Khan
Zamzam Kordiboroujeni
Mithilesh Kumar
Fernando Las-Heras**

**Jie Li
Yun-Fei Mao
Abdolkhalegh Mohammadi
Claudio Montiel
B Moore
Marco Mussetta
Andrew Peterson
Dr. Pichon
Sohrab Safavi
Binay Sarkar
Christoph Statz
Gonul Turhan-Sayan
Yasemin**

THE APPLIED COMPUTATIONAL ELECTROMAGNETICS SOCIETY
JOURNAL

Vol. 28 No. 11

November 2013

TABLE OF CONTENTS

“Hybrid Binary-Real GA Optimization Approach for Breast Microwave Tomography” A. Sabouni, A. Ahtari, S. Noghianian, G. Thomas, and S. Pistorius	1005
“Imaging 2D Breast Cancer Tumor Margin at Terahertz Frequency Using Numerical Field Data Based on DDSCAT” T. C. Bowman, A. M. Hassan, and M. El-Shenawee	1017
“Synthesis of Conical Conformal Array Antenna Using Invasive Weed Optimization Method” Y. Li, F. Yang, J. Ouyang, and P. Yang	1025
“Fast Calculation of 3D Conductive Target Backscatter in a Random Medium Using Coherence Based Monte Carlo Integration (CBMI) Method” G. Togtema, H. El-Ocla, and M. Al Sharkawy	1031
“A Novel Approach to Synthesis of Nonuniform Conformal Reflectarray Antennas” M. Karimipour and A. Pirhadi	1040
“Novel Bandwidth-Agile Bandpass Filter Using Defected Ground Structure” Z.-H. Bao, Q.-Y. Lu, C. Shao, J.-X. Chen, and S. Zhang	1050
“Square Dual-Mode Quasi-Elliptic Bandpass Filter with Wide Upper Stopband” Y. Ma, W. Che, W. Feng, and J.-X. Chen	1056
“Analysis of a Novel Ka Horn Antenna With Low Cross Polarization” Y.-Z. Liu, S. Xiao, and B.-Z. Wang	1061
“An Unequal Wilkinson Power Divider Using Half Mode Substrate Integrated Waveguide” Z. Mazani and G. Moradi	1068
“Simple and Compact Dual Band-Notched Monopole Antenna Using U-Shaped Forms on the Conductor-backed Plane for UWB Applications” M. Moosazadeh and Z. Esmati	1074
“HEV Characterization Using Generalized Notion of Power” N. Al-Aawar and A. A. Arkadan	1080

“An Equivalent Model for Wiring Harness Induced Current in Automobiles” Y. Zheng, Q. Wang, G. Wang, Z. An, Q. Liu, and X. Li	1088
“Effective Analysis of Ridged Circular Waveguides with a Curvilinear Frequency-Domain Finite-Difference Approach” A. Fanti, G. Montisci, G. Mazzarella, and G. A. Casula.....	1100
“A Simplified Analytical Solution for Characterizing Edge Currents Along a Finite Ground Plane” C. Obiekezie, D. W. Thomas, A. Nothofer, S. Greedy, L. R. Arnaut, and P. Sewell	1111
“Issues in Antenna Optimization - A Monopole Case Study” Richard A. Formato	1122

Hybrid Binary-Real GA Optimization Approach for Breast Microwave Tomography

A. Sabouni¹, A. Ahtari², S. Noghianian³, G. Thomas⁴, and S. Pistorius⁵

¹Department of Electrical Engineering and Physics,
Wilkes University, Wilkes-Barre, PA, 18766, USA
abas.sabouni@wilkes.edu

²Invenia Technical Computing Company, Manitoba, Winnipeg, MB, R3T 6A8, Canada
ali.ashtari@invenia.ca

³Department of Electrical Engineering,
University of North Dakota, Grand Forks, ND, 58203, USA
sima.noghianian@engr.und.edu

⁴Department of Electrical and Computer Engineering, University of Manitoba
Winnipeg, MB, R3T 5V6, Canada
gabriel.thomas@ad.umanitoba.ca

⁵Department of Physics and Astronomy, University of Manitoba, Winnipeg, MB, R3T 5V6, Canada
stephen.pistorius@cancercare.mb.ca

Abstract — A microwave tomography imaging system, which uses a hybrid binary-real genetic algorithm (GA) is described in this work. This method utilizes global optimization for solving the inverse scattering problem based on hybrid version of GA, which is the combination of both real and binary-coded GA. This method is principally aimed at breast imaging for the detection of malignant tumors. The proposed technique is based on a time-domain inverse solver, which uses the multi-illumination technique and includes the dispersive and heterogeneous characteristic of the breast tissues. In this algorithm, real-coded GA acts as a regularizer for binary-coded GA and rejects the non-true solutions. The proposed technique is validated using a numerical breast phantom created based on magnetic resonance imaging (MRI) of actual patients. The results are compared with non-hybrid binary and real GAs and the superior efficiency of the proposed method over the methods that solely employ real or binary GA is illustrated.

Index Terms - Breast cancer imaging, heterogeneous and dispersive breast tissue, hybrid binary-real GA optimization, inverse scattering problem, and microwave tomography.

I. INTRODUCTION

Traditional inverse scattering methods usually remove the ill-posed solutions by assuming a smooth profile [1]. This often causes the removal of the correct solution because in many applications, such as breast imaging, the dielectric profile being imaged is not smooth. In this paper, a new approach for treating the ill-posedness is proposed that uses *a-priori* information for regularization. It involves incorporating realistic assumptions about the breast, based on the measurements of breast dielectric properties. The authors developed the numerical simulation method based on the frequency dependence finite-difference time-domain ((FD)²TD) and binary-coded genetic algorithm for detecting breast cancer [2]. The contribution of this paper is to

demonstrate the ability of microwave tomography (MWT) technique, based on numerical methods for solving partial differential equations (PDEs) such as $(FD)^2TD$ and global optimization methods such as real and binary coded genetic algorithm (GA). To the best of our knowledge, this is the first attempt in using the combination of $(FD)^2TD$ and hybrid GA to reconstruct the location, shape, and dielectric properties of heterogeneous and dispersive media.

The previous technique presented in [2] uses $(FD)^2TD$ and binary GA for reconstructing the image and it works for simple structures of tissue composition. The RGA in the hybrid GA technique presented in [3] was based on optimizing two variables (permittivity and conductivity values) for each cell within the search space, while in the current paper the RGA is based on optimizing only one parameter (water content). In this paper the proposed technique is extended to objects with large distribution of dielectric properties, which includes the water dependency of dielectric properties of breast tissues using $(FD)^2TD$ /hybrid-GA. Furthermore, the examples in previous paper were only hypothetical cases, while in this paper the proposed technique is evaluated using model driven from magnetic resonance imaging (MRI) data. In [4] the authors evaluated the real and binary GA with respect to the speed of convergence for limited number of generations for microwave imaging. The study of noise effects on $(FD)^2TD$ /GA algorithm for solving the inverse scattering problem for heterogeneous and dispersive object is presented in [5].

The paper is organized as follows: in section II, we provide the notation and methodology. In section III, we cast the MWT problem as an optimization problem, where in an appropriate cost-function is to be minimized. Within this framework, we explain the use of hybrid GA as an optimization method in details. Section IV shows inversion results from synthetic data, followed by conclusion in section V.

II. METHODOLOGY

The problem's geometry is depicted in Fig. 1 where Ω is the imaging domain (or search space domain), which is occupied by single or multiple scatterers and V is the problem domain where the scattered field is collected. The Object of Interest

(OI) is surrounded by measurement probes that are able to acquire samples of the scattered field outside the imaging domain at the observation points.

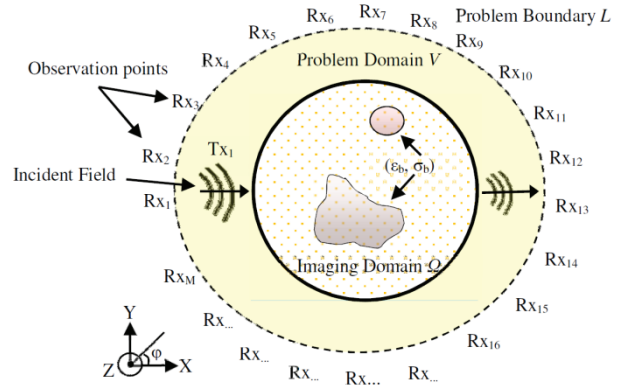


Fig. 1. Geometry of the MWT.

The region Ω is illuminated by a set of transverse magnetic (TM) fields (incident fields), denoted by E_i^{inc} , $i=1,2,3,\dots,N$ (N is the maximum number of illumination angles). The scattered field is measured around the object. The value of the scattered field is denoted by $E_{ij}^{scat}(r)$, $j=1,2,\dots,M$, and $i=1,2,3,\dots,N$ where the index j denotes the j^{th} measurement point (observation point), located at different angles around the object. Since there are M measurement points and N incident angles, the scattered field can be stored in a matrix of size $N \times M$. In this paper, we consider the OI to be infinitely long in the z -direction (this creates a 2D problem). This approximation is made for efficiency in terms of runtime and memory. In fact, the behavior of the electric field within a 2D environment can be repeatedly evaluated very quickly, while this evaluation is much slower for 3D problems. This allows the iterative imaging algorithm to converge to a solution in a reasonable amount of time. In the framework of 2D inversion algorithms, we consider the TM polarization for illumination. In particular, we consider TM to z (TM $_z$). This polarization is often used for 2D MWT [6, 7]. It should be noted that there is recent evidence that TE (transverse electric) polarization might provide better imaging results [8], however to the best of the author's knowledge, there is currently no TE MWT system capable of collecting all three components of the field.

III. MWT METHOD USING (FD)²TD AND GA

MWT is based on solving an inverse scattering problem. The most common way to solve the inverse scattering problems is to formulate it as a minimization problem. The cost-function is evaluated using the difference between the measured and predicted scattered fields for a particular choice of the material parameters (equation (1)). We propose to calculate the simulated scattered field at the observation points using ((FD)²TD). This method has been selected due to the fact that the dispersive characteristic of material can be easily taken into account [9-12]. The GA is chosen for global optimization methods for optimizing the cost-function. The reason stems from the fact that the GA is able to deal with discrete cost-functions with multiple minima and it is possible to parallelize it so it reduces the computational time barrier in using global optimization. Equation (1) shows the proposed cost-function,

$$fitness = -\frac{1}{N} \sum_{i=1}^N \left| \sum_{f=f_1}^{f_2} \sum_{m=1}^M \frac{(E_{m,f,i}^{meas.} - E_{m,f,i}^{simu.})^2}{(E_{m,f,i}^{meas.})^2} \right| \quad (1)$$

where $E_{m,f,i}^{meas.}$ is the measured scattered electric fields, $E_{m,f,i}^{simu.}$ is the simulated scattered fields corresponding to the estimated dielectric properties of the imaging domain obtained by performing a forward simulation, M is the total number of observation points, and N is the total number of transmitters. In equation (1), f refers to different frequencies within f_1 to f_2 sampling frequency band. Increasing the number of observation points increases the possibility of convergence; however, there is a practical limit on the number of observation points. This is due to the limited space and mutual coupling between antennas. To mitigate the ill-posedness of the problem, a multi-illumination system is adopted to collect sufficient amount of data. This approach is based on the use of illuminating electromagnetic source at multiple angles around the observation domain where the scattered electromagnetic field is measured. Mainly, by illuminating the OI with a source at multiple angles, different values of the scattered field are measured.

A. Hybrid genetic algorithm

In inverse problem we propose to find the solution by minimizing the cost-function by using hybrid GA. Hybrid GA combines two different GAs: binary-coded GA (BGA) and real-coded GA (RGA). The BGA and RGA will be discussed separately in the following sections and then we will introduce the hybrid GA, which is the combination of BGA and RGA.

1) Binary-coded GA (BGA):

In BGA optimization, the region is discretized into a number of cells (n). One gene is the type of the specific material and it is distinguished by the Debye parameters. We designed a BGA that considers only limited material types taken from a look-up table, instead of randomly selecting the dielectric properties. The look-up table is created based on *a-priori* information and can be modified for different applications. Since the optimization variables are discrete with integer values, a coding procedure is needed. Each tissue type is represented by a string of q bits, where $q = \log_2(L)$ and L is the total number of different tissue types. For example, if we assume four tissue types (fatty, transitional, fibro-glandular, and malignant tumour) then $L=4$ and $q=2$. After the discretization of the investigation domain (Fig. 2), the number of cells (n) multiplied by the number of bits (q) (that is assigned to each material) will be the size of one chromosome ($q \times n$). Therefore, if the OI is divided into n cells and in the look-up table for each material, two bits are assigned, then the size of the chromosome will be $2n$ bits. The number of unknowns for optimization depends on the number of cells in the investigation domain. Generally, in BGA, as the number of parameters increases, the convergence rate decreases and the memory requirement increases.

2) Real-coded GA (RGA)

In RGA optimization, the chromosome is a floating point number. In the proposed RGA the enclosed imaging domain is discretized into the same number of cells as BGA. Each cell corresponds to a tissue type. Tissue types are differentiated based on their dielectric properties using Debye model [13, 14] (see Table I).

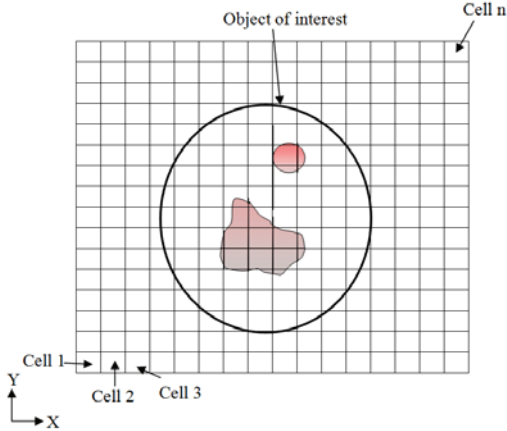


Fig. 2. Discretized the imaging domain for MWT.

Therefore each cell has a set of Debye parameter ($D_j, j=1,2,\dots,n$). j is the index to the cell location (Fig. 2). In conventional RGA, each element is initialized with parameters within the desired range. Depending on the application, the boundary of the permittivity and conductivity is determined. Each gene is a random number picked from a uniform distribution: ($\varepsilon_1 < \varepsilon_j < \varepsilon_2$) and ($\sigma_1 < \sigma_j < \sigma_2$), where ε_1 and ε_2 are the minimum and maximum possible values of the relative permittivity and σ_1 and σ_2 are minimum and maximum values for conductivity. It should be noted that this maximum and minimum number can be defined at a single-frequency, which will not work for a dispersive object. Each gene represents a variable of the problem without any coding or decoding procedure. An array of genes that shows the dielectric properties distribution for an entire imaging domain makes a chromosome. Therefore, for n cells each chromosome has n floating point numbers. Increasing n means that the resolution of imaging domain, and therefore, the search space is increased.

3) Hybrid GA (HGA):

The RGA-based procedure is very slow to converge, and the BGA-based procedure is not able to “fine-tune” the optimum solution. Each of them has some advantages and disadvantages. In fact, the RGA alone might be able to converge to the solution, but it is a laborious and time consuming process. On the contrary, the proposed BGA requires a limited number of possible dielectric properties that may not be realistic in some applications. To overcome these problems, a

hybrid method (HGA) combining the BGA and RGA is introduced.

Figure 3 shows the block diagram of our proposed HGA optimization method. Since the inverse scattering is an ill-posed problem, the solution is non-unique. Therefore, to reduce the search space and regularize the problem, we combined BGA and RGA. First, we start with a BGA procedure until a given stop condition is reached, and then the best candidate solutions found by BGA are chosen as an initial estimate in the first generation of RGA. One of the most critical points for accuracy in image reconstruction is the ability to accurately measure the field at the observation points. Moreover, measurement is always under the influence of external electromagnetic artifacts, which might change the measured scattered field. As well, due to the instability of the inverse problem, the image accuracy might decrease and non-real solution might be resulted by the reconstruction methods. However, the fine-tune capability of RGA in hybrid BGA/RGA improves the image accuracy in the presence of noise in the measurements. We recommend the HGA inverse solver for those applications that deal with complex and large distribution of dielectric properties.

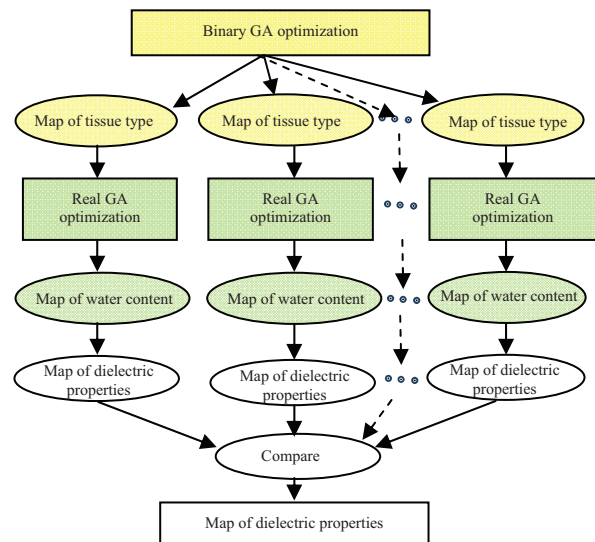


Fig. 3. Block diagram of HGA optimization method.

IV. INVERSION RESULTS

While the ultimate test of any inversion algorithm must involve experimentally collected scattered fields, for validation purpose it is very

useful to have a synthetic data set where the true image is known. We have created synthetic scattered data from a breast model that include a tumour. This application has been chosen due to the heterogeneous structure and dispersive characteristics of the breast. However, the proposed technique can be applied to many other applications. In the MWT imaging technique for breast cancer detection, the patient lies in prone position and the transmitter and receiver antennas are located on a circle around the uncompressed breast (Fig. 4). One antenna transmits a short, low-power microwave pulse and the receiver antennas collect the scattered field around the breast. The scattered signals are then processed to create a two-dimensional image. While a realistic model of the numerical breast phantom should be three-dimensional, two-dimensional models are quite prevalent mainly due to their simplicity [6, 7]. Also, a three-dimension image can be generated using a set of two-dimension images.

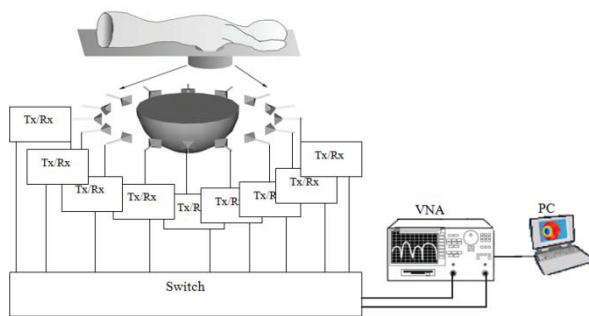


Fig. 4. Clinical imaging system configuration for MWT.

For simulations in this paper, the following parameters have been used. The mesh used for $(FD)^2TD$ simulations consists of 600×600 pixels chosen based on the size of the breast. The cell size (for inversion) is $\Delta = 0.5 \text{ mm}$, which is $\lambda/10$ (where λ is the effective wavelength in the breast tissues at $f=10\text{GHz}$), and the time step is $\Delta t=0.8ps$. Increasing the resolution for the inversion will increase the size of the search space, and consequently, the computational cost. We utilized multiple-frequencies in our techniques for the frequency band between 3 GHz–10GHz, in 1 GHz steps. To enhance the accuracy of the image and reduce the ill-posedness of the problem, four different incident angles (0° , 90° , 180° , and 270°)

have been used (the plane wave rotates 90° for each measurement). With respect to the number of the receivers, increasing the number of receivers provides more information about the object at almost no computational cost. In these simulations there are 100 observation points located in the far-field zone, and the time domain scattered field is measured on a circle around the numerical breast phantom with uniform spacing in the step of 3.6° . From a practical point of view, using 100 probe positions at the observation points around the breast may not be possible in reality due to the size of antenna and mutual coupling between them. We chose this number for the proof of concept. Since we are interested in creating an image of the inner structure of objects, we limit our search space to only the interior of the object. In order to do this, information about the position, dimension, orientation, and surface of the object is required. This information can be found using surface detection methods [16, 17]. This information will be used in the inverse program in order to discretize only inside the object.

The dielectric properties of different tissue types, including normal, malignant, and benign breast tissues were obtained from reduction and cancer surgeries, in the frequency range of 0.5 GHz–20GHz, performed by Lazebnik *et al.* [13, 14]. Figure 5 shows the dielectric properties of different breast tissues created based on Debye model having different levels of water content for 3 GHz–10GHz. As can be seen in this figure, breast tissues may exhibit very low to very high loss at microwave frequencies. These variations depend on the tissue type, and more precisely, on the water content. The water dependency of dielectric properties of breast tissues can be efficiently described in $(FD)^2TD$ numerical method by using the single-pole Debye model [15],

$$\epsilon = \epsilon_0 \left(\epsilon_\infty + \frac{\epsilon_s - \epsilon_\infty}{1 + j\omega\tau_0} - j \frac{\sigma_s}{\omega\epsilon_0} \right) \quad (2)$$

where ϵ_0 is the permittivity of the free space, ϵ_s and ϵ_∞ are the dielectric constants at zero (static) and infinite frequencies, respectively. σ_s is the conductivity at low frequency, ω is the angular frequency, and τ_0 is the relaxation time constant. In order to simplify the problem, the breast tissues are divided into seven groups: three different groups of fibro-glandular tissues, three different

groups of fatty tissues, and one transitional group (Fig. 5). Each group has an upper bound and a lower bound value of dielectric properties, depending on the amount of water content and the frequency. The dielectric properties can be given by,

$$\varepsilon(\omega) = p\varepsilon_u(\omega) + (1-p)\varepsilon_l(\omega) \quad (3)$$

$$(\omega) = p\sigma_u(\omega) + (1-p)\sigma_l(\omega), \quad (4)$$

where the parameter p is a coefficient showing the percentage of water content and it can vary between $[0-1]$, ε_u and σ_u are the relative permittivity and conductivity at the upper bound, respectively, and ε_l and σ_l are the relative permittivity and conductivity at the lower bound of the corresponding group at a specific frequency, respectively.

Therefore, by substituting equations (3) and (4) into the first-order Debye formula the parameters of the Debye model become functions of both water content and the dielectric properties of the lower and upper bounds of each group, can be defined as,

$$\sigma_s = p\sigma_{us} + \sigma_{sl} - p\sigma_{sl} \quad (5)$$

$$\varepsilon_\infty = p\varepsilon_{\infty u} + \varepsilon_{\infty l} - p\varepsilon_{\infty l}, \quad (6)$$

$$\varepsilon_s = p\varepsilon_{us} + \varepsilon_{sl} - p\varepsilon_{sl}, \quad (7)$$

where σ_{su} and σ_{sl} are conductivity at the upper and lower bounds of the corresponding group, respectively, $\varepsilon_{\infty u}$ and $\varepsilon_{\infty l}$ are permittivity at infinite frequency for the upper and lower bounds of the corresponding group, and ε_{su} and ε_{sl} are relative permittivity at zero frequency for the upper and lower bounds of the corresponding group, respectively. The single-pole Debye parameters for the breast tissues are based on the results described by Zastrow *et al.* [18, 19]. At this point, by substituting the new parameters of the Debye model, the water content dependency has been included in (FD)²TD program.

In the following example, we examined the HGA for solving the inverse scattering problem for breast cancer imaging. The HGA is divided into two steps of optimization. At the first step, the BGA is employed in order to determine the type of the tissue for each cell of search space. In the second step, by using RGA, percentages of water content is found. In the BGA, the look-up table consists of first-order Debye parameters for four different tissue types: fibro-glandular, fatty, transitional, and malignant tissues with the water

content percentage of 50 %, given in Table I. Note that in this table we combined all three groups of fibro-glandular tissues into one group of fibro-glandular tissue and all three groups of fatty tissues into one group of fatty tissue and we chose the Debye parameters of the corresponding tissue with 50 % water content.

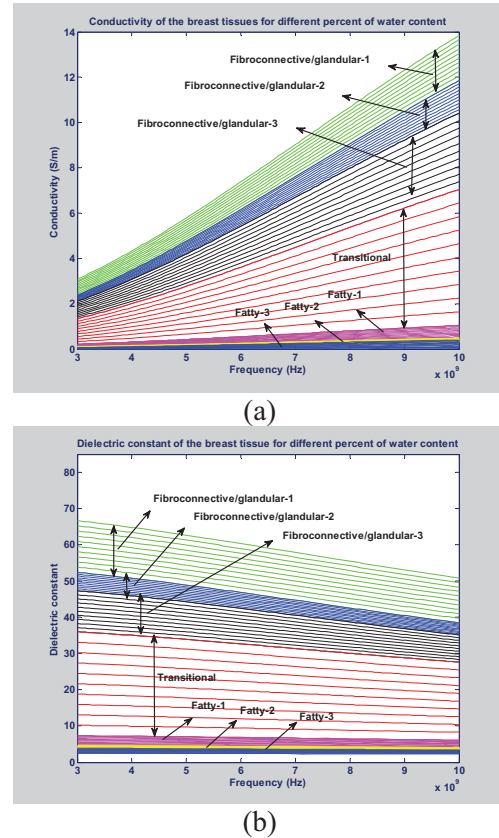


Fig. 5. Debye model of breast tissues dielectric properties (a) conductivity and (b) permittivity.

Table I. Look-up table of the Debye parameters for the BGA.

Medium	Fat	Transitional	Fibro-glandular	Malignant
ε_∞	4.33	22.46	52.02	76.17
ε_s	2.98	8.48	14.00	25.52
$\sigma_s(S/m)$	0.02	0.23	0.78	1.20
τ_0	13.0	13.0	13.0	13.0

The BGA optimization stops when the fitness value does not improve after some number of generations. Then, the best individuals of the last generation in terms of fitness value are passed to the second stage of the optimization, which is RGA. After the process of BGA, the behavior of

the best fitness values at different generations for each individual are studied to choose those individuals that show an increase in the fitness value consistently, and they were passed to RGA. This selection can decrease the chances of getting stuck in a local minimum and can increase the chance of finding the global optimum solution. For the RGA, the look-up table consists of first-order Debye parameters from the upper to lower end of the range for four different types of breast tissue (Table II).

Table II. Look-up table of the Debye parameters for the RGA.

Medium	Fat	Transitional	Fibro-glandular	Malignant
$\epsilon_{\infty U}$	3.987	12.990	23.200	9.058
$\epsilon_{\infty L}$	7.535	37.190	69.250	60.360
$\sigma_{su}(S/m)$	0.080	0.397	1.306	0.899
$\epsilon_{\infty l}$	2.309	3.987	12.990	23.200
ϵ_{sl}	2.401	7.535	37.190	69.250
$\sigma_{sl}(S/m)$	0.005	0.080	0.397	1.306
$\tau_0(ps)$	13.0	13.0	13.0	13.0

In this stage, for those individuals that are chosen by BGA, the tissue types remain constant, but the percentage of water content (p) can vary between 0% and 100%. RGA uses $p_i, i=1,2,\dots,n$ as genes. A combination of n gene gives a chromosome, where p is a floating point number between 0 and 1. Then equations (3), (4), and Table II are used to find tissue properties. Figure 6 shows a sub-sampled version of a cross-section of an MRI in the numerical breast phantoms repository of [20]. The measurement scattered field values are replaced by simulated data (hypothetical measured data) obtained by the Richmond method [21] to avoid the inverse crime. A 2D cross-section of a breast is divided into 18 equal regions.

In the first stage of the optimization process, typical Debye parameters are assigned to each category of the tissue type (fatty, transitional, fibro-glandular) assuming 50 % water content (Table I). Then, the BGA is used to find the tissue type. The best 4 solutions are then passed to the second stage where the RGA is used to find the water content. In this stage, the search space is limited to the range of the dielectric properties of each tissue type. After 200 generations of the RGA, the best candidate is chosen for further calibration and the other three candidates are

removed from the optimization process. For the winning candidates, the GA runs for 300 more generations to obtain the final result. Parallel programming is used in RGA [22, 23].

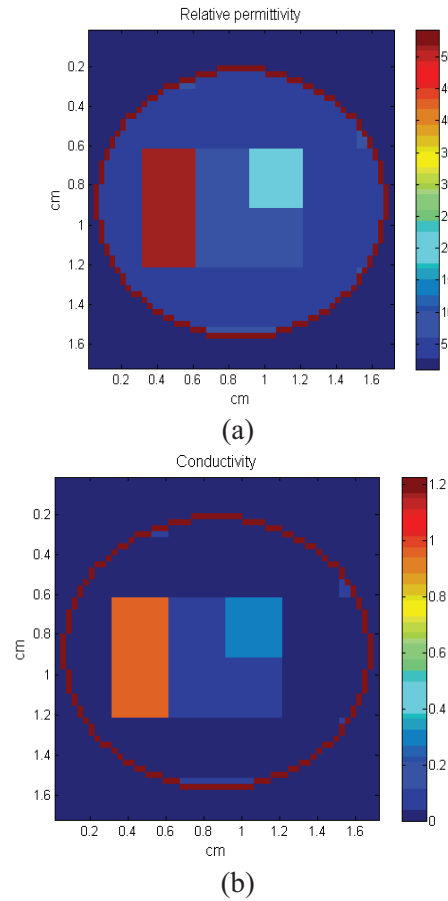


Fig. 6. (a) Relative permittivity and (b) conductivity of the numerical breast phantom obtained by sub-sampled breast MRI at $f=6$ GHz.

Figure 7 (a) shows the average fitness value of the solutions of the BGA over 200 generations. Figure 7 (b) shows the improvement of the 4 candidates after 300 generations. The fitness value of one of the candidates significantly improves while for the other 3 do not show a significant improvement. This implies that for those candidates, the tissue type was not predicted correctly in the first stage. Figure 8 shows the reconstructed dielectric properties of the phantom shown in Fig. 6. It shows that the hybrid technique was able to correctly recognized the tissue types but the amount of water content was slightly different from the original image. This is due to the limited number of generations that we considered in this example.

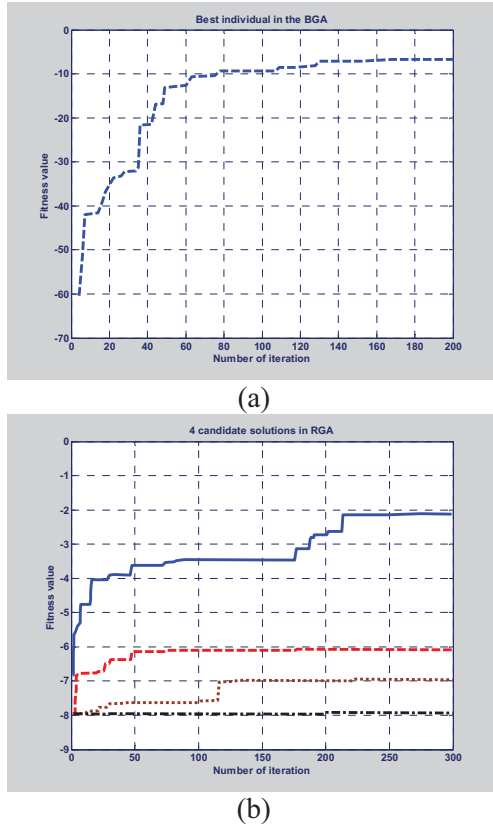


Fig. 7. (a) Trajectory of the fitness value of the best individual in the BGA and (b) trajectory of the fitness value of the 4 candidate solutions passed to RGA.

Two other optimization methods using BGA only and RGA only are implemented for comparison purposes. The hybrid method overall performs $(4 \text{ (angle)} \times 30 \text{ (individual)} \times 200 \text{ (BGA generation)}) + (4 \text{ (angle)} \times (\text{individual}) \times 300 \text{ (RGA generation)}) = 60,000$ function evaluations. In order to be comparable with the hybrid method, the BGA and the RGA should run for 500 generations with 30 individuals in each iteration. This results in 60,000 function evaluations. In this case, we used Table I for BGA and for the RGA, we considered the reconstructed relative complex permittivity within physical ranges $1.0 \leq \epsilon_r \leq 80.0$ and $0.0 \leq \sigma \leq 15.0$ S/m, with one decimal point accuracy. Figure 9 shows the result of the BGA and the RGA after 500 generations. Neither of these methods (RGA alone or BGA alone) was able to converge to the right solution within 500 iterations. In addition, because four cases are optimized in parallel by RGA, the hybrid method is faster than both BGA and RGA alone. The

convergence of the examples provided in this paper by using 64 nodes and 64G RAM took around four hours and thirty minutes.

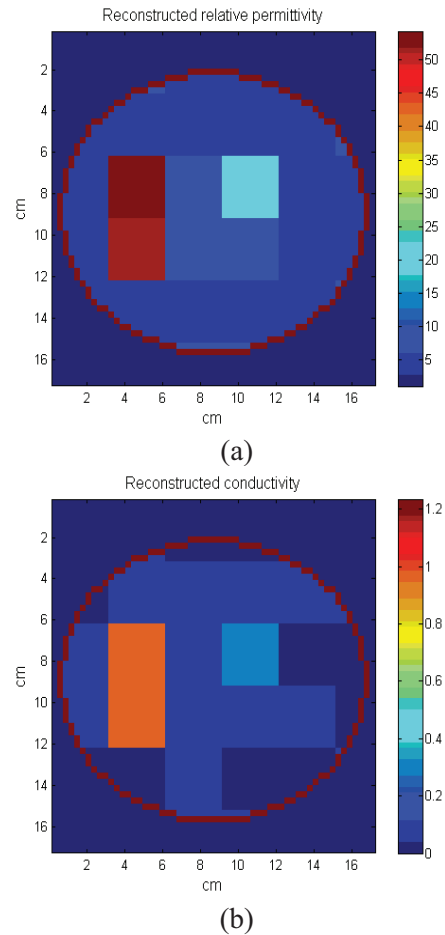


Fig. 8. Result of the HGA method for the numerical phantom of Fig. 6 (a) permittivity and (b) conductivity at $f=6$ GHz.

In breast imaging, the typical range of the dielectric properties is limited and is determined by *a-priori* knowledge about the tissues existing in the breast. By limiting the search space to first finding the tissue type and then finding the water content for a specific tissue type, the proposed method decreases the possibility of the non-physical solutions from the search space. This is an advantage over many of the local optimization methods used in inverse scattering, and those that use a regularization terms with smoothing effects. Additionally, the proposed method is potentially able to reconstruct sharp profiles, which occur frequently in breast imaging.

From a practical point of view, the use of the 2D-TM approximation for what is really a 3D problem will introduce modeling error into the utilized inversion algorithm. Therefore, the modeling calibration is required to reduce the error. While reducing the model error is feasible, it needs substantial additional work that is beyond the scope of this paper. In this section, we propose ways to do the modeling calibration. Modeling calibration is the process of adjusting the raw 3D scattered field data such that it can be effectively employed by the approximate 2D models upon which the inversion algorithms are based. To reduce this modeling error, effort needs to be placed on calibrating the 3D model into 2D approximation. We need to introduce a calibration step (modeling calibration) in order to eliminate some of the experimental errors affecting field measurements, such as antennas, mutual coupling between co-resident non-active antennas, and the effects of boundaries on antenna characteristics. In order to calculate the calibration factor, we should have modeled the entire setup including the antennas and boundary using a more accurate (but much slower) 3D numerical technique for a given chamber configuration and the calibration factors should be provided as an input to the inversion algorithms without slowing them down. This procedure of simulating the 3D of the entire imaging chamber can be expedited using symmetric algorithm [24]. The modeling calibration is made for efficiency, because the behavior of electric fields within a 2D environment can be easily described with 2D FDTD and it can be repeatedly evaluated very quickly (when compared to a much slower 3D techniques) allowing the iterative imaging algorithms to converge to a solution in a reasonable amount of time.

V. CONCLUSION

In breast imaging, the typical range of the dielectric properties is limited and are determined by *a-priori* knowledge about the tissues existing in breast. By limiting the search space to first finding the tissue type and then finding the water content inside the range of the dielectric properties of that tissue type, the proposed method enables non-physical solutions to be removed from the search space. This is in contrast with many of the local optimization methods that are used in inverse

scattering, which use a regularization term with smoothing effects. Hence, the proposed method is potentially able to reconstruct sharp profiles that occur frequently in breast imaging.

In conclusion, the proposed hybrid binary-real genetic algorithm increases the convergence speed in the application of microwave imaging for breast cancer. This method uses *a-priori* knowledge of the dielectric properties of the breast tissue and inherent advantage of binary GAs in discrete search spaces and real GAs in continuous search spaces.

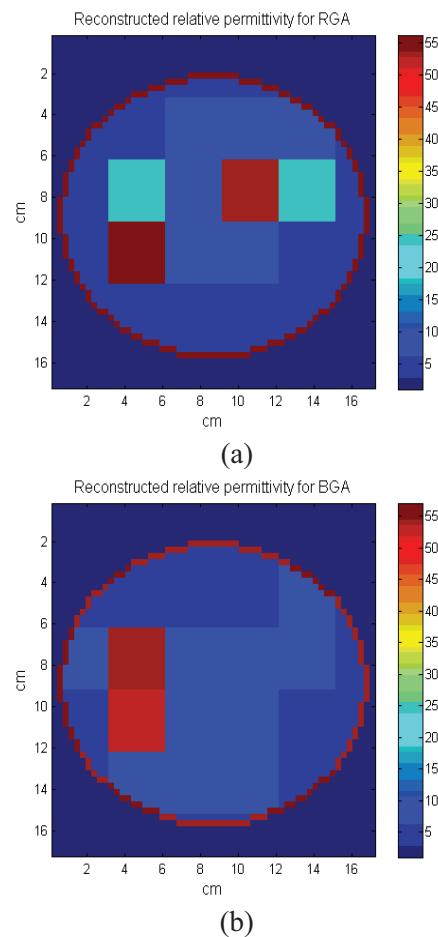


Fig. 9. Result of the (a) RGA and (b) BGA methods for relative permittivity at $f = 6$ GHz.

ACKNOWLEDGMENT

The authors would like to acknowledge the financial support of Wilkes University, Natural Sciences and Engineering Research Council of Canada, Cancer Care Manitoba, and University of North Dakota. Also constructive discussions with

Dr. L. Shafai and Dr. P. Thulasiraman are greatly appreciated.

REFERENCES

- [1] M. Pastorino, "Stochastic optimization methods applied to microwave imaging: A review," *IEEE Trans. Antennas Propagat.*, vol. 55, no. 3, pp. 538-548, 2007.
- [2] A. Sabouni, S. Noghianian, and S. Pistorius, "A global optimization technique for microwave imaging of the inhomogeneous and dispersive breast," *Canadian Journal of Electrical and Computer Engineering*, vol. 35, no.1, pp. 15-24, 2010.
- [3] A. Sabouni, A. Ashtari, S. Noghianian, G. Thomas, and S. Pistorius, "Hybrid binary-real GA for microwave breast tomography," *IEEE Antennas and Propagation Society International Symposium*, 2008.
- [4] A. Ashtari, S. Noghianian, A. Sabouni, and G. Thomas, "Hybrid binary real genetic algorithms for microwave image reconstruction," *24th Annual Review of Progress in Applied Computational Electromagnetics Society*, pp. 116-121, Niagara Falls, Canada, 2008.
- [5] A. Sabouni and S. Noghianian, "Study of penetration depth and noise in microwave tomography technique," *Applied Computational Electromagnetics Society (ACES) Journal*, vol. 28, no. 5, pp. 391-403, 2013.
- [6] T. Rubk, P. Meaney, P. Meincke, and K. Paulsen, "Nonlinear microwave imaging for breast-cancer screening using Gauss-Newton's method and the CGLS inversion algorithm," *IEEE Trans. Antennas Propagat.*, vol. 55, no. 8, pp. 2320-2331, 2007.
- [7] P. Meaney, K. Paulsen, S. Geimer, S. Haider, and M. Fanning, "Quantification of 3-d field effects during 2-d microwave imaging," *IEEE Trans. Biomed. Eng.*, vol. 49, no. 7, pp. 708-720, 2002.
- [8] A. Sabouni, S. Noghianian, and L. Shafai, "Transverse electric and magnetic components of field measurement for microwave breast cancer imaging," *International Symposium on Antenna Technology and Applied Electromagnetics the American Electromagnetics Conference*, Ottawa, Canada, 2010.
- [9] A. Taflov and S. C. Hagness, *Computational Electrodynamics: The Finite-Difference Time-Domain Method*, 3rd ed. Artech House, Norwood, 2005.
- [10] A. Elsherbeni and V. Demir, *The Finite Difference Time Domain Method for Electromagnetics: With MATLAB Simulations*, SciTech Publishing Inc., 2009.
- [11] M. Bui, S. Stuchly, and G. Costache, "Propagation of transients in dispersive dielectric media," *IEEE Trans. Microw. Theory Tech.*, vol. 39, no. 7, pp. 1165-1172, 1991.
- [12] A. Sabouni, S. Noghianian, and S. Pistorius, "Frequency dispersion effects on FDTD model for breast tumor imaging application," *IEEE International Symposium on Antennas and Propagation*, pp. 1410-1413, 2006.
- [13] M. Lazebnik, L. McCartney, D. Popovic, B. Watkins, M. Lindstrom, J. Harter, S. Sewall, A. Magliocco, J. Booske, M. Okoniewski, and S. Hagness, "Large-scale study of the ultra wideband microwave dielectric properties of normal breast tissue obtained from reduction surgeries," *Physics in Medicine and Biology*, vol. 52, pp. 2637-2656, 2007.
- [14] M. Lazebnik, D. Popovic, L. McCartney, C. Watkins, M. Lindstrom, J. Harter, S. Sewall, T. Ogilvie, A. Magliocco, T. Breslin, D. Temple, W. Mew, J. Booske, M. Okoniewski, and S. Hagness, "A large-scale study of the ultra wideband microwave dielectric properties of normal, benign, and malignant breast tissues obtained from cancer surgeries," *Physics in Medicine and Biology*, vol. 52, pp. 6093-6115, 2007.
- [15] A. Sabouni, S. Noghianian, and S. Pistorius, "Water content and tissue composition effects on microwave tomography results," *International Review of Progress in Applied Computational Electromagnetics (ACES)*, 2008.
- [16] D. Woten and M. El-Shenawee, "Quantitative analysis of breast skin for tumor detection using electromagnetic waves," *Applied Computational Electromagnetics Society (ACES) Journal*, vol. 24, no. 5, pp. 458-463, 2009.
- [17] T. Williams, J. Sill, J. Bourqui, and E. Fear, "Tissue sensing adaptive radar for breast cancer detection: Practical improvements," *IEEE International Symposium on Antennas and Propagation*, 2010.
- [18] E. Zastrow, S. Davis, M. Lazebnik, F. Kelcz, B. Veen, and S. Hagness, "Database of 3d grid-based numerical breast phantoms for use in computational electromagnetics simulations," *Instruction manual*, 2007.
- [19] E. Zastrow, S. Davis, M. Lazebnik, F. Kelcz, B. Veen, and S. Hagness, "Development of anatomically realistic numerical breast phantoms with accurate dielectric properties for modeling microwave interactions with the human breast," *IEEE Trans. Biomed. Eng.*, vol. 55, no. 12, pp. 2792-2800, 2008.
- [20] E. Zastrow, S. Davis, M. Lazebnik, F. Kelcz, B. Veen, and S. Hagness, "Database of 3D grid-based numerical breast phantoms for use in

computational electromagnetics simulations,” *Instruction Manual*, University of Wisconsin-Madison.

- [21] J. Richmond, “Scattering by a dielectric cylinder of arbitrary cross sectionshape,” *IEEE Trans. Antennas Propagat.*, vol. 13, no. 3, pp. 334-341, 1965.
- [22] M. Xu, A. Sabouni, P. Thulasiraman, S. Noghianian, and S. Pistorius, “Image reconstruction using microwave tomography for breast cancer detection on distributed memory machine,” *International Conference on Parallel Processing*, 2007.
- [23] —, “A parallel algorithmic approach for microwave tomography inbreast cancer detection,” *IEEE International Parallel and Distributed Processing Symposium*, pp. 1-8, 2007.
- [24] A. Sabouni, M. Pavlovic, M. Ostadrahimi, and S. Noghianian, “Three dimensional accurate modeling of the microwave tomography imaging system,” *IEEE Antenna Propagation International Symposium*, Spoken, USA, 2007.



Abas Sabouni received the M.Sc. degree inelectrical engineering from K. N. Toosi University, Tehran, Iran, in 2005, and Ph.D. degreein electrical engineering, from the Universityof Manitoba, Winnipeg, MB, Canada, in 2011.

Since 2013, he has been an Assistant Professor in the Departmentof Electrical Engineering and Physics, Wilkes University, Wilkes-Barre, PA, USA. From 2010 to 2013, he was a Post-Doctoral Fellow in Biomedical Engineering Department at the Ecole Polytechnique de Montreal, and Research Associate at the Department of Electricaland Computer Engineering at the Concordia University. He was a Research and Development Engineer at Parto Dadeh Inc., Tehran, Iran during 2001 through 2004. During 2005 and 2006, he was a Research Assistant in the Electromagnetic Group, Universityof Manitoba and a Research Associate at Cancer Care Manitoba. From 2009 to 2010, he was a Research Associate in the Department of Electrical Engineering, University of North Dakota, Grand Forks, North Dakota, USA. His research interests include inverse scattering problem, microwave imaging, UWB antenna design and modeling, and transcranial magnetic stimulation. Dr. Sabouni is the recipient of the IEEE AP-S Honorable Mention Student Paper Contest 2008. In 2013, he served as the Vice-President of IEEE Montreal section. From 2010 to 2013, he was the Chair of IEEE Montreal Antenna Propagation Chapter.



Ali Ashtari received bachelor and masters of science in Electrical Engineering from Sharif University of Technology, Iran and a PhD in Electrical and Computer Engineering from University of Manitoba, Canada in 2001, 2004 and 2009 respectively. He is currently the Research Lead at Invenia Technical Computing. Ali has extensive academic (Ph.D) and industrial experience in signal processing, statistics, numerical methods and optimization applied to various problems ranging from biomedical applications and renewable energy to electricity markets.



Sima Noghianian received the B.Sc. degree in Electrical Engineering from the Sharif Universityof Technology, Tehran, Iran, in 1992, and the M.Sc. and Ph.D. degrees, both in Electrical Engineering, from the University of Manitoba, Winnipeg, Canada, in

1996 and 2001, respectively. In 2001, she was at Yotta Yotta Corporation, Edmonton, Canada. She was an Assistant Professor in the Department of Electrical Engineering, Sharif University of Technology during 2002 and 2003. From 2003 to 2008, she was an Assistant Professor in the Departmentof Electrical and Computer Engineering, University of Manitoba. Since 2008, she has been an Assistant Professor in the Departmentof Electrical Engineering, University of North Dakota, Grand Forks. Her research interests include antenna design and modeling, wireless channel modeling, ultrawideband antennas, and microwave imaging. Dr. Noghianian was IEEE Winnipeg Waves (joint Chapter of Antennaand Propagation/Microwave Theory and Techniques/Vehicular Technologysocieties) Chapter Chair during 2004 and 2005. She received a Postdoctoral Fellowship from Natural Sciences and Engineering Research Council of Canada at the University of Waterloo in 2002.



Gabriel Thomas received the B.Sc. degree in Electrical Engineering from the Monterrey Institute of Technology, Monterrey, Mexico, in 1991, and the M.Sc. and Ph.D. degrees in Computer Engineering from the University of Texas, El Paso, in

1994 and 1999, respectively. Since 1999, he has been a faculty member in the Department of Electrical and Computer Engineering, University of Manitoba,

Winnipeg, MB, Canada, where he is currently an Associate Professor. He is coauthor of the book "Range Doppler Radar Imaging and Motion Compensation". His current research interests include digital image and signal processing, computer vision and nondestructive testing.



Stephen Pistorius is a Physics Professor and an Associate Professor of Radiology at the University of Manitoba (UM) and a Senior Scientist at Cancer Care Manitoba (CCMB). Educated in South Africa, he holds B.Sc., Hons. B.Sc. (Radiation Physics), M.Sc. (Medical Physics) and Ph.D. degrees. Prior to certifying as a Medical Physicist in 1986 he worked in industry. He practiced in Cape Town before moving to Canada as a Senior Medical Physicist at CCMB. In 1995 he was appointed Director of Medical Physics and was promoted to Provincial Director in 2000, an executive position which oversaw 70+ staff responsible for RT Physics, Imaging, Radiation Protection, Engineering, Teaching and Research. He is a Senior Member of the IEEE and a professional physicist and in 2005 he obtained a Post-Graduate Diploma in Business Administration from the Edinburgh Business School. Prof. Pistorius served as the President of the Canadian Organization of Medical Physicists (COMP) and is currently the Director of Professional Affairs for the Canadian Association of Physicists. In 2010 he chose to focus on research and teaching and currently serves as the Director of the UM Medical Physics graduate program and Vice-Director of the Biomedical Engineering graduate program. Prof. Pistorius uses fundamental physics to improve and quantify diagnostic and therapeutic techniques and is interested in radiation transport in clinical imaging and treatment modalities. He has supervised and examined 30+ graduate students and currently advises 3 PDF's and 10 graduate students working on cancer imaging research; developing systems for cancer diagnosis which use photon scattering to enhanced CT and PET; microwave imaging and the use of MV radiation to image RT patients to optimize treatments by accounting for motion. He is the author of over 170 publications and presentations, serves on many scientific advisory boards and grant review panels and has a number of national and international awards to his name. In 2012 he was honored as a Fellow of COMP.

Imaging 2D Breast Cancer Tumor Margin at Terahertz Frequency using Numerical Field Data based on DDSCAT

T. C. Bowman, A. M. Hassan, and M. El-Shenawee

Department of Electrical Engineering
University of Arkansas, Fayetteville, AR 72701, USA
tcbowman@uark.edu, amhassan@uark.edu, magda@uark.edu

Abstract – This work presents tomography of breast cancer tumor margins in the terahertz frequency band. The discrete dipole approximation is employed to calculate the electromagnetic fields scattered from simulated heterogeneous breast tumors. Two-dimensional Comedo with necrotic core and papillary breast tumor patterns are computer-generated for this investigation. The Rytov approximation is applied to terahertz scattered field data calculated at a line of receivers in the far field from the samples. The obtained tomography images demonstrate a potential for terahertz frequency for identifying and assessment of breast cancer tumor margins.

Index Terms – Breast cancer, discrete dipole approximation (DDSCAT), Rytov tomography, and terahertz imaging.

I. INTRODUCTION

In the conservative treatment of sufficiently small breast tumors, lumpectomy is the preferred procedure for excising cancerous tissues. In this treatment, the tumor is removed via surgery in addition to a few millimeters of healthy tissue surrounding the tumor. The margins of this removed tumor are examined by pathologists via histo-pathological analysis and classified into one of three types. A *positive* margin indicates that cancerous tissue exceeds the edge of the healthy margin; a *negative* margin indicates that there is no cancerous tissue within 1-2mm of the edge; and a *close* margin indicates that the cancerous tissue lies less than 1 mm of the margin boundary but does not exceed it. In the case of a positive or close margin identified in the excised tissue, a

second surgery is required to remove the remaining cancerous tissues.

However, pathology analysis of these margins generally requires several days in order to be processed fully, meaning that any secondary procedure will require the patient to return at a later date. Furthermore, it is reported in [1] that up to 20-70 % of the time, pathology reports indicate the presence of positive margins following the lumpectomy. It is also mentioned that the need for a second surgery at a later date increases the risk of patient breast disfigurement, increases the resource burden on the patient, and decreases patient morale and confidence in the surgeon [1].

As reported in [2], an ideal technique for improving cancer margin assessment would be able to analyze the excision intra-operatively with a sensing depth of at least 1-2 mm. It would furthermore need to provide a 3D image of the tumor surface that is easily read by a surgeon in the operating room. The developed technique would need to be accurate enough to reduce repeated surgery rates by allowing surgeons to detect and remove cancerous tissue within the same procedure as the lumpectomy.

Recently, the terahertz (THz) frequency range has been suggested as a potential tool in the use of cancer detection and classification [3-5]. THz imaging is attractive for its ability to penetrate materials to a depth of several millimeters, giving it an advantage over optical techniques in addressing the concerns reported in [2]. Terahertz waves also lack the polarization energy of x-rays, making them more attractive for *in vivo* applications, as well as having a higher resolution than microwave imaging. The THz range from 0.01 THz to 2 THz has been shown to be

particularly useful for cancer detection due to noticeable differences in electrical properties between cancerous and healthy tissue in tumors taken from the breast and colon [3-5]. The assertion of inherent contrast of cancerous cells at high frequency has also been suggested in model-based photonics for the early detection of breast cancer [6]. However, the focus of this work is the use of a numerical THz model based on the discrete dipole approximation (DDSCAT). Additionally, the model is not for detecting breast tumors but for investigating the scattering from excised cancerous tissue in the terahertz band.

The authors of this work conducted preliminary experimental THz measurements from very few excised breast tissue samples fixed in formalin and embedded in paraffin (FFPE) [7]. The experimental THz imaging measurement reported in [7] was based on the directly reflected electric field from flat tissue samples. While the reported THz images in [7] were not adequate to assess tumor margins or cancer regions, the conclusions motivated the authors to first conduct modeling and simulation of the problem before proceeding further with the experimental work. An abstract of the current work has been previously presented in conferences [8, 9].

The goal of this paper is to simulate the tomography problem of cancer margins in order to understand the strengths and limitations, if any, of THz techniques for this application. The idea is to employ a modeling technique to calculate scattered electric fields from excised breast tumor samples using the setup diagrammed in Fig. 1 and to implement a computer tomography method to reconstruct the cancer margins. This work adopts the DDSCAT that has proven capability for calculating the scattered electric and magnetic fields from heterogeneous two- and three-dimensional objects [10-14]. To reconstruct the image of tumor margins, the well-known Rytov tomography algorithms will be applied to the synthetic simulated data [15-19]. Section II discusses the modeling methods and section III presents the numerical results. Conclusion and future work are presented in the section IV.

II. METHODOLOGY

A. Tumor model

In this work, the tumor patterns are generated using a multiple-nutrients tumor growth model

developed by Ferreira *et al.* [20]. In the model, two nutrients are employed: (i) nutrient M necessary for survival of the cancerous cells and (ii) nutrient N necessary for the division of the cancerous cells. The utilization of two nutrients provides extra degrees of freedom that can be used to generate a wide variety of histologically accurate tumor patterns. The model is based on the diffusion of the nutrients M and N and the consumption of these nutrients by cancerous and healthy cells [20]. Healthy cells consume both nutrients N and M at a rate of α normalized values per unit time whereas cancerous cells consume nutrient N at a rate of $\lambda_N \times \alpha$ and consume nutrient M at a rate of $\lambda_M \times \alpha$. The parameters λ_N and λ_M are assumed larger than unity to account for the elevated consumption of nutrients by cancer cells. At each time step, the values of the nutrients N and M are updated according to their diffusion and consumption by cancer and healthy cells.

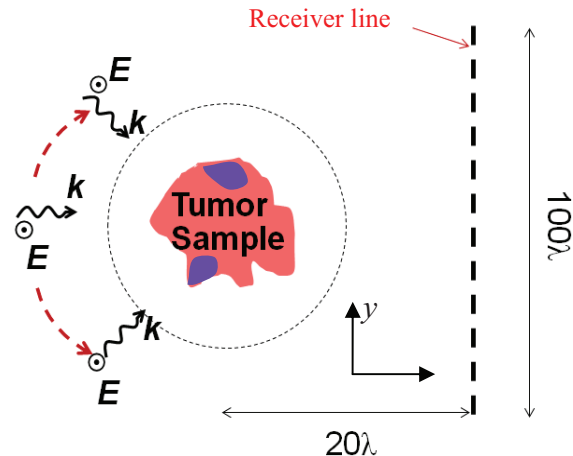


Fig. 1. 2D computational configuration of tumor sample, incident plane waves, and receiver line.

In addition, two cellular activities are implemented: (i) cell division and (ii) cell death. The probability of a cell dividing at a certain pixel is expressed as a function of the nutrient N at that pixel. The probability of a cell dying at a certain pixel is expressed as a function of the nutrient M at that pixel [20]. By varying the parameters α , λ_N , and λ_M , different tumor patterns can be generated [21]. The particular tumor patterns developed and used in this paper are the Comedo pattern with a central necrotic core and the papillary pattern, as shown in Fig. 2 [21]. Each black square in the figure represents a cancer cell. These tumor

patterns were generated using a square computational domain of size 60×60 pixels [21]. The parameters used to generate the Comedo pattern in Fig. 2 (a) are ($\alpha = 0.032$, $\lambda_N = 220$, $\lambda_M = 220$), and the parameters used to generate the papillary pattern in Fig. 2 (b) are ($\alpha = 0.05$, $\lambda_N = 250$, $\lambda_M = 20$). More details about the model implementation and parameters are found in [20-21].

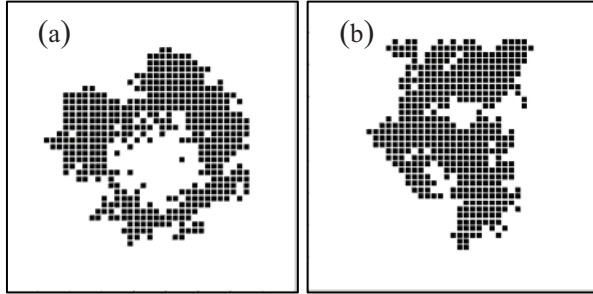


Fig. 2. (a) Comedo tumor pattern with necrotic core and (b) Papillary tumor pattern [21].

B. Discrete dipole approximation (DDSCAT)

For simplicity, in this work a two dimensional (2D) forward model will be implemented using the open source DDSCAT computer code available in serial or in MPI accelerated computer codes [13, 14]. The DDSCAT method is used for calculating the scattered electric fields from a simulated heterogeneous breast sample tissue as demonstrated in Fig. 1. This model is very desirable to simulate objects made of dispersive materials where the target under test is discretized into smaller particles, i.e., dipoles, of size very small compared with the wavelength. Examples of this discretization are shown in Fig. 3.

Each dipole in Fig. 3 can be made of a different anisotropic material. Therefore, the DDSCAT has the advantage of modeling highly heterogeneous targets, which presents a realistic method to model breast cancer tumor tissue. While there are other forward solvers to handle heterogeneous objects such as the finite difference time domain and finite element, among others, the DDSCAT requires that only the target be discretized and not the whole domain, making it attractive from the perspective of CPU time and memory requirements. The accuracy of the DDSCAT was numerically compared with four known methods: the Mie theory, the T-matrix

method, the finite element method (ANSOFT HFSS), and the finite difference time domain (numerical FDTD solutions version 5.0) [22].

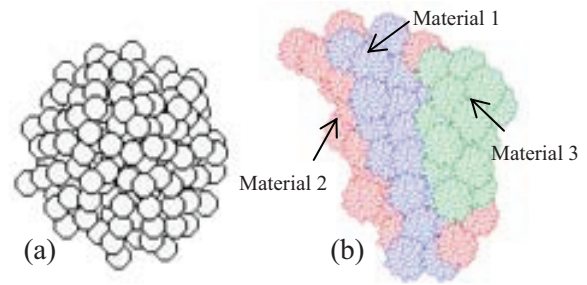


Fig. 3. (a) Sketch of a homogeneous object discretized into particles (i.e., dipoles) and (b) heterogeneous medium of irregular boundaries discretized into dipoles (reproduced) [11].

The dipoles of the discretized object in Fig. 3 acquire dipole moments in response to a local electric field. The method converges when $|n|kd < 0.5$, where k is the wavenumber, d is the dipole size, and n is the complex index of refraction [10-14]. The method solves for the dipole moments at all dipole positions. The main equation of the open source code and additional details are given in appendix A and in references [10-14].

C. Linearized inverse scattering technique

The well-known Rytov algorithm approximates the nonlinear inverse scattering problem as a linear problem [15-19]. Thus the relation of the scattered field phase to the function of the object shape becomes linear. The refractive index of the unknown object is then obtained using the filtered back propagation (FBP) scheme. While Rytov linearized tomography method has the limitation of low contrast between the target and background, it offers implementation simplicity and good results in THz applications [23].

In Rytov approximation, the assumption is that the phase of the scattering field has small variations over a single wavelength. As the result, a linear relationship is assumed between the phase of the scattered field and the target object [16-18]. The relationship between the phase of the scattered and incident fields is expressed as follows [16-18, 24],

$$\psi_s(\vec{r}) = \frac{1}{\psi_{inc}(\vec{r})} \int_V G(\vec{r} - \vec{r}') \psi_{inc}(\vec{r}') O(\vec{r}') d\vec{r}' \quad (1)$$

where $\psi_s(\vec{r})$ represents the phase of scattered fields and $\psi_{inc}(\vec{r})$ represents the phase of the incident fields, \vec{r} and \vec{r}' represent the position vectors of the observation and source, respectively, V is the computational volume, $G(\vec{r}-\vec{r}')$ is the dyadic Green's function, and $O(\vec{r}')$ is the profile of the unknown object to be reconstructed. The Fourier diffraction theorem is employed to reconstruct the profile of the unknown object. There are two possible methods to produce final results: the direct Fourier interpolation (DFI) and the filtered back propagation (FBP) algorithm. The difference between these methods lies in the way that the Fourier transform of the scattered-field data is interpolated. It is proven in [19] that the FBP method produces more reliable results and avoids some artifacts associated with the interpolation in the spatial frequency domain [19].

The Rytov algorithm requires the availability of the scattered fields from multiple incident directions, where the phase of these fields are as shown used in equation (1). In DDSCAT the excitation is a plane wave propagating in the positive x -direction (see Fig. 4). To achieve these multiple incident directions in DDSCAT, the target is rotated around the z -axis, which is effectively equivalent to rotating the incident directions. Thirty six equally-spaced orientations of the target around its axis are simulated. In each simulation, the fields scattered from the target are calculated. Since the simulation at each orientation is completely independent from the other orientations, an MPI code was developed to call 36 instances of DDSCAT, one for each orientation, in parallel on the STAR of Arkansas supercomputer. This reduces the computational time significantly to 1/36 of the value that would have been necessary if the orientations were run sequentially. Once the unknown index of refraction of the tissue is obtained using equation (1) at each pixel of the domain of Fig. 1, the image is reconstructed. More details can be found in [15-19].

III. NUMERICAL RESULTS

All examples in this Section are modeled at frequency $f=1$ THz ($\lambda = 300 \mu\text{m}$) with 36 incident plane waves at angles evenly distributed around the 2D tumor sample shown in Fig. 1. The

scattered electric fields are calculated on a line of 36 receivers of 100λ long and at a distance of 20λ from the center of the simulation domain as shown in Fig. 1.

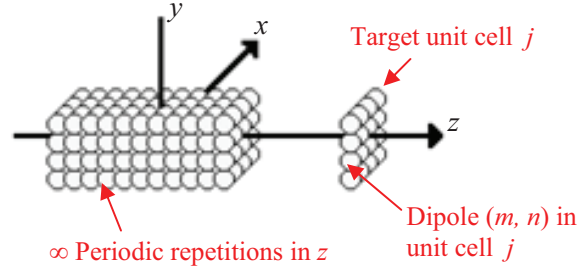


Fig. 4. DDSCAT model of infinite cylinder (reproduced) [11].

Figure 5 shows the DDSCAT model of the Comedo tumor pattern given in Fig. 1 (a). At 1 THz, cancerous tissue has $\epsilon_r = 4$ and fibrous tissue has $\epsilon_r = 3.6$. However, in this setup the cancerous tissue is assumed to have $\epsilon_r = 1.133$ and the surrounding fibrous (i.e., fibroglandular) tissue background $\epsilon_r = 1.03$. These values were selected such that the relative contrast between cancer and fibrous tissue is retained as $1.133/1.03 = 1.1$ compared to $4/3.6 = 1.1$ using the actual permittivity values. The lower permittivity values in this model are necessary for the use of Rytov approximation to find the contrast from the scattered field [15], since reconstructing the properties of the cancerous tissue relative to the fibrous background is the main interest of this work. The spacing of the dipoles is set to 0.04λ at 1 THz.

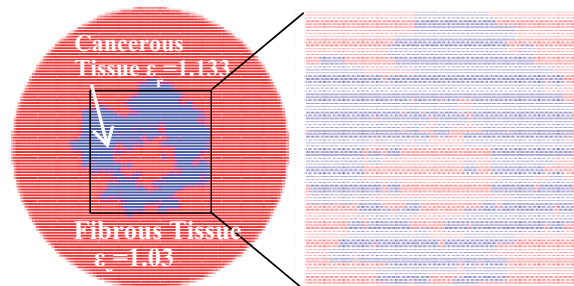


Fig. 5. 2D dipole discretization of necrotic breast cancer tumor type using $N = 12281$ dipoles, tumor size $\sim 1.5\text{mm}$. Dipole size $d = 0.04 \lambda = 12 \mu\text{m}$.

In all cases in this section, the tumor is discretized into $N = 12281$ dipoles with tumor size ~ 1.5 mm, and the dipole size is $d = 0.04 \lambda = 12 \mu\text{m}$ with an infinitesimal gap between dipoles (i.e., distance from center to center between each two dipoles is also d). The viability of tomography algorithms in imaging cancer tumor patterns is investigated through several different cancer tissue orientations. In the first example of Fig. 6, the goal is to show whether the algorithm could properly reconstruct the permittivity of cancerous tissue at the middle or the edge of tumor tissue (i.e., for negative and close to positive margins). The results show good reconstruction of cancerous tissue in both cases in Fig. 6. These simulations did not account for any noise.

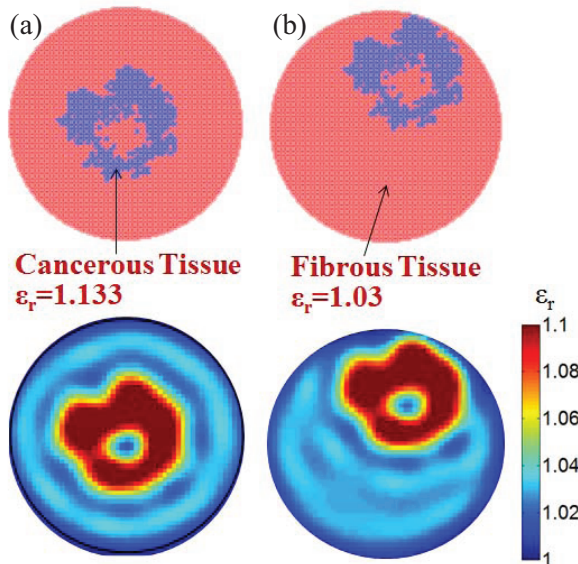


Fig. 6. Discretized DDSCAT comedo tumor (top) and reconstructed permittivity (bottom) of (a) a cancerous region with a negative margin and (b) a positive margin.

The case of Fig. 6 is repeated including random noise added to the data, up to SNR of 0 dB. The obtained images showed insignificant difference with Fig. 6 (not presented here). Figure 7 represents a similar case to Fig. 6 but for the papillary tumor pattern. The same relative permittivities of Fig. 6 are used in this case. The results show good image reconstruction as well. In order to determine the algorithm's ability to distinguish heterogeneous regions of fibrous or other normal tissue, the example of Fig. 8 is shown. In this case the permittivity of the cancerous tissue and primary

background tissue are the same as in Fig. 6, but a secondary region of fibrous tissue with $\epsilon_r = 1.08$ is used in the model. The results show successful reconstruction of the permittivity of all three tissue regions.

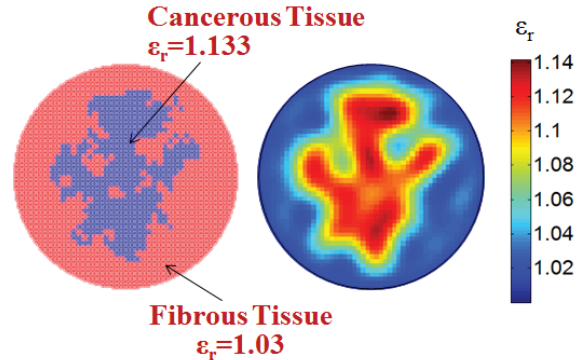


Fig. 7. Discretized DDSCAT papillary tumor (left) and reconstructed permittivity (right).

As a final demonstration of the algorithm to show the limitations of Rytov approximation in the application of the THz band, the same setup found in Fig. 8 is repeated with permittivity values corresponding to the actual electrical properties of the modeled tissues at 1 THz [4]. Note that the purpose of this setup is simply to show the need for alternative techniques for determining the shape and properties of the cancerous region when the actual permittivities of the breast tissues are used. For this setup, the tissue types are reclassified into adipose or fat tissue with $\epsilon_r = 2.5$, fibrous tissue with $\epsilon_r = 3.6$, and cancerous tissue with $\epsilon_r = 4.0$. As Fig. 9 shows, the resulting reconstruction of the permittivity is not viable due to the low contrast limitation of the approximation. The reconstructed image in Fig. 9 is clearly severely degraded.

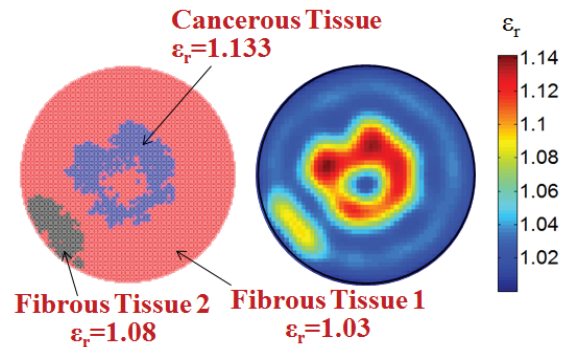


Fig. 8. Discretized DDSCAT tumor model (left) and reconstructed permittivity (right) of heterogeneous background tissue.

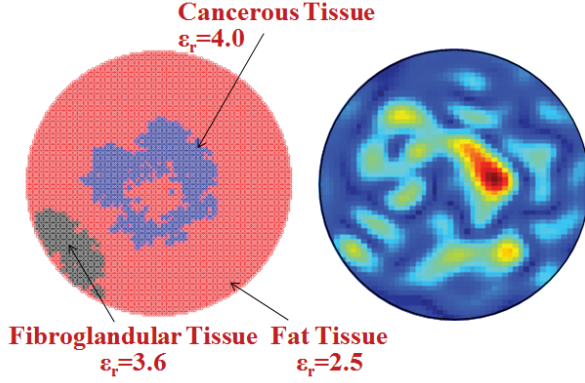


Fig. 9. Larger contrast heterogeneous tumor model (left) and reconstructed permittivity (right).

IV. CONCLUSION AND FUTURE RESEAECH

The obtained results demonstrated imaging breast cancer margins using the linearized Rytov approximation at 1 THz. The scattered fields were calculated using the open source DDSCAT at multiple receivers created by multiple incident waves. The DDSCAT was shown to successfully model the scattered electric fields from heterogeneous and irregular tumor patterns. The reconstructed images at 1 THz demonstrate that terahertz technology has potential for the use of tumor margin assessment. However, the Rytov approximation was not particularly effective in moving toward the experimental application due to its low contrast limitation and insufficient resolution. Therefore improved imaging methods are necessary for investigating the use of THz in this application.

Ongoing research involves the use of a new nonlinear inverse scattering tomography algorithm such as the linear sample method (LSM) [25]. The Authors believe that the LSM would be able to greatly increase the resolution of the image reconstruction of breast cancer margins regardless of the contrast between cancerous and normal tissues. The use of a linear technique provides the advantage of rapid assessment of results at relatively low computational cost. It has also been shown that the LSM is not subject to the low permittivity limitations imposed on the Born approximation when utilized to determine the contrast of scatterers against the background [26]. In addition, ongoing research is focusing on measuring THz fields reflected from ex-vivo

breast cancer samples in order to test the new tomography algorithm on experimental data.

APPENDIX A

In DDSCAT, at position j the dipole moment is related to the electric field as $\bar{P}_j = \alpha_j \bar{E}_{ext,j}$ where α_j is the polarizability tensor and $\bar{E}_{ext,j}$ is the total electric field at dipole j due to both the excitation of incident waves and the interactions with the other $N-1$ dipoles. The electric field at position j due to the dipole position k is given by [10-14],

$$\bar{A}_{jk} \bar{P}_k = \frac{\exp(ikr_{jk})}{r_{jk}^3} \left[\begin{array}{l} k^2 \bar{r}_{jk} \times (\bar{r}_{jk} \times \bar{P}_k) + \\ \frac{1 - ikr_{jk}}{r_{jk}^2} \times \\ \left(r_{jk}^2 \bar{P}_k - 3\bar{r}_{jk} (\bar{r}_{jk} \cdot \bar{P}_k) \right) \end{array} \right], \quad (A1)$$

where $i = \sqrt{-1}$ and \bar{r}_{jk} is the position vector between dipole j and dipole k . Thus the complex dipole moment can be expressed as,

$$\bar{P}_j = \alpha_j \left(\bar{E}_{inc,j} - \sum_{k \neq j}^N \bar{A}_{jk} \bar{P}_k \right), \quad (A2)$$

which can be arranged in the matrix format,

$$\sum_{k=1}^N \bar{A}_{jk} \bar{P}_k = \bar{E}_{inc,j}. \quad (A3)$$

Equation (A3) requires solving a linear system of equations of order $3N \times 3N$. The factor 3 is due to the vector position nature of the system solution at x , y , and z . For simplicity and reduced CPU time, the target sample is modeled as infinitely periodic targets (2D) with no variation in the z -direction as shown in Fig. 4. Once the complex dipole moment is obtained, the electric fields can be calculated at any point as follows [9-13],

$$\bar{E}(\bar{r}) = \sum_j \sum_{m,n} \left[\begin{array}{l} \frac{\exp(jk_0 R_{jmn})}{|R_{jmn}|^3} \varphi(R_{jmn}) \\ \left\{ \begin{array}{l} k_0^2 \bar{R}_{jmn} \times (\bar{P}_{jmn} \times \bar{R}_{jmn}) + \\ \frac{(1 - jk_0 R_{jmn})}{R_{jmn}^2} \left[\begin{array}{l} 3\bar{R}_{jmn} (\bar{R}_{jmn} \cdot \bar{P}_{jmn}) \\ -R_{jmn}^2 \bar{P}_{jmn} \end{array} \right] \end{array} \right\} \end{array} \right], \quad (A4)$$

where $\bar{R}_{jmn} = \bar{r} - \bar{r}_{jmn}$, \bar{r} is the position vector of the field point and \bar{r}_{jmn} is the position vector of dipole jmn . The vector \bar{P}_{jmn} represents the polarization of dipole jmn and $\phi(R_{jmn})$ is a smoothing factor added to reduce the contributions from distant dipoles. In this dipole numbering, j represents dipoles in the unit cell, m and n represent the replica dipoles when 2D periodic boundary conditions are implemented as adopted in this work and is shown in Fig. 4.

ACKNOWLEDGMENT

This work was sponsored by the Army Research Laboratory and was accomplished under Cooperative Agreement Number W911NF-10-2-0093. The views and conclusions contained in this document are those of the authors and should not be interpreted as representing the official policies, either expressed or implied, of the Army Research Laboratory or the U.S. Government. The U.S. Government is authorized to reproduce and distribute reprints for Government purposes not withstanding any copyright notation herein.

This work was supported in part by the National Science Foundation under Grants ARI # 0963249, MRI #0959124 (Razor), EPS #0918970 (CI TRAIN), and a grant from the Arkansas Science and Technology Authority, managed by the Arkansas High Performance Computing Center.

Funding for purchase and maintenance of the Pulsed Terahertz System is provided by NSF/MRI award #1228958. This work was supported by the NSF GRFP, the NSF GK12 Program as part of award #1228958, the Arkansas Biosciences Institute (ABI), and the Arkansas Breast Cancer Research Program (ABCRP).

REFERENCES

- [1] L. Jacobs, "Positive margins: The challenge continues for breast surgeons," *Ann. Surg. Oncol.*, vol. 15, no. 5, pp. 1271-1272, May 2008.
- [2] J. Brown, T. Bydlon, L. Richards, B. Yu, S. Kennedy, J. Geradts, L. Wilke, M. Junker, J. Gallagher, W. Barry, and N. Ramanujam, "Optical assessment of tumor resection margins in the breast," *IEEE Journal of Selected Topics in Quantum Electronics*, vol. 16, no. 3, pp. 530-544, 2010.
- [3] P. Ashworth, E. Pickwell-MacPherson, E. Provenzano, S. Pinder, A. Purushotham, M. Pepper, and V. Wallace, "Terahertz pulsed spectroscopy of freshly excised human breast cancer," *Opt. Express.*, vol. 17, no. 15, pp. 12444-54, 2009.
- [4] A. Fitzgerald, V. Wallace, M. Jimenez-Linan, L. Bobrow, R. Pye, A. Purushotham, and D. Amone, "Terahertz pulsed imaging of human breast tumors," *Radiology*, vol. 239, no. 2, pp. 533-540, 2006.
- [5] M. Brun, F. Formanek, A. Yasuda, M. Sekine, N. Ando, and Y. Eishii, "Terahertz imaging applied to cancer diagnosis," *Phys. Med. Biol.*, vol. 55, pp. 4615-4623, 2010.
- [6] C. Ruiz and J. Simpson, "Cepstral analysis of photonic nanojet-illuminated biological cells," *Applied Computational Electromagnetics Society (ACES) Journal*, vol. 27, no. 3, pp. 215-222, March 2012.
- [7] A. Hassan, D. Hufnagle, M. El-Shenawee, and G. Pacey, "Terahertz imaging for margin assessment of breast cancer tumors," *Proceedings of 2012 IEEE MTT-S International Microwave Symposium Digest*, June 2012.
- [8] A. Hassan, D. Hufnagle, G. Pacey, and M. El-Shenawee, "Terahertz tomography technique for the assessment of breast cancer tumor margins," *Proceedings of 2012 IEEE Antennas and Propagation Society International Symposium*, Chicago, Illinois, July 2012.
- [9] T. Bowman, A. Hassan, and M. El-Shenawee, "Terahertz frequency Born and Rytov tomography for breast cancer tumor margins," *2012 ABI Fall Research Symposium*, University of Arkansas, 23 October 2012.
- [10] B. Draine and P. Flatau, "Discrete dipole approximation for scattering calculations," *J. Opt. Soc. Am. A*, vol. 11, pp. 1491-1499, 1994.
- [11] B. Draine, "The discrete dipole approximation and its application to interstellar graphite grains," *J. Astrophys.*, vol. 333, pp. 848-872, 1998.
- [12] B. Draine and P. Flatau, "Discrete-dipole approximation for periodic targets: theory and tests," *J. Opt. Soc. Am. A*, vol. 25, pp. 2593-2703, 2008.
- [13] P. Flatau and B. Draine, "Fast near-field calculations in the discrete dipole approximation for regular rectilinear grids," *Optics Express*, vol. 20, pp. 1247-1252, 2012.
- [14] B. Draine and P. Flatau, "User guide to the discrete dipole approximation code DDSCAT 7.1," <http://arxiv.org/abs/1002.1505v1>, 2010.
- [15] W. Chew, *Waves and Fields in Inhomogeneous Media*, Chapter 9, pp. 511-570, *IEEE Press*, 1995.

- [16] W. Chew, "Imaging and inverse problems in electromagnetics," *Advances in Computational Electrodynamics: The Finite-Difference Time-Domain Method*, ch. 12, A. Taflove, Ed. Norwood, MA: Artech House, 1998.
- [17] A. Vouldis, C. Kechribaris, T. Maniatis, K. Nikita, and N. Uzunoglu, "Investigating the enhancement of three-dimensional diffraction tomography by using multiple illumination planes," *Journal of Optical Society of America*, vol. 22, no. 7, pp. 1251-1262, July 2005.
- [18] G. Dunlop, W. Boerner, and R. Bates, "On an extended Rytov approximation and its comparison with the Born approximation," *Proc. of Antennas and Propagation Society International Symposium*, vol. 14, pp 587-591, Oct. 1976.
- [19] A. Vouldis, C. Kechribaris, T. Maniatis, K. Nikita, and N. Uzunoglu, "Three-dimensional diffraction tomography using filtered back propagation and multiple illumination planes," *IEEE Transactions on Instrumentation and Measurement*, vol. 55, no. 6, pp. 1975-1984, Dec. 2006.
- [20] S. Ferreira Jr., M. Martins, and M. Vilela, "Reaction-diffusion model for the growth of avascular tumor," *Physical Review E*, vol. 65, no. 2, pp. 021907-1 021907-8, 2002.
- [21] A. Hassan and M. El-Shenawee, "Biopotential signals of breast cancer versus tumor types and proliferation stages," *Physical Review E*, vol. 85, no. 2, pp. 021913, 2012.
- [22] J. Parsons, C. Burrows, J. Sambles, and W. Barnes, "A comparison of techniques used to simulate the scattering of electromagnetic radiation by metallic nanostructures," *Journal of Modern Optics*, vol. 57, no. 5, pp. 356-365, 2010.
- [23] R. Dahlbäck, T. Rubæk, M. Persson, and J. Stake, "A system for THz imaging of low-contrast targets using the Born approximation," *IEEE Transactions on THz Science and Technology*, vol. 2, no. 3, pp. 361-370, 2012.
- [24] M. Hajihashemi, *Inverse Scattering Level Set Algorithm for Retrieving the Shape and Location of Multiple Targets*, Ph.D. dissertation, University of Arkansas, Fayetteville, AR, 2010.
- [25] L. Crocco, I. Catapano, L. Donato, and T. Isernia, "The linear sampling method as a way to quantitative inverse scattering," *IEEE Trans. Antenn. Propag.* vol. 60, no. 4, April 2012.
- [26] I. Catapano, L. Crocco, L. Donato, and T. Isernia, "Advances in inverse scattering arising from the physical meaning of the linear sampling method," *Proc. of IEEE 6th European Conference on Antennas and Propagation (EUCAP)*, pp. 3210-3214, 2001.

Synthesis of Conical Conformal Array Antenna Using Invasive Weed Optimization Method

Y. Li, F. Yang, J. Ouyang, and P. Yang

Department of Microwave Engineering
University of Electronic Science and Technology of China, Chengdu, 611731, China
liyaanem@gmail.com, yangf@uestc.edu.cn, antenna_ou@163.com, yangpeng@uestc.edu.cn

Abstract — Invasive weed optimization (IWO), which shows high performance in the electromagnetic community, is used to synthesize the conical conformal array antenna in this paper. Radiation pattern of the conformal array antenna is obtained by the superposition of the active element radiation pattern in the presence of platform, which includes the mutual coupling information of the array antenna and effects of the platform. Compared with partial swarm optimization (PSO), performance of IWO is more stable and lower side-lobe is obtained with IWO. A linear antenna array mounted on conical carrier is optimized and fabricated, measured results agree well with the optimized results. In addition, the proposed method can be used for the pattern synthesis of any kind of antenna array.

Index Terms — Conical conformal array antennas, invasive weed optimization, and radiation pattern.

I. INTRODUCTION

Conformal array antennas have the advantages of aerodynamic superiority, wide angle coverage and volume saving, so it is a very hot topic in antenna design society and have attracted more attention in different applications such as aircraft, missile, and satellite.

For synthesis of conformal array antenna, it is an inverse problem and in many cases nonlinear. At the same time, there is usually no unique solution to the problem [1]. So globe optimized methods are often used to address this issue. Simulated annealing (SA) is used to synthesize the cylindrical arrays for a desired radiation pattern in [2]. Genetic algorithm (GA) is also used for

pattern synthesis of arrays mounted on arbitrarily-shaped three-dimensional platforms in [3]. Conformal array antenna pattern are optimized by hybrid optimization method named HIGAPSO in [4]. Pattern of conformal array antenna in the presence of platform is synthesized with difference evolution (DE) in [5]. The element layout of conformal array antenna is optimized with PSO in [6]. By introducing time sequences, a 4D conformal array antenna is proposed and optimized with DE in [7]. The active element pattern (AEP) is employed in [8] to compute the radiation pattern of the conformal array antenna. However, GA and DE have the operations of selection, crossover, and mutation, so they are complicated to implement. Compared with GA and DE, PSO has the advantages of simple locations and velocities updating formulas, while convergence of the PSO algorithm depends on the choice of boundary conditions and the maximum velocity. As we know, they are difficult to perceive, so it always makes the PSO be trapped in local minima.

A new numerical stochastic optimization algorithm called invasive weed optimization (IWO) was proposed by Mehrabian and Lucas in 2006 [9]. It has been recently introduced to electromagnetics community and shown high performance in the synthesis of antenna array. Features of IWO are discussed in [10]. In [11-14], IWO was used to optimize the patterns of the linear and planar array antenna. Reflector antenna is optimized with IWO in [15] to form cosecant squared pattern. A meander-shaped MIMO antenna for wireless applications is designed using IWO in [16]. A broadband patch antenna with symmetric radiation pattern was designed using

IWO in [17]. Directivity of Yagi-Uda antenna is optimized with IWO in [18]. It is found that the IWO outperforms the other methods such as GA and PSO. IWO has the features of easy implementation and skipped local minima. So the issues discussed above have been addressed by IWO.

Beam direction and side-lobe of the conformal array antenna mounted on conical carrier are optimized in this paper. With the active element radiation pattern, mutual coupling and the effects of the platform are considered in the synthesis of the antenna array. Compared with PSO, performance of IWO is more stable and lower side-lobe is obtained. The optimized radiation pattern is verified by the measured results. Both of them agree well with each other.

II. INVASIVE WEED OPTIMIZATION METHOD

IWO has the features of fast reproduction and distribution, robustness, and adaptation to the changes in the environment [17]. In this paper, only the main steps of the IWO are given, which includes initialize a population, reproduction, spatial dispersal, and competitive exclusion. Details of IWO can be found in [9, 10]. The flowchart of IWO is shown in Fig. 1 [10].

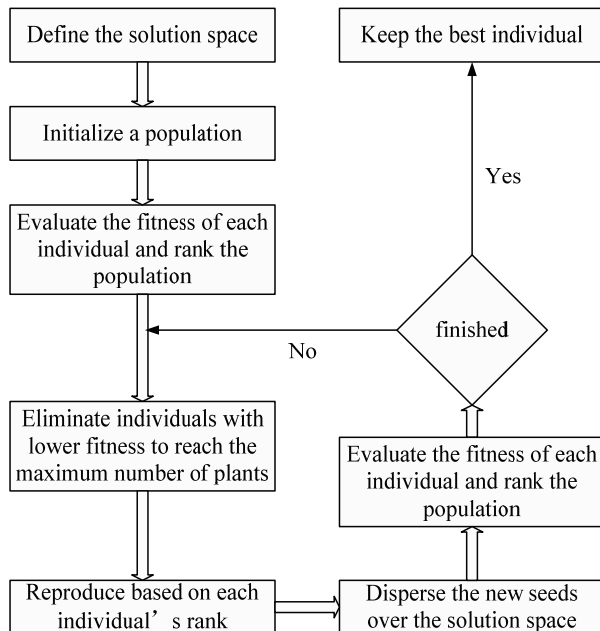


Fig. 1. Flowchart of IWO.

III. SYNTHESIS OF CONICAL CONFORMAL ARRAY ANTENNA WITH IWO

A 16 element linear array mounted on conical carrier is considered in this paper. As shown in Fig. 2, conventional rectangular microstrip antenna operated at 10 GHz is chosen as the radiation element and the distance between each element is $0.57 \lambda_0$. Dimensions of conical carrier and position of antenna array on the conical carrier are shown in Fig. 3. Apparently, the array factor theory can not be used here because every element has different radiation pattern. In addition, to consider the mutual coupling and effects of the platform, active element radiation pattern is calculated firstly, and then radiation pattern of the conformal array antenna is obtained by the superposition of the calculated active element radiation pattern. So the total electric field should be obtained using equation (1) rather than the array factor theory,

$$\vec{E}(\theta, \varphi) = \sum_{n=1}^N \vec{E}_n(\theta, \varphi) \quad (1)$$

where $\vec{E}_n(\theta, \varphi)$ is the electric field radiated by the n^{th} element in the presence of the other elements with matching loading and the platform; N is the number of the element.

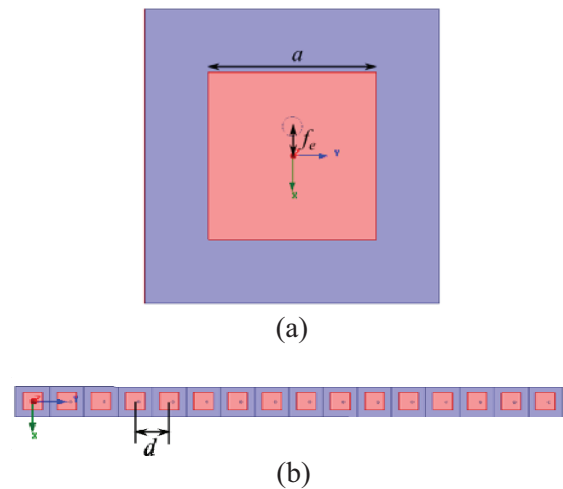


Fig. 2. Configuration of the antenna element and array (a) antenna element and (b) antenna array with substrate characteristics of: $\epsilon_r = 2.55$, $h = 1$ mm and dimensions: $a = 8.55$ mm, $f_e = 1.5$ mm, $d = 17$ mm.

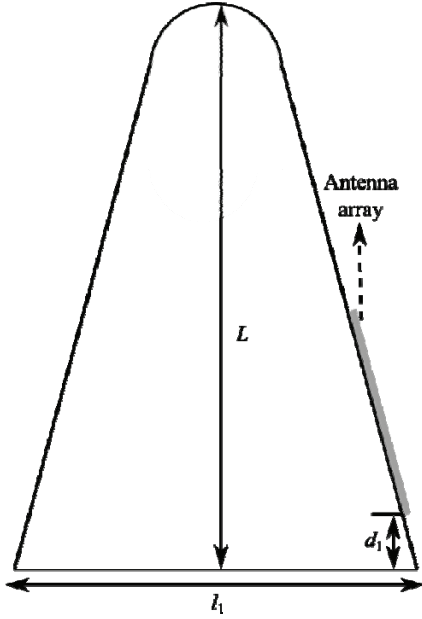


Fig. 3. Configuration of conical carrier and position of the antenna array dimensions: $L = 1388$ mm, $l_1 = 400$ mm, and $d_1 = 65$ mm.

Beam direction and side-lobe are optimized with PSO and IWO at the same time in this paper. The objective function is defined as,

$$f = \text{abs}(\theta - \theta_s) + \max(\text{PSLL}) \quad (2)$$

where θ_s defines the desired beam direction and PSLL defines the peak side-lobe level. The parameters used in IWO and PSO are shown in Tables I and II, respectively. Both IWO and PSO run 5 times. The objective function values of PSO and IWO are shown in Fig. 4 (a), it is found that IWO outperforms PSO, lower objective function values is obtained with stable characteristics. As shown in Fig. 4 (b), with the same beam direction, lower side-lobe is achieved using IWO. Optimized radiation pattern with different beam direction and low side-lobe is shown in Fig. 5, it is found that the desired beam direction and low side-lobe is obtained. When the beam scans to 20° and 30° , the PSLL is below -20 dB. However, when the beam scans to 45° , the PSLL is only below -15 dB, which is because of strong coupling at the large scanning angle. The optimized amplitude and current distribution for different beam direction are shown in Table III to IV.

Table I: Parameters used in the IWO.

Number of initial population (n_{ini})	maximum number of iterations ($Iter_{max}$)	maximum number of plants (P_{max})	maximum number of seeds (S_{max})
80	500	20	5
minimum number of seeds (S_{min})	nonlinear modulation index (N)	initial value of standard deviation ($SD_{initial}$)	final value of standard deviation (SD_{final})
0	3	8	0.1

Table II: Parameters used in the PSO.

Number of initial population (n_{ini})	maximum number of iterations ($Iter_{max}$)	inertia weight (c_0)
100	500	From 0.9 to 0.4
acceleration constant (c_1)	acceleration constant (c_2)	
2	2	

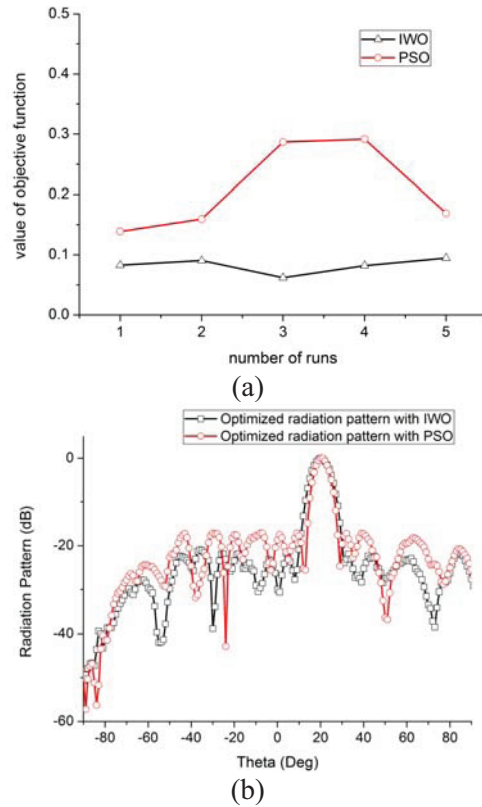


Fig. 4. Performance comparisons of PSO and IWO (a) objective function values obtained from IWO and PSO and (b) radiation pattern optimized by IWO and PSO.

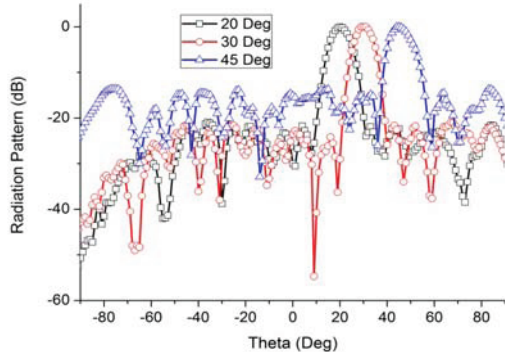


Fig. 5. Optimized radiation patterns using IWO.

Table III: Amplitude and phase distribution for beam steering 20°.

	20°	
	amplitude	phase (°)
element 1	0.1770	-3.3060
element 2	0.2110	37.3568
element 3	0.4673	-120.3727
element 4	0.3936	150.4874
element 5	0.9127	99.8322
element 6	0.9697	18.8790
element 7	0.9014	-50.3172
element 8	1	-127.3227
element 9	0.7963	-176.9294
element 10	0.9923	100.8692
element 11	0.8506	23.3366
element 12	0.4353	-28.2354
element 13	0.5723	-98.4571
element 14	0.4217	171.3889
element 15	0.1687	151.0317
element 16	0.1072	-8.7032

IV. EXPERIMENTAL RESULTS

To verify the optimized amplitude and phase distributions for each antenna element, a prototype is fabricated and measured. The amplitude distribution is realized by the power divider and attenuator, while the phase distribution is obtained by the phase shifter. The feeding network is shown in Fig. 6. Then it was connected with the fabricated antenna array. As shown in Fig. 7, the integrated antenna array is measured in microwave chamber. Measured radiation patterns are shown in Fig. 8. It is found that measured results agree well with the simulated results in the main lobe area, while there is a discrepancy in the other area, it is caused by the excitation distribution errors and measurement errors. The desired beam direction and PSLL is achieved with the optimized amplitude and phase distribution.

Table IV: Amplitude and phase distribution for beam steering 30°.

	30°	
	amplitude	phase (°)
element 1	0.4841	108.9365
element 2	0.5848	-32.8935
element 3	0.4143	176.2590
element 4	0.6218	132.2616
element 5	0.9003	25.5654
element 6	0.8957	-87.5250
element 7	0.8208	174.5344
element 8	0.9176	80.4261
element 9	1	-30.5902
element 10	0.6969	-128.1878
element 11	0.8237	136.1176
element 12	0.6475	37.6376
element 13	0.6943	-67.7924
element 14	0.5238	-153.1115
element 15	0.4699	66.2053
element 16	0.0797	-91.6561

Table V: Amplitude and phase distribution for beam steering 45°.

	45°	
	amplitude	phase (°)
element 1	0.4225	133.0532
element 2	0.6560	-30.1147
element 3	0.8442	175.1303
element 4	0.9120	-7.1963
element 5	0.8937	-169.5497
element 6	0.8539	78.8734
element 7	0.9118	-55.9150
element 8	1	131.3334
element 9	0.9302	-25.2101
element 10	0.8865	-159.4427
element 11	0.4443	40.8061
element 12	0.9286	-111.8184
element 13	0.7290	126.1195
element 14	0.5152	-40.1529
element 15	0.7749	-169.8648
element 16	0.3710	13.9916

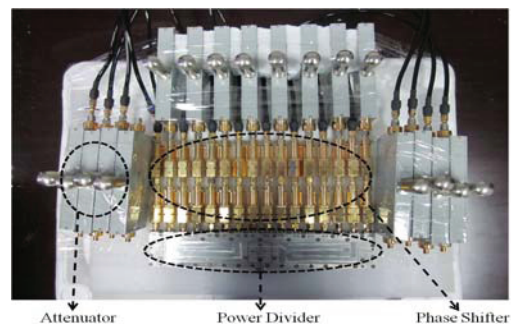


Fig. 6. Feeding network.



Fig. 7. Integrated antenna array.

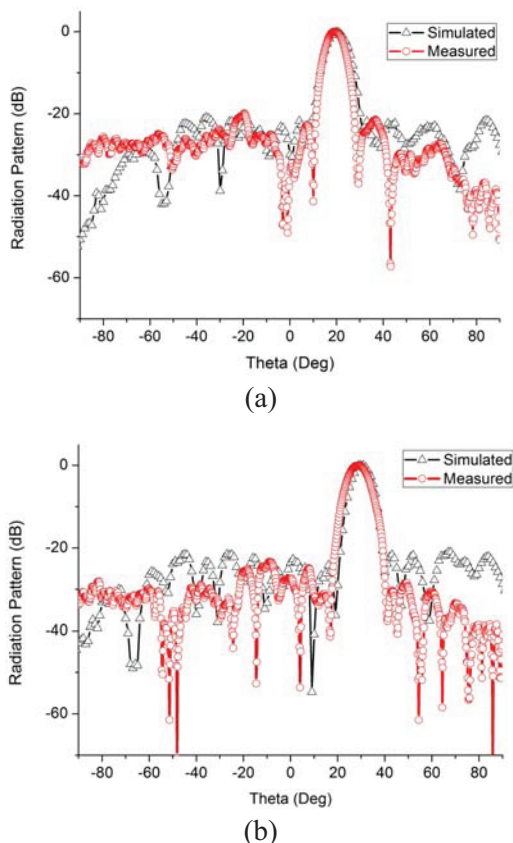


Fig. 8. Measured and simulated radiation pattern (a) beam steering 20° and (b) beam steering 30° .

V. CONCLUSIONS

Conical conformal array antenna is synthesized using IWO because of its better performances in this paper. With the active element radiation pattern, mutual coupling and the effects of platform are considered. Radiation pattern with desired beam direction and low side-lobe for a linear antenna array are optimized in the presence of the platform with the proposed universal method. The measured results demonstrated the effectiveness of the proposed

method. -20 dB peak side-lobe levels is achieved when the antenna array scan to 20° and 30° .

ACKNOWLEDGMENT

This work was supported in part by Innovation Research Funds of China Academy Space Technology (Xi'an), in part by the Fundamental Research Funds for the Central Universities, and in part by the Natural Science Foundation of China (No. 11176007 and No.61001029).

REFERENCES

- [1] L. Josefsson and P. Persson, *Conformal Array Antenna Theory and Design*, Wiley-Interscience, 2006.
- [2] J. Ferreira and F. Ares, "Pattern synthesis of conformal arrays by the simulated annealing technique," *Electron. Lett.*, vol. 33, no. 14, pp. 1187-1189, 1997.
- [3] R. Allard, D. Werner, and P. Werner, "Radiation pattern synthesis for arrays of conformal antennas mounted on arbitrarily-shaped three-dimensional platforms using genetic algorithms," *IEEE Trans. Antennas Propagat.*, vol. 51, no. 5, pp. 1054-1062, May 2003.
- [4] W. Li, X. Shi, Y. Hei, S. Liu, and J. Zhu, "A hybrid optimization algorithm and its application for conformal array pattern synthesis," *IEEE Trans. Antennas Propagat.*, vol. 58, no. 10, pp. 3401-3406, Oct. 2010.
- [5] J. Guo and J. Li, "Pattern synthesis of conformal array antenna in the presence of platform using differential evolution algorithm," *IEEE Trans. Antennas Propagat.*, vol. 57, no. 9, pp. 2615-2621, 2009.
- [6] K. Yang, Z. Zhao, J. Ouyang, Z. Nie, and Q. Liu, "Optimisation method on conformal array element positions for low sidelobe pattern synthesis," *IET Microw. Antennas Propag.*, vol. 6, no. 6, pp. 646-652, June 2010.
- [7] S. Yang, C. Liu, L. Zheng, and Q. Zhu, "A study on 4D antenna arrays conformed to a cylindrical platform," *7th European Conference on Antennas and Propagation (EUCAP 2013)*, Sweden, April 2013.
- [8] X. Yang, H. Qian, B. Wang, and S. Xiao, "Radiation pattern computation of pyramidal conformal antenna array with active element pattern technique," *IEEE Antennas Propag. Mag.*, vol. 53, no. 1, pp. 28-37, Jan. 2011.
- [9] A. Mehrabian and C. Lucas, "A novel numerical optimization algorithm inspired from weed colonization," *Ecol. Inform.*, vol. 1, no. 4, pp. 355-366, April 2006.

- [10] S. Karimkashi and A. Kishk, "Invasive weed optimization and its features in electromagnetics," *IEEE Trans. Antennas Propag.*, vol. 58, no. 4, pp. 1269-1278, April 2010.
- [11] S. Karimkashi and A. Kishk, "Antenna array synthesis using invasive weed optimization: A new optimization technique in electromagnetics," *Antennas and Propagation Society International Symposium, APSURSI '09, IEEE*, Charleston, SC, June 2009.
- [12] S. Pal, A. Basak, S. Das, and A. Abraham, "Linear array antenna synthesis with invasive weed optimization algorithm," *International Conference of Soft Computing and Pattern Recognition, SOCPAR*, Malacca, Dec. 2009.
- [13] A. Basak, S. Pal, S. Das, and A. Abraham, "Circular antenna array synthesis with a differential invasive weed optimization algorithm," *International Conference on Hybrid Intelligent Systems (HIS)*, Atlanta, GA, Aug. 2010.
- [14] A. Basak, S. Pal, S. Das, A. Abraham, and V. Snaesel, "A modified invasive weed optimization algorithm for time-modulated linear antenna array synthesis," *IEEE Conference on Evolutionary Computation (CEC)*, Barcelona, July 2010.
- [15] A. Mallahzadeh and P. Taghikhani, "Cosecant squared pattern synthesis for reflector antenna using a stochastic method," *Applied Computational Electromagnetics Society (ACES) Journal*, vol. 26, no. 10, pp. 823-830, Oct. 2011.
- [16] B. Bahreini, A. Mallahzadeh, and M. Soleimani, "Design of a meander-shaped MIMO antenna using IWO algorithm for wireless applications," *Applied Computational Electromagnetics Society (ACES) Journal*, vol. 25, no. 7, pp. 631-638, July 2010.
- [17] F. Monavar, N. Komjani, and P. Mousavi, "Application of invasive weed optimization to design a broadband patch antenna with symmetric radiation pattern," *Antennas Wireless Pro pag. Lett.*, vol. 10, pp. 1369-1372, 2011.
- [18] Y. Li, F. Yang, J. Ouyang and H. Zhou, "Yagi-Uda antenna optimization based on invasive weed optimization method," *Electromagnetics*, vol. 31, no. 8, pp. 571-577, 2011.



Yan LI was born in Shaanxi, China. He received the B.S. degree in electronic engineering and M.S. degree in electromagnetics and microwave technology from the University of Electronic Science and Technology of China (UESTC) in 2007 and 2010, respectively, where he is currently working toward the

Ph. D. degree. From Feb, 2010 to Aug, 2011, he was a Research Assistant with the Department of Electrical and Electronic Engineering at the University of Hong Kong. His research interests include antenna theory and design, antenna array optimization, and passive microwave circuits design.



Jun Ouyang received the B.S., and Ph.D. degrees in electromagnetic field and microwave technology from the University of Electronic Science and Technology of China (UESTC), Chengdu, in 2004 and 2008, respectively. He is currently with the Department of Electronic Engineering, UESTC. His research interests include antenna theory and computational electromagnetics.



Feng YANG was born in Shaanxi, China. He received the M.S. degree and Ph.D. degree in electromagnetics and microwave technology from the University of Electronic Science and Technology of China, Chengdu, China, in 1995 and 1998 respectively. He is currently a Professor in the Department of Microwave Engineering, University of Electronic Science and Technology of China. He has published more than 90 journal papers. His research interests include antenna theory and techniques, electromagnetic scattering and inverse scattering, and UWB communication.



Peng YANG was born in Kunming, Yunnan, China. He received the B.S. degree in electronic engineering in 2001, M.S. degree and Ph.D. degree in electromagnetics and microwave technology from the University of Electronic Science and Technology of China (UESTC) in 2008 and 2011 respectively. From January 2009 to November 2010, he was a Research Assistant with the Department of Electrical and Electronic Engineering at the University of Hong Kong. He is currently a lecture in the University of Electronic Science and Technology of China. His research interests include microstrip antenna theory and design, metamaterials, and smart antenna systems.

Fast Calculation of 3D Conductive Target Backscatter in a Random Medium using Coherence Based Monte Carlo Integration (CBMI) Method

G. Togtema¹, H. El-Ocla^{1,2}, and M. Al Sharkawy³

¹Lakehead University, Thunder Bay, ON, Canada
gtogtema@lakeheadu.ca, hosam@lakeheadu.ca

²University of Bahrain, Bahrain

³Department of Electronics and Communication Engineering, Arab Academy for Science, Technology & Maritime Transport, Alexandria, Egypt
msharkawy@aast.edu

Abstract – In this paper, a fast method to perform backscattering calculations from perfect electrically conducting (PEC) objects embedded in continuous random media is presented. The current generator method (CGM) is revisited and is modified for speed, removing the need to perform matrix inverse operations. The presented formulations are adequate to solve two and three dimensional problems. A Monte Carlo technique will be employed to speed the high ordered integration by using the de-correlation in space found within the fourth moment of Green's function as an 'importance sampling' distribution. This incoherence is explicitly shown in the current generator formulation. The revisited formulation has improved functionality in its ability to consider three dimensional objects. Its algorithmic performance is analyzed and is found to be significantly faster than other candidate matrix based methods.

Index Terms – Current generator method, electric field integral equation, monostatic backscatter, Monte Carlo integration, radar cross section, and random media.

I. INTRODUCTION

Prior knowledge of monostatic backscattering from particles and objects is a useful tool for radar and optical imaging instrumentation. It helps to

classify the returned signal into target types like snow, light / dense rain, wind, etc. [1, 2]. Furthermore, it helps the aircraft developers to optimize the effectiveness of the plane body design in a way to hide from radar, preventing a costly guess-and-test prototyping process. Calculating the scattering profile from arbitrarily shaped conducting targets is becoming trivial as a research question since many methods already exist: physical optics (PO), method of moments (MoM), finite difference time domain (FDTD). To be accurate, this task is straight forward when one neglects the space between the target and the observer, opting to consider only 'free space' conditions. On the other hand, when the aircraft is surrounded by random media (i.e., clouds, air pressure fluctuations, fog, rain, snow etc.); the calculation becomes significantly slow and some of the above methods produce erroneous results due to various physical conditions.

In this paper, the current generator method [3, 4] is revisited and altered to remove any inverse matrix operations. The complexity of the quadruple surface integral found in the electric field integral equation (EFIE) by the MoM can be reduced by implementing the Monte Carlo integration as will be shown later. Sampling points on the target surface are chosen such that they are most likely to contribute to the integration, neglecting those that do not. This probability distribution is based on signal coherence properties. Thus, the modified current generator method outperforms the MoM in

terms of its asymptotic complexity with respect to the number of basis functions, and the usage of the coherence Monte Carlo integration provides an even larger improvement in computation speed. It is well known that calculating the backscattered intensity of large targets requires a quadratic polynomial increase in sample points. Thus, computational time saving of this method may facilitate quick calculations of large targets like stealth aircrafts.

II. THE CURRENT GENERATOR METHOD

This approach is a boundary value method, and as such, we express the backscattered field as a function of current density on the boundary of the object. Due to the targets being PEC, either the Dirichlet condition ($u(r) = 0$) for E-wave incidence or the Neumann condition ($\frac{\partial u(r)}{\partial n} = 0$) holds on the surface, and will greatly simplify the final expressions. Since there is little difference in the current generator method between the two configurations, we develop the method for E-wave incidence for simplicity's sake and refer to the current generator in H waves so the reader can make an analogy [5].

We start by re-emphasizing the radar process: incident wave, $u_{in}(r_1)$ is generated by a source distribution, $f(r_1)$, and travels in the random media. It is transformed on the target into current, which then acts as a new source to reradiate to the observer. Mathematically, and rather intuitively, $u_s(r)$, is related to the E-wave polarized incident field via [6],

$$u_s(r) = \iint_s G(r|r_2)[Y(r_2|r_1)u_{in}(r_1)]dr_1dr_2 \quad (1)$$

where $Y(r_2|r_1)$ is a current generator operator that maps incident field to target surface current density, r_1 is the wave incidence point and r_2 is the point at which current is generated due to $u_{in}(r_1)$. Here, $G(r|r_2)$ satisfies the following Helmholtz equation for random media. The entire spatial fluctuations are represented by dielectric variation [7],

$$\left[\nabla^2 + k_0^2 (1 + \delta\epsilon(r)) \right] G(r|r_2) = \delta(r - r_2) \quad (2)$$

Here, k_0 is the wave number in free space, and $\delta\epsilon(r)$ is the spatial fluctuation of dielectric. According to the current generator method [6, 8],

we expand the surface current, $J_s(r_2)$ into harmonics and find an expression for their coefficients,

$$J_s(r_2) = \sum_{m=0}^M \sum_{n=0}^N b_{mn} \Psi_{mn}(r_2) \quad (3)$$

Here, $\Psi_{mn}(r_2)$ is the three dimensional basis function and b_{mn} is its weighting coefficient. For a given coordinate system, this, albeit, places its limitations on the shapes of considerable targets. Nevertheless, for any target depicted by, say, spherical coordinates, the function

$$\Psi_{mn}(r) = \sqrt{2/\pi} k_0 j_n(k_0 r) y_m^n(\theta, \phi) \quad (4)$$

solves the separable wave equation and therefore its set reconstructs any current distribution [9].

Here, $y_m^n(\theta, \phi) = \sqrt{\frac{2n+1}{4\pi} \frac{(n-m)!}{(n+m)!}} P_m^n(\sin\theta) e^{im\phi}$ is the spherical harmonic function and P_m^n is the Legendre function of degree n and order m . More details on the choice of basis functions and its properties are given in the appendix, but it suffices to say $\Psi_{mn}(r)$ in equation (4) forms an orthonormal set according to [10]. This orthogonality is used in the following approach to arrive at an expression for the coefficients, b_{mn} , much in the same way they are for the Fourier transform. We multiply equation (3) by $\Psi_{m'n'}^*(r_2)$ on both sides and integrate over the target surface,

$$\int_s \Psi_{m'n'}^*(r_2) J_s(r_2) dr_2 = \sum_{m=0}^M \sum_{n=0}^N b_{mn} \int_s \Psi_{mn}(r_2) \Psi_{m'n'}^*(r_2) dr_2 \quad (5)$$

The orthogonal property of $\Psi_{mn}(r)$ states,

$$\int_s \Psi_{mn}(r_2) \Psi_{m'n'}^*(r_2) dr_2 = \delta_{m,m'} \delta_{n,n'} \quad (6)$$

where the definition of the delta function is,

$$\delta_{m,m'} = \begin{cases} 1 & m = m' \\ 0 & m \neq m' \end{cases} \quad (7)$$

which is similar for $\delta_{n,n'}$. The normal part of the orthonormal property of $\Psi_{mn}(r_2)$ ensures that the value of $\delta_{m,m'}$ for $m = m'$ is indeed 1, and not a normalizing constant. With the orthogonal relationship, equation (5) reduces to an equation where m' and n' becomes a particular value of m and n , respectively, and thus the summations are dropped. We are left with

$$b_{mn} = \int_s J_s(r') \Psi_{mn}^*(r') dr', \quad (8)$$

where r' denotes an arbitrary integration parameter on S . In the following section, we derive another expression for $J_s(r')$ which, when substituted into equation (8) provides a more useful expression for b_{mn} .

A. Expression for the surface current

According to Huygen's principle [11],

$$u_s(r) = \int_s \left[u(r_2) \frac{\partial G(r|r_2)}{\partial n_2} - G(r|r_2) \frac{\partial u(r_2)}{\partial n_2} \right] dr_2 \quad (9)$$

where n_2 is the unit normal from the target surface S . When the Dirichlet boundary condition is applied, this becomes

$$u_s(r) = - \int_s G(r|r_2) \frac{\partial u(r_2)}{\partial n_2} dr_2. \quad (10)$$

This is analogous to equation (1) where $\int_s Y(r_2|r_1) u_{in}(r_1) dr_1 = J_s(r_2)$, yielding,

$$J_s(r_2) = - \frac{\partial u(r_2)}{\partial n_2}. \quad (11)$$

Finally, we use equation (11) to determine the current generator operator by applying to equation (8),

$$b_{mn} = - \int_s \frac{\partial u(r')}{\partial n'} \Psi_{mn}^*(r') dr'. \quad (12)$$

B. The current generator operator

Considering that the total field, the sum of incidence and scattering, is zero on the target ($u(r') = u_{in}(r') + u_s(r') = 0$), we can expand the expression of b_{mn} in equation (12) to add the extra terms,

$$b_{mn} = - \int_s \left[\begin{array}{c} \Psi_{mn}^*(r') \frac{\partial u_{in}(r')}{\partial n'} \\ -u_{in}(r') \frac{\partial \Psi_{mn}^*(r')}{\partial n'} \end{array} \right] dr' - \int_s \left[\begin{array}{c} \Psi_{mn}^*(r') \frac{\partial u_s(r')}{\partial n'} \\ -u_s(r') \frac{\partial \Psi_{mn}^*(r')}{\partial n'} \end{array} \right] dr'. \quad (13)$$

Applying the Divergence theorem and using the radiation condition as in [8, 11], we find

$$\int_s \Psi_{mn}^*(r') \frac{\partial u_s(r')}{\partial n'} - u_s(r') \frac{\partial \Psi_{mn}^*(r')}{\partial n'} = 0 \quad (14)$$

and hence,

$$b_{mn} = - \int_s \left[\begin{array}{c} \Psi_{mn}^*(r') \frac{\partial u_{in}(r')}{\partial n'} \\ -u_{in}(r') \frac{\partial \Psi_{mn}^*(r')}{\partial n'} \end{array} \right] dr'. \quad (15)$$

With the expression of b_{mn} , we can now use equations (1), (3), and (15) to obtain the expression for the current generator.

$$Y(r_2|r_1) u_{in}(r_1) dr_1 = - \int_s \sum_{m=0}^M \sum_{n=0}^N \Psi_{mn}^*(r_1) \left[\begin{array}{c} \Psi_{mn}^*(r_1) \frac{\partial}{\partial n_1} \\ -u_{in}(r_1) \frac{\partial \Psi_{mn}^*(r_1)}{\partial n_1} \end{array} \right] dr_1. \quad (16)$$

This equations is, by analogy, the current generator operator acting on u_{in} ,

$$Y(r_2|r_1) = - \sum_{m=0}^M \sum_{n=0}^N \left[\begin{array}{c} \Psi_{mn}^*(r_2) \times \\ \Psi_{mn}^*(r_1) \frac{\partial}{\partial n_1} \\ - \frac{\partial \Psi_{mn}^*(r_1)}{\partial n_1} \end{array} \right]. \quad (17)$$

We now have the expression for one term in equation (1). Note that, unlike previous current generator formulations [5, 6, 8], the expression for $Y(r_2|r_1)$ does not require the computation of a matrix inverse. The inverse integral transform property found in equation (8) allows for this simplification. As we will see, however, equation (1) is a little less straight forward due to random media components, and needs revisiting. The following section completes the current generator formulation and establishes a basis for CBMI.

III. RADAR SIGNAL COHERENCE AND RANDOM MEDIA

Any signal is comprised of both coherent and incoherent parts,

$$u(r) = \langle u(r) \rangle + \Delta u(r) \quad (18)$$

where the ensemble average, $\langle u(r) \rangle$ denotes the coherent component at the observer while Δu represents the incoherent part. Based on equation (18), one can rewrite the scattered equations due to an E-wave polarized incident field,

$$u_s(r) = \int_s dr_1 \int_s dr_2 Y(r_2|r_1)G(r_1|r_t)G(r|r_2) \quad (19)$$

$$\langle u_s(r) \rangle = \int_s dr_1 \int_s dr_2 Y(r_2|r_1)\langle G(r_1|r_t)G(r|r_2) \rangle. \quad (20)$$

Here, the $u_i(r_1)$ is displayed in its Green's function representation. Fundamentally, $u_i(r_1) = \int_{V_T} G(r_1|r')f(r')dr'$, where r' describes the source distribution. For a source of unit strength, the $u_i(r_1)$ has been replaced with its point source Green's function representation, $u_i(r_1) \cong G(r_1|r_t)$, where r_t is the position of the transmitter within V_T . For monostatic conditions, $r_t = r$, so $u_i \cong G(r|r_1)$ after reciprocity has been employed $G(r_1|r) = G(r|r_1)$. Since radar antennas measure signal power, and not field, one must take the average of u_s^2 as,

$$\langle |u_s(r)|^2 \rangle = \int_s d^4r Y(r_2|r_1)Y^*(r'_2|r'_1) \times \langle G(r|r_1)G(r|r_2)G^*(r|r'_1)G^*(r|r'_2) \rangle \quad (21)$$

where r_1 is the point of incidence, r_2 is the point where the current is generated due to $u_i(r_1)$, r_1 and r_2 are the indices for complex waves of incidence and scattering, respectively, finally, $\int_s d^4r = \int_s dr_1 \int_s dr_2 \int_s dr'_1 \int_s dr'_2$. This expression is still too analytically complex. In addition to evaluating the product of the current generator, the average of the Green's function needs to be simplified.

A. Fourth moment of Green's function in random media

The fourth moment of Green's function, M_2 , in equation (21) is simplified using a common statistical identity,

$$\langle UV \rangle = \langle U \rangle \langle V \rangle + \text{covariance}(U, V) \quad (22)$$

leading to,

$$M_2 \cong \langle G(r|r_1)G^*(r|r'_1) \rangle \langle G(r|r_2)G^*(r|r'_2) \rangle + \langle G(r|r_1)G^*(r|r'_2) \rangle \langle G(r|r_2)G^*(r|r'_1) \rangle. \quad (23)$$

In order for this to be true, the incidence wave must sufficiently uncorrelated from the scattered wave [12]. Many natural processes, like those in the atmosphere, are aggregations of independent and identically distributed variables that have Gaussian distribution. To be even more complete, one can consider a small region of free space around the target to minimize the likelihood of reflected waves passing through the same random media as during incidence [6, 7]. We can view the fourth moment decomposition approximation as just that, something with sources of error, and therefore do not require this extra region. To describe the problem as to be practically accepted, however, restrictions on the random media intensity, $B = \langle \delta\varepsilon(r)\delta\varepsilon(r') \rangle \ll 1$, and scale size, $l \gg 1$ must be kept to remove the depolarization effects. The first term in equation (23) represents the low spatial frequencies in the media (lf), while the second term is the base for high spatial frequency (hf) expansion. Furthermore, judging from research into the spatial frequency spectrum of atmospheric air flow velocity structure function [13], its wave number $k_{\delta\varepsilon}$ decays proportional to a strong negative power $\sim k_{\delta\varepsilon}^{-5/3}$. This indicates there is little natural high frequency energy as far as air pressure is concerned that would invalidate the above approximation. One could place a low-pass filter on their random media spectrum without much detriment to accuracy.

B. Second moment of Green's function

The two expressions M_2^{lf} and M_2^{hf} are the products of the 2nd moment of Green's function M_1 . The expression of M_1 in random media is expressed as,

$$M_1 = M_1^i m(\rho_0 d) \quad (24)$$

$$M_1^i = G_0(r|r_1)G_0(r|r_2), \quad (25)$$

$$m(\rho_0 d) = \exp \left\{ -\frac{k_0}{4} \int_{z_0}^z D_t \left[\frac{z'-z_0}{z-z_0} (\rho_0 d), z'|z_0 \right] dz' \right\}, \quad (26)$$

$$D_t[\rho, z'|z_0] = \int_0^{z-z_0} D \left[\rho, z - \frac{z'}{2}, z' \right] dz', \quad (27)$$

$$D \left[\rho, z - \frac{z'}{2}, z' \right] = 2 \begin{bmatrix} B \left(0, z - \frac{z'}{2}, z' \right) \\ -B \left(\rho, z - \frac{z'}{2}, z' \right) \end{bmatrix}. \quad (28)$$

Here, G_0 is the Green's function in free space, and D is the random medium structure function in the transverse plane [14]. The symbol ρ is the

transverse distance from the primary axis (i.e., the line of sight) and $\rho_{0d} = \rho_2 - \rho_1$. The symbol z is the coordinate along the primary axis of the observer and z_0 describes the target size. Further description on the problem configuration is illustrated in Fig. (1).

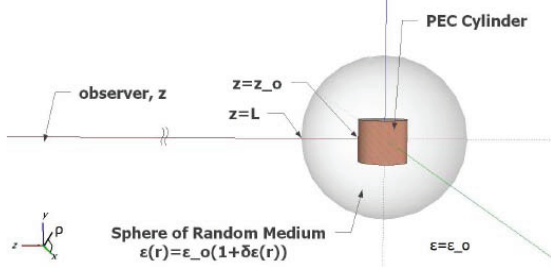


Fig. 1. Problem description of a 3D PEC target in random medium.

C. Expression of the coherent backscattered intensity

The expression of the backscattered power for a conductive target in random media is calculated through the product of the current generators and the derived expression of M_2 , which can be shown as,

$$\begin{aligned} \langle |u_s(r)|^2 \rangle &= \int_s d^4 r_{(1,2,1',2')} \times \\ &\left[\sum_{m=0}^M \sum_{n=0}^N \Psi_{mn}(r_2) \frac{\partial X}{\partial n_2} \left\{ \Psi_{mn}^*(r_1) \frac{\partial X}{\partial n_1} \right. \right. \\ &\quad \left. \left. - \frac{\partial \Psi_{mn}^*(r_1)}{\partial n_1} \right\} \right] \times \\ &\times \left[\sum_{m=0}^M \sum_{n=0}^N \Psi_{mn}^*(r_2) \frac{\partial X}{\partial n_2} \left\{ \Psi_{mn}(r_1) \frac{\partial X}{\partial n_1} \right. \right. \\ &\quad \left. \left. - \frac{\partial \Psi_{mn}(r_1)}{\partial n_1} \right\} \right] \\ &\times (M_\alpha + M_\beta) M_0. \end{aligned} \quad (29)$$

where,

$$M_\alpha = \exp \left\{ -\frac{k_0^2}{4} \mu \gamma(z, z_0) [(\rho_1 - \rho_1')^2 + (\rho_2 - \rho_2')^2] \right\}, \quad (30)$$

$$M_\beta = \exp \left\{ -\frac{k_0^2}{4} \mu \gamma(z, z_0) [(\rho_2 - \rho_1)^2 + (\rho_1 - \rho_2')^2] \right\}, \quad (31)$$

$$M_0 = \frac{1}{[8\pi k_0(z-z_0)]^2} \exp(X), \quad \mu = \sqrt{\pi} \frac{BL^3}{l(z-z_0)^2}, \quad (32)$$

and

$$X = -jk_0(z_1 - z_1' + z_2 - z_2') + \frac{jk_0}{2(z-z_0)} (\rho_1^2 - \rho_1'^2 + \rho_2^2 - \rho_2'^2). \quad (33)$$

IV. COHERENCE BASED MONTE CARLO INTEGRATION

The quadruple surface integral found in equation (29) makes computations very slow and memory intensive. A mesh grid of even ten samples in each of the θ and ϕ directions discretizes the target into 100 samples, making the four-fold integration require $100^4 = 10^8$ evaluations of the integrand. Each of M_0 , M_α and M_β may also have 10^8 allocations in memory. Due to the oscillatory nature of the basis functions, Ψ_{mn} , the exponential decay of M_α and M_β , and the target dependent nature of $\frac{\partial X}{\partial n}$, it is logical to think that certain points on the mesh will not contribute to the integration. Avoiding computational efforts toward these “useless” points is the reason why Monte Carlo integration is used. Consequently, the integrand is evaluated at a random set of sample points that have a probabilistic emphasis toward converging to the true answer faster. An estimate of the mean value of the integrand is calculated and from the Mean Value Theorem the integral is determined. Mathematically, denoting the integrand of equation (29) as I , the integral

$$\langle |u_s(r)|^2 \rangle = \int_s d^4 r. I \quad (34)$$

that can be calculated by the expected value of the integrand via

$$\langle I \rangle = \frac{1}{A^4} \int_s d^4 r. I \quad \int_s d^4 r. I = A^4 \langle I \rangle, \quad (35)$$

where A is the surface area of the target. Introducing a normalized function, R , leads,

$$\begin{aligned} \langle |u_s(r)|^2 \rangle &= \int_s d^4 r. \frac{I(r_{1,2,3,4})}{R(r_{1,2,3,4})} R(r_{1,2,3,4}) \\ &= \int_s \frac{I(r_{1,2,3,4})}{R(r_{1,2,3,4})} d\hat{R}(r_{1,2,3,4}) \end{aligned} \quad (36)$$

where $r_{1,2,3,4}$ are the four integral dependence and

$$\hat{R}(r_{1,2,3,4}) = \int_0^{r_{1,2,3,4}} R(r'_{1,2,3,4}) d'r_{1,2,3,4}. \quad \text{Here, the zero vector, } 0, \text{ denotes any starting point for the surface}$$

integration, and $r'_{1,2,3,4}$ is an arbitrary parameter on S . Making the change of variables, $t = R(r)$ rewrites equation (34) as

$$\left\langle |u_s(r)|^2 \right\rangle = \int_{\hat{R}(r)} \frac{I(\hat{R}^{-1}(t))}{R(\hat{R}^{-1}(t))} dt. \quad (37)$$

The difference between equation (34) and equation (37) is that, in the former, a uniform sampling distribution within $r_{1,2,3,4}$ may produce elements of $I(r_{1,2,3,4})$ that do not effectively contribute to $\langle I \rangle$, where as the latter does if I/R deviates less from the mean than I alone. At run time, one can check the variance of the estimate via,

$$\text{var}(\langle I \rangle) = \frac{\left\langle \left(\frac{I}{R} \right)^2 \right\rangle - \left\langle \frac{I}{R} \right\rangle^2}{N_r} \quad (38)$$

where N_r is the number of samples already calculated at run time. The whole idea lies in the choice of the sampling points.

A. Interpreting coherent backscattered intensity

The Monte Carlo method described above has an effective I/R arrangement when the function, R , 'follows' the integrand; when the distribution is zero or large, so should the integrand. Paradoxically, we are unable to generate the perfect distribution since we would need to know the analytic expression of equation (29) and hence not need Monte Carlo integration in the first place. Therefore we look at the expression in equation (29) and break down its physical meaning to provide insight on the choice of R .

The interpretation is very similar to that of other work, namely the combined field integral equation (CFIE) in [15], but with an added term for random media. The expression for M_0 is the complex free space propagation 'transfer function' between the source field intensity and the received field intensity. It represents the effect of the $1/r$ power law while taking into account spatial sinusoidal changes due to $e^{jk_0 r}$. The expressions for M_α and M_β each have $\exp\{-\mu\gamma\rho^2 D\}$ dependence (where ρD is used to denote the difference between the appropriate ρ 's for either M_α or M_β), which can be explained as the signal decorrelation due to the random media effects μ and γ . Lastly, the expression within the square brackets, as mentioned in [15], is the translation

response from incident wave to current density. We denote this as a unit plane wave response of current. To see this, the total field intensity integral equation (not just the coherent intensity) has a fourth moment of $M_2 = M_0$, and not $M_2 = M_0(M_\alpha + M_\beta)$ [5]. M_0 is already exposed as the propagation transfer function, and the square brackets is the only remaining physical process: the generation of current on the target. To summarize,

$$U_{TF} = M_0 \quad (39)$$

$$U_{dec} = M_\alpha + M_\beta, \quad (40)$$

$$U_p = \left[\sum_m^M \sum_n^N \left\{ \Psi_{mn}(r_2) \frac{\partial X}{\partial n_2} \times \left\{ \Psi_{mn}^*(r_1) \frac{\partial X}{\partial n_1} - \frac{\partial \Psi_{mn}^*(r_1)}{\partial n_1} \right\} \right] \right] \quad (41)$$

$$\times \left[\sum_m^M \sum_n^N \left\{ \Psi_{mn}^*(r_2') \frac{\partial X}{\partial n_2'} \times \left\{ \Psi_{mn}(r_1') \frac{\partial X}{\partial n_1'} - \frac{\partial \Psi_{mn}(r_1')}{\partial n_1'} \right\} \right] \right],$$

where the subscripts TF means propagation transfer function, dec means a de correlating function, and p is for the plane wave response.

B. Choice of 'importance sampling' distribution

For an observer positioned very far from the target, U_{TF} does not vary much from one point on the target to the next. Therefore, our easiest choice for R closely resembles the uniform distribution and does not follow the integrand well. The next easiest choice comes from U_p . It is somewhat easy to emulate since it has a common factor within the summation,

$$U_p = \left(NM \frac{\partial X}{\partial n_2} \right) \left(NM \frac{\partial X}{\partial n_2'} \right)$$

$$\times \left[\sum_m^M \sum_n^N \left\{ \Psi_{mn}(r_2) \times \left\{ \Psi_{mn}^*(r_1) \frac{\partial X}{\partial n_1} - \frac{\partial \Psi_{mn}^*(r_1)}{\partial n_1} \right\} \right] \right]$$

$$\times \left[\sum_m^M \sum_n^N \left\{ \Psi_{mn}^*(r_2') \times \left\{ \Psi_{mn}(r_1') \frac{\partial X}{\partial n_1'} - \frac{\partial \Psi_{mn}(r_1')}{\partial n_1'} \right\} \right] \right], \quad (42)$$

where $\frac{\partial X}{\partial n}$ can be found under the far field approximation ($z-z_0 \gg 1$) as,

$$\frac{\partial X}{\partial n_1} = \hat{n}_1 \cdot \nabla X = \hat{n}_1 \cdot \pm jk_0 \begin{pmatrix} \hat{z} + \frac{4\rho_1 x_1}{2(z-z_0)} \hat{x} \\ + \frac{4\rho_1 y_1}{2(z-z_0)} \hat{y} \end{pmatrix} \quad (43)$$

$$\approx jk_0 \hat{n}_1 \cdot \hat{z}_1.$$

Unfortunately, choosing $R = jk_0 (\hat{n}_1 \cdot \hat{z}_1 - \hat{n}_1' \cdot \hat{z}_1')$ will only speed up integration in the r_1 and r_1' directions. Furthermore, if the target boundary is not analytic, we will need to perform surface integral computations to normalize R via

$$\int_s dr_1 \int_s dr_1' R = 1, \quad (44)$$

rendering the algorithm slow. Lastly, the most powerful choice of R lies in U_{dec} . Due to the sharp descent of the $\exp\{-\mu\gamma\rho^2 D\}$ function, the signal contribution from different sections on the target that would normally occur in free space may no longer be correlated (coherent). This effect is excellent to consider as a sampling distribution to emphasize the presence of random media. The choice of

$$R = \frac{M_\alpha(r_{1,2,1',2'}) + M_\beta(r_{1,2,1,2'})}{\int d^4 r_{1,2,1',2'} [M_\alpha(r_{1,2,1',2'}) + M_\beta(r_{1,2,1,2'})]}, \quad (45)$$

samples points that are most likely to be coherent and hence the name coherence based Monte Carlo integration (CBMI) is the most appropriate.

V. COMPUTATIONAL INTENSITY

In this section, the current generator and the CBMI are analyzed for their computational performance. These advantages are compared to that of the MoM.

A. Generation of basis coefficients

CBMI and the current generator's performance relative to the MoM technique depend on the management of basis vectors. MoM performances are specified as it applies to manipulating the bases vectors, often assuming an analytic fourth moment in free space that does not slow the computation process. Considering different Green's functions (like that in random

media) will add extra complexity on account of the integration. A traditional MoM approach involves filling the $N_b \times N_b$ coefficient matrix whose elements represent interdependence of bases (inner products), storing this information in memory, and solving the linear system. Here, N_b is the number of unknown basis functions. According to [16] and [17], this approach has a computational complexity of $\mathbf{O}(N_b^2)$ for each step. Assuming a double summation expression, which one would expect for the term I of the current generator method shown in equation (34), where the summation inside the integrand computes very simple terms. This in turn, causes the current generator to have a very fast effective "fill time" of $\mathbf{O}(N_b)$, where a matrix is not needed. Fast Fourier Transform method (FFT) has matrix filling and solving complexities of $\mathbf{O}(N_b^{1.5} \log N_b)$ and Adaptive Cross Approximation (ACA) algorithms scale to $\mathbf{O}(N_b^{4/3} \log N_b)$ for moderately sized targets [18]. Fast Multipole Method (FMM) and multilevel FMM (MLFMM), which have achieved $\mathbf{O}(N_b \log N_b)$ in free space, are dependent on the analytical form of Green's function and can be translated to account for random media [16]. Ultimately, neither of these achieve the ultimate goal of removing interdependence among bases to reduce the complexity from $\mathbf{O}(N_b^2)$ to $\mathbf{O}(N_b)$.

B. CBMI computational intensity

The quadruple integral required by the current generator equation should scale with a complexity of $\mathbf{O}(N_s^4)$, if one were to use a quadrature integration. However, as the number of sample points increases in CBMI, the estimate of the Monte Carlo integral decreases and, according to the law of large numbers, its variance reduces as $1/\sqrt{N_s}$. This continues until an acceptable error level has been reached. Therefore, the quadruple surface integral within the current generator method that requires N_s^4 points using quadrature integration should converge as $\sqrt{N_s^4} = N_s^2$ using CBMI. As previously noticed, the double summation over M and N adds an extra order of complexity, bringing the overall performance of equation (34) to $\mathbf{O}(N_s^3)$. This is better than the MoM, that brings its total complexity to $\mathbf{O}(N_s^{5.5})$.

VI. ALGORITHM PERFORMANCE

While asymptotic analysis is useful, especially when assessing targets of large electrical size, it is important to consider computational advantages. The first is how Monte Carlo implementation stops once it has achieved a low variance in its estimate. One can make this stopping threshold fairly high since calculations need not be more precise than the noise floor of the receiver system. To be specific, $\text{var}(A^4 \langle I \rangle) < k_b T \cdot R_a \cdot \Delta v \cdot G \cdot F^2$ where $k_b T$ is the thermal energy, Δv is the bandwidth of the receiver, R_a is the antenna resistance, G is the antenna sensitivity to electric field, and $F = \text{noise}_{out} / \text{Gain} \cdot \text{noise}_{in}$ is the voltage noise figure of the preamp. In Radar Systems, one can choose a noise floor of a predetermined strength (e.g. ~ -60 dBm) and use G to determine the level of $\text{var}(A^4 \langle I \rangle)$. Due to the Gaussian-Like nature of the integrand of equation (34), there is a confident feel that $\text{var}(A^4 \langle I \rangle)$ represents more accurately the error. A second speed advantage is that knowledge of the system at hand can reduce the algorithm speed. Knowing the number of wavelengths on the target determines the number of harmonic modes required. Moreover, CBMI lends itself to be used easily in parallel processing applications. Due to the integral being evaluated as an average of sample points, tasks can be distributed among many modules, each performing their own estimate of $\langle I \rangle$, with almost no modification to the algorithm.

VII. CONCLUSION

We have presented a method for the fast calculation of backscatter from arbitrary 3D PEC objects embedded in continuous random media for E-wave polarization. The method was developed for 3D targets in spherical coordinates but could be applied to targets that conform to any other system (cylindrical, polar etc.). The formulation of a field intensity integral equation called the current generator method was modified to not contain any matrix inverse operations. This expression was broken into physical processes and a Monte Carlo integration based on the signal decorrelation greatly reduced the total algorithmic computational complexity to $\mathbf{O}(N_s^3)$ compared to that of fast MoM ($\sim \mathbf{O}(N_s^{5.5})$). Signal decorrelation, as described by M_α and M_β , depends heavily on

the second moment of Green's function, whose analytical expression is described and is very involved. The consideration of random media characteristics, intensity and distribution are, therefore, critical aspects in adapting the formulation to specific scenarios. The computational speed shows promise and may justify the efforts. Since, by the Nyquist criterion, N_s is tied directly to $(k_0 a)^2$, backscattered intensity calculations of airplanes observed by UHF and higher frequencies may become possible with the decrease in complexity.

ACKNOWLEDGMENT

This work was supported in part by the National Science and Engineering Research Council of Canada (NSERC) under Grant 250299-02.

REFERENCES

- [1] T. Otto and H. Russchenberg, "Estimation of specific differential phase and differential backscatter phase from polarimetric weather radar measurements of rain," *IEEE Geosci. Remote Sens. Letters*, vol. 8, no. 5, pp. 988-992, 2011.
- [2] J. Leinonen, D. Moiseev, V. Chandrasekar, and J. Koskinen, "Mapping radar reflectivity values of snowfall between frequency bands," *IEEE Trans. Geosci. Remote Sens.*, vol. 49, no. 8, pp. 3047-3058, 2011.
- [3] S. Chang, C. Fleuraru, Y. Mao, and S. Sherif, "Attenuation compensation for optical coherence tomography imaging," *Optics Commun.*, vol. 282, pp. 4530-4507, 2009.
- [4] H. El-Ocla and M. Tateiba, "Strong backscattering enhancement for partially convex targets in random media," *Waves Rand. Media*, vol. 11, pp. 21-32, 2001.
- [5] H. El-Ocla, "Effect of the illumination region of targets on waves scattering in random media with H-polarization," *Waves Rand. Complex Media*, vol. 19, no. 4, pp. 637-653, 2009.
- [6] H. El-Ocla, "Target configuration effect on wave scattering in random media with horizontal polarization," *Waves Rand. Complex Media*, vol. 19, no. 2, pp. 305-320, 2009.
- [7] Z.-W. Xu, J. Wu, Z.-S. Wu, and L.-W. Li, "Analytical solution to the n-nth moment equation of wave propagation in continuous random media," *IEEE Trans. Antennas and Prop.*, vol. 55, no. 5, pp. 1407-1415, 2007.
- [8] M. Tateiba and Z. Meng, "Wave scattering from conducting bodies embedded in random media-

- theory and numerical results,” *Prog. Electromag. Research*, vol. 14, pp. 317-361, 1996.
- [9] A. Ishimaru, *Electromagnetic Wave Propagation, Radiation, and Scattering*, pp. 112-114, 1991.
- [10] Q. Wang, O. Ronneberger, and H. Burkhardt, “Fourier analysis in polar and spherical coordinates,” *Published Internal Report* <http://lmb.informatik.unifreiburg.de/papers>, 2008.
- [11] A. Ishimaru, *Electromagnetic Wave Propagation, Radiation, and Scattering*, pp. 149-153, 1991.
- [12] R. Frehlich and M. Kavaya, “Coherent laser radar performance for general atmospheric refractive turbulence,” *Applied Optics*, vol. 30, no. 36, pp. 5325-5352, 1991.
- [13] E. Lindborg, “Can the atmospheric kinetic energy spectrum be explained by two-dimensional turbulence?,” *J. Fluid Mech.*, vol. 388, pp. 259-288, 1999.
- [14] A. Ishimaru, *Wave Propagation and Scattering in Random Media*, pp. 512, 1997.
- [15] L. Zhanhe, H. Peilin, G. Xu, L. Ying, and J. Jinzu, “Multi-frequency RCS reduction characteristics of shape stealth with MLFMA with improved MMN,” *Chinese J. Aeronautics*, vol. 23, pp. 327-333, 2010.
- [16] R. Burkholder and J.-F. Lee, “Fast dual-MGS block-factorization algorithm for dense MoM matrices,” *IEEE Trans. Antennas Prop.*, vol. 52, no. 7, pp. 1693-1699, 2004.
- [17] P. De Vita, F. De Vita, A. Freni, P. Pirinoli, F. Vipiana, and G. Vecchi, “Performances of MR-preconditioned fast MoM techniques,” *Microwave Opt. Tech. Letters*, vol. 52, no. 8, pp. 1719-1724, 2010.
- [14] K. Zhao, M. Vouvakis, and J.-F. Lee, “The adaptive cross approximation algorithm for accelerated method of moments computations of EMC problems,” *IEEE Trans. EMC*, vol. 47, no. 4, pp. 763-773, 2005.

A Novel Approach to Synthesis of Non-uniform Conformal Reflectarray Antennas

M. Karimipour and A. Pirhadi

Faculty of Electrical and Computer Engineering
Shahid Beheshti University G.C (SBU), Tehran, +98, Iran
M.Karimipour@mail.sbu.ac.ir, a_pirhadi@sbu.ac.ir

Abstract — This paper presents an accurate method to synthesize a shaped-beam conformal reflectarray (RA) antenna based on the phase synthesis of its equivalent aperture. For this purpose particle swarm optimization (PSO) is used to determine the optimal phase distribution on the reflective surface of the antenna. Furthermore, a method based on meshing the aperture of the antenna has been adopted to evaluate its radiation fields. By dividing the equivalent aperture of the antenna into small parts, the induced current in each part is approximated appropriately. Then the radiation fields can be evaluated via the sum of simple integrals. This approach provides a direct correlation between the amplitude and the phase of reflection coefficient of the RA elements with the radiation fields of the antenna. Therefore, the effect of elements can be considered directly in the optimization process. Another advantage of this method is that it can be used to synthesize non-flat RA antennas. Furthermore, in the proposed method the effects of the angle, polarization, amplitude, and phase of the radiated fields from the feed antenna are fully considered in the synthesis procedure. To verify the proposed method a shaped beam parabolic RA antenna in the X-band has been synthesized. The simulation results represent a good agreement with the simulation results obtained from the commercial full-wave electromagnetic (EM) software, CST microwave studio.

Index Terms - Optimization process, reflectarrays, radiation fields, and shaped-beam antenna.

I. INTRODUCTION

Antennas with shaped beam radiation patterns are required in many communication systems such as satellite communications, radar, and wireless communications. Reflector antennas and array antennas are among the most frequently used antenna types for these purposes. In most of the reflector antennas, the shaped radiation pattern is obtained by shaping the surface of the reflector, which makes it difficult to fabricate [1]. In array antennas, making the shaped radiation pattern is done by suitable excitation of the array elements that needs a complex feeding network [2].

The shaped radiation pattern can also be obtained using RA antennas. The RA antenna is a combination of reflector and array antennas. It consists of a reflective surface including the radiation elements and a feed, which is located in a certain distance from the reflective surface [3]. In printed RA antennas the radiation elements are designed using printed structures such as printed microstrip patches, dipoles, rings, split rings [3], etc. One important feature of the RA antennas is their ability to produce an arbitrary radiation pattern by creating the appropriate EM field distribution on their aperture. This is done by suitable embedding of the radiation elements on the reflective surface [4]. Unlike shaped beam reflector antennas and array antennas, it is not necessary to shape the reflective surface or design the complex feeding network. In these antennas the radiation elements are used to create the shaped radiation pattern by tuning their corresponding reflection phases. Based on this property the RA antennas can also be used to design a multi-beam radiation pattern, electronically scanned radiation pattern [4, 5], etc.

The first steps for designing a shaped beam RA antenna is obtaining the amplitude and phase distributions of the EM fields on the reflective surface or equivalent aperture based on the desired radiation pattern. The second step is designing the radiation elements according to the extracted EM field distributions in the first step. To realize the first step, radiated far fields must be calculated based on EM characteristics of the reflective surface (including the magnitude and the phase of the tangential fields), afterward the EM characteristics of the reflective surface must be adjusted using a suitable iterative process in order to shape the radiation pattern. Different methods have been used for this purpose. The most important method is the array concept method. In this method, the conventional array theory is used to calculate the far field radiation pattern from the RA elements [6-10]. Other method is the equivalent aperture field method based on the physical optic (PO) approximation. The array concept method is simple and fast but the feed antenna effect is not considered in this analysis method. The equivalent aperture method is more accurate than the array concept method and takes the feed antenna into account in the analysis procedure.

The amplitude of the EM field components on the reflective surface or the equivalent aperture of the RA antenna is directly determined from the radiated field of the feed. Therefore, only the phase of the field components on the reflective surface or equivalent aperture can be used to shape the radiation pattern of the RA antenna. For this reason, most of the synthesis methods of RA antennas are carried out to approximate or optimize the phase distribution on the surface of the RA antennas. It must be noticed that the direct optimization process, in which all the element dimensions are simultaneously optimized in an iterative process to obtain the required radiation pattern, is computationally unaffordable because of the large number of elements [11].

Alternating projection method also known as intersection approach [12] is one of the most widely used methods to synthesize RA antennas [13-15]. This approach is significantly useful for large RA antennas synthesis because of the reduced computational time for convergence. In some cases, especially in non-symmetric designs, this optimization procedure is trapped in local

minima and cannot satisfy the goal function [15]. Therefore it is necessary to use an optimization algorithm based on the local and global searches to solve this problem.

In the second step, after determining the optimum phase distribution of the fields on the aperture of RA antennas, appropriate elements must be designed to provide this phase distribution. The main challenges in this step are designing the radiation elements as phase shifters with a linear phase characteristic, low sensitivity with respect to the incident angle and a wide operating frequency bandwidth (in order to improve the bandwidth of RA [16]). Microstrip patches with the same dimensions and variable stubs [3], patches with variable sizes [9] and variable rotation angles [17], rings with or without a split [18, 19] and using the same elements in an irregular grid [20] are some of the structures that have been used so far.

In this paper in the first step an accurate analysis method is developed to obtain the radiated far fields of the RA antenna from the tangential fields on its surface based on the PO approximation. To evaluate the radiation integrals, which describe the relation between the amplitude and phase of the tangential fields on the surface of the RA and the radiation fields, a procedure based on meshing the equivalent aperture of the reflective surface has been adopted [21]. In principle, this method has been used to analyze reflector antennas and is developed to analyze and synthesize RA antennas in this paper. The most advantageous feature of this method is that it can be implemented on non-flat surfaces. In this method the equivalent aperture of the reflective surface is divided into some meshes and the amplitude and phase of the tangential electric fields in each mesh are approximated by linear functions. For evaluating the radiation fields accurately, especially in the side lobe regions, the mesh density must be 1 to 3 meshes per wavelength. Based on this analysis method and using PSO algorithm, the optimum phase distribution of the tangential fields on the RA surface is determined for shaping the radiation field patterns. In each mesh the amplitude of the tangential electric fields on the reflective surface is also obtained from the full-wave modeling of the feed antenna. In this analysis method, by considering the position of the radiation elements

with respect to the feed, the effects of the polarization and the incident angle are taken into account in the design process, which leads to an increase in the accuracy of the synthesis method. After obtaining the optimum phase distribution of the tangential fields on the reflective surface, phase distribution is implemented using appropriate radiation elements. These elements are constructed of a combination of square patches and rings. In order to verify the suggested design procedure, a conformal RA antenna with a cosecant squared radiation pattern in the elevation plane and a pencil beam radiation pattern in the azimuth plane, has been designed and simulated in the X-band. Results from the optimization procedure indicate a good agreement with the simulation results obtained from the full-wave commercial software (CST microwave studio [22]).

In section II the basic design equations for the analysis of RA antennas for a general curved surface are presented. In section III, a conformal RA is synthesized based on the method in section II and PSO algorithm. Section IV presents the full-wave simulation results of the optimized structure.

II. THE BASIC DESIGN EQUATIONS FOR REFLECTARRAY ANTENNAS

The general configuration of the RA antenna with an arbitrary cross section and a curved surface is shown in Fig. 1.

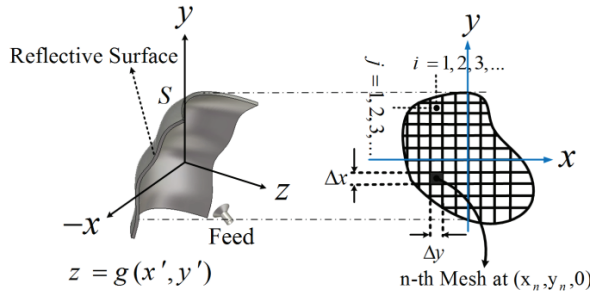


Fig. 1. Geometry of the RA antenna.

The analysis method should be in a way that it can be used for non-flat reflective surfaces. Based on the PO approximation of the radiated far field from a surface with an arbitrary curvature, the electric radiation field is calculated as [23],

$$\bar{E} = -j\beta \frac{e^{-j\beta r}}{2\pi r} \hat{r} \times \iint_s \hat{n} \times \bar{E}_a e^{jk \cdot \bar{r}'} ds \quad (1)$$

where $\hat{n} \times \bar{E}_a$ is the tangential electric field on the radiating surface and $\hat{n} = n_x \hat{x} + n_y \hat{y} + n_z \hat{z}$ is the normal vector at any point of the radiating surface. The radiating surface curvature is demonstrated as $z = g(x, y)$. Therefore, the radiation integral in equation (1) can be expressed as,

$$\bar{E} = -j\beta \frac{e^{-j\beta r}}{2\pi r} \hat{r} \times \iint_{s'} \sqrt{1 + \left(\frac{\partial g}{\partial x'}\right)^2 + \left(\frac{\partial g}{\partial y'}\right)^2} \hat{n} \times \bar{E}_a e^{jk \cdot \bar{r}'} ds' \quad (2)$$

where s' is the projection of the reflective curvature on the XY plane. By expanding equation (2) the radiated far field components are,

$$E_x^{ff} = -j\beta \frac{e^{-j\beta r}}{2\pi r} \iint_{s'} [(n_x E_{\theta y} - n_y E_{\theta x}) (\sin \theta \sin \phi) - (n_z E_{\theta x} - n_x E_{\theta z}) \cos \theta] \times \sqrt{1 + \left(\frac{\partial g}{\partial x'}\right)^2 + \left(\frac{\partial g}{\partial y'}\right)^2} \times e^{jk_0 [x' \sin \theta \cos \phi + y' \sin \theta \sin \phi + g(x', y') \cos \theta]} ds' \quad (3a)$$

$$E_y^{ff} = -j\beta \frac{e^{-j\beta r}}{2\pi r} \iint_{s'} [(n_y E_{\theta x} - n_z E_{\theta y}) \cos \theta - (n_x E_{\theta y} - n_y E_{\theta x}) (\sin \theta \cos \phi)] \times \sqrt{1 + \left(\frac{\partial g}{\partial x'}\right)^2 + \left(\frac{\partial g}{\partial y'}\right)^2} \times e^{jk_0 [x' \sin \theta \cos \phi + y' \sin \theta \sin \phi + g(x', y') \cos \theta]} ds' \quad (3b)$$

$$E_z^{ff} = -j\beta \frac{e^{-j\beta r}}{2\pi r} \iint_{s'} [(n_z E_{\theta x} - n_x E_{\theta z}) \sin \theta \cos \phi - (n_y E_{\theta z} - n_z E_{\theta y}) (\sin \theta \sin \phi)] \times \sqrt{1 + \left(\frac{\partial g}{\partial x'}\right)^2 + \left(\frac{\partial g}{\partial y'}\right)^2} \times e^{jk_0 [x' \sin \theta \cos \phi + y' \sin \theta \sin \phi + g(x', y') \cos \theta]} ds' \quad (3c)$$

For an arbitrary surface, solving the radiation integrals of equation (3a-3c) is complicated and time consuming. To reduce the complexity and solve the radiation integrals in equation (3), the equivalent aperture is divided into small sub-sections (based on the proposed method in [21]). Then in general form, the integrands of equations (3a-3c) are approximated as sum of linear functions with unknown coefficients as,

$$A = \sum_{i=1}^N \sum_{j=1}^M \int_{x_i}^{x_{i+1}} \int_{y_j}^{y_{j+1}} a_{p-ij} \times e^{j[\alpha_{p-ij} + \beta_{p-ij}(x'-x_i) + \gamma_{p-ij}(y'-y_j)]} \times (a_2 x' + b_2 y' + c_2) \times e^{jk_0 [x' \sin \theta \cos \phi + y' \sin \theta \sin \phi + (a_1 x' + b_1 y' + c_1) \cos \theta]} ds' \quad (4)$$

The integrand in equation (4) consists of three parts. The first part

$$a_{p_ij} \times e^{j[\alpha_{p_ij} + \beta_{p_ij}(x'-x_i) + \gamma_{p_ij}(y'-y_j)]}$$

, which is the approximation of the tangential electric field in each sub-section on the equivalent aperture. The subscript (ij) denotes the position of the sub-sections and the subscript (p) denotes the electric field components. The unknown coefficients α_{y_ij} , β_{y_ij} and γ_{y_ij} are used to represent the phase distribution of the tangential fields in each sub-section. These coefficients are adjusted to produce the desired radiation pattern. Therefore, this analysis procedure is only based on the phase synthesis of the aperture. The second part,

$$\sqrt{1 + \left(\frac{\partial g}{\partial x'}\right)^2 + \left(\frac{\partial g}{\partial y'}\right)^2} \times n_p(x', y', z')$$

with a linear function as $(a_2x' + b_2y' + c_2)$ and finally, in the third part, the function $g(x', y')$ is approximated with $(a_1x' + b_1y' + c_1)$ in each sub-section. The coefficients a_1 , b_1 , c_1 , a_2 , b_2 , and c_2 are determined based on linear approximations of the corresponding functions in each sub-section. Therefore, the radiation integrals in equation (3) can be expressed as the sum of simple integrals with exponential integrands that can be solved easily in the closed forms. The smaller sub-sections, lead to the more accurate radiation fields. Calculations show that a good accuracy is obtained for sub-sections with dimensions of about $\lambda/2$ or smaller.

In most analyses of the RA antennas, the radiation fields from the feed antenna are approximated by a cosine function (\cos^q) [6, 8, 13]. In this approximation, the effect of the phase center of the feed and its cross-polarization component are not considered. In our analysis, to solve these problems the radiated fields from the horn antenna are obtained using the full-wave EM simulator. In this case the a_{p_ij} coefficients in equation (4) are replaced by the amplitude of the radiated fields from the feed at each sub-section of the RA surface.

III. SYNTHESIS OF SHAPED-BEAM CONFORMAL REFLECTARRAY ANTENNAS

In the previous section it was shown how we can obtain the radiation fields from the aperture by

approximating the tangential fields on it. In this section, based on this analysis method, a shaped beam conformal RA antenna, which is designed at 10 GHz, is synthesized.

A. Antenna configuration and radiated fields formulation

The geometry of the antenna is shown in Fig. 2. As shown in this figure a non-flat surface with a parabolic cross section is considered as the reflective surface in which the curve function is

$$g(x', y') = \frac{x'^2}{4a} - b. \text{ where } a=10\text{cm and } b=0.06\text{cm.}$$

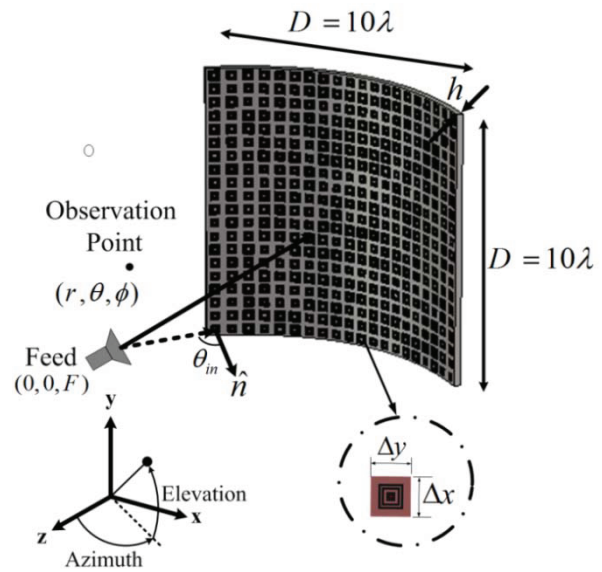


Fig. 2. Geometry of the proposed conformal RA antenna.

The radiation elements are placed on the reflective surface to provide the suitable phase distribution in order to generate the desired radiation pattern. A conical horn antenna is used as the feed, which has 40° and 45° , 3 dB beam-widths in E- and H-Planes, respectively. The feed antenna is designed to produce a vertical polarization. The vertical polarization is considered as the co-Polarization component of the radiation fields. Therefore, E_y^{ff} is used in the elevation and the azimuth planes to construct the radiation patterns. Based on equations (3b) and (4), the co-Polarization electric field can be written as

$$E_{co_pol}^{ff} = j\beta \frac{e^{-j\beta r}}{2\pi r} [\sin\theta \cos\phi A_1 + \cos\theta A_2], \quad (5)$$

where A_1 and A_2 are

$$A_1 = \sum_{i=1}^N \sum_{j=1}^M a_{y_ij} \times e^{j[\alpha_{y_ij} - \beta_{y_ij} x_i - \gamma_{y_ij} y_j - k_0 b \cos \theta]} \times I_1 I_2, \quad (6a)$$

$$A_2 = \sum_{i=1}^N \sum_{j=1}^M a_{y_ij} \times e^{j[\alpha_{y_ij} - \beta_{y_ij} x_i - \gamma_{y_ij} y_j - k_0 b \cos \theta]} \times I_2 I_3, \quad (6b)$$

and I_1 , I_2 , and I_3 are as follows,

$$I_1 = \int_{x_i}^{x_{i+1}} \frac{-x'}{2a} e^{j[(k_0 \sin \theta \cos \phi + \beta_{y_ij})x' + a_1(x' - x_i) + b_1]} dx', \quad (7a)$$

$$I_2 = \int_{y_j}^{y_{j+1}} e^{j[k_0 \sin \theta \sin \phi + \gamma_{y_ij}]y'} dy', \quad (7b)$$

$$I_3 = \int_{x_i}^{x_{i+1}} e^{j[(k_0 \sin \theta \cos \phi + \beta_{y_ij})x' + a_1(x' - x_i) + b_1]} dx'. \quad (7c)$$

In which a_1 and b_1 are,

$$a_1 = \frac{y_{i+1} - y_i}{x_{i+1} - x_i} = \frac{k_0 \cos \theta}{4a} \left(\frac{x_{i+1}^2 - x_i^2}{\Delta x} \right) \quad (8a)$$

$$b_1 = \frac{k_0 \cos \theta}{4a} x_i^2. \quad (8b)$$

In the optimization procedure, the phase coefficients of all sub-sections (α_{y_ij} , β_{y_ij} , and γ_{y_ij}) are considered as the inputs of the optimization algorithm and the desired radiation pattern is considered as the goal function. In this study, the goal function is a shaped beam with a cosecant squared form in the elevation plane and a pencil beam in the azimuth plane. The optimization procedure to determine the unknown coefficients is described in the following section based on the PSO algorithm.

B. Using the PSO algorithm for optimizing the structure

As is stated in the previous section, an intelligent evolutionary algorithm called PSO is used to adjust the phase coefficients of the approximation function of the tangential fields of the reflective surface. In this method, local and global search methods are combined to achieve the optimal results. In the PSO algorithm, particles move in a multi dimensional search space. During this movement, every particle adjusts its position with respect to adjacent particles while considering their prior experience. In general the position of each particle at each stage is expressed as follows [24],

$$\bar{v}_k(t) = \bar{v}_k(t-1) + c_1 r_1 \times [\bar{P}_k(t-1) - \bar{k}(t-1)] + c_2 r_2 \times [\bar{G}_k(t-1) - \bar{k}(t-1)] \quad (9)$$

$$\bar{k}(t) = \bar{k}(t-1) + \bar{v}_k(t)$$

In equation (9) \bar{k} and \bar{v} represent the position and the velocity of coefficients (α_{y_ij} , β_{y_ij} , and γ_{y_ij}), respectively. The positive constant c_1 and c_2 are usually $c_1 = c_2 = 2$. The best previous position (the position giving the best fitness value) of the k -th particle (coefficient) is presented as $\bar{P}_k(t-1)$ and $\bar{G}_k(t-1)$ denotes the best k -th particle among all the particles in the group. Also, r_1 and r_2 are two random values in the range (0, 1). Equation (9) is used to update the velocity of the coefficients as a function of their previous velocity, the previous position, $k(t-1)$, the best experienced (position) personal, $P_k(t-1)$, and the best experienced group, $G_k(t-1)$. Afterward, the coefficients move toward a new position. These coefficients are used to calculate the radiation fields of the antenna in each step. In the next step, the error function or the fitness function is defined as the absolute difference between the target and the calculated radiation fields. The optimization procedure is continued until the error function converges to the acceptable value.

Optimal radiation patterns or mask functions are represented in Fig. 3 for the elevation and azimuth planes. The mask functions are a cosecant squared pattern in the elevation plane with a 35° coverage region and a pencil beam pattern in the azimuth plane with a 5° coverage region. Moreover, the side lobe levels in the elevation and azimuth planes are -20dB and -30dB, respectively.

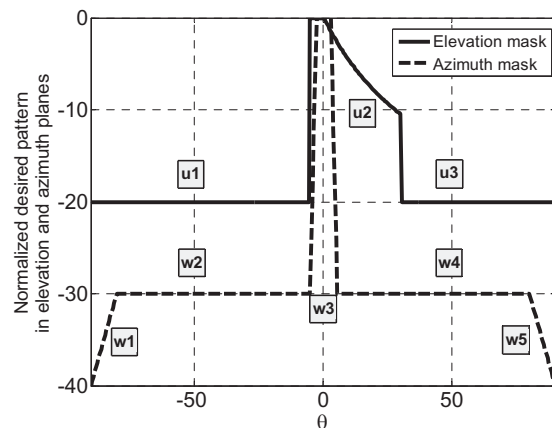


Fig. 3. Desired radiation patterns in the elevation and azimuth planes.

The Error function by assuming $w_1 = w_5$ and $w_2 = w_4$ is defined as follows,

$$\begin{aligned} \text{Fitness function} = & 2 \left[w_3 \sum_{\theta=0}^5 |F_A - F_{Desired}| + \right. \\ & w_4 \sum_{\theta=5}^{80} |F_A - F_{Desired}| + w_5 \sum_{\theta=80}^{90} |F_A - F_{Desired}| \left. \right] \\ & + \left[u_1 \sum_{\theta=-90}^{-5} |F_E - F_{Desired}| + u_2 \sum_{\theta=-5}^{30} |F_E - F_{Desired}| \right. \\ & \left. + u_3 \sum_{\theta=30}^{90} |F_E - F_{Desired}| \right], \end{aligned} \quad (10)$$

where F_A and F_E are the calculated radiation patterns in the azimuth and elevation planes and $F_{Desired}$ is the desired radiation pattern in each step of the PSO. According to Fig. 3 the assigned weights are shown by u and w for each region in the radiation patterns. Given the importance of the radiation pattern in the shaped region in the azimuth and elevation planes, higher weights are assigned to form the radiation patterns.

C. Synthesis results using the PSO algorithm

In this section synthesis results using the PSO algorithm are presented. For this purpose, the area of each cell is considered by about $\lambda/2 \times \lambda/2 \times \lambda/2$, which leads to 400 sub-sections, as shown in Fig. 2. The feed antenna is located at $(0, 0, 233 \text{ mm})$ in which the maximum incident angle to the reflector is about 30° . The PSO input parameters to start the optimization procedure are assumed as, $(\alpha_{ij}, \beta_{ij}, \gamma_{ij}) \in [-11, 11]$, $(V_{\alpha_{ij}}, V_{\beta_{ij}}, V_{\gamma_{ij}}) \in 0.2 \times [-11, 11]$, $u_1 = 3.9$, $u_2 = 8.2$, $u_3 = 4.9$, $w_3 = 8.2$, $w_4 = 5.9$, and $w_5 = 3$. The number of particles is 100 and the number of iterations is 3000. Figure 4 shows the optimized phase distribution of the tangential electric fields obtained by the PSO algorithm on the RA surface. The produced phase distribution on the RA surface from the radiated fields of the feed antenna is transformed to the optimal phase distribution by the RA elements. Considering the optimal phase distribution, co-polarization and cross-polarization components of the radiated far fields are shown in Fig. 5. As is shown in Fig. 5 there is a good agreement between the optimized radiation patterns and the desired patterns. The convergence of the fitness function with respect to the iteration steps is shown in Fig. 6.

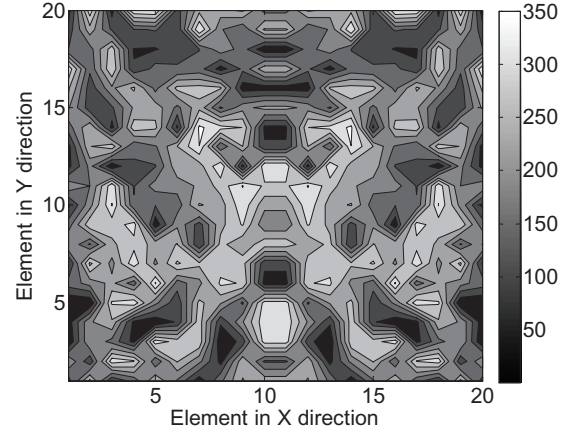
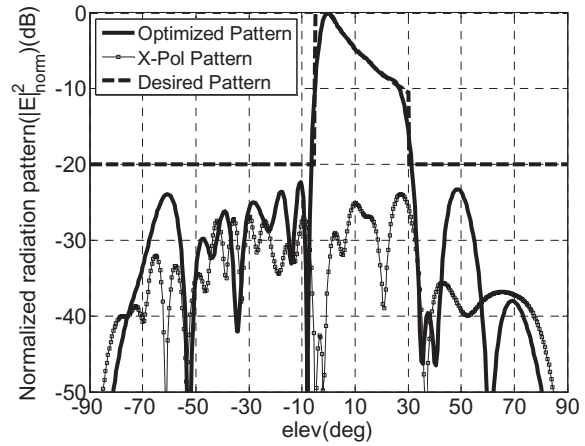
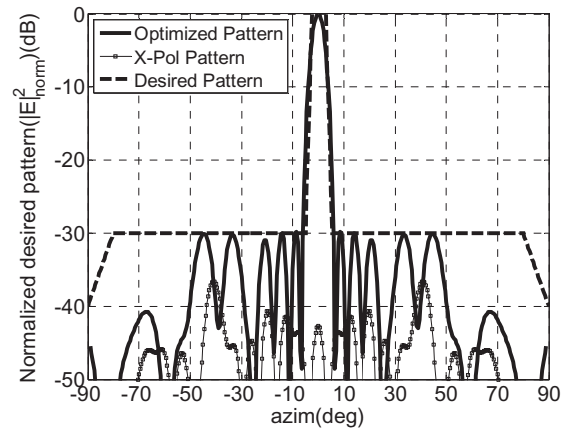


Fig. 4. The optimal phase distribution (in degrees) obtained from the PSO on the RA surface.



(a)



(b)

Fig. 5. Optimized radiation patterns (a) elevation plane and (b) azimuth plane.

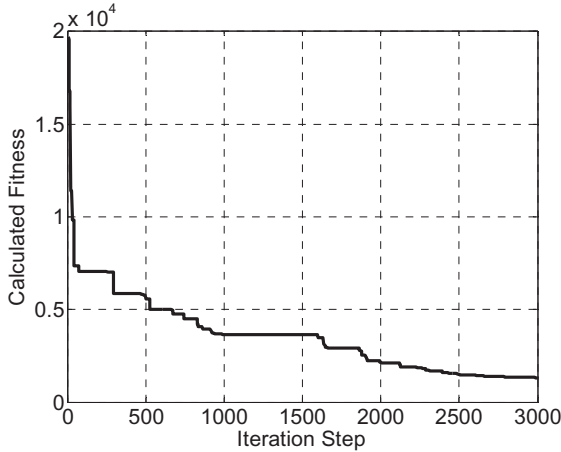


Fig. 6. The convergence of the fitness function with respect to the iteration steps.

D. Designing the elements to obtain the optimum phase distribution

Knowing the phase of the radiated fields from the feed antenna on the sub-sections of the RA surface, $\phi_{Incident}$ and the optimal phase distribution from the PSO, $\phi_{Desired}$, the phase for the elements $\phi_{Elements}$, can be determined as,

$$\phi_{Element}(i,j) = \phi_{Desired}(i,j) - \phi_{Incident}(i,j) \quad (11)$$

Different types of radiation elements have been used to provide the required phase [3, 25]. In this paper a single layer square patch and rings are used as the RA elements [26]. The geometry of a single cell of this structure is shown in Fig. 7. The reflection phase coefficient of this structure is stable for relatively large incident angles. Therefore, study of normal incident angles is sufficient to obtain the reflection phase properties. The HFSS software using the Floquet's port and periodic boundary conditions concept is used to simulate the reflection phase coefficient of a single cell. The simulation results have been depicted in Fig. 7 for the incident plane wave with horizontal polarization and various incident angles. The substrate of the structure is a type of foam with $\epsilon_r = 1.006$, $\tan\delta = 0$, $L = 1.5$ cm, and $t = 7$ mm.

In each sub-section, the dimensions of elements are determined in a way that they realize the optimal phase distribution. To this end the parametric study shows that $w = 0.125 L_2$, $L_1/L_2 = 0.5$, and $L_3 = 3w + L_2$ can provide our required reflection phase coefficients. Because of the wide variety of the optimum phase distributions on the RA surface, it is necessary to design the radiation

elements with different dimensions in each sub-section on the RA, which is a time consuming process. In this paper, in order to simplify this procedure a neural network is used. This network is trained so that the reflection phase coefficients and incident angles are considered as the inputs and the dimensions of the elements are considered as the outputs of the network. After training the network, based on the optimum phase distribution on the RA, the dimensions of suitable element in each subsection is determined quickly.

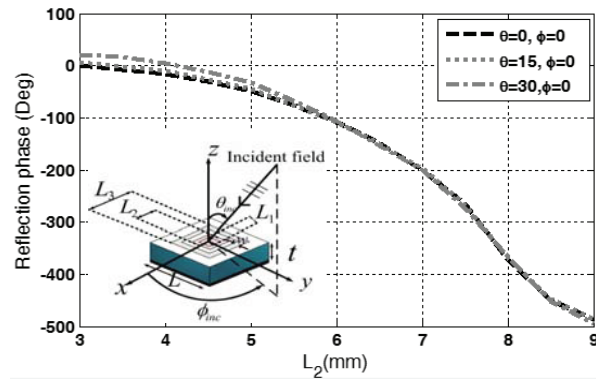


Fig. 7. Reflection phase coefficient of the proposed element at 10 GHz.

IV. SIMULATION RESULTS

To validate the proposed synthesis method, the dimensions of the elements are extracted by neural networks and located in their place on the reflective surface. Then the whole structure is simulated by the full-wave electromagnetic simulator, CST software, using the integral equation solving method. The normalized electric radiation field patterns of the antenna for the elevation and azimuth planes are represented in Fig. 8. As can be seen in this figure, the desired radiation patterns have been well realized in the elevation and azimuth planes.

One of the most advantageous features of the conformal RA antenna in comparison with the flat type is its wider bandwidth [8]. In order to show this, the radiation patterns of the synthesized conformal RA antenna in the previous section and a flat RA antenna with the same aperture size are studied for a given frequency band. As shown in Figs. 9 and 10, both of the conformal and flat RA antennas are synthesized in the 10 GHz frequency and show a good agreement with the desired radiation patterns in the azimuth and elevation

planes. Study of these structures in the lower and upper operating frequencies indicates that the conformal RA has a more stable behavior compared with the flat one. This means that the conformal RA antenna, regardless of its elements, has a wider frequency bandwidth in comparison with the flat one.

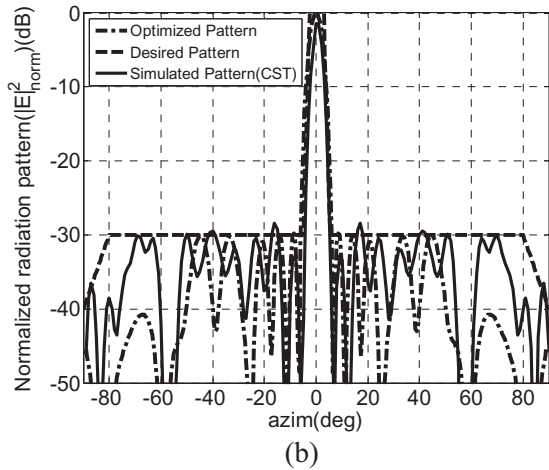
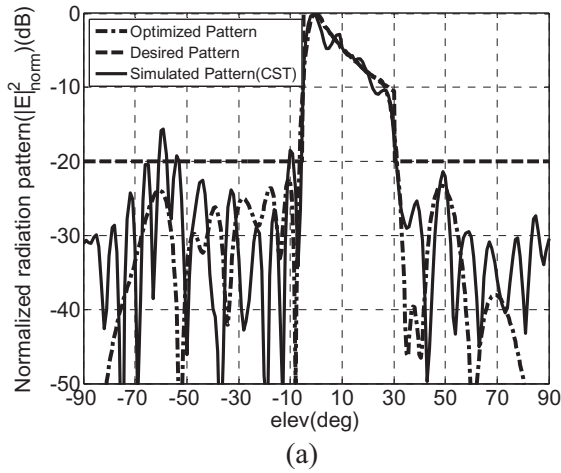


Fig. 8. The optimized pattern in Matlab and the simulated pattern in CST (a) elevation plane and (b) azimuth plane.

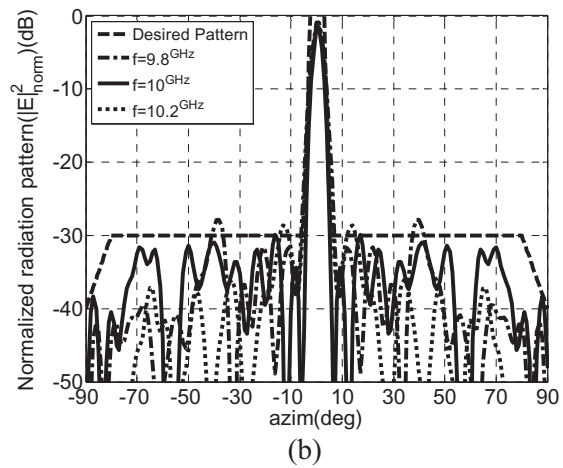
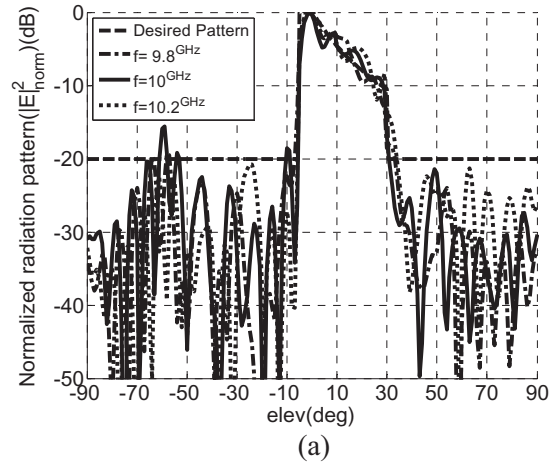
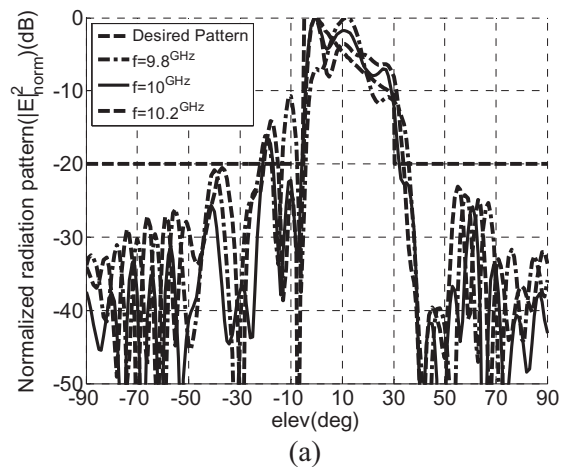


Fig. 9. Simulated radiation patterns of the conformal RA antenna for different frequencies (a) elevation plane and (b) azimuth plane.



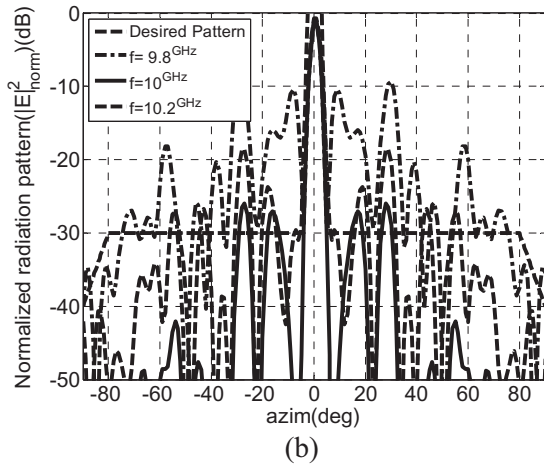


Fig. 10. Simulated radiation patterns of the flat RA antenna for different frequencies (a) elevation plane and (b) azimuth plane.

V. CONCLUSION

A method with the PSO algorithm was used to synthesize a shaped beam conformal RA antenna. The capability of the proposed method to synthesize the conformal structures has been evaluated by synthesis of a parabolic RA antenna. Employing this technique shows significant improvement in analyzing the non-flat RA antennas. It was shown that there is a good agreement between the desired and simulated radiation patterns, especially in the shaped beam regions. Moreover, it was shown that the conformal RA antenna in comparison with the flat one has a wider operating bandwidth.

ACKNOWLEDGMENT

The authors would like to thank the Iran Telecom Research Center (ITRC) for the support of this research.

REFERENCE

- [1] J. Bergmann, R. Brown, P. Clarricoats, and H. Zhou, "Synthesis of shaped-beam reflector antenna patterns," *Microwaves, Antennas and Propagation, IEE Proceedings H*, vol. 38, pp. 48-53, 1988.
- [2] T. Ismail and Z. Hamici, "Array pattern synthesis using digital phase control by quantized particle swarm optimization," *IEEE Trans. Antennas Propagat.*, vol. 58, no. 6, June 2010.
- [3] J. Huang and J. Encinar, *Reflectarray Antennas*, IEEE Press, John Wiley & Sons, Inc., Hoboken, New Jersey, 2007.
- [4] P. Nayeri, F. Yang, and A. Elsherbini, "Design and experiment of a single-feed quad-beam reflectarray antenna," *IEEE Trans. Antennas Propagat.*, vol. 60, no. 2, pp. 1166-1171, Feb. 2012.
- [5] S. Hum, M. Okoniewski, and R. Davies, "Realizing an electronically tunable reflectarray using varactor diode-tuned elements," *IEEE Microwave and Wireless Components Letters*, vol. 15, no. 6, pp. 422-424, June 2005.
- [6] E. Almajali, D. McNamara, J. Shaker, and M. Chaharmir, "Derivation and validation of the basic design equations for symmetric sub-reflectarrays," *IEEE Trans. Antennas Propagat.*, vol. 60, no. 5, pp. 2336-2346, Feb. 2012.
- [7] A. Trastoy, F. Ares, and E. Moreno, "Phase-only synthesis of non- ϕ -symmetric patterns for reflectarray antennas with circular boundary," *IEEE Antennas and Wireless Propagation Letters*, vol. 3, pp. 246-248, 2004.
- [8] G. Zhao and Y. Jiao, "Design of broadband dual-polarization contoured-beam reflectarray for space applications," *28th Annual Review of Progress in Applied Computational Electromagnetics (ACES)*, pp. 790-794, Columbus, Ohio, April 2012.
- [9] D. Pozar and T. Metzler, "Analysis of a reflectarray antenna using microstrip patches of variable size," *Electronics Letters*, vol. 29, no. 8, pp. 657-658, Apr. 1993.
- [10] J. Encinar, "Design of two-layer printed reflectarrays using patches of variable size," *IEEE Trans. Antennas Propagat.*, vol. 49, no. 10, pp. 1403-1410, Oct. 2001.
- [11] J. Encinar, M. Arrebola, L. de la Fuente, and G. Toso, "A transmit-receive reflectarray antenna for direct broadcast satellite applications," *IEEE Trans. Antennas Propagat.*, vol. 59, no. 9, pp. 3255-3264, Sep. 2011.
- [12] O. Bucci, G. Franceschetti, G. Mazzarella, and G. Panariello, "Intersection approach to array pattern synthesis," *IEE Proceedings*, vol. 137, no. 6, pp. 349-357, Dec. 1990.
- [13] P. Nayeri, A. Elsherbeni, and F. Yang, "Design, full-wave simulation, and near-field diagnostics of reflectarray antennas using FEKO electromagnetic software," *28th Annual Review of Progress in Applied Computational Electromagnetics (ACES)*, pp. 503-508, Columbus, Ohio, Apr. 2012.
- [14] J. Zornoza, R. Leberer, J. Encinar, and W. Menzel, "Folded multilayer microstrip reflectarray with shaped pattern," *IEEE Trans. Antennas Propagat.*, pp. 510-518, vol. 54, no. 2, Feb. 2006.
- [15] J. Encinar and J. Zornoza, "Three-layer printed reflectarrays for contoured beam space applications," *IEEE Trans. Antennas Propagat.*, vol. 52, no. 5, pp. 1138-1148, May 2004.

- [16] J. Encinar and J. Zornoza, "Broadband design of three-layer printed reflectarrays," *IEEE Trans. Antennas Propagat.*, vol. 51, no. 7, pp. 1662-1664, July 2003.
- [17] J. Huang and R. Pogorzelski, "A Ka-band microstrip Reflectarray with elements having variable rotation angles," *IEEE Trans. Antennas Propagat.*, vol. 46, pp. 650-656, May 1998.
- [18] Y. Li, M. Biakowski, K. Sayidmarie, and N. Shuley, "Single-layer microstrip reflectarray with double elliptical ring elements for bandwidth enhancement," *Microwave and Optical Technology Letters*, vol. 53, no. 5, May 2011.
- [19] S. Yusop, N. Misran, M. Islam, and M. Ismail, "Design of high performance dual frequency concentric split ring square element for broadband reflectarray antenna," *Applied Computational Electromagnetics Society (ACES) Journal*, vol. 27, no. 4, pp. 334-339, Apr. 2012.
- [20] M. Zhou, S. Sorensen, P. Meincke, E. Jorgensen, O. Kim, O. Breinbjerg, and G. Toso, "Design and analysis of printed reflectarrays with irregularly positioned array elements," *European Conference on Antennas and Propagation*, pp. 1619-1623, 2011.
- [21] C. Scott, *Modern Method of Reflector Antenna Analysis and Design*, Artech House, 1990.
- [22] CST, (Computer Simulation Technology), Microwave Studio 2011, Integral-Equation Simulation Tool.
- [23] C. Balanis, *Antenna Theory Analysis and Design*, 3rd ed., John Wiley & Sons, Inc., Hoboken, New Jersey 2005.
- [24] Y. Shi and R. Eberhart, "Empirical study of particle swarm optimization," *Proceedings of the 1999 Congress on Evolutionary Computation*, pp. 1945-1950, 1999.
- [25] M. Maddahali and K. Forooghi, "Design of broadband single layer printed reflectarray using Giuseppe Peano fractal ring," *Applied Computational Electromagnetics Society (ACES) Journal*, vol. 28, no. 2, pp. 150-155, Feb. 2013.
- [26] Q. Li, Y. Jiao, and G. Zhao, "A novel microstrip rectangular-patch/ring-combination reflectarray element and its application," *IEEE Antennas and Wireless Propagation Letters*, vol. 8, pp. 1119-1122, 2009.



Majid Karimipour received his B.S. and M.S. degrees in Electrical Engineering 2008 and 2011 from Shahrekord University, Shahrekord, Iran and Shahid Beheshti University (SBU), Tehran, Iran, Respectively. His major research interests are the development and design of reflectarray antennas for wireless communications, evolutionary algorithms, and shaped beam antennas synthesis.



Abbas Pirhadi received B.S. degree in Electrical Engineering from the Isfahan University of Technology, Isfahan, Iran 2000, and M. S. and Ph.D. degree in Communication Engineering from Tarbiat Modares University (TMU), Tehran, Iran in 2002 and 2007, respectively. From 2002 to 2006, he joined the Antenna and Propagation Group of the Iran Telecommunication Research Center (ITRC) as a researcher. Also, in 2008 he joined the Shahid Beheshti University (SBU) where he is the Assistant Professor at the faculty of Electrical and Computer engineering. His research interests include microwave antennas, theoretical and computational electromagnetic with applications to antenna theory and design.

Novel Bandwidth-Agile Bandpass Filter using Defected Ground Structure

Z.-H. Bao, Q.-Y. Lu, C. Shao, J.-X. Chen, and S. Zhang

School of Electronics and Information
Nantong University, Nantong, 226019, China
jjxchen@hotmail.com

Abstract — A novel microstrip bandpass filter (BPF) with tunable passband width using defected ground structure (DGS) is proposed. In this DGS, a pair of slotted radial stubs that can be equivalent to a capacitor and an inductor in parallel are incorporated to realize an attenuation pole (AP) in the higher stopband of the proposed BPF without increasing the circuit size, and the equivalent circuit of the BPF is also given. By properly adding varactor diodes into the slotted stubs to tune the equivalent capacitance of the stubs, the corresponding AP can be shifted, and then the passband width of the BPF can be accordingly tuned, leading to a bandwidth-agile BPF.

Index Terms — Bandpass filter (BPF), defected ground structure (DGS), and tunable filter.

I. INTRODUCTION

Bandpass filter (BPF) [1-10] is an essential component in various microwave and wireless communication systems. However, a single filter may not be able to satisfy the demands for all operating bands. It is well known that the frequency spectrum is valuable and limited, and it is always being used for several purposes. Therefore, electronically reconfigurable or tunable microwave filters are drawing more attention for research and development because of their significance in improving the capability of current and future design. Since microstrip filters can easily promote this kind of integration with a small size, there has been increasing interest in developing tunable or reconfigurable filters based on microstrip line. So far, much work in this field has been conducted [11-18], and most of them

employ the varactor diode to tune center frequency [11-15] and the passband width [16-18] due to its high tuning speed (in nanoseconds) and low cost. However, the varactors are all loaded onto microstrip line structure in these bandwidth-agile filters.

Defected ground structure (DGS) [19-23], which is etched from the ground plane of the transmission line, is broadly applied to the designs of microwave circuits owing to its numerous advantages, such as band-gap feature, slow-wave effect and so on. For instance, in the past few years, the DGS is used to design various microwave filters [19-22], showing attractive performance.

In this paper, a novel DGS bandwidth-agile BPF is proposed. By incorporating a pair of slotted radial stubs in the original DGS in [20], the attenuation pole (AP) in the higher stopband can be obtained. Accordingly, the varactor diodes are added in the slotted stubs to tune the AP, and then vary the passband width of the proposed BPF. Finally, a demonstration BPF is designed and fabricated. The measured results shows good agreement with the theoretical predictions.

II. PROPOSED BPF DESIGN

Figure 1 shows the layout of the proposed DGS BPF. A pair of slotted radial stubs are added in the middle of the original DGS in [20] without increasing the overall DGS size, and there is a slit on the $50\ \Omega$ microstrip line. The substrate material utilized in this structure is FR4 with thickness of 1mm and dielectric constant of 4.6. The operation frequency of the proposed BPF is determined by the DGS area ($a_1 \times a_2$), and the larger the area, the

lower the operation frequency, as shown in Fig. 2. Benefiting the quasi-elliptic function of the DGS without the slotted radial stubs [20], an AP in the lower stopband can be obtained, as shown in Fig. 2.

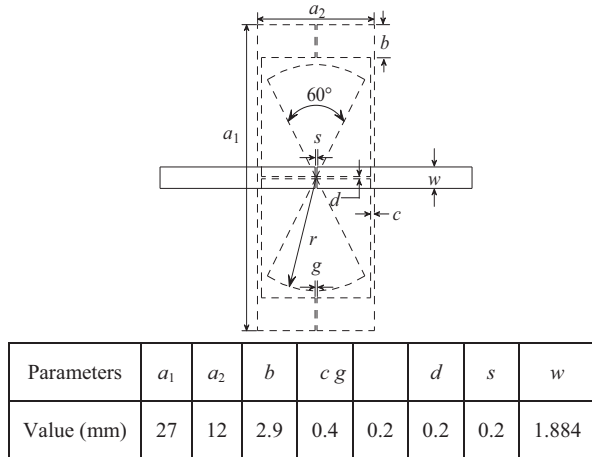


Fig. 1. Layout of the proposed DGS BPF; (solid line is layout of microstrip line and dashed line is layout of the DGS).

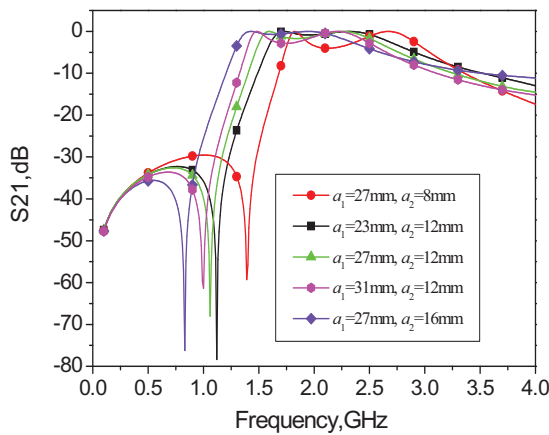


Fig. 2. Simulated results of the proposed BPF with tunable operation frequency (the DGS without the slotted radial stubs).

The slotted radial stubs in the middle of the DGS are similar to the dumb-bell slot in [20] and the equivalent circuit for the proposed entire DGS filter is shown in Fig. 3. The slotted radial stubs, which can be equivalent to a capacitor C_2 and inductor L_1 in parallel, is used to realize an AP in the higher stopband to improve the attenuation skirt, as shown in Fig. 4. As the radius r of the

radial stub is increased, the AP in the higher stopband is shifted down. As a result, the higher passband edge is also moved down, while the lower passband edge is fixed, resulting in the decrease of the passband width. Therefore, it is predictable that the passband width can be controlled by adding the varactor diodes in the radial stubs to tune the value of C_2 in Fig. 3.

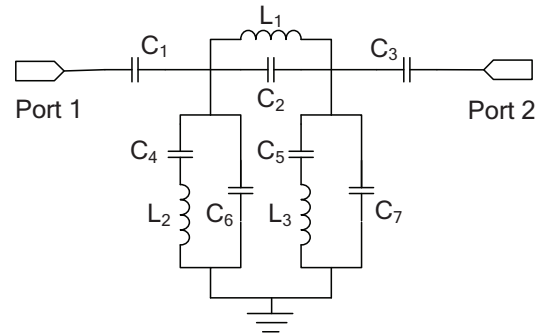


Fig. 3. Equivalent circuit model for the BPF in Fig. 1.

Figure 5 shows the sketch of the implemented BPF with tunable bandwidth, while Fig. 6 shows the fabricated BPF for demonstrating the aforementioned prediction. In the slotted radial stub, a pair of arced metal strips with width w_1 is used for loading the varactor diodes (Var). By tuning the reversed bias voltage V_b of the diodes, the AP in the higher stopband changed, resulting in tunable passband width. In Fig. 5, the dimensions r_1 , r_2 , and w_1 are fixed at 10mm, 8mm, and 1mm, respectively, while other dimensions are shown in Fig. 1. The employed varactor diodes are JDV2S71E from Toshiba in this design, and its SPICE model is shown in Fig. 7.

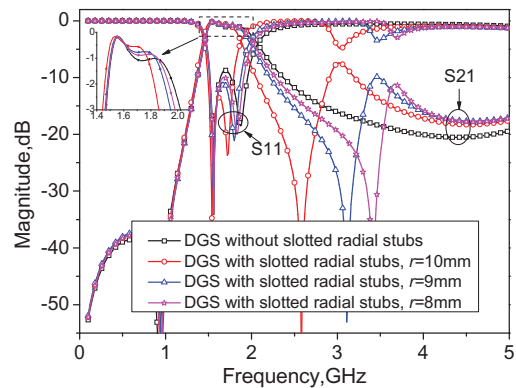


Fig. 4. Simulated results of the DGS BPF with and without the slotted radial stubs.

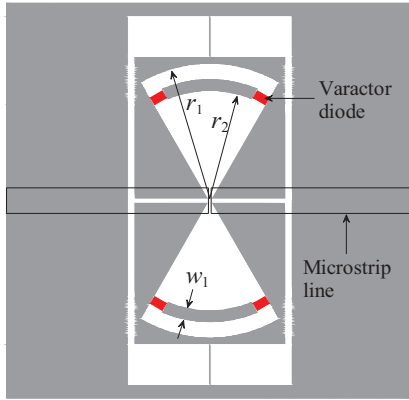


Fig. 5. Sketch of the implemented DGS bandwidth-agile BPF (the biasing circuit of the varactor diodes is not given).

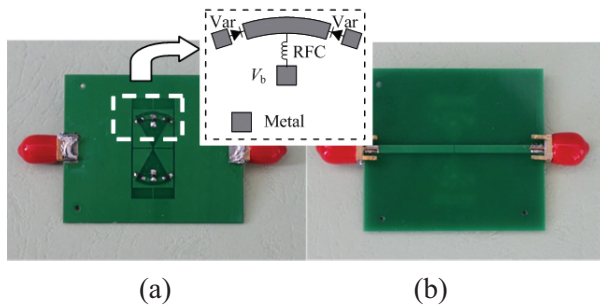


Fig. 6. Photograph of the fabricated circuit; (a) bottom view and (b) top view.

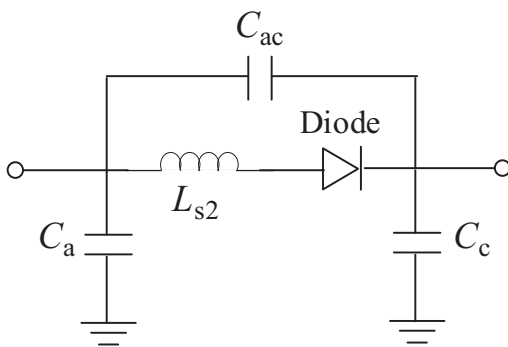


Fig. 7. SPICE model of the varactor diode JDV2S71E.

III. RESULTS

The simulation and measurement are carried out by Ansoft HFSS and Agilent E5071C network analyzer. Figure 8 shows the simulated and measured results of the proposed DGS BPF with tunable bandwidth, showing good agreement. Table I summarizes the measured performance of

the BPF. As V_b reduces from 25 V to 12 V, i.e., the capacitance of the varactor diodes increases; the AP in the higher stopband is shifted down from 2.168 GHz to 1.913 GHz, as shown in Fig. 8. The higher passband edge also moved down from 1.807 GHz to 1.701 GHz while the lower passband edge is fixed at 1.446 GHz, resulting in the decrease of the 1-dB passband width from 361 MHz to 255 MHz. Figure 9 shows the nonlinear performance of the proposed BPF in the case of two-tone test with 500 KHz frequency spacing. The measured input 3rd inter modulation point (IIP₃) keeps almost the same and is about 24 dBm as V_b varies, as shown in Table II. As can be seen from Fig. 8, some discrepancy between the simulated and measured results can be observed, especially for the insertion losses of the passband. This can be attributed to the resistance (1 Ω for each diode) of the varactor diode and the unexpected tolerance of fabrication.

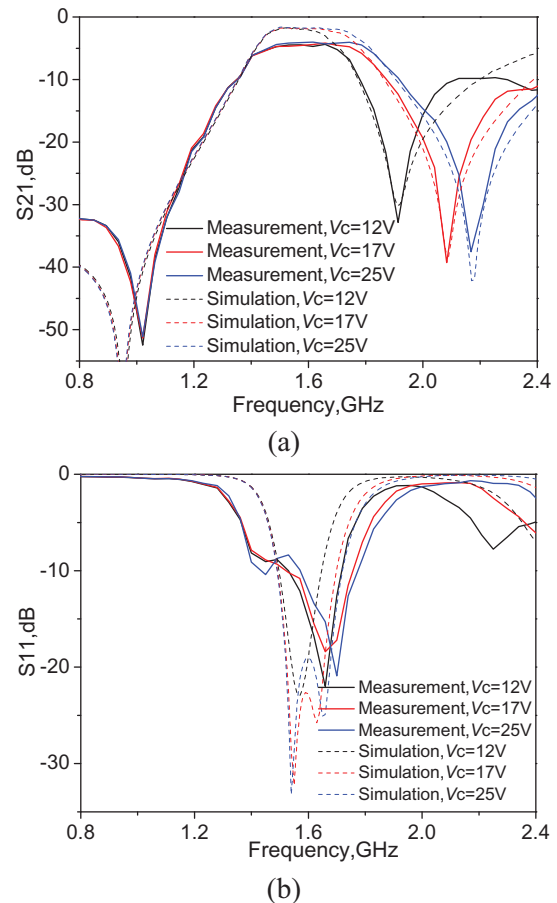
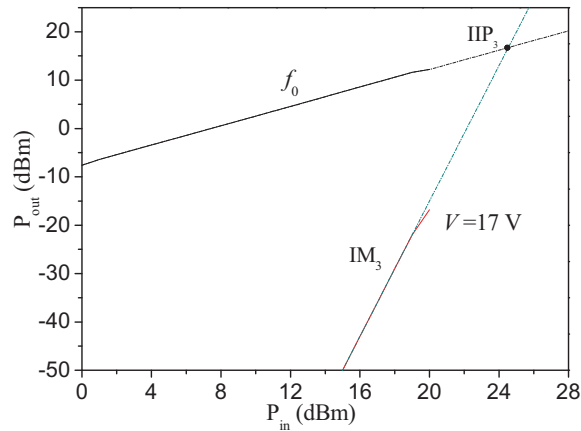


Fig. 8. Simulated and measured results of the proposed bandwidth-agile BPF; (a) S21 and (b) S11.

Table I. Measured performance of the proposed bandwidth-agile BPF against V_b .

$V_b(V)$	12	17	25
1-dB Bandwidth (MHz)	255	318	361
1-dB Lower Passband Edge (GHz)	1.446	1.446	1.446
1-dB Higher Passband Edge (GHz)	1.701	1.764	1.807
Minimum Insertion Loss (dB)	4.35	4.18	4.0

Fig. 9. Measured IIP₃ at 1.5 GHz.Table II. Measured IIP₃ in the case of different V_b .

$V_b(V)$	IIP ₃ (dBm)
12	23
17	24.5
25	24

VI. CONCLUSION

In this letter, a novel DGS pattern with a pair of slotted radial stubs has been developed for the design of microstrip bandwidth-agile BPF. The radial stubs in the middle of the proposed DGS are used to realize an AP in the higher stopband. By properly adding the varactor diodes in the radial stubs, the AP can be varied, leading to tunable passband width. Equivalent circuit for the proposed bandwidth-agile filter has been given to provide detailed design process and explain the transmission response for the bandwidth-agile bandpass filter. The measured results show good agreement with the simulated data. These would make the proposed DGS bandwidth-agile BPF useful for modern wireless communication systems.

ACKNOWLEDGMENT

The work was supported by the National Natural Science Foundation of China under Grants 61271136, 61371111, and 61371112, by Program for New Century Excellent Talents in University (NCET-11-0993), by the Natural Science Foundation of Jiangsu Province, China (Grant No. BK2012657), by Six types of Talents Project of Jiangsu Province (2011-DZXX-014) and by Graduate Research and Innovation Plan Project of the Universities of Jiangsu Province under Grant YKC13007.

REFERENCES

- [1] F. Karshenas, A. Mallahzadeh, and J. Rashed-Mohassel, "Size reduction and harmonic suppression of parallel coupled-line bandpass filters using defected ground structure," *Applied Computational Electromagnetics Society (ACES) Journal*, vol. 25, no. 2, pp. 149-155, Feb. 2011.
- [2] N. Garmjani and N. Komjani, "Improved microstrip folded tri-section stepped impedance resonator bandpass filter using defected ground structure," *Applied Computational Electromagnetics Society (ACES) Journal*, vol. 25, no. 11, pp. 975-983, Nov. 2010.
- [3] S. Rehman, A. Sheta, and M. Alkanhal, "Compact bandpass filters with bandwidth control using defected ground structure (DGS)," *Applied Computational Electromagnetics Society (ACES) Journal*, vol. 26, no. 7, pp. 624-630, July 2011.
- [4] G. Al-Omair, S. Mahmoud, and A. Al-Zayed, "Lowpass and bandpass filter designs based on DGS with complementary split ring resonators," *Applied Computational Electromagnetics Society (ACES) Journal*, vol. 26, no. 11, pp. 907-914, Nov. 2011.
- [5] M. Al Sharkawy, A. Boutejdar, F. Alhefnawi, and O. Luxor, "Improvement of compactness of lowpass/bandpass filter using a new electromagnetic coupled crescent defected ground structure resonators," *Applied Computational Electromagnetics Society (ACES) Journal*, vol. 25, no. 7, pp. 570-577, July 2010.
- [6] M. Challal, A. Boutejdar, M. Dehmas, A. Azrar, and A. Omar, "Compact microstrip low-pass filter design with ultra-wide reject band using a novel quarter-circle DGS shape," *Applied Computational Electromagnetics Society (ACES) Journal*, vol. 27, no. 10, pp. 808-815, Oct. 2010.
- [7] L. Yang, Y. Hongchun, W. Yawei, and X. Shaoqiu, "Ultra-wideband bandpass filter based on parallel-coupled microstrip lines and defected ground structure," *Applied Computational*

- Electromagnetics Society (ACES) Journal*, vol. 28, no. 1, pp. 185-187, April 2012.
- [8] S. Gao, S. Xiao, and J. Li, "Compact ultra-wideband (UWB) bandpass filter with dual notched bands," *Applied Computational Electromagnetics Society (ACES) Journal*, vol. 27, no. 10, pp. 795-800, Oct. 2012.
- [9] M. Hayati, A. Khajavi, and H. Abdi, "A miniaturized microstrip dual-band bandpass filter using folded UIR for multimode WLANs," *Applied Computational Electromagnetics Society (ACES) Journal*, vol. 28, no. 1, pp. 35-40, Jan. 2011.
- [10] H. Aghayari, N. Komjani, and N. Garmjani, "A novel integrated corrugated waveguide bandpass filter," *Applied Computational Electromagnetics Society (ACES) Journal*, vol. 27, no. 1, pp. 97-73, Jan. 2012.
- [11] E. Pistono, L. Duvillaret, J. Duchamp, A. Vilot and P. Ferrari, "Improved and compact 0.7 GHz tune-all bandpass filter," *Electron. Lett.*, vol. 43, no. 3, pp. 165-166, Feb. 2007.
- [12] X. Zhang, Q. Xue, C. Chan, and B.-J. Hu, "Low-loss frequency-agile bandpass filters with controllable bandwidth and suppressed second harmonic," *IEEE Trans. Microwave Theory Tech.*, vol. 58, no. 6, pp. 1557-1564, June 2010.
- [13] K. Kim, "Tunable dual-mode filter using varactor and variable ring resonator on integrated BST/TiO₂/Si substrate," *Electron. Lett.*, vol. 46, pp. 509-511, April 2010.
- [14] E. Djoumessi, M. Chaker, and K. Wu, "Varactor-tuned quarter-wavelength dual-bandpass filter," *IET Microw. Antennas Propag.*, vol. 3, no. 7, pp. 117-124, 2009.
- [15] J. Chen, J. Shi, Z. Bao, and Q. Xue, "Tunable and switchable bandpass filters using slot-line resonators," *Progress In Electromagnetics Research*, vol. 111, pp. 25-41, 2011.
- [16] X.-G. Huang, Q.-Y. Feng, and Q.-Y. Xiang, "Bandpass filter with tunable bandwidth using quadruple-mode stub-loaded resonator," *IEEE Microw. Wireless Compon. Lett.*, vol. 22, no. 4, pp. 176-178, April 2012.
- [17] A. Serrano, F. Corraera, T.-P. Vuong, and P. Ferrari, "Synthesis methodology applied to a tunable patch filter with independent frequency and bandwidth control," *IEEE Trans. Microw. Theory Tech.*, vol. 60, no. 3, pp. 484-493, March 2012.
- [18] H.-J. Tsai, N.-W. Chen, and S.-K. Jeng, "Reconfigurable bandpass filter with separately relocatable passband edge," *IEEE Microw. Wireless Compon. Lett.*, vol. 22, no. 11, pp. 559-561, Nov. 2012.
- [19] D. Ahn, J. Park, C. Kim, J. Kim, Y. Qian, and T. Itoh, "A design of the low-pass filter using the novel microstrip defected ground structure," *IEEE Trans. Microwave Theory Tech.*, vol. 49, no. 1, pp. 86-92, Jan. 2001.
- [20] J. Chen, J. Li, K. Wan, and Q. Xue, "Compact quasi-elliptic function filter based on defected ground structure," *IEE Proc.-Microw. Antennas Propag.*, vol. 153, no. 4, pp. 320-324, Aug. 2006.
- [21] G. Wu, W. Mu, X. Dai, and Y. Jiao, "Design of novel dual-band bandpass filter with microstrip meander-loop resonator and CSRR DGS," *Progress In Electromagnetics Research*, vol. 78, pp. 17-24, 2008.
- [22] J. Chen, Z. Weng, Y. Jiao, and F. Zhang, "Lowpass filter design of Hilbert curve ring defected ground structure," *Progress In Electromagnetics Research*, vol. 70, pp. 269-280, 2007.
- [23] X. Chen, X. Shi, Y. Guo, and M. Xiao, "A novel dual band transmitter using microstrip defected ground structure," *Progress In Electromagnetics Research*, vol. 83, pp. 1-11, 2008.



Zhi-Hua Bao was born in Nantong, Jiangsu Province, China, in 1955. He received his B.S. degree from Chongqing University, Chongqing, China, in 1982, the M.S. degree from Nanjing University of Posts and Telecommunications, Nanjing, China, in 1985. In 1988,

he joined Nantong University as a Lecturer, where he is currently a Professor with the School of Electronics and Information. He has authored or coauthored over 60 journal papers. He has owned 4 Chinese patents. His research interests include modern communication theory and technology, communications-specific integrated circuit designs and RF/microwave active and passive circuits.



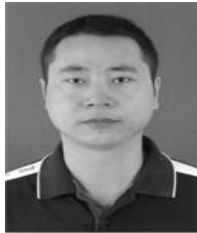
Qing-Yuan Lu received the B.Sc. degree from NJU, Nanjing, China, in 2010, and is currently working toward the M.Sc. degree in Electromagnetic Field and Microwave Technology in NTU, China. His research interests include balanced circuits and

antenna, etc.



Chuan Shao received the B.Sc. degree from Nantong University, Nantong, China, in 2012, and is currently working toward the M.Sc. degree in Electromagnetic Field and Microwave Technology in Nantong University, China. His research interests include

microwave filters, etc.



Jian-Xin Chen was born in Nantong, Jiangsu Province, China, in 1979. He received the B.S. degree from HuaiYin Teachers College, Huai'an City, Jiangsu Province, China, in 2001, the M.S. degree from the University of Electronic Science and Technology of China (UESTC), Chengdu, China, in 2004, and the Ph.D. degree from the City University of Hong Kong, Kowloon, Hong Kong, in 2008. Since 2009, he has been with Nantong University, Jiangsu Province, China, where he is currently a Professor. His research interests include RF/microwave active and passive circuit designs. Dr. Chen was the recipient of the Best Paper Award presented at the Chinese National Microwave and Millimeter-Wave Symposium, Ningbo, China, in 2007.



Shibing Zhang received the B.S. degree from Dalian Maritime University, China, and the M.S. degree and the Ph.D. degree from Nanjing University of Posts and Telecommunications, China respectively in 1983, 1989 and 2007. He worked as an associate engineer in the Nantong Changjiang Communication and Navigation Management Section from Sept. 1983 to Aug. 1986, engineer in the Yancheng Electronic Equipment Manufactory from Feb. 1989 to Apr. 1997 and senior engineer in the Haimen Economical Information Centre from May. 1997 to Mar. 2001 respectively. Since Apr. 2001, he has been working in Nantong University as a professor. From Jul. 2009 to Mar. 2010, Dr Zhang was a visiting scholar with the Department of Electrical and Computer Engineering, University of Victoria. His current research interests include wireless communications and networking, OFDM system, ultra-wideband communications, cognitive radio, cooperative communications.

Square Dual-Mode Quasi-Elliptic Bandpass Filter with Wide Upper Stopband

Y. Ma^{1,2}, W. Che¹, W. Feng¹, and J.-X. Chen³

¹ Department of Communication Engineering, Nanjing University of Science and Technology, Nanjing 210094, China
yeeren_che@163.com

² Faculty of Mathematics and Physics, Huaiyin Institute of Technology, Huai'an 223003, China

³ School of Electronics and Information, Nantong University, Nantong 226019, China

Abstract — A square dual-mode quasi-elliptic bandpass filter (BPF) with a wide stopband is proposed. To realize the quasi-elliptic response and harmonic suppression for the filter, the inductive source-load coupling is introduced. To achieve wider stopband suppression, the open-circuited stubs are adopted. A demonstration filter with 3-dB fractional bandwidth (2.84 GHz – 3.28 GHz) about 14.3 % has been designed, fabricated, and measured. Simulated and measured results indicate that the proposed filter can effectively suppress 6th harmonic response referred to a suppression degree of 16.5 dB.

Index Terms — Bandpass filter, dual-mode, quasi-elliptic, and wide upper stopband.

I. INTRODUCTION

To meet the requirements of modern microwave communication systems, compact microwave BPFs with wide stopband suppression and low cost are highly required. The dual-mode microstrip resonators are attractive because each resonator can be used as a doubly tuned circuit, therefore, the number of resonators required for a given degree of filter is reduced by half, resulting in a compact design [1]. Open stub loaded dual-mode filters have an inherent transmission zero [2]. The dual-mode filters with two transmission zeros were obtained by introducing capacitive and inductive source-load coupling in [3] and [4], respectively. A hexagonal dual-mode inductance-load filter with four transmission zeros

was presented in [5]. Harmonic suppression is not considered in [3-5]. Generally, designing bandpass filters with wideband harmonic suppression is a challenge [6-10]. Dual-mode filters with harmonic suppression were realized by source-load coupling in [6-7]. The stopband is extent to $3f_0$ (f_0 : passband center frequency) in [6], but there is only one transmission zero and the selectivity is not good. The BPF with a short-stub-loaded odd-even mode open loop stepped impedance resonator achieving 60 % size reduction is presented in [7], but the first spurious passband occurs at $3f_0$. Another miniaturized dual-mode BPF with 67 % size reduction in [8] is realized using odd-even mode loop resonator. A coupling and routing scheme is presented to suppress the first harmonic response, yet the stopband is only extended up to $2.72f_0$.

In this letter, a square dual-mode quasi-elliptic BPF using the short-circuited and open-circuited stubs with a wide stopband is proposed. The inductive source-load coupling introduces another transmission zero at lower stopband edge to realize quasi-elliptic response and harmonic suppression partly. The stopband is extended to $6.4f_0$ by employing the open-circuited stubs. The theoretical design, simulation, and experimental results are given and discussed.

II. ANALYSIS AND DESIGN OF PROPOSED BPF

The circuit of the proposed square dual-mode resonator under weak coupling is shown in Fig. 1 (a), consisting of a half-wavelength resonator with

a shunt open stub. Z_1 is the characteristic impedance of the half-wavelength resonator with the electrical length $\theta_1 + \theta_2 + \theta_3 = 90^\circ$, $Z_1/2$ and Z_2 are the characteristic impedance of the open stubs with the electrical length θ_4 and θ_0 , respectively. Two microstrip lines with characteristic impedance $Z_0 = 50 \Omega$ are connected to ports 1 and 2. The even-odd mode equivalent circuits of the proposed filter are shown in Figs. 1 (b) and (c). The frequency responses of the resonator under weak coupling are shown in Fig. 2 (a) and (b) for the case of different L_0 and L_1 . It is easy to see that L_0 only controls the even-mode resonant frequency while the even-odd mode resonant frequencies are controlled by L_1 . Thus, the required central frequency and passband can be achieved by controlling L_0 and L_1 with the proper characteristic impedance.

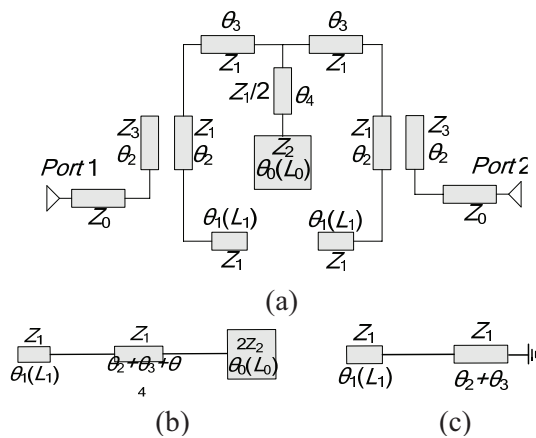
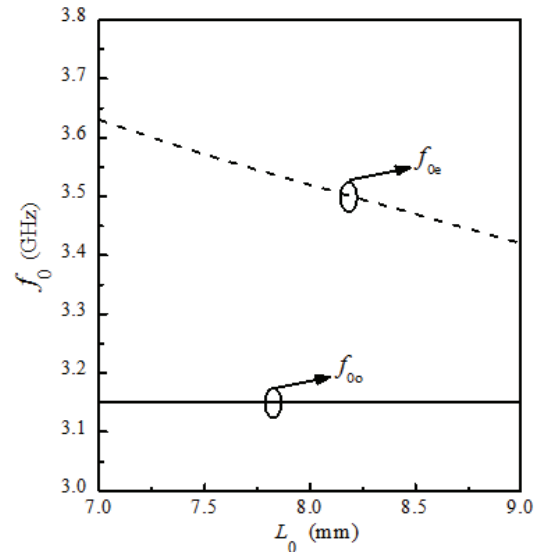


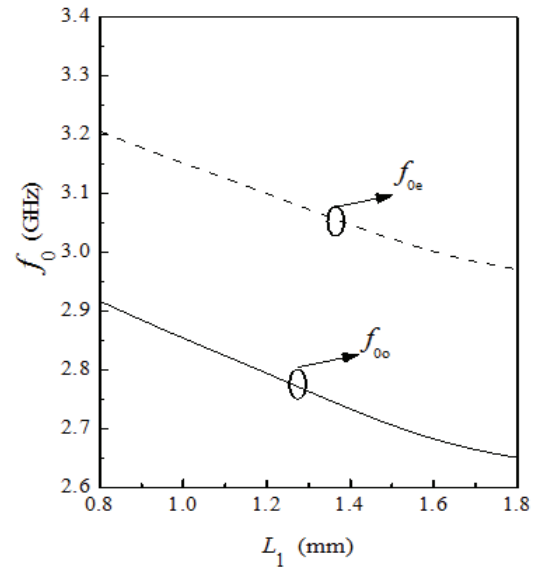
Fig. 1. (a) Circuit of proposed dual-mode resonator, (b) even-mode circuit, and (c) odd-mode circuit.

The layout of the proposed filter is shown in Fig. 3. The via holes are used to realize the required inductance. A transmission zero caused by the inductive cross-coupling between source and load is introduced at lower stopband for improving the selectivity, which can be controlled by tuning the coupling gap (S_3). As shown in Fig. 4 (a), when S_3 decreases from 1.5 mm to 0.5 mm, the lower transmission zero moves towards the passband edge while the upper inherent transmission zero changes barely. The quasi-elliptic response of the filter is realized with the two transmission zeros. It may be seen that the stopband is affected by S_3 . In order to achieve the

narrower roll-off skirts and wider stopband suppression, S_3 is designed as 1 mm. The stopband may be further broadened by introducing two quarter-wavelength open-circuited stubs [10].



(a)



(b)

Fig. 2. (a) Simulated even-odd mode frequency responses under different L_0 and (b) simulated even-odd mode frequency responses under different L_1 .

Figure 4 (b) shows the simulated frequency responses of the proposed filter with two same quarter-wavelength open-circuited stubs under the optimized values of W_3 and L_4 (as shown in Fig. 3).

With the introduction of the two different embedded open-circuited stubs (EOCS) wider stopband can be realized. The two open-circuited stubs acts as bandstop way [11] to generate two more transmission zeros in the upper stopband as be seen in Fig. 4 (b) for harmonic suppression. Figure 4 (b) shows the simulated frequency responses of the proposed filter with the two EOCS s under the optimized values of $g_1, g_2, g_3, t_1, t_2,$ and W_5 (as shown in Fig. 3). In this way, a square dual-mode quasi-elliptic BPF with a wide stopband using the short-circuited and open-circuited stubs can be realized.

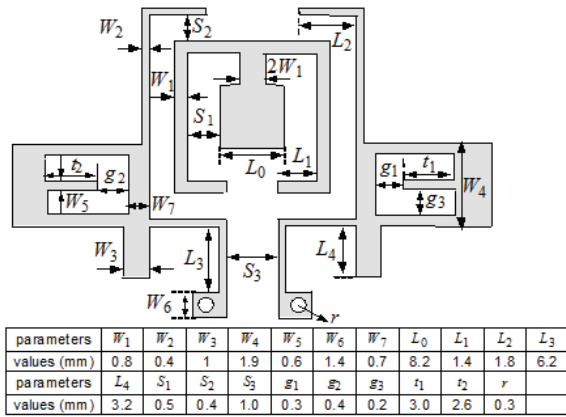


Fig. 3. Layout and parameters of proposed filter.

III. MEASURED RESULTS AND DISCUSSIONS

One prototype of the proposed dual-mode quasi-elliptic BPF with a wide stopband is designed and fabricated on an RO4003c substrate with $\epsilon_r = 3.38$ and $h = 0.8$ mm. The structure parameters of the filter are shown in Fig. 3. The size of the filter is 19.3 mm \times 20.0 mm, which corresponds to an electrical size of $0.33\lambda_g \times 0.34\lambda_g$, where λ_g is the guided wavelength at the center frequency of the passband. Figure 5 shows the photograph of the fabricated filter. The measured S -parameters are illustrated in Fig. 6. As can be seen from this figure, the measured 3-dB fractional bandwidth is about 14.3 % (2.84 GHz – 3.28 GHz), with the minimum insertion loss less than 1 dB. Inside the passband, the return loss is better than 15.3 dB. Two transmission zeros (at 1.87 GHz and 3.84 GHz) are near the edges of the passband, realizing the quasi-elliptic response. Furthermore, the proposed filter also exhibits a wide stopband

performance of 6th harmonic suppression referred to a 16.5 dB suppression degree. Table I shows the performance comparison of the proposed design with several previous designs. Hence, the advantages of the proposed filter can be clearly observed.

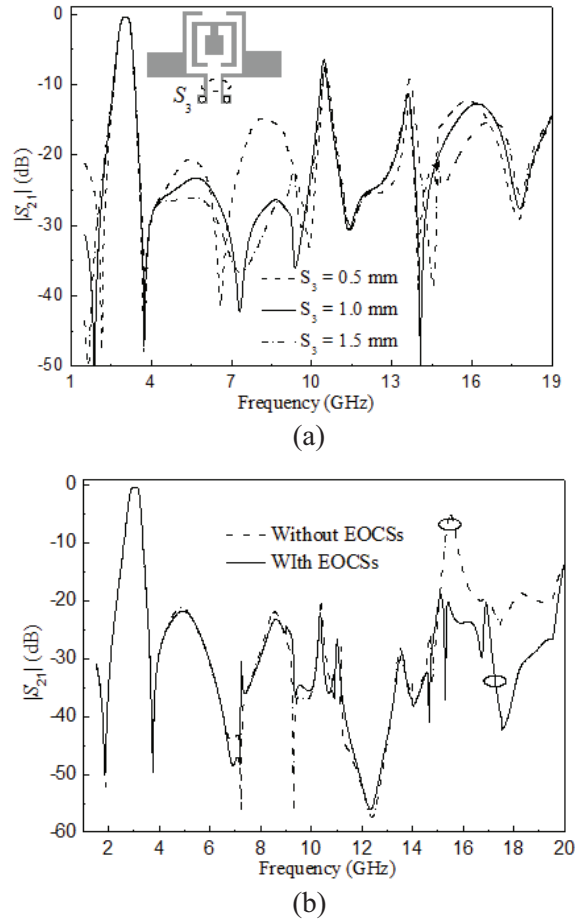


Fig. 4. (a) Frequency responses of the BPF with S-L coupling under different S_3 and (b) frequency responses of the BPF with/without EOCSs.

Table I: Performance comparison of filters.

Ref.	Harmonic suppression
[2]	No
[3]	No
[4]	No
[5]	No
[6]	2 nd
[7]	3 rd
[8]	2 nd
This work	6 th

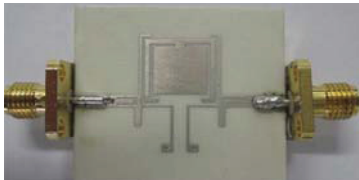


Fig. 5. Photograph of the proposed dual-mode BPF.

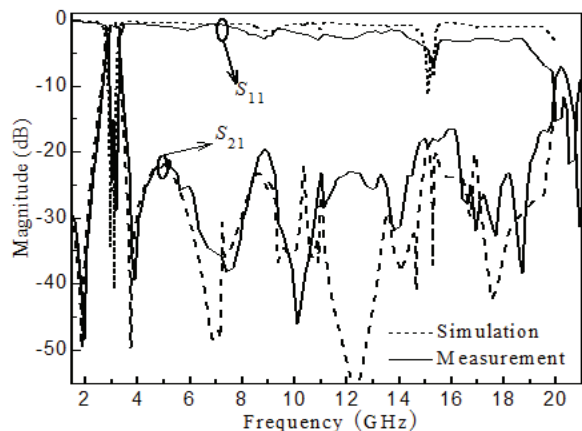


Fig. 6. Simulated and measured results of the dual-mode BPF.

IV. CONCLUSION

A square dual-mode quasi-elliptic BPF with a wide stopband is proposed. Both wide stopband and the quasi-elliptic response can be obtained by employing the open-circuited and short-circuited stubs. Simulated and measured results show that the proposed BPF has the properties of low insertion loss, wider stopband, and high selectivity. With all these good performances the proposed filter could be applicable for modern wireless communication system.

ACKNOWLEDGEMENT

This work was supported by the Natural Science Foundation of China (60971013), the 2009 Innovative Graduate Projects of Jiangsu Province and the Program for New Century Excellent Talents in University (NCET-11-0993).

REFERENCES

- [1] J. Hong and M. Lancaster, *Microstrip Filter for RF/Microwave Application*, Wiley, New York, USA, 2001.
- [2] C. Liao, P. Chi, and C. Chang, "Microstrip realization of generalized Chebyshev filter with

box-like coupling schemes," *IEEE Trans. Microw. Theory Tech.*, vol. 55, no. 1, pp. 147-153, Jan. 2007.

- [3] X. Zhang, Z. Yu, and J. Xu, "Design of microstrip dual-mode filters based on source-load coupling," *IEEE Microw. Wirel. Compon. Lett.*, vol. 18, no. 10, pp. 677-679, Oct. 2008.
- [4] C. Wei, B. Jia, Z. Zhu, and M. Tang, "Novel trigonal dual-mode filter with controllable transmission zeros," *IET Microw. Antennas Propag.*, vol. 5, no. 13, pp. 1563-157, Oct. 2011.
- [5] C. Wei, B. Jia, Z. Zhu, and M. Tang, "Hexagonal dual-mode filter with four transmission zeros," *Electron. Lett.*, vol. 47, no. 3, pp. 195-196, Feb. 2011.
- [6] F. Xiao, X. Tang, L. Wang, and T. Wu, "Compact dual-mode H-shaped filter with source/load coupling for harmonic suppression," *Microw. Opt. Tech. Lett.*, vol. 52, pp. 1431-1434, June 2010.
- [7] L. Athukorala and D. Budimir, "Compact dual-mode open loop microstrip resonators and filters," *IEEE Microw. Wirel. Compon. Lett.*, vol. 52, no. 6, pp. 698-670, Nov. 2009.
- [8] J. Wang, J. Li, J. Ni, S. Zhao, W. Wu, and D. Fang, "Design of miniaturized microstrip dual-mode filter with source-load coupling," *IEEE Microw. Wirel. Compon. Lett.*, vol. 22, no. 6, pp. 698-670, June 2010.
- [9] F. Karshenas, A. Mallahzadeh, J. R.-Mohassel, "Size reduction and harmonic suppression of parallel coupled-line bandpass filter using defected ground structure," *Applied Computational Electromagnetics Society (ACES) Journal*, vol. 25, no. 2, pp. 149-155, Feb. 2010.
- [10] W.-H. Tu and K. Chang, "Compact microstrip bandstop filter using open stub and spurline," *IEEE Microw. Wireless Compon. Lett.*, vol. 15, no. 4, pp. 268-270, Apr. 2005.
- [11] P. Sarkar, R. Ghatak, M. Pal, and D. Poddar, "Compact UWB bandpass filter with dual notch bands using open circuited stubs," *IEEE Microw. Wireless Compon. Lett.*, vol. 22, no. 9, pp. 453-455, Sep. 2012.



Yalin Ma received the M. Sc. degree from UESTC, Chengdu, China, in 2006. He is currently working toward the Ph.D. degree in Electromagnetic Field and Microwave Technology in NJUST. His research interest is the design of tunable circuits, differential

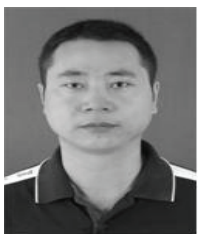
network, etc.



Wenquan Che received the M.Sc. degree from NUST, Nanjing, China, in 1995, and the Ph.D. degree from the City University of Hong Kong (CITYU), Kowloon, Hong Kong, in 2003. She is currently a Professor with NUST, Nanjing, China. Her research interests include electromagnetic computation, planar/coplanar circuits and subsystems in RF/microwave frequency, microwave monolithic integrated circuits (MMICs) and medical application of microwave technology. Dr. Che was the recipient of the 2007 Humboldt Research Fellowship presented by the Alexander von Humboldt Foundation of Germany, the 5th China Young Female Scientists Award in 2008 and the recipient of Distinguished Young Scientist awarded by the National Natural Science Foundation Committee (NSFC) of China in 2012.



Wenjie Feng received the M. Sc. degree from NUST, Nanjing, China, in 2010, and is currently working toward the Ph.D. degree in Electromagnetic Field and Microwave Technology in NJUST. His research interests include ultra-wideband (UWB) circuits and technologies, etc.



Jian-Xin Chen received the M.S. degree from UESTC, Chengdu, China, in 2004, and the Ph.D. degree from CITYU, Kowloon, Hong Kong, in 2008. He is currently a Professor with Nantong University, Jiangsu Province, China. His research interests include RF/microwave active and passive circuit designs.

Analysis of a Novel Ka Horn Antenna with Low Cross-Polarization

Y.-Z. Liu, S. Xiao, and B.-Z. Wang

Institute of Applied Physics
University of Electronic Science and Technology of China, Chengdu, 610054, China
yuanzhuliu@vip.qq.com, xiaoshaoqiu@uestc.edu.cn, bzwang@uestc.edu.cn

Abstract – A Ka combined horn antenna with low cross-polarization is presented in this paper. The antenna consists of an edge-slotted waveguide linear array, a metallic-grid plane in the horn throat and a horn. The effects of metallic-grid and single-ridged waveguide to the cross-polarization are analyzed. Three kinds of 62-element Taylor linear array at Ka band are fabricated and measured and the measured cross-polarization level is less than -35 dB in operating bandwidth. The proposed antennas are benefit for fabrication and fixation with low cross-polarization and can be extensively used in radar and communication systems.

Index Terms – Cross-polarization, edge slot, horn, ridge waveguide, and waveguide array.

I. INTRODUCTION

Due to many advantages, such as simple feeding, easy manufacture, high efficiency, low cost, precise controlling of aperture distribution and low loss, the rectangular slotted waveguide arrays have been found wide applications in radar and communication systems [1-3]. In some slotted waveguide array applications, edge-wall slots are preferred to their broad wall counterparts mainly due to their ability to electronically scan a wider angular sector without introducing a grating lobe, thanks to its smaller element spacing [3, 4]. And a number of investigations have been presented on the analysis of the edge-slotted structures [5-9]. The horns are often attached to the edge-slotted waveguide linear arrays to decrease the vertical (in elevation) beamwidth of the antenna, and to increase the gain [10, 11]. However, the most common edge-slotted waveguide arrays are composed of inclined shunt slots, which have

severe cross-polarization problems due to the inclined field vectors with respect to the vertical plane at the slot aperture [3]. In [12-14], non-inclined slots on the edge wall of a rectangular waveguide have been implemented to reduce the cross-polarization. However, both of these structures are mechanically challenging especially for the application in the Ka band. In this paper, infinite array characterization technique is applied to the two-slot cell and using this characterization data, an edge-slotted waveguide array can be designed effectively. In [15], a modified double-ridged antenna for 2 GHz – 18 GHz was designed. In order to decrease the cross-polarization effectively, we adopt a symmetric rectangular single-ridged slotted waveguide, where longitudinal metallic grid is located on the right side-wall and the radiated slots connected to the radiation waveguide on the left side-wall. Using this technique, the cross-polarization can be improved about 20dB compared to the case of without grid. And a combined horn antenna with low cross-polarization level and narrow beamwidth is designed for the FMCW radar system operating at the Ka band. The proposed combined horn antenna whose aperture is 343 mm \times 76 mm in the orthogonal section is analyzed, so are the effects of the metallic grid on the horn throat and the single-ridged waveguide to the cross-polarization in this paper. All the simulations presented here are carried out by commercial software Ansoft HFSS and compared with measurement results.

II. SLOT CELL DESIGN

The cross-section view profile of the proposed antenna is shown in Fig. 1 (a). The slot cell comprises two cross-inclined edge-slots as shown

in Fig. 1 (b). The radiated waveguide is a non-standard waveguide ($W = 7$ mm and $L = 3$ mm), and a symmetric rectangular single-ridged slotted waveguide ($U_W = 7$ mm and $U_L = 9$ mm) with longitudinal grids located on the right side-wall and the radiated slots on the left side-wall is connected to the radiated waveguide. The surface fields on the edge-slotted radiation plane are the superposition field excited by the dominant mode and higher modes. The higher modes transmitting in the single-ridged waveguide will degrade rapidly. The electric field distributions at the slots'-aperture are illustrated in Fig. 2 (a). The electric field E_1 and E_2 can be divided into two orthogonal components (E_{1x} , E_{1y} , E_{2x} , and E_{2y}) along the x-axial and y-axial, respectively. The E_{1x} and E_{2x} are the co-polarization components we needed while the E_{1y} and E_{2y} are the cross-polarization components, which should be restrained. In order to reduce the cross-polarization components, we utilize a single-ridged waveguide with a longitudinal grid ($G_W = 3.4$ mm and $G_X = 2.12$ mm) located on the right side-wall of the single-ridged waveguide added outside of the radiated waveguide, as shown in Fig. 1 (a). Due to the existing grid, only small cross-polarization components (E_{1y} and E_{2y}) pass through the grid, and thus are restrained effectively. From Fig. 2 (b), we can observe that many E_y components are generated in the single-ridged waveguide, and the electric field components along the y-axial decline rapidly after passing through the longitudinal grid plane compared to that in the single-ridged waveguide. By choosing proper G_X and G_W , we can obtain the cross-polarization level needed in engineering. For the aperture of the single-ridged waveguide is a bit larger than that of the radiation waveguide, the matching to the free space can be improved. In order to further match the free space, a horn is added along the z-axial outside of the grids shown in Fig. 1 (a) where θ_c is the horn angle and FL is the horn length. The higher modes will be excited again on the grid plane of the single-ridged waveguide, and then degraded after some transmission distance in the horn, but the cross-polarization level has been improved greatly. The reflection caused by the discontinuity between the single-ridged waveguide and the horn can be neglected when θ_c is minor and the problem can be transformed into the radiation of H-plane rectangle horn aperture.

Because the edge-slotted array with horn antenna is usually quite long, its quasi-two-dimensional characteristic allows one to consider it analogous to an H-plane sector horn. By selecting suitable size of G_W , G_X , U_W , and U_L , the dominant mode will propagate in the single-ridged waveguide while the higher modes will cut off. In order to greatly reduce simulation time we utilize infinite array approach to obtain the characterization data of the cross-inclined slot. For the linear array simulations, periodic boundary conditions are applied along the transverse direction to the waveguide. For the combined horn antenna presented in this paper, the main impact factor to the cross-polarization are the grid strip-width G_W and single-ridged waveguide depth U_L . Because the structure is assumed to be two-dimensional, the analysis can be greatly simplified and the influences of the above parameters on the antenna can be acquired, respectively by the full-wave electromagnetic simulation software Ansoft HFSS.

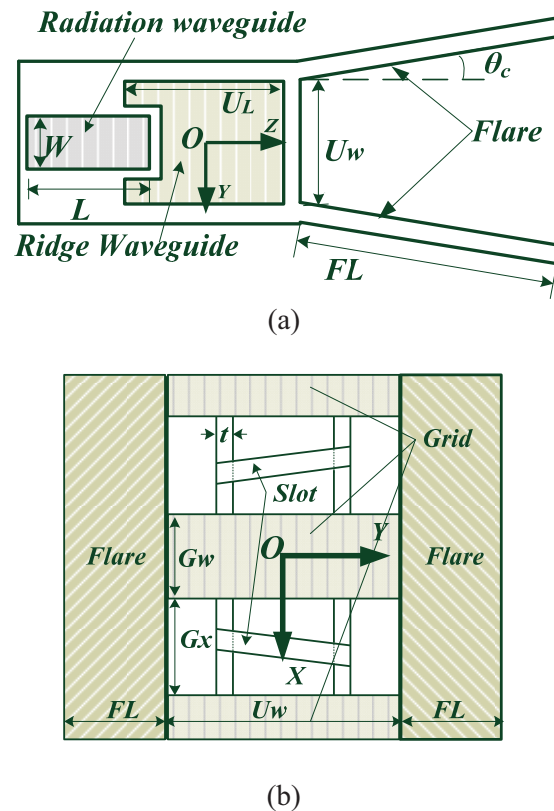


Fig. 1. Geometry of the proposed antenna (a) cross-sectional view and (b) top view.

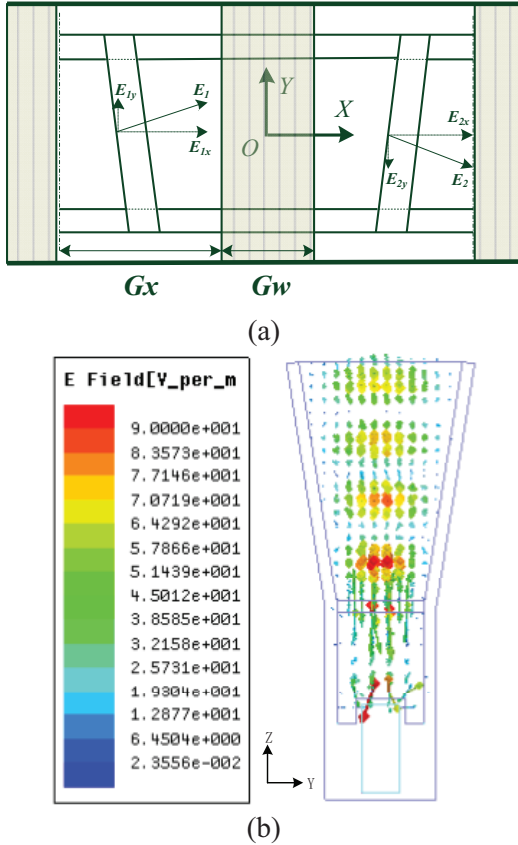


Fig. 2. (a) Electric field at the slots aperture and (b) electric field in the structure.

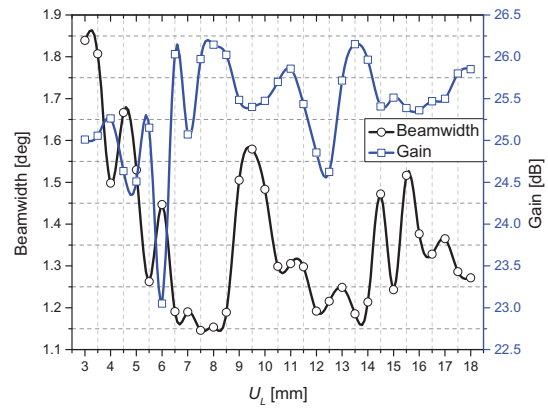
III. ARRAY DESIGN

The edge-slotted waveguide linear array feeds the horn antenna. The elements in the linear array are arranged along the x-axis and the polarization of the antenna is the same as the direction of x-axis, and the slot elements have Taylor distribution, which is designed for a -27 dB side-lobe level (SLL). In order to reduce the influence of cross-polarization, the effects of different single-ridged waveguide depth U_L and grid strip-width G_W to cross-polarization are studied in this paper.

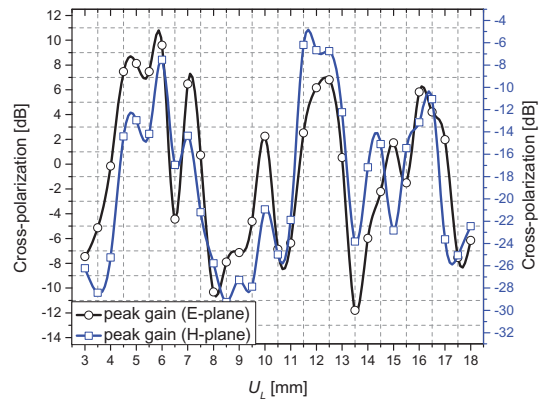
A. Effects on cross-polarization for different U_L

Figure 3 (a) illustrates that the beamwidth and the gain change with U_L periodically. Due to the higher mode's attenuation and fundamental mode's propagation in the single-ridged waveguide, a minimum value can be obtained every about $\lambda_0/2$ (λ_0 is the wavelength in free space). The peak gain curve of the cross-polarization in E- and H-planes for different U_L is

shown in Fig. 3 (b). Evidently, the periodical variation trend is almost coherent between E-plane and H-plane while the cross-polarization in E-plane is at least 10 dB larger than that in H-plane. The results shown in Fig. 3 depict that we can acquire specific antenna performances easily by choosing proper U_L , which satisfies the special needs in engineering projects. For the proposed antenna, we choose the $U_L = 9$ mm to satisfy the requirement of low cross polarization level, high radiation gain, and narrow beamwidth.



(a)



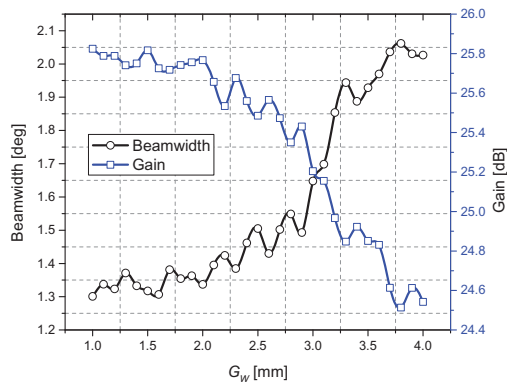
(b)

Fig. 3. (a) Beamwidth / gain versus U_L and (b) cross-polarization versus U_L .

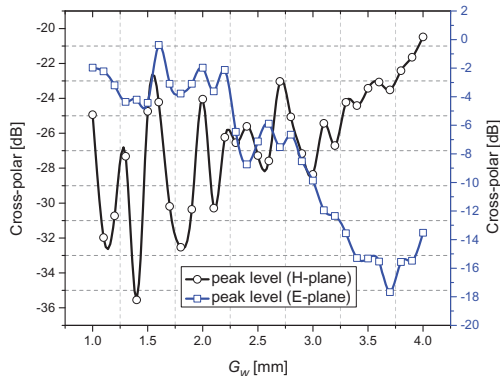
B. Effects on cross-polarization for different G_W

The grid on the horn throat has great influence on the cross-polarization in the E-plane. As can be seen from Fig. 4 (a), when $G_W \leq \lambda_0/2$, the beamwidth increases with G_W and the gain decreases with U_L . The peak gain level of the

cross-polarization in the H-plane is smaller than that in the E-plane as shown in Fig. 4 (b). For the purpose of meeting the low cross-polarization requirement, the grid strip-width (G_W) should be chosen reasonably to compromise the cross polarization in the E- and H-planes. According to the curves illustrated in Fig. 4, we set $G_W = 3.4$ mm to obtain low cross-polarization for the designed antenna, whose peak gain level of the cross-polarization is -15.2 dB and -24.4 dB in the E- and H-planes, respectively.



(a)

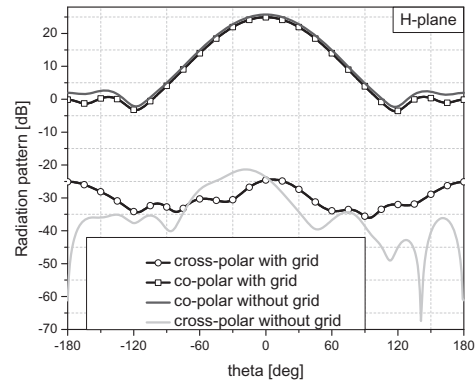


(b)

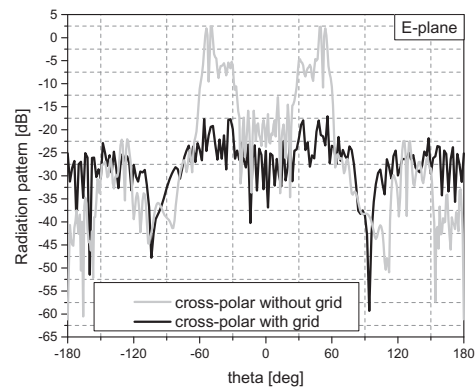
Fig. 4. (a) Beamwidth / gain versus G_W and (b) cross-polarization versus G_W .

In order to study the cross-polarization, we present three kinds of experimental models shown in Fig. 6. The measured results in Fig. 5 illustrate the comparison of the radiation pattern in E- and H-planes between *Case A* (without grid) and *Case B* (with grid). From Fig. 5, we can observe that the grid structure on the horn throat makes a bit improvement to the cross-polarization in the H-

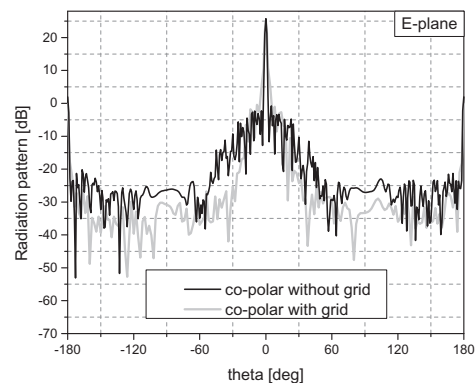
plane and a great enhancement in the E-plane while the co-polarization reduces slightly. The use of the grid makes it possible to acquire lower cross-polarization for the proposed antenna.



(a)



(b)



(c)

Fig. 5. Comparison between *Case A* and *Case B* (a) co-polarization in H-plane, (b) cross-polarization in E-plane, and (c) co-polarization in E-plane.

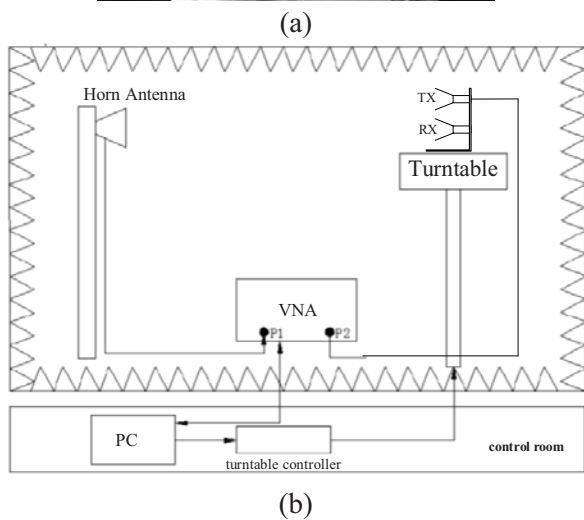
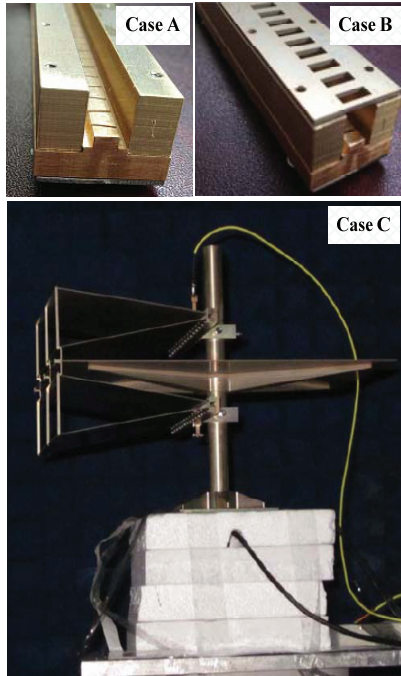
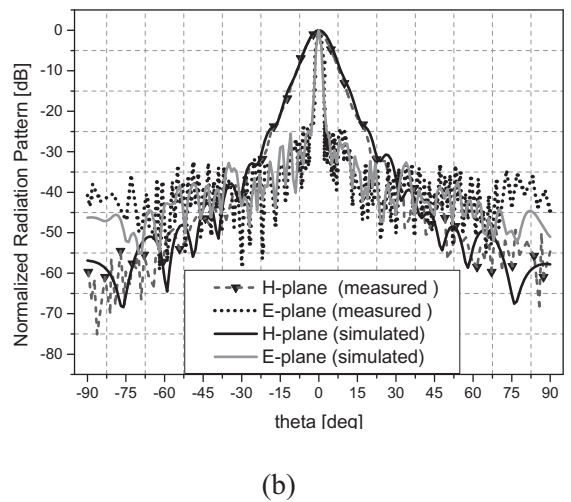
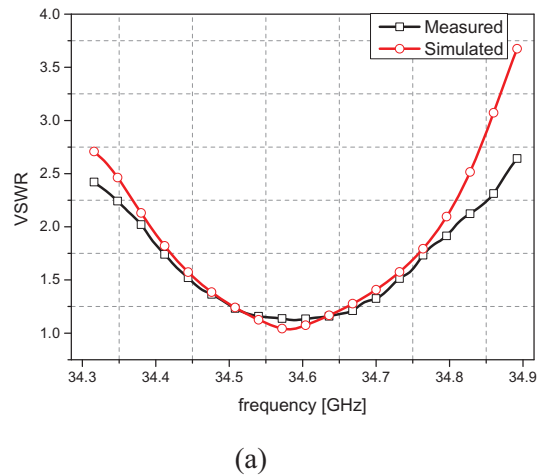
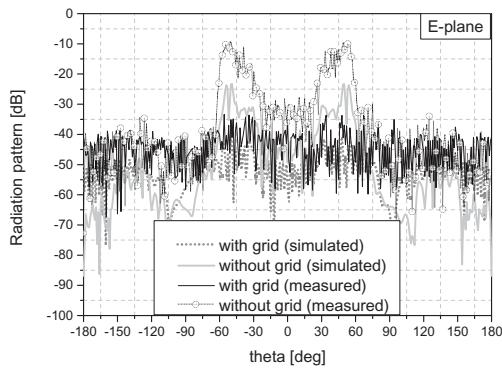


Fig. 6. (a) Experimental model for the three cases and (b) measurement setup.

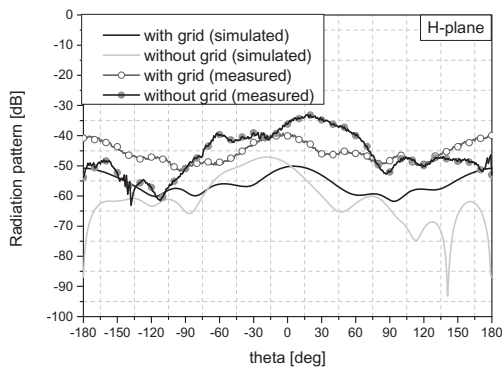
For the *Case C* in Fig. 6 (a), the horn length (FL) is 220 mm and the horn angle θ_c is 9° whose aperture is 343 mm \times 76 mm. The combined antenna consists of the single-ridged waveguide, grid on the horn throat and horn. The structure in *Case C* is made up of the two same combined-antennas and is benefit for fabrication and fixation with low cost, high gain, low side lobe level, and low cross-polarization, which is suitable for application of FMCW radar system. The measured VSWR results are revealed in Fig. 7 (a). Its value

in the bandwidth from 34.45 GHz to 34.7 GHz is lower than 1.5. The comparison between simulated and measured normalized radiation pattern of co-polarization and cross-polarization is illustrated in Fig. 7 (b), (c), and (d), respectively. As can be seen from Fig. 7 (b), the measured 3-dB beamwidth of the proposed antenna in the E- and H-planes are 1.5° and 8° , respectively. The simulated and measured results are in good agreement, which indicates that the pretty narrow beam is achieved. Figure 7 (c) and (d) illustrate that the improvement of the cross-polarization mainly concentrated in the E-plane, which improve about 20 dB for the cross-polarization performance. The comparison of the cross-polarization in the E-plane for different types of antenna is listed in Table I.





(c)



(d)

Fig. 7. Simulation versus measured results (a) VSWR, (b) co-polarization radiation pattern, (c) cross-polarization radiation pattern (E-plane), and (d) cross-polarization radiation pattern (H-plane).

Table I: Comparison of cross-polar in E-plane.

Antenna type	Cross-polar
ANT (with grid)	-40dB
ANT (without grid)	-25dB
ANT in [11]	-25dB
ANT in [12]	-35dB
Edge-slotted waveguide linear array	-28dB

IV. CONCLUSION

In this paper, the combined horn antenna with narrow beamwidth and low cross polarization is presented. The achievement of the key parametric analysis of the proposed antenna conduces to expanding the application field of the antenna. The cross polarization is mainly controlled by the

single-ridged waveguide width and metallic grids strip-width and the radiation beam in the H-plane is formed by dominating the horn length (FL) and the horn angle θ_c . In the meantime, the horn for the designed antenna has hardly effects on the radiation in the E-plane. Accordingly, it can be realized only by controlling slot parameters in the feed linear array, single-ridged waveguide depth, grid strip-width, and the horn parameters which increase the degree of design freedom. Three kinds of 62-element Taylor linear array at Ka band are fabricated and measured, which show good conformance to the simulated results. The measured cross-polarization level in *Case C* is less than -40 dB and the radiation gain is more than 30 dB at the operating bandwidth. The proposed antenna is benefit for fabrication and fixation with low cost, low cross polarization, and extensive use in radar and communication systems.

ACKNOWLEDGMENT

This work was supported in part by the National Natural Science Foundation of China (Grant 61271028), the Fundamental Research Funds for the Central Universities (Grant ZYGX2011J036), and the Fok Ying Tong Education Foundation (Grant 131107).

REFERENCES

- [1] R. Hansen, *Phased Array Antennas*, Wiley, New York, 1998.
- [2] W. Wang, S.-S. Zhong, Y.-M. Zhang, and X.-L. Liang, "A broadband slotted ridge waveguide antenna array," *IEEE Trans. Antennas Propagat.*, vol. 54, no. 8, pp. 2416-2420, August 2006.
- [3] R. Gilbert and J. Volakis, *Antenna Engineering Handbook*, Fourth Edition, McGraw-Hill, 2007.
- [4] M. Ando, J. Hirokawa, and J. Young, "Analysis of a linear slot array comprised of tilted edge slots cut in the narrow wall of a rectangular waveguide," *IEEE/ACES International Conference on Wireless Communications and Applied Computational Electromagnetics*, pp. 602-605, Hawaii, USA, April 2005.
- [5] B. Das, J. Ramakrishna, and B. Sarap, "Resonant conductance of inclined slots in the narrow wall of a rectangular waveguide," *IEEE Trans. Antennas Propagat.*, vol. 32, pp. 759-761, July 1984.
- [6] J. Young, J. Hirokawa, and M. Ando, "Analysis of a rectangular waveguide, edge slot array with finite wall thickness," *IEEE Trans. Antennas Propagat.*, vol. 55, no. 3, pp. 812-819, March 2007.

- [7] B. Lai, X.-W. Zhao, Z.-J. Su, and C.-H. Liang, "Higher-order MoM analysis of the rectangular waveguide edge slot arrays," *IEEE Trans. Antennas Propagat.*, vol. 59, no. 11, pp. 4338-4341, Nov. 2011.
- [8] G. Wu, Z. Song, X. Zhang, and B. Liu, "Study on coupling characteristics of electromagnetic wave penetrating metallic enclosure with rectangular aperture," *Applied Computational Electromagnetics Society (ACES) Journal*, vol. 26, no. 7, pp. 611-618, July 2011.
- [9] A. Jensen and S. Rengarajan, "Genetic algorithm optimization of a traveling wave array of longitudinal slots in a rectangular waveguide," *Applied Computational Electromagnetics Society (ACES) Journal*, vol. 21, no. 3, pp. 227-341, Nov. 2006.
- [10] M. Koerner and R. Rogers, "Gain enhancement of a pyramidal horn using E- and H-plane metal baffles," *IEEE Trans. Antennas Propagat.*, vol. 48, pp. 529-538, 2000.
- [11] J. Yong, M. Sugano, Y. Shibuya, A. Takahashi, and T. Itagaki, "Vertical beam shaping with metal strip in a linear edge slot array," *European Conference Antenna and Propagation (EuCAP)*, pp. 1-5, 2007.
- [12] D. Dogan and Ö. Civi, "Edge wall slotted waveguide antenna with low cross polarization," *International Symposium of Antenna and Propagation (ISAP)*, pp. 1-4, 2010.
- [13] S. Hashemi-Yeganeh and R. Elliott, "Analysis of untilted edge slots excited by tilted wires," *IEEE Trans. Antennas Propagat.*, vol. 38, no. 11, pp. 1737-1745, Nov. 1990.
- [14] W. Wang, J. Jin, J.-G. Lu, and S.-S. Zhong, "Waveguide slotted antenna array with broadband, dual-polarization and low cross-polarization for X-band SAR applications," *IEEE International Radar Conference*, 2005.
- [15] A. Mallahzadeh and A. Imani, "Modified double-ridged antenna for 2-18 GHz," *Applied Computational Electromagnetics Society (ACES) Journal*, vol. 25, no. 2, pp. 137-143, Feb. 2010.



Yuan-zhu Liu was born in Heilongjiang Province, China, in 1980. He received the B.S degree in communication engineering from Sichuan University and the M.S. degree in electromagnetic field and microwave engineering from the University of Electronic Science and Technology of China (UESTC), Chengdu, in 2007, where he is currently working toward the Ph.D. degree in radio physics. His current research interests

include phased arrays, conformal antenna, slotted waveguide arrays, RF circuit and its application.



Shaoqiu Xiao received the Ph.D. degree in electromagnetic field and microwave engineering from the University of Electronic Science and Technology of China (UESTC), Chengdu, in 2003. From January 2004 to June 2004, he was with UESTC as an Assistant Professor. From July 2004 to March 2006, he was with the Wireless Communications Laboratory, National Institute of Information and Communications Technology of Japan (NICT), Singapore, as a Researcher with a focus on the planar antenna and smart antenna design and optimization. From July 2006 to June 2010, he was with UESTC as an Associate Professor. He is now a Professor with UESTC. His current research interests include planar antenna and arrays, microwave passive circuits, and electromagnetics in ultra-wide band communication. He has authored/coauthored more than 160 technical journals, conference papers, books, and book chapters.



Bing-zhong Wang received the Ph.D. degree in Electrical Engineering from the University of Electronic Science and Technology of China (UESTC), Chengdu, China, in 1988. He joined the UESTC in 1984 and is currently a Professor there. He has been a Visiting Scholar at the University of Wisconsin-Milwaukee, a Research Fellow at the City University of Hong Kong, and a Visiting Professor in the Electromagnetic Communication Laboratory, Pennsylvania State University, and University Park. His current research interests are in the areas of computational electromagnetics, antenna theory and techniques, electromagnetic compatibility analysis, and computer-aided design for passive microwave integrated circuits.

An Unequal Wilkinson Power Divider using Half Mode Substrate Integrated Waveguide

Z. Mazani and G. Moradi

Microwave Measurement Research Lab., Electrical Engineering Department,
Amirkabir University of Technology, Tehran, 15914, Iran
Zahra_mazani@yahoo.com, ghmoradi@aut.ac.ir

Abstract — A new unequal Wilkinson power divider is presented in this paper. The structure benefits from half mode substrate integrated waveguide (HMSIW). In order to increase the characteristic impedance of the HMSIW line, an inductive post is used in the line. Different dividing ratios are obtained by changing the diameter of the inductive post. The experimental results show that the power dividing ratio is 5.1:1 over the frequency range of 9.1 GHz to 12.8 GHz. The input and output ports are well-matched and the output ports are isolated from each other over this frequency range. The experimental results and simulation results of CST Microwave Studio are in good agreement.

Index Terms — Half mode substrate integrated waveguide, substrate integrated waveguide, and Wilkinson power divider.

I. INTRODUCTION

Power dividers and combiners are passive components in microwave and millimeter-wave systems that are widely used in balanced amplifiers, mixers, and wireless communication systems. The division of power can be equal or unequal depending on the system requirements. Wilkinson power divider that has been proposed by E. Wilkinson in 1960 [1], is commonly used due to its good isolation, good output return loss, and reciprocity. This device consists of two quarter wave transmission lines and one isolation resistor that connect these lines at the end. It can be designed for equal or unequal power splits. One way to design an unequal power divider is using quarter wave lines with different impedances. In this method, when the quarter wave parts are made

of planar lines, the power dividing ratio cannot be high (more than 3). That is because the high characteristic impedance, which is needed for the lines, makes these lines too narrow to be fabricated. To solve this problem, different methods like defected ground structures (DGS) [2] and grooved substrates [3] have been applied to design unequal power dividers. However, increasing the impedance of the lines by DGS is limited and grooved substrates are difficult to be physically implemented.

Recently, substrate integrated waveguide (SIW) has been used for designing passive and active circuits [4]. This is based on combining the advantages of waveguides and planar lines in one line. So it has low attenuation and high Q-factor like waveguides along with having small size and integration compatibility like planar lines. An SIW line consists of two metal layers on top and bottom of substrate that are connected by rows of metallic vias on either side. SIW is a wideband line because TM mode cannot propagate in this line and it just can guide TE_{n0} mode [5]. That is because the spaces between vias dissipate TM mode. But the problem of SIW devices is having larger width compared to that of planar devices. One way to solve this problem is using half mode substrate integrated waveguide (HMSIW).

HMSIW has the advantages of SIW but in smaller size. It is obtained by dividing the SIW line into two parts by cutting the symmetric plane along the transmission direction. This line has less attenuation compared to that of SIW and microstrip lines [6]. Two kinds of HMSIW Wilkinson power dividers are presented in [7, 8] but both of them split the power equally. In [9, 10] the non-uniform transmission lines method has

been used to design unequal Wilkinson power divider with microstrip lines. However, in this paper, a novel unequal Wilkinson power divider with high power dividing ratio i.e., 6 is proposed that benefits from HMSIW transmission line.

In section II, the basic of HMSIW unequal Wilkinson power divider is discussed. Section III presents the simulation and measured results, and finally section IV gives a brief conclusion.

II. HMSIW UNEQUAL WILKINSON POWER DIVIDER

Figure 1 shows the structure of SIW and HMSIW lines. In order for an SIW line to have less radiation attenuation, no band gap effect and no excitation of higher order modes, one should consider the following equations [11],

$$0.05 < p/\lambda_c < 0.25 \tag{1}$$

$$1 < p/d < 2, \tag{2}$$

where d and p are the diameter of each via and the distance between two adjacent vias, respectively.

Metallic via

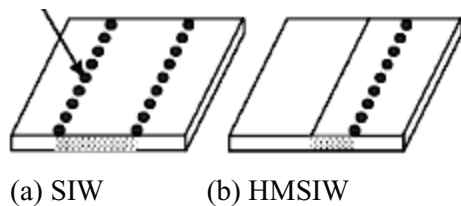


Fig. 1. The structure of SIW and HMSIW.

An equivalent rectangular waveguide for a substrate integrated waveguide is presented in [12]. This waveguide is filled with the same material as substrate of SIW. The width of equivalent waveguide can be obtained by the following equation [12],

$$W' = w - 1.08d^2/p + 0.1d^2/w \tag{3}$$

where w is the width of SIW and W' is the width of equivalent rectangular waveguide.

In this paper, the cutoff frequency of HMSIW line is chosen to be 7.5 GHz. The diameter of each via is 0.7 mm and the distance between two adjacent vias is 1.2 mm. The dielectric constant of the considered material for substrate is 3.55 and the height of the substrate is 0.508 mm. Thus, according to the equation of cutoff frequency in a

rectangular waveguide, $W'=10$ mm, then referring to equation (1), we obtain $w = 10.4$ mm. Thus the width of HMSIW is $w/2 = 5.2$ mm. The guided wavelength of an SIW line and corresponding HMSIW is [13],

$$\lambda_g = 2\pi / \sqrt{(\omega^2 \times \epsilon_r / c^2) - (\pi/w)^2} \tag{4}$$

Thus, at $f = 10.5$ GHz, the quarter wavelength is about 5.8 mm. The equal HMSIW Wilkinson power divider, which is presented in [8] is shown in Fig. 2. This circuit consists of two quarter wave HMSIW with a gap between them. These lines are connected to the ports through microstrip feed lines. The proposed unequal power divider in this paper is developed based on this structure.

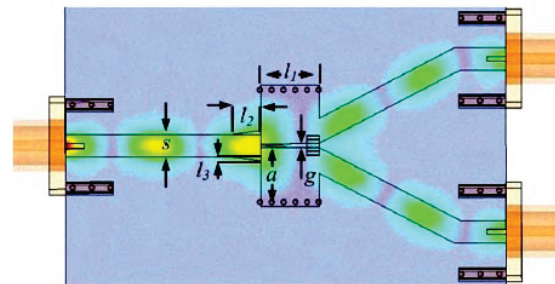


Fig. 2. An unequal HMSIW Wilkinson power divider presented in [8].

In order to design an unequal HMSIW power divider, HMSIW lines with different characteristic impedances are required. Since a HMSIW is equivalent to a rectangular waveguide, the idea of using discontinuities in a waveguide [14] can be used in HMSIW too. Thus, one way to change the impedance of a HMSIW line is using an inductive post in a place inside the HMSIW. Figure 3 indicates the equivalent circuit of an inductive post in a rectangular waveguide.

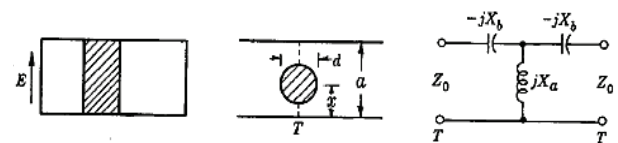


Fig. 3. Equivalent circuit of an inductive post [14].

When $d/a < 0.1$, X_b is negligible and the metal post is equivalent to X_a , which depends on the frequency and the size of the post [14]. Figure 4 indicates the transmission line model of the proposed unequal HMSIW Wilkinson power

divider. Figure 5 displays the layout of this structure. It consists of two HMSIW with a 0.5 mm gap between them. The upper side of the structure consists of a quarter wave HMSIW line, which is connected to 50 Ω microstrip feed lines by a tapered microstrip line with $Z_0 = 50 \Omega$. The characteristic impedance of the HMSIW line according to the equivalent rectangular waveguide is about $Z_1 = 30 \Omega$ at around 10.5 GHz.

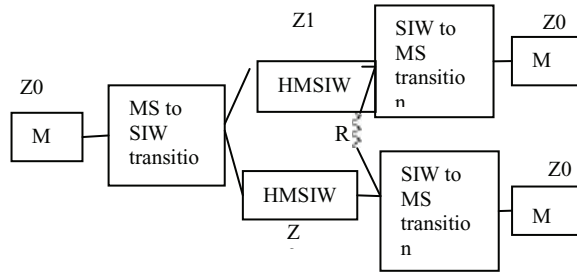


Fig. 4. Transmission line model of the proposed power divider.

For designing a 1:6 unequal Wilkinson power divider, the second line must be 180 Ω . With this characteristic impedance, the length of the second HMSIW will be about 28 mm, which is too long for this structure. To solve this problem, an inductive post is added to the second line to provide a high impedance line with smaller size. The length of this line and the place and diameter of the inductive post are obtained by tuning and optimization to have 180 Ω characteristic impedance and wider bandwidth. Since there are transition parts between HMSIW and microstrip feed lines to transform the dominant mode of HMSIW to quasi-TEM mode of microstrip, the matching circuits are designed in the transition part. The dimensions of the transition parts are obtained by tuning and optimization. The width of input and output microstrip lines is 1.1 mm to provide 50 Ω characteristic impedance. Finally, the amount of isolation resistor is equal to the sum of impedances of ports 2 and 3, which are both 50 Ω . Thus, R equals 100 Ω . Table I shows the geometrical parameters of the proposed unequal power divider.

III. SIMULATION AND EXPERIMENTAL RESULTS

The proposed structure is designed and optimized by CST Microwave Studio. The simulation results for $di = 0.5$ mm, 1 mm, and 2.4

mm are shown in Figs. 6 and 7 when the other parameters kept fixed. Table II shows a comparison between the simulation results. It is clear that when di increases, the power split becomes higher. Figures 7 (a) and (b) show the simulation and measured results of the proposed unequal Wilkinson power divider from 8 GHz to 18 GHz when $di = 1$ mm.

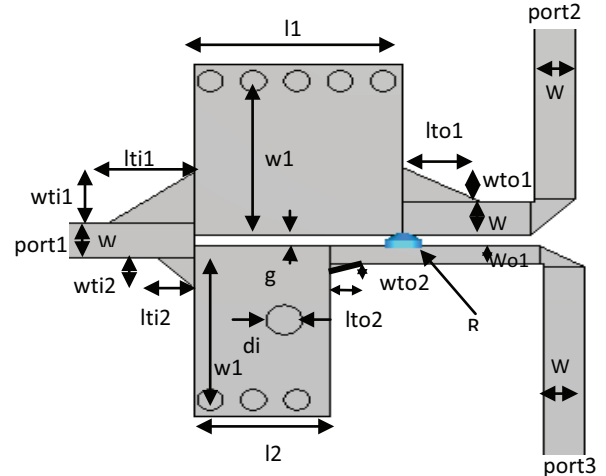


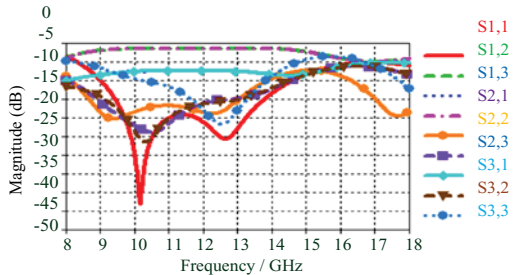
Fig. 5. Layout of the proposed unequal Wilkinson power divider.

Table I: The geometrical parameters of the proposed unequal power divider.

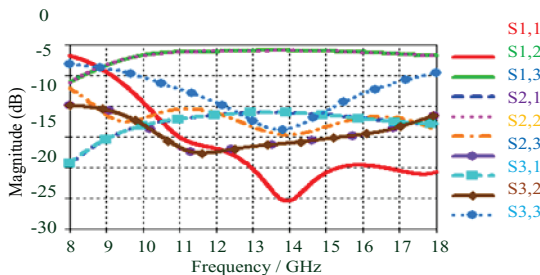
Parameter	value (mm)	Parameter	value (mm)
W1	5.2	l1	5.8
l2	3.8	g	0.5
w1	1.7	l1	2.4
w2	1.0	l2	1.0
w3	1.1	l3	2.1
w4	0	l4	0
W	1.1	W1	0.6
Di	0.5		

The measured results over the frequency range of 9.1 GHz to 12.8 GHz show that the insertion loss of port 2 is 2 ± 0.6 dB and the insertion loss of port 3 is 9.1 ± 0.6 dB. Thus, the power dividing ratio is about 5.1. From the simulation results the power split of 6 was expected. The little differences between the simulation and measured results can be due to the loss of substrate and test devices and the fabrication precision. The input return loss is better than 10 dB, the isolation is

better than 14.2 dB and the output return loss of ports 2 and 3 are better than 10 dB over the mentioned frequency range. Figure 8 displays the fabricated unequal HMSIW Wilkinson power divider.

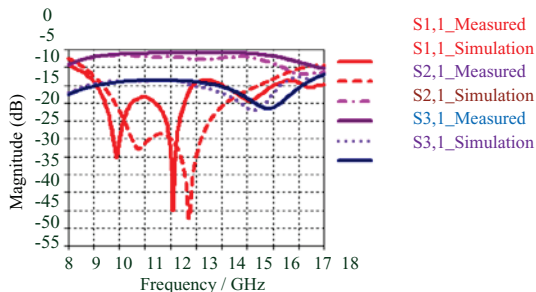


(a)

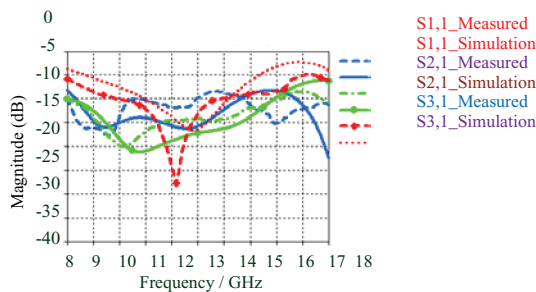


(b)

Fig. 6. Simulation results of the proposed structure (a) $di = 0.5$ mm and (b) $di = 2.4$ mm.



(a)



(b)

Fig. 7. Experimental and simulation results of the proposed structure for $di = 1$ mm (a) S11, S21, S31, and (b) S22, S33, S32.

Table II: The simulation results of CST for different values of di .

	$di = 0.5\text{mm}$	$di = 1\text{mm}$	$di = 2.4\text{mm}$
Power split	5	6	9
Bandwidth	31%	27%	24%
Input return loss	<15dB	<12.5dB	<17dB
Output return loss (port2)	<10.5dB	<10.1dB	<11.5dB
Output return loss (port3)	<10dB	<10dB	<10dB
Isolation	<13dB	<19dB	<15dB

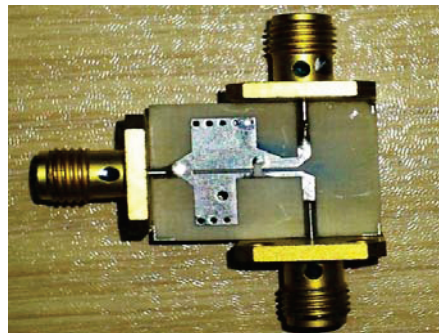


Fig. 8. The fabricated unequal HMSIW Wilkinson power divider for $di = 1$ mm.

The phase response of the output ports, which indicated in Fig. 9 shows that the proposed power divider is in phase.

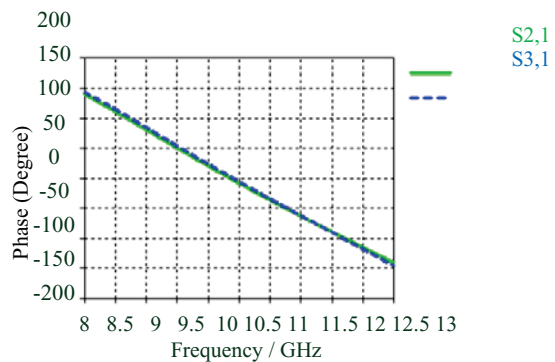


Fig. 9. Phase response of the proposed unequal power divider.

IV. CONCLUSION

A new compact unequal Wilkinson power divider is proposed in this paper. The main difference between this structure and previously published unequal Wilkinson power dividers is that this structure benefits from the advantages of half mode substrate integrated waveguides. In order to increase the characteristic impedance of the HMSIW line, an inductive post is added inside it. High power dividing ratios i.e., 6 and 9 are obtained by different diameters for the inductive post. This method can be used even for higher power dividing ratios. The output ports of the proposed structure are isolated from each other. All the input and output ports are matched. This power divider is designed in microwave Ku band. The output matching networks are designed inside the transition parts between HMSIW and microstrip lines. Thus, the size of the structure does not increase too much compared to that of HMSIW equal power divider.

REFERENCES

- [1] E. Wilkinson, "An N-way hybrid power divider," *IRE Trans. Microwave Theory Tech.*, vol. 8, pp. 116-118, Jan. 1960.
- [2] J. Koo, S. Oh, M. Hwan, C. Park, and etc, "A new DGS unequal power divider," *European Microwave Conference*, pp. 556 – 559, Oct 2007.
- [3] M. Moradian and H. Oraizi, "Application of grooved substrates for design of unequal Wilkinson power dividers," *Electronics Letters*, vol. 44, no. 1, pp. 32-33, Jan. 2008.
- [4] K. Wu, D. Deslandes, and Y. Cassivi, "The substrate integrated circuits - A new concept for high-frequency electronics and opto-electronics," *6th International Conference On Telecommunications In Modern Satellite, Cable And Broadcasting Service (TELSIKS)*, vol. 1, pp. 448-452, Oct. 2003.
- [5] F. Xu and K. Wu, "Guided-wave and leakage characteristics of substrate integrated waveguide," *IEEE Trans. Microwave Theory Tech.*, vol. 53, no. 1, pp. 66-73, Jan. 2005.
- [6] W. Hong, B. Liu, Y. Wang, Q. Lai, H. Tang, X. Yin, Y. Dong, Y. Zhang, and K. Wu, "Half mode substrate integrated waveguide: A new guided wave structure for microwave and millimeter wave application," *International Joint Conference on Infrared Millimeter Waves and Terahertz Electronics (IRMMW-THz)*, pp. 219, Sep. 2006.
- [7] Z. Zhang and K. Wu, "Broadband half-mode substrate integrated waveguide (HMSIW) Wilkinson power divider," *IEEE MTT-S International Microwave Symposium Digest*, pp. 879-882, June 2008.
- [8] N. Smith and R. Abhari, "Compact substrate integrated waveguide Wilkinson power dividers," *IEEE International Symposium on Antennas and Propagation*, Charleston, SC, pp. 1-4, June 2009.
- [9] D. Hawatmeh, K. Shamaileh, and N. Dib, "Design and analysis of multi-frequency unequal-split Wilkinson power divider using non-uniform transmission lines," *Applied Computational Electromagnetics Society (ACES) Journal*, vol. 27, pp. 248-255, 2012.
- [10] K. Shamaileh, A. Qaroot, N. Dib, and A. Sheta, "Design of miniaturized unequal split Wilkinson power divider with harmonics suppression using non-uniform transmission lines," *Applied Computational Electromagnetics Society (ACES) Journal*, vol. 26, pp. 530-538, 2011.
- [11] D. Deslandes and K. Wu, "Accurate modeling, wave mechanisms, and design considerations of a substrate integrated waveguide," *IEEE Trans. Microw. Theory Tech.*, vol. 54, no. 6, pp. 2516-2526, June 2006.
- [12] L. Qinghua, C. Fumeaux, W. Hong, and R. Vahldieck, "Characterization of the propagation properties of the half-mode substrate integrated waveguide," *IEEE Trans. Microwave Theory Tech.*, vol. 57, no. 8, pp. 1996-2004, Aug. 2009.
- [13] J. Rayas-Sanchez and V. Gutierrez-Ayala, "A general EM-based design procedure for single-layer substrate integrated waveguide interconnects with microstrip transitions," *IEEE MTT-S Int. Microwave Symp. Dig.*, Atlanta, GA, pp. 983-986, June 2008.
- [14] N. Marcuvitz, *Waveguide Handbook*, Piscataway, NY, IEEE Electromagnetic Waves Series, 1986.



Zahra Mazanir received her M.S degree in Electrical Engineering from Amirkabir University of Technology in Tehran, Iran. Since 2010, she has been in Microwave measurement research lab. She is interested in microwave and millimeter wave components, active circuits and wireless communication. In her M.S thesis, she used HMSIW and SIW components in microwave passive and active circuits. Now she is a PhD student of Electrical Engineering at Amirkabir University of Technology.



Gholamreza Moradi received his PhD degree in Electrical Engineering from Amirkabir University of Technology, Tehran, Iran in 2002. His main research interests are numerical Electromagnetics, antennas, active microwave and mm-wave circuits and systems. In 2003, he was selected as the exemplary researcher of Iranian Ministry of Road and Transportation. During 1997 till 2006, he was a faculty member at Civil Aviation Technology College, Tehran, Iran. He joined Amirkabir University of Technology, Tehran, Iran in 2006. Dr. Moradi has published several papers in the refereed journals and international conferences. Also, he coauthored five academic books. One of his books entitled *Active Transmission Lines* was selected as the book of the year of Iran in 2008. He is currently an associate Professor with the Electrical Engineering Department, Amirkabir University of Technology.

Simple and Compact Dual Band-Notched Monopole Antenna Using U-Shaped Forms on the Conductor-backed Plane for UWB Applications

M. Moosazadeh and Z. Esmati

Department of Electrical Engineering, Urmia Branch, Islamic Azad University, Urmia, Iran
m.moosazadeh14@gmail.com, Zahra.esmati@yahoo.com

Abstract— A planar ultra-wideband antenna with dual band-notched characteristics is proposed. The main features of the proposed antenna are the extremely compact dimensions and band-notched characteristics that are obtained without modifying the radiator. The dual band-notched characteristics are achieved by a pair of mirror U-shaped slots and an inverted U-shaped slot at the conductor-backed plane. The measured results of the manufactured (15 mm × 15 mm) antenna on 1.6 mm FR4 substrate show that the antenna operates with VSWR less than two over the frequency band from 3 GHz to 11.2 GHz. That wideband is featured by the existence of two notched bands VSWR is more than five aimed at suppressing any interference from IEEE802.11a WLAN 5 GHz (5.15 GHz - 5.825 GHz) and ITU 8 GHz (8.025 GHz - 8.4 GHz) band. The antenna has a desirable VSWR level, radiation pattern, and gain characteristics for ultra wideband frequency band range.

Index Terms – Coplanar waveguide (CPW) antennas, frequency band notched function, and ultra wideband (UWB) antenna.

I. INTRODUCTION

There is a tremendous applications that use the ultra wideband (UWB) technology due to its unlimited applications in short-range wireless communications. One of the key elements to secure a successful UWB system is an UWB antenna with compact dimensions, proper characteristics, and immunity to interferences from nearby systems that use parts of the UWB

spectrum. The main parameters in designing UWB antennas, especially for indoor applications, are easy to manufacture structure, compact size, and omnidirectional radiation pattern across the band from 3.1 GHz to 10.6 GHz [1-2]. Different methods such as the truncated slot on the antenna patch have been proposed for increasing impedance bandwidth. Since there are several existing systems operating within the UWB frequency spectrum, such as the IEEE802.11a WLAN (5.15 GHz - 5.825 GHz) and the ITU (8.025 GHz - 8.4 GHz) the UWB antenna is required to have the capability to notch those bands and thus to cancel any interference between those systems and the UWB system. Some UWB antennas with band-notched characteristics are available in the published literature. One common method is to use different types of slots on the patch and ground plane and parasitic elements [3-16]. Such antennas with various types of slots have large dimensions in comparison to that proposed antenna in this paper. In this paper, the target is to present a compact structure with dual band-notched characteristics that are achieved without modifying the patch in a step-by-step design procedure. The main radiator of the proposed antenna is a simple square patch that is fed using a microstrip line. The ground plane is located at the bottom layer with a pair of mirror semi C-shaped notches for a perfect matching. A conductor-backed plane that is used to achieve the band-notched characteristics of the antenna is located at the bottom layer. The first notched frequency band is achieved by using an inverted U-shaped slot embedded in the conductor-backed plane, whereas the second notched band is realized

by using a pair of mirror inverted U-shaped slots inside the conductor-backed plane. The final performance of the antenna is aimed at achieving the required UWB and to have dual notched bands that can be adjusted using an empirical formula. The impedance bandwidth is enhanced by using slotted conductor-backed plane. The presented design is validated by simulations and measurements.

II. ANTENNA DESIGN

Figure 1 shows the configuration of the proposed ultra-wideband (UWB) antenna. The top layer include the main radiator in the form of square patch with initial dimensions that are chosen to be $\lambda_g/2 \times \lambda_g/2$, (where λ_g is the guide wavelength, which is equal to $c/(\sqrt{\epsilon_r}f_c)$ at the center of the UWB, i.e., at 6.85 GHz, and c is speed of light in free space). The bottom layer includes a pair of mirror semi C-shaped notches in the corners of the ground plane and slotted conductor-backed plane. In the design, the antenna is constructed with a substrate made of FR4, with thickness of 1.6 mm and relative dielectric constant $\epsilon_r = 4.4$. The initial dimensions of the substrate are chosen to be $\lambda_g \times \lambda_g$. The width of the feed-line microstrip (W_f) is fixed at 2 mm for 50 Ω impedance. In the first step of the design, the dimensions of the substrate, square patch as radiator are optimized using the software HFSS for an UWB frequency coverage. The optimized dimensions are 15mm \times 15 mm for the substrate and 7.5 mm \times 7.5 mm for the radiator. The optimum gap between the square patch and the ground plane is 4.1 mm for proper impedance matching of the bandwidth. The optimization of the structure is obtained using the Ansoft simulator (HFSS).

In order to show the impact of using the truncated ground plane, the antenna's performance is simulated for different cases as indicated in Fig. 2 (a), (b), and (c). If the proposed antenna is used with the different structures of ground plane, rectangular-shaped and a pair of mirror L-shaped notches, in the manner shown in Fig. 2 (a) and (b) the impedance matching is poor at the frequency band between 8.5 GHz and 10.6 GHz, which should be part of the UWB spectrum. To improve the performance at that band, a pair of mirror semi C-shaped notches is included at the bottom layer with proper dimensions as depicted in Fig. 2 (c). It

is found that by using this form on the ground plane, impedance bandwidth is improved especially at the high frequencies. Figure 3 shows the simulated VSWR curves with different structures of ground plane.

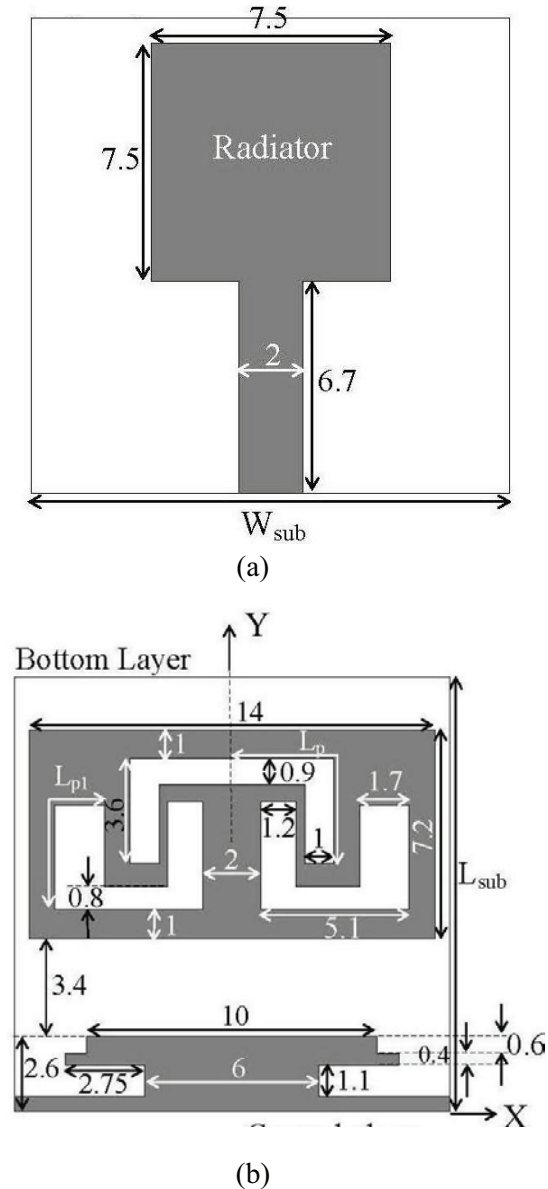


Fig. 1. Configuration of the proposed antenna, (a) top layer with square patch and (b) bottom layer with U-shaped forms in the conductor-backed plane (units in mm).

To modify the performance of the antenna by creating two notched sub-bands at the WLAN (5.15 GHz – 5.825 GHz), and ITU (8.025 GHz – 8.4 GHz), the rectangular-shaped conductor-

backed plane with the dimensions of $14 \text{ mm} \times 7.2 \text{ mm}$ is slotted in the manner shown in Fig. 1 (b). A pair of mirror U-shaped slots at the two sides of the conductor is created the first notched band centered at 5.65 GHz, whereas the inverted U-shaped slot inside the conductor is responsible for making the second notched band centered at 8.1 GHz. The slot's length L_p defines the first notched band, whereas the strip's length L_{p1} defines the second notched band. In this paper, the center-rejected frequency (f_p and f_{p1}) is approximately by,

$$L_p = \frac{c}{4f_p\sqrt{\epsilon_{eff}}} \quad (1)$$

$$L_{p1} = \frac{c}{4f_{p1}\sqrt{\epsilon_{eff}}} \quad (2)$$

$$\epsilon_{eff} = \frac{\epsilon_r + 1}{2} + \frac{\epsilon_r - 1}{2\sqrt{1 + \frac{12h}{W_f}}} \quad (4)$$

where c , h , W_f , ϵ_r , and ϵ_{eff} are the speed of light in free space, thickness of substrate, the width of the feed line, dielectric constant, and effective dielectric constant, respectively. Moreover, the relation between the center of the notched bands (f_p and f_{p1}) and those two design parameters is ϵ_{eff} , which can be calculated for the microstrip structures using the formula in [12]. For the notched bands that are centered at the frequencies 5.65 GHz and 8.1 GHz, the values of the designed parameters L_p and L_{p1} can be calculated using equations (1) and (2) as 7.1 mm and 5.3 mm. In order to verify the validity of the design equations (1) and (2), the performance of the antenna for different values of L_p and L_{p1} is calculated using the simulation tool and the results are shown in Figs. 4 and 5. It is shown that the effective parameter in the position of the lower rejected sub-band is the length L_p shown in Fig. 1 (b). The simulated results for different values of this parameter are shown in Fig. 4. Decreasing that design parameter results in an increase in the frequency of the lower rejected sub-band with negligible effect on the upper rejected sub-band. Concerning the upper rejected sub-band, the main parameter that defines that band is shown to be L_{p1} . The simulated performance of the antenna for different values of that parameter is shown in Fig. 5. The decrease in the value of L_{p1} causes the upper rejected sub-band to shift up in the frequency without almost any impact on the lower rejected sub-band. It is possible to show using the

design equation of microstrip structures [17] that for the utilized structure, the effective dielectric constant is given approximately as $\epsilon_{eff} = 3.2$. If this value is substituted in equations (1) and (2) along with the values of L_p and L_{p1} that are used to generate the simulation results of Figs. 3 and 4, the location of the center of the notched bands (f_p and f_{p1}) calculated from equations (1) and (2) are almost the same simulated values shown in Figs. 4 and 5. The whole structure of the antenna is optimized using HFSS for the widest possible bandwidth using the most compact structure. The optimal parameters of the constructed antenna are as follows: $W_{sub} = 15 \text{ mm}$, $L_{sub} = 15 \text{ mm}$, $L_p = 7.1 \text{ mm}$, and $L_{p1} = 5.3 \text{ mm}$.

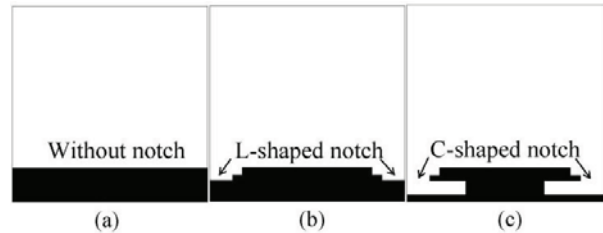


Fig. 2. (a) Rectangular-shaped ground plane without notch, (b) ground plane with a pair of mirror L-shaped notches, and (c) ground plane with a pair of mirror semi C-shaped notches.

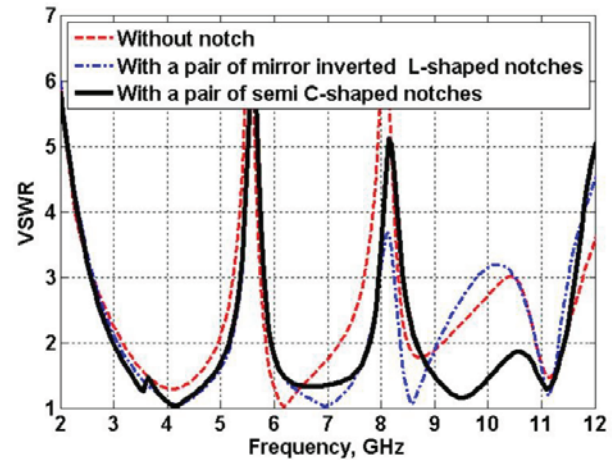


Fig. 3. Simulated VSWR for the different structures of ground slotted conductor-backed plane.

The other optimized dimensions of the antenna are indicated in Fig. 1. In order to show how the slotted conductor-backed plane becomes effective in the rejection of the dual-notched bands, the

current distribution at the structure of that plane is calculated using the simulation tool HFSS at the first and second notched frequency bands. It is clear from Fig. 6 (a) that the current flows in opposite directions at the two edges of the half-slot of the inverted U-shaped from at 5.6 GHz. Thus, the total effective radiation from the antenna becomes almost zero, and thus a notched band is achieved. In Fig. 6 (b), the current at 8 GHz at the right and left side of the two edges of the U-shaped slots are in opposite directions. Thus, the total radiation from the antenna at this band is very limited and a second notched band is achieved.

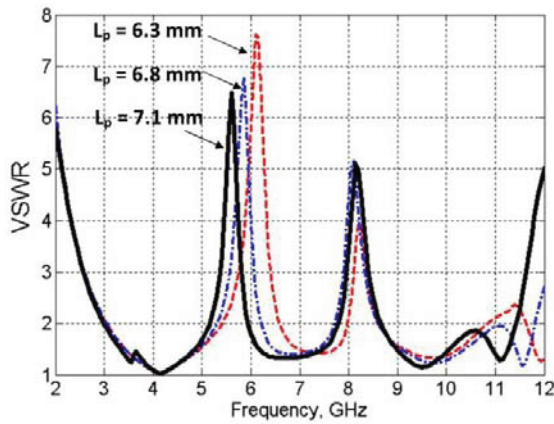


Fig. 4. Simulated VSWR of the antenna with different values for L_p .

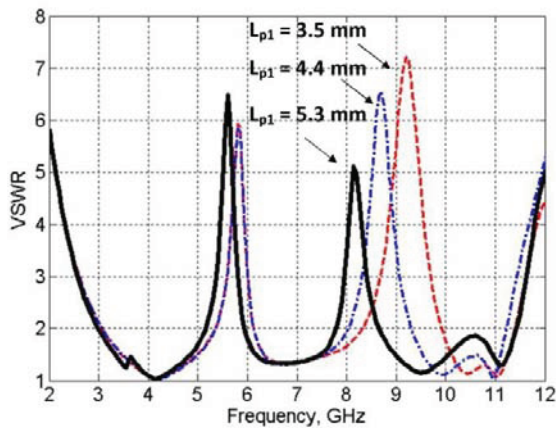


Fig. 5. Simulated VSWR of the antenna with different values for L_{p1} .

III. RESULT AND DISCUSSIONS

The designed antenna is fabricated and tested. The impedance bandwidth with dual band-notched characteristics that has the dimensions $W_{sub} = 15$ mm and $L_{sub} = 15$ mm is tested by using an

Agilent 8722ES vector network analyzer (VNA). The simulated and measured VSWR of the antenna depicted in Fig. 7 reveal that the antenna covers the ultra-wideband frequency range from 3 GHz to more than 11.2 GHz in the measurement assuming $VSWR < 2$ as a reference. Figure 7 clearly show that the constructed antenna exhibits two notched bands centered at 5.65 GHz and 8.1 GHz. There is generally a good agreement between the simulated data and measured result except a slight down shift in the center of the lower and upper rejected bands; these could be due to the effect of the SMA port in the laboratory. On the other hand, it can be observed that by using this filter structures, the lowest frequency is significantly decreased from 3.3 GHz to 3 GHz. Figure 8 shows the effect slotted conductor-backed plane on the maximum antenna gain from 3 GHz to 11 GHz in comparison to same antenna without conductor.

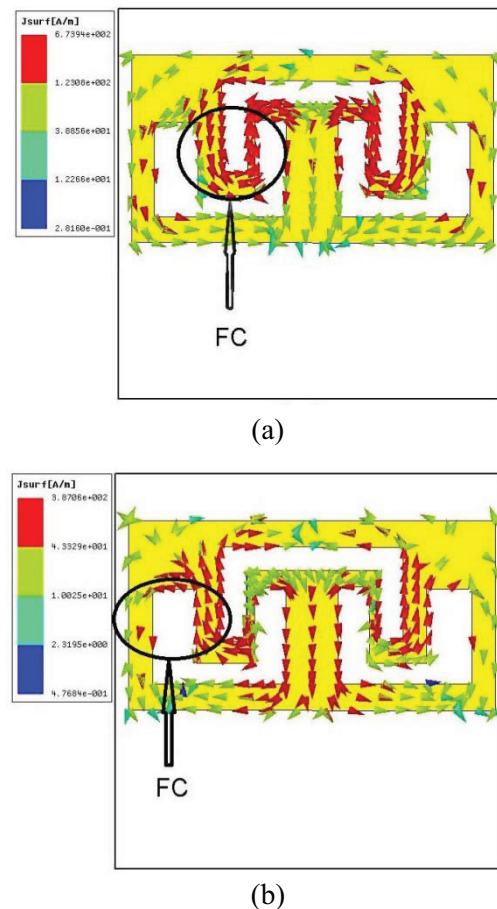


Fig. 6. Simulated current distribution of the band-notched monopole antenna at (a) 5.6 GHz and (b) 8 GHz (FC: field cancellation).

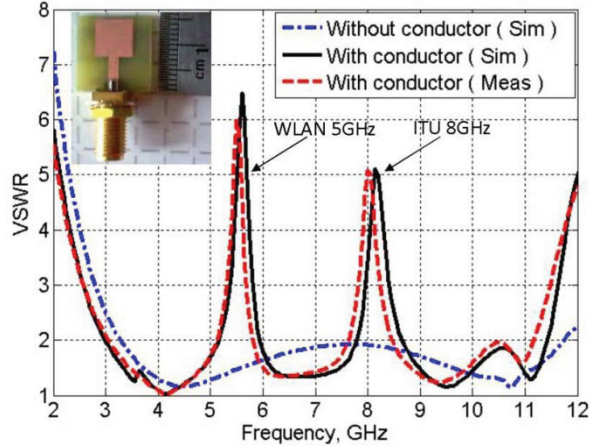


Fig. 7. Measured and simulated VSWR of the proposed dual band-notched monopole antenna with and without conductor (inset).

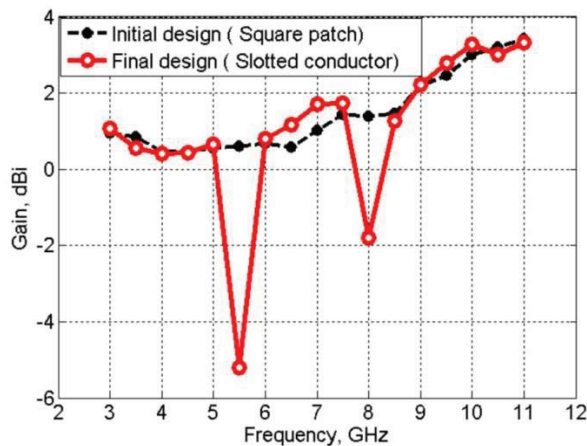


Fig. 8. Comparison between the gain of the square patch (without conductor) and the slotted conductor-backed plane.

The values in Fig. 8 indicate that the realized dual band-notched antenna has good gain flatness except in the two notched bands, where the gain decreases drastically at 5.5 GHz and 8 GHz. The radiation pattern of the antenna is also tested to confirm the omni-directional behavior of the antenna as mainly required by the short range indoor UWB communication systems. Figure 9 show the measured radiation patterns including co-polarization and cross-polarization at the frequencies 4 GHz, 7 GHz, and 9 GHz, in the H-plane (xz-plane) and E-plane (yz-plane). From overall view of these radiation patterns, it can be clearly seen that xz-plane patterns are almost omni-directional, but they are more directional in the higher band.

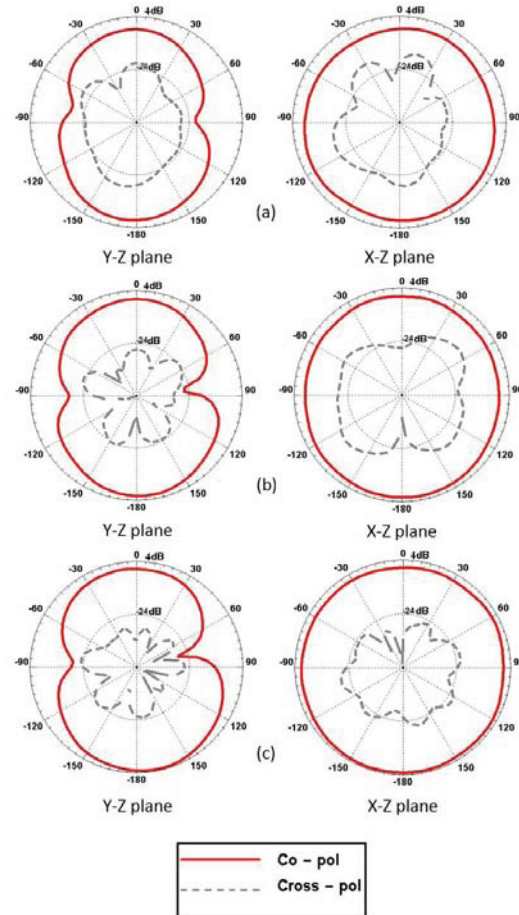


Fig. 9. Measured radiation pattern of the antenna at (a) 4 GHz, (b) 7 GHz, and (c) 9 GHz. Solid line, co-polarization and dashed line, cross-polarization.

IV. CONCLUSION

A compact microstrip-fed printed monopole antenna with ultra-wideband presented. By inserting a pair of mirror semi C-shaped notches in the corners of the ground plane, additional resonance is achieved and the impedance bandwidth of the proposed antenna is increased. A slotted conductor-backed plane is placed at the bottom layer to create two notched bands in the radiation of the antenna. The dual band-notched characteristics are achieved by using a pair of U-shaped slots and an inverted U-shaped slot embedded inside a rectangular-shaped conductor-backed plane. The first notched band aimed at preventing any interference with existing 5 GHz WLAN systems is achieved by using an inverted U-shaped slot in the conductor-backed plane, which exempt from interfaces. The second notched band aimed at preventing the interference

with the 8 GHz ITU systems is achieved by using a pair of mirror U-shaped slots inside the slotted conductor-backed plane. The measured results show the proposed antenna operates over the frequency band between 3 GHz and 11.2 GHz, defined by $VSWR < 2$. The two bands WLAN (5.15 GHz – 5.825 GHz) and ITU (8.025 GHz – 8.4 GHz) are already notched, which centered at 5.65 GHz and 8.1 GHz, respectively.

REFERENCES

- [1] M. Moosazadeh, C. Ghobadi, and M. Dousti, "Small monopole antenna with checkered-shaped patch for UWB application," *IEEE Anten. Wireless Propag. Lett.*, vol. 9, pp. 1014-1017, 2010.
- [2] Q. Wu, R. Jin, J. Geng, and M. Ding, "Printed omni-directional UWB monopole antenna with very compact size," *IEEE Trans. Antennas Propagat.*, vol. 56, pp. 895-899, 2008.
- [3] M. Abdollahi, H. DaliliOskouei, M. akbari, and M. Mighani, "A novel compact UWB antenna with triple band-notches for WiMAX/WLAN/ITU bands," *Appl. Comp. Electro. Society (ACES) Journal*, vol. 27, no. 12, pp. 1014-1021, 2012.
- [4] D.-O. Kim and C.-Y. kim, "CPW-fed ultra-wideband antenna with triple-band notch functions," *Electro. Lett.*, vol. 44, pp. 1246-1248, 2010.
- [5] M. Moosazadeh and Z. Esmati, "A small cpw-fed ultra wideband antenna with dual band-notched characteristics," *Microwave Opt. Tech. Lett.*, vol. 54, pp. 1528-1532, 2012.
- [6] J. Wliam and R. Nakkeeran, "A new UWB slot antenna with rejection of WiMAX and WLAN bands," *Appl. Comp. Electro. Society (ACES) Journal*, vol. 25, no. 9, pp. 787-793, 2010.
- [7] M. Moosazadeh, A. Abbosh, and Z. Esmati, "Design of compact planar ultra wideband antenna with dual-notched conductor-backed plane," *IET Microwave Antennas Propagat.*, vol. 6, pp. 290-294, 2012.
- [8] L.-Y. Cai, G. Zeng, H.-C. Yang, and X.-W. Zhan, "Compact printed ultra-wideband antennas with band-notched characteristics," *Electron. Lett.*, vol. 46, pp. 817-819, 2010.
- [9] X.- L. Ma, W. Shao, and G.-Q. He, "A novel dual narrow band-notched cpw-fed UWB slot antenna with parasitic strip," *Appl. Comp. Electro. Society (ACES) Journal*, vol. 27, no. 7, pp. 581-586, 2012.
- [10] A. Moradhesari, M. Moosazadeh, and Z. Esmati, "Design of compact planar antenna with dual notched bands using slotted rectangular patch for ultra wideband applications," *Microwave Opt. Tech. Lett.*, vol. 54, pp. 2053-2056, 2012.
- [11] A. Abbosh and M. Bialkowski, "Design of UWB planar band notched antenna using parasitic elements," *IEEE Trans. Antennas Propagat.*, vol. 57, pp. 796-799, 2009.
- [12] Z.-L. Zhou, L. Li, and J.-S. Hong, "A novel compact monopole antenna with triple high quality rejected bands for UWB applications," *Appl. Comp. Electro. Society (ACES) Journal*, vol. 27, no. 8, pp. 654-659, 2012.
- [13] R. Eshtiaghi, J. Nourinia, and C. Ghobadi, "Electromagnetically coupled band-notched elliptical monopole antenna for UWB applications," *IEEE Trans. Antennas Propagat.*, vol. 58, pp. 1397-1402, 2010.
- [14] L. Li, Z.-L. Zhou, and J.-S. Hong, "Compact UWB antenna with four band-notches for UWB applications," *Electron. Lett.*, vol. 47, pp. 1211-1212, 2011.
- [15] M. Mighani, M. Akbari, and N. Felegari, "A CPW dual band notched UWB antenna," *Appl. Comp. Electro. Society (ACES) Journal*, vol. 27, no. 4, pp. 352-359, 2012.
- [16] J.-W. Jang and H.-Y. Hwang, "An improved band-rejection UWB antenna with resonant patches and a slot," *IEEE Antennas Wirel. Propag. Lett.*, vol. 8, pp. 299-302, 2009.
- [17] K. Gupta, R. Garg, I. Bahl, and P. Bhartia, *Microstrip Lines and Slot Lines*, Artech House, 2nd edn., 1996.



Mahdi Moosazadeh was born in 1980 in Oroumie, Iran. He received his B.Sc degree in Electrical Engineering from Azad University, Urmia Branch and M.Sc. degree in Electrical Engineering from science and Research Branch, Tehran Branch. From 2010 until 2012, he is a Teaching assistant with the Department of Electrical Engineering, Islamic Azad University, Urmia Branch, Iran. His research interests include analysis and design of microstrip antennas monopole antenna, microwave structures, and electromagnetic theory. From 2013, he is working toward the Ph.D degree at University of Western Sydney.



Zahra Esmati was born in 1987 in Oroumie, Iran. She received her B.Sc degree in Electrical Engineering from Azad University, Urmia Branch. Her research interests include analysis and design of microstrip antennas monopole antenna, ultra-wideband (UWB) and small antennas for wireless communications, and microwave/millimeter systems.

Hybrid Electric Vehicle Characterization Using Generalized Notion of Power

N. Al-Aawar^{1,2} and A. A. Arkadan^{1,2}

¹Rafik Hariri University, Mechref, Damour, 2010, Lebanon

²Marquette University, Milwaukee, WI, 53203, USA
a.a.arkadan@marquette.edu

Abstract—This paper presents a novel mathematical model based on the generalized notion of power (GNP) to accurately predict the performance characteristics of hybrid electric vehicles (HEVs). The uniqueness of this technique is the ability to represent both internal combustion engine and electrical propulsion machines in one system of state space equations. Thus, it allows proper characterization and control of the interaction of both systems by taking into account large and small load disturbances and the irreversibility of entropy generation by the internal combustion engine. The superiority of the proposed model is demonstrated by applying it to a prototype HEV configuration and by comparison to readily available benchmark data.

Index Terms - Electric machines, hybrid electric vehicles, internal combustion engines, magneto-statics, and mathematical models.

Nomenclature

HEV	Hybrid Electric Vehicle
EMG	Electric Motor Generator
ICE	Internal Combustion Engine
I	EMG Windings Current
R	EMG Windings Resistance
L	EMG windings Inductance
ω	Electric angular speed
θ	Rotor position
U_V	EMG Windings Voltage
J	Moment of inertia of the EMG rotor
T_{dev}	Developed torque of the EMG
T_{load}	Load torque
q_E	Flow variable at electric port

e_E	Effort variable at electric port
q_M	Flow variable at mechanical port
e_M	Effort variable at mechanical port
U_i	Internal energy
S_i	Entropy
V_i	Volume
T_i	Temperature
P_i	Pressure
i	Index the thermodynamic state
m	Mass of the air
C_v	Specific heat at constant volume of the air
R_g	Ideal gas constant.

I. INTRODUCTION

The demand for more environmentally friendly and fuel efficient vehicles has increased in response to growing concerns for clean environment and energy savings. In this context, the hybrid electric vehicle (HEV) has emerged as a viable solution to meet these requirements. There are different powertrain configurations in HEVs. However, all involve integrating several power sources, mainly internal combustion engine, ICE, and electrical motor generator (EMG) unit in the vehicle to improve its performance. The performance of HEVs depends on the design of the powertrain system and the integration of the power sources. Accordingly, accurate performance characterization, including the interaction of mechanical and electrical components, is essential to optimize the design of the powertrain and thus the performance of the HEV. However, this proves to be very challenging because of the dynamic nature of the interactions among various components of HEV [1, 2]. In [1] an integrated

team artificial intelligence electromagnetic, T-AI-EM environment was developed to accurately determine the performance characteristics of synchronous reluctance machines (SynRM) with axially laminated anisotropic rotor configurations for powertrain usage. In another work, the PLC network was used to improve the communication inside the hybrid electric vehicle [3]. Much of the earlier works involved the use of finite state machine (FSM) to model the interaction between the ICE and EMG. It simulates an offline control strategy that manages the developed power to balance the load power for a given state of operation of the HEV [2, 4, 5]. The drawback of such approaches is its inability to capture the effect of small load disturbances. Thus, the HEV will not operate at near optimum conditions. This paper presents a novel technique that models both EMG and ICE into one system of state space equations. Accordingly, it enables the use of real time control strategies that could adaptively change the degree of hybridization of the vehicle in response to large and small load disturbances to achieve near optimum performance conditions. In the following, we present the conventional and the proposed GNP models. The models are next applied to a prototype HEV configuration and the results are compared to available benchmark data for validation.

II. THE CONVENTIONAL MODEL

The conventional model of HEV starts by adopting certain configuration of connecting the ICE and the EMG, such as the series, parallel or split power configuration, Fig. 1. Next, each of the ICE and EMG is modeled as a standalone component and are integrated by using a power balance equation to simulate the propulsion of the vehicle in accordance with the status of the operation of the vehicle [6]. One way is to model the EMG by nonlinear state space equations as follows,

$$\dot{I} = L^{-1} \left(R + \omega \frac{\partial L}{\partial \theta} \right) I + L^{-1} U_v \quad (1)$$

$$\dot{\omega} = \frac{T_{dev} - T_{load}}{J} \quad (2)$$

$$T_{dev} = I^T \omega \frac{\partial L}{\partial \theta} I \quad (3)$$

where, I is the current, R is the resistance, L is the inductance, ω is the electric angular speed, θ is the rotor position, U_v is the voltage, J is the moment of inertia of the rotor, T_{dev} is the EMG developed torque, and T_{load} is the load torque. The complex structure and the nonlinear nature of the magnetic material of the EMG system cause the inductances of the electric machine to be function of the rotor position and load current. Thus, the family of curves technique [7] is adopted and nonlinear magnetic field solutions are used to represent each inductance by a set of curves function of rotor position and current load condition, Fig. 2. The state space model is used to compute the winding currents and the developed torque for the given input voltages and load torque [7, 8]. A computational electromagnetic (EM) module is used to model the EMG. This module accounts for the non-linearity of the EMG magnetic material, space harmonics due to its geometry, as well as the time harmonics resulting from switching electronics in the load. This module utilizes an indirectly coupled FE-SS approach to compute sets of winding inductances as function of load and rotor position. The method is outlined in Fig. 2 where for each rotor position the EM solutions corresponding to a range of the excitation currents are computed. These solutions are used to compute the device windings inductances. Next, the rotor is moved an increment, $\Delta\theta$, to a new position and the task is repeated to cover a complete AC cycle. In this work, $\Delta\theta$ was chosen at a value that moves the rotor to positions alternatively between “middle of slot” and “middle of tooth” of the stator to account for the slotting effects. Once a full electrical cycle of the rotor motion is completed, a set of family of curves is obtained [7]. A sample family of curves, for the stator winding mutual inductance L_{ab} is shown in Fig. 3, which is function of load and rotor position. These sets of curves are integrated with the state space model in order to accurately predict the performance characteristics of the EMG.

As for the ICE model, the engine efficiency map of Fig. 4 is used. Here, the ICE is assumed to operate at the optimum operating line (OOL), which is a sequence of intersections of the constant engine power lines with the peak efficiency contours [9]. The EMG and ICE combine to develop the torque required to propel

the vehicle. The finite state machine of Fig. 5 is used to define the state of operation of the HEV powertrain. The HEV state of operation like starting, cruising, breaking, Fig. 5, decides the degree of hybridization of the vehicle. The degree of hybridization is defined as the power developed by the EMG over the required load power. The state of operation of the HEV can be based on a load-following strategy or an on/off strategy. In the case of a load-following strategy, the power from the power propulsion unit (PPU) is closely related to the power demand from the chassis. If the strategy is the on/off type, the power from power propulsion unit is related to the state of charge (SOC) of the batteries. At some specific SOC, the PPU is turned on or off. In practice, a combination of the strategies might be the most appropriate choice [9]. The main principle is that when a specific state is active an output related to that state would be generated. An example of the generated output for “starting state is: Motor_enable=1, Generator_enable=1 and Ice_enable=0; in this mode the HEV works as an electric vehicle. A state of operation of the vehicle is activated based on the “throttle” and “breaking” positions. A state will remain active till a change occurs, such as change of vehicle speed and or pedal position; then another state will become active, Fig. 5. As can be appreciated, this type of operation cannot be used to adaptively change the degree of hybridization when small disturbances occur in the load. Therefore, the HEV performance will be far from being optimum.

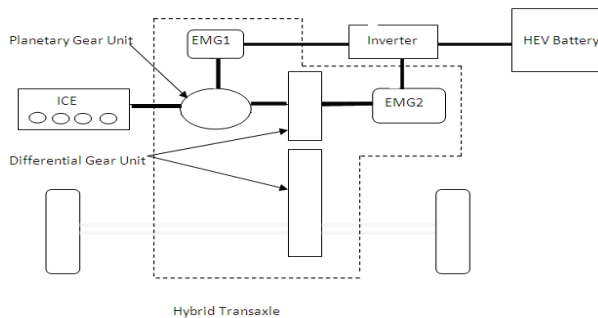


Fig. 1. Toyota prius split power configuration.

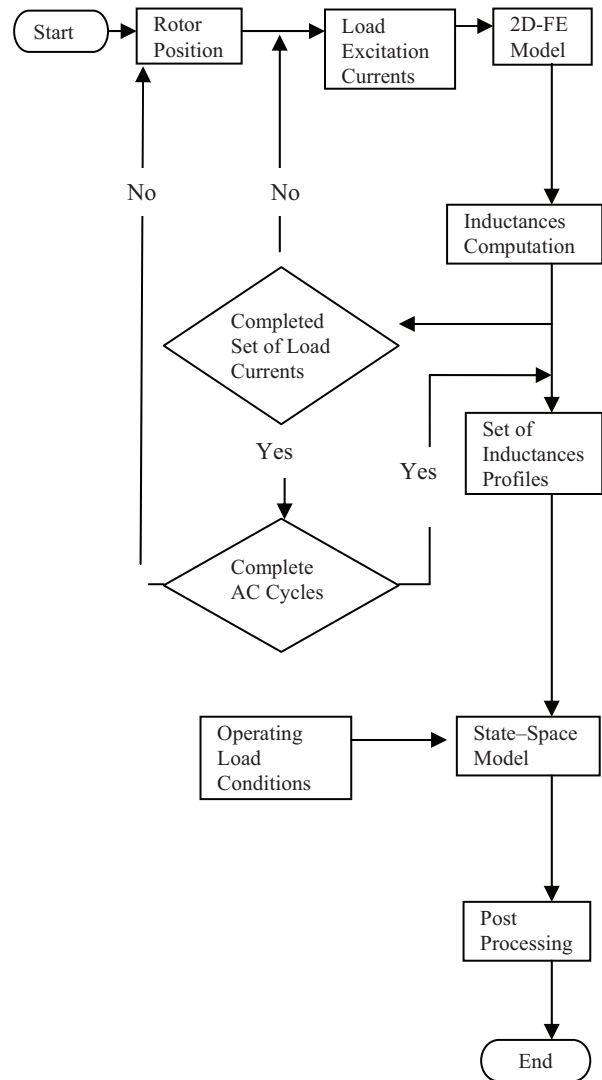


Fig. 2. Inductance family of curves computation.

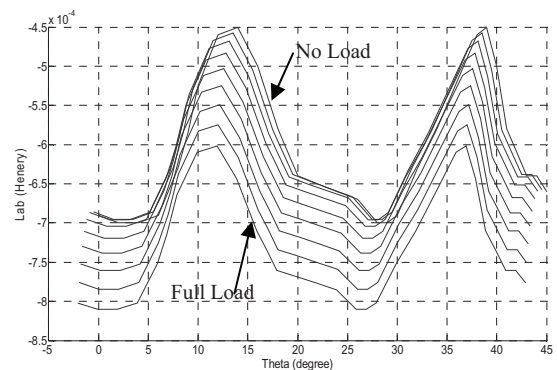


Fig. 3. Family of curves of mutual inductance L_{ab} .

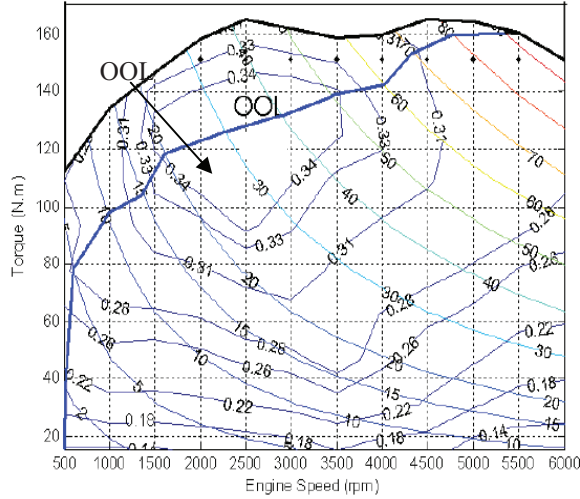


Fig. 4. Engine efficiency map.

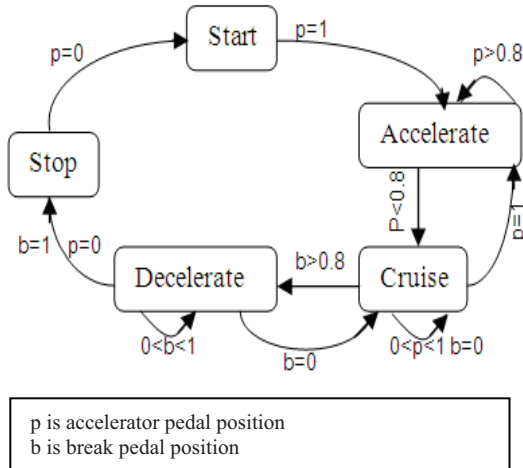


Fig. 5. Finite state machine of HEV.

III. GENERALIZED NOTION OF POWER MODEL

The aim of this work is to develop an accurate model that precisely predicts the performance of the HEV for all types of driving cycles including small road disturbances. The main principle is to develop a torque equal to a load torque to propel the car while maintaining optimum performance of the ICE and SOC higher than 20 % to protect the batteries [8]. The generalized notion of power [10] is used in this work to unify the notation for both EMG and ICE systems so it can be modeled in one system of state space equations. The GNP is implemented as the vector multiplication of effort variable e and the generalized displacement

vector q to arrive to the power and thus the torque. The adoption of the GNP model facilitates the use of real time controller such as the proportional-integral-derivative (PID) controller to manage the interactions between the EMG and the ICE at near optimum performance conditions. The details of developing the GNP model for the HEV are given below.

A. The EMG model

An electric motor generator (EMG), according to its structure, can be represented as a dual-port system. The first port is the electrical winding and the second is the mechanical shaft. The machine dynamics are described by two power variables at each port. Using the generalized notion of power representation, the current in the EMG system is treated as a displacement variable, q , and the voltage as an effort variable, e . Moreover, the rotor angular velocity and the developed torque are the displacement and effort, respectively, at the mechanical port, Fig. 6. Using the GNP representation in equations (1) to (3) above will result in equations (4) to (6),

$$\dot{q}_E = L^{-1} \left(R + q_M \frac{\partial L}{\partial q_M} \right) q_E + L^{-1} e_E \quad (4)$$

$$\dot{q}_M = \frac{e_M - e_{load}}{J}, \quad (5)$$

$$e_M = q_E^T q_M \left(\frac{\partial L}{\partial \theta} \right) q_E. \quad (6)$$

where L is the inductance matrix and e_M is the effort of the mechanical port. The inductance matrix, L , of equation (4) can be calculated from nonlinear magnetic field solutions or test data and represented by the family of curves approach outlined above in Fig. 2. Accordingly, it accounts for the nonlinearity of the magnetic material and the complex structure of the EMG.

B. The ICE Model

The ICE is a thermodynamic device that generates mechanical work and heat based on the first and second laws of thermodynamics as shown in the P-V and T-S diagrams of Fig. 7. The Otto cycle consists of adiabatic compression, heat addition at constant volume, adiabatic expansion, and rejection of heat at constant volume. In the case of a four-stroke Otto cycle, technically there

are two additional processes: one for the exhaust of waste heat and combustion products (by isobaric compression) and one for the intake of cool oxygen-rich air (by isobaric expansion); however, these are often omitted in a simplified analysis. The Otto cycle is summarized by the following process [9]:

- Process 0-1 represents an isentropic compression of the working gas as the piston moves up the cylinder.
- Process 1-2 is a constant-volume ignition of the air fuel mixture.
- Process 2-3 is an isentropic expansion while the piston is pushed down the cylinder. This phase is known as the power stroke.
- Process 3-0 is the rejection of the exhaust gas out of the cylinder at constant volume.

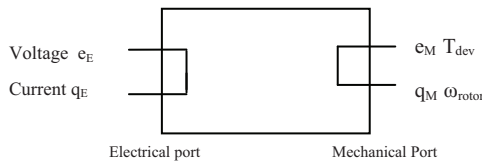


Fig. 6. Schematic of EMG using GNP notation.

Hence, the internal energy $U(S,V)$ is a scalar potential function defined in the space of displacements spanned by S (entropy) and V , volume. The efforts in the two domains (thermal and mechanical) may be defined as $e = [T,P]^T$, where T is the temperature and P is the pressure. For simplicity, the equations are linearized about a nominal operating point defined by S_0 and V_0 where,

$$\begin{aligned} \delta S &= S - S_0 \\ \delta V &= V - V_0, \\ \delta T &= T - T_0(S_0, V_0), \\ \delta P &= P - P_0(S_0, V_0). \end{aligned} \tag{7}$$

Taylor series expansion is utilized as follows:
 $\delta T = \partial T/\partial S|_{S_0V_0} \delta S + \partial T/\partial V|_{S_0V_0} \delta V +$ higher order terms;
 $\delta P = \partial P/\partial S|_{S_0V_0} \delta S + \partial P/\partial V|_{S_0V_0} \delta V +$ higher order terms. Neglecting the higher-order terms and dropping the δ prefix for convenience; a linearized model of the ICE is obtained as shown in the equation below,

$$\begin{aligned} T &\approx AS - BV \\ P &\approx BS - CV, \end{aligned} \tag{8}$$

where A , B , and C are positive constants defined by,

$$\begin{aligned} A &= \partial T/\partial S = T_0/mC_v \\ B &= \partial P/\partial S = -\partial T/\partial V = P_0/mC_v, \\ C &= -\partial P/\partial V = \left(\frac{P_0}{V_0}\right)\left(\frac{R_g}{C_v} + 1\right). \end{aligned} \tag{9}$$

The symbol m is the mass of the air, C_v is the specific heat at constant volume of the air, and R_g is ideal gas constant. The Internal energy corresponding to this linearized approximation is a quadratic form in S and V and is given by:

$$U = 1/2 A S^2 - B SV + 1/2 C V^2. \tag{10}$$

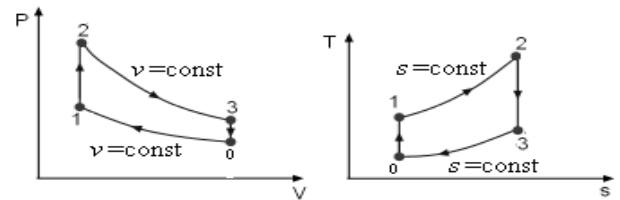


Fig. 7. P-V and T-S diagram of internal combustion engine.

The Otto cycle summarized in Fig. 7 is described as follows, STATE 0: everything at thermal equilibrium (S_0, V_0),

$$\begin{aligned} T_0 &= AS_0 - BV_0 \\ P_0 &= BS_0 - CV_0, \\ U_0 &= 1/2AS_0^2 - BS_0V_0 + 1/2CV_0^2. \end{aligned} \tag{11}$$

The transition between state 0 to state 1 is represented by an adiabatic compression of the working gas as seen in Fig. 7. This compression occurs at constant entropy and at a volume change, $-\Delta V$. STATE 1: is represented by the variables (S_0) and ($V_0 - \Delta V$) thus temperature and pressure increases as follows,

$$\begin{aligned} T1 &= AS_0 - B(V_0 - \Delta V) = T_0 + B\Delta V \\ P1 &= BS_0 - C(V_0 - \Delta V) = P_0 + C\Delta V. \end{aligned} \tag{12}$$

The energy generated is given by the following equation,

$$U1 = 1/2AS_0^2 - BS_0(V_0 - \Delta V) + 1/2 C(V_0 - \Delta V)^2 \tag{13}$$

The internal energy increases by an amount equal to the work done on the gas and is given by,

$$U1 - U_0 = P_0\Delta V + 1/2C\Delta V^2. \tag{14}$$

Each of these transition processes of Fig. 6 can be developed in a similar way as from state 0 to state 1 and they can be represented in state space format as follows,

$$\begin{bmatrix} \delta T \\ \delta P \end{bmatrix} = \begin{bmatrix} \frac{\partial T}{\partial S} & \frac{\partial T}{\partial(-V)} \\ \frac{\partial P}{\partial S} & \frac{\partial P}{\partial(-V)} \end{bmatrix} \begin{bmatrix} \delta S \\ \delta(-V) \end{bmatrix}. \quad (15)$$

The torque developed by the ICE as result of the above analysis computed for all the Otto cycle is given as follows,

$$e_{\text{eng}} = A \Delta S^2 / \omega_{\text{eng}} \quad (16)$$

where ω_{eng} is the angular rotation of the crank shaft of the ICE.

C. Integration of EMG and ICE

The key objective of this work is to develop a GNP based model of the HEV powertrain. This model can be used with a real time control strategy to adaptively change the degree of hybridization of the vehicle in response to large and small load disturbances and to achieve near optimum performance. This is demonstrated by simulating a PID real time control strategy that manages the interaction between the ICE and the EMG of the HEV powertrain system. The strategy is summarized in Fig. 8. In this strategy, the load torque is computed from the driving cycle. Also, an initial voltage and initial pedal position are selected. The pedal position is used to iteratively determine the entropy and the displaced volume of the ICE and therefore the torque. The selected EMG voltage is used to initiate an iterative process between the state space model and family of curves to accurately calculate the winding currents and the EMG developed torque. Next the total developed torque ($T_{\text{dev}} + T_{\text{eng}} = e_M + e_{\text{eng}}$) and the degree of hybridization ($T_{\text{dev}} / (T_{\text{dev}} + T_{\text{eng}})$) are computed. This developed torque is used in the kinematic and kinetic equations of the HEV to determine the load torque and actual driving cycle. This driving cycle is checked with the reference driving cycle. The controller will continue on changing the initial dc bus voltage and the pedal position till both driving cycles match (within 5 % error).

IV. APPLICATION AND RESULTS

The split power configuration of Fig. 1 for a prototype Toyota Prius was modeled using both conventional and proposed GNP models presented in this paper. As shown in Fig. 1, this configuration consists of two EMGs of the internal permanent magnet (IPM) type.

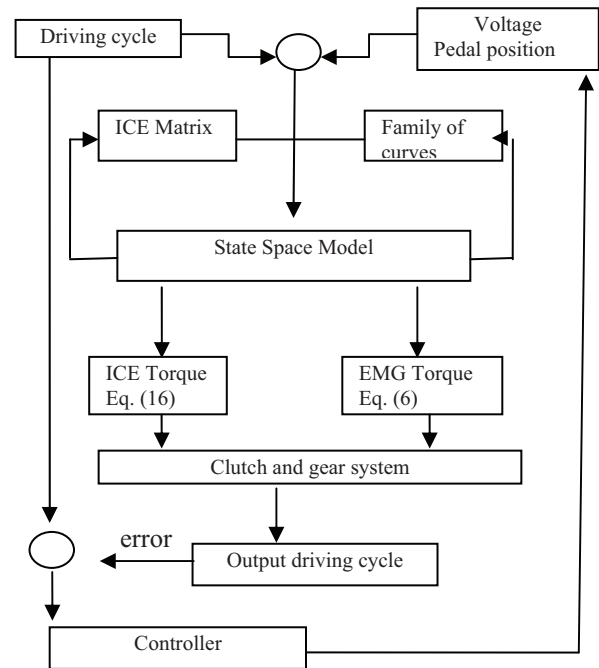


Fig. 8. Real time control strategy of HEV.

These two EMGs are rated at 28 kW and 50 kW, respectively. The bank of batteries consists of 168 cells of NINH type that is rated at 21 kW [6]. The ICE is a 4-cylinder aluminum double overhead cam (DOHC) 16-valve VVT with displacement of 1.5 L [2]. The vehicle is tested for urban driving cycle, UDC. The results presented in this paper are generated using the conventional model and the novel GNP model proposed in this work for the same operating conditions of references [2, 6]. The results are shown in Fig. 9 to Fig. 12 and are compared to available benchmark data [2, 6]. Figures 9 and 10 show the predicted load torque and SOC as computed by both models and compared to benchmark data. As can be appreciated from these results, the GNP model presented in this work better captures the effects of small load disturbances as compared to the conventional model. Also the GNP model results agree more with the benchmark data. In addition, Figs. 11 and 12 present a comparison between fuel consumption of the ICE as predicted by the GNP and conventional models, respectively. An inspection of these results reveals that the GNP model prediction of fuel consumption is closer to the benchmark data than that of the conventional model. It also reveals the superiority of the GNP model as it allows the use of real time PID

controller that adaptively changes the degree of hybridization by idling the ICE at very low engine rpm and activating the EMG. This translated into less fuel consumption, which is shown to be at 3.6 % for the urban drive cycle (UDC) simulated in this work as shown in Table I. In addition, Table I shows the values of two main performance indicators (fuel consumption and batteries SOC) as predicted by the GNP and conventional models and compared to readily available benchmark data. As can be appreciated from these results, the GNP model better captures the performance characteristics of the HEV powertrain system.

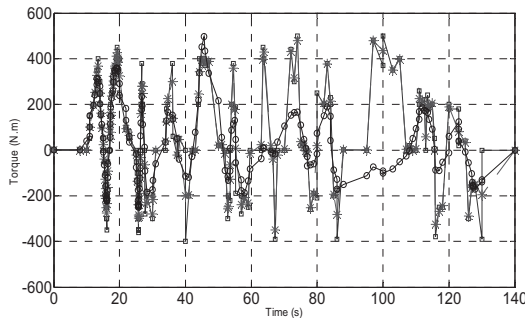


Fig. 9. Load torque versus time as computed by conventional (-o-), GNP(-*-), and benchmark(-).

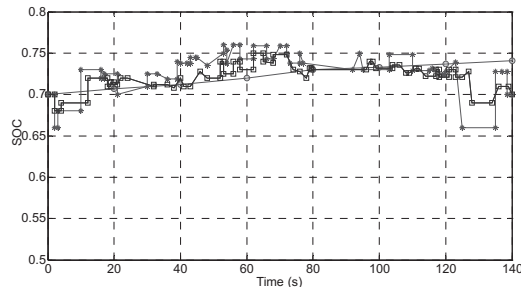


Fig. 10. SOC versus time and computed using conventional (-o-), GNP (-*-), and Benchmark (-).

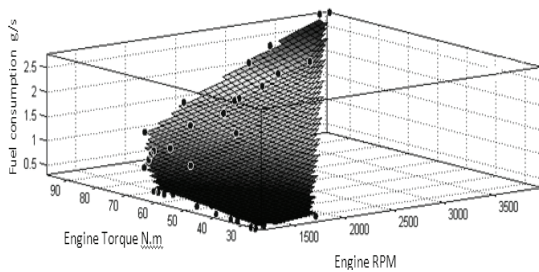


Fig. 11. Fuel consumption of ICE as predicted by the GNP model and compared to benchmark data (.).

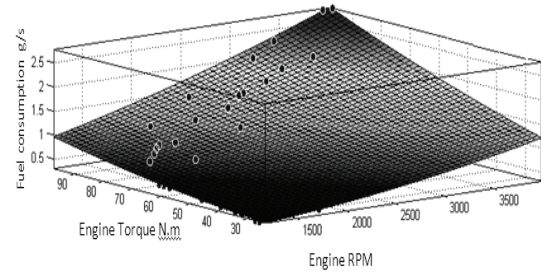


Fig. 12. Fuel consumption of ICE as predicted by the conventional model and compared to benchmark data (.).

Table I: Comparison of performance indicators as obtained from GNP and conventional models and benchmark data.

Description	Benchmark	GNP Model	Conventional Model
Fuel consumption	45 mpg	46.6 mpg	42.9 mpg
SOC at End of Cycle	0.74	0.7	0.7

V. CONCLUSIONS

A novel mathematical model, based on the generalized notion of power to accurately predict the performance characteristics of hybrid electric vehicles, was presented. As was shown, the uniqueness of this technique is the ability to represent both internal combustion engine and electrical propulsion machines in one system of state space equations. Thus allowing proper characterization and control of the interaction of both systems by taking into account small load disturbances and irreversibility of the entropy generation by the internal combustion engine. The validity of this approach was shown by applying both GNP and conventional models to a split power configuration of an HEV powertrain system and by comparing the results to available benchmark data. The superiority of the GNP model was demonstrated as it allows the use of real time PID controller that adaptively changes the degree of hybridization of the powertrain system and as it can better capture the effects of small load disturbances.

REFERENCES

[1] N. Al-Aawar, A. Hanbali and A. Arkadan, "Characterization and design optimization of ALA rotor synchronous reluctance motor drives for

traction applications,” *22nd Annual Review of Progress in Applied Computational Electromagnetics (ACES)*, pp. 249-256, Florida, USA, March 2006.

- [2] USA DOE Plug-in Hybrid Electric Vehicle R&D Plan, 2007.
- [3] S. Barmada, M. Raugi, and M. Tucci, “Analysis of power line communications channels on board a fully electric vehicle,” *26th Annual Review of Progress in Applied Computational Electromagnetics (ACES)*, pp. 441-446, Tampere, Finland, April 2010.
- [4] A. Rousseau, P. Sharer, and F. Besnier, “Feasibility of reusable vehicle modeling: Application to hybrid vehicles,” *SAE World Congress*, Detroit, March 2004.
- [5] L. Boulon, A. Bouscayrol, D. Hissel, O. Page, and M.-C. Pera, “Inversion-based control of highly redundant military HEV,” *IEEE Transactions on Vehicular Technology*, vol. 62, no. 2, pp. 500-510, 2013.
- [6] N. Barcaro, N. Bianchi, and F. Magnussen, “PM motor for hybrid electric vehicle,” *The Open Fuels and Energy Science Journal*, pp. 135-141, 2009.
- [7] A. Arkadan, R. Heiden, and J. Defenbaugh, “Effects of forced power transfer on high speed generator-load system,” *IEEE Transactions on Energy Conversion*, vol. 11, no. 2, pp. 344-352, June 1996.
- [8] N. Al-Awar, T. Hijazi, and A. Arkadan, “Particle swarm optimization of coupled electromechanical systems,” *IEEE Transaction On Magnetics*, vol. 47, no. 5, pp. 1314-1317, 2011.
- [9] P. Curto-Risso, “Theoretical and simulated models for irreversible Otto cycle,” *IEEE Journal of Applied Physics*, vol. 104, no. 9, pp. 094911-094911-11, Nov. 2008.
- [10] J. Ginsberg, *Advanced Engineering Dynamics*, 2nd ed. Cambridge, UK: Cambridge University Press, ISBN: 9780521470216, 1995.



Nizar Al-Awar received his Bachelor of Engineering in Mechanical Engineering from American University of Beirut, Beirut Lebanon in 1994 and his Master degree from Marquette University in Electrical and Computer Engineering in 2003. He is currently completing his PhD in Electrical and Computer Engineering at Marquette University. During the period 2005 -2008 he worked in industry. In 2008, he joined the Department of Mechanical and

Mechatronics at Rafik Hariri University as a lecturer. Mr. Al-Awar authored and co-authored more than 20 technical papers in the archival literature as well as in National and International Conference records. In addition, he co-authored a white paper on assessment and solution to the problem facing electricity and water sector in Lebanon. Mr. Al-Awar received several awards for his achievements.



A. A. Arkadan received his Bachelor of Science degree from the University of Mississippi, Oxford, Mississippi in 1980, his Masters of Science degree from Virginia Tech, Blacksburg, Virginia in 1981 and his Ph.D. from Clarkson University, Potsdam, New York in 1988, all in Electrical Engineering. During the period 1981-1984 he worked in industry. In 1988, he joined the Department of Electrical and Computer Engineering at Marquette University, Milwaukee, Wisconsin, as an Assistant Professor and was later promoted to Associate Professor and Full Professor in 1993 and 1998, respectively. He has many years of teaching, curriculum development and research, as well as industrial and consulting experience. Currently, he is a Professor and President of Rafik Hariri University, in Mechref Lebanon. Dr. Arkadan is a Fellow of the Institute of Electrical and Electronics Engineers, IEEE. He authored and co-authored more than 100 technical papers in the archival literature as well as in National and International Conference records. In addition, he authored book chapters, numerous technical and project reports. Dr. Arkadan received several awards for excellence in research including several IEEE society awards. Dr. Arkadan is active in several IEEE and other international societies. Also he serves or served on the Editorial Boards of several International Conferences. In addition, Dr. Arkadan chaired several international conferences including the First IEEE International Electric Machines and Drives Conference, IEMDC, held in Milwaukee Wisconsin, May 1997, and the IEEE Conference on Electromagnetic Field Computations, CEFC, held in Chicago, Illinois, in May 2010. He is also the Chair of CEFC International Steering Committee.

An Equivalent Model for Wiring Harness Induced Current in Automobiles

Y. Zheng¹, Q. Wang¹, G. Wang², Z. An¹, Q. Liu¹, and X. Li³

¹ State Key Laboratory of Power Transmission Equipment & System Security and New Technology, Chongqing University, Chongqing 400040, China
yaya9304@163.com, wangquandi@cqu.edu.cn, anzongyu123@163.com, lqs234@163.com

² Chengdu Qingbaijiang Power Supply Company of the State Grid, Chengdu 610300, China
cqu2002wgh@163.com

³ Changan Automotive Engineering Institute, Chongqing 401120, China
lixu@changan.com.cn

Abstract – This paper presents an equivalent model for the simulation of the induced current along wiring harnesses in automobiles. The equivalent model is based on multi-transmission line theory. Then, this model is simulated by using the commercial FEM software, HFSS. The common-mode current simulation results show that the presented method is effective and the equivalent model can reduce the computation time and complexity of the wire harness model. Finally, the proposed equivalent method is proved by experiment. The equivalent model can handle automotive wiring harness for electromagnetic radiation sensitivity problems in the high frequency range.

Index Terms – Electromagnetic radiation sensitivity, electromagnetic compatibility, equivalent model, multi-conductor transmission line, induced current, and wiring harness.

I. INTRODUCTION

With increasing electronic devices in automobiles, electromagnetic compatibility (EMC) becomes extremely important. To improve the design and the production of the automobiles, the full numerical model of a car has become a strategic challenge in automotive industries [1, 2]. The automobile EMC models include car body, wiring harnesses and electrical component models,

which indicate the importance of wiring harness modeling [3].

Several studies on the electromagnetic radiation sensitivity of conductors have been performed by using the methods of Taylor, Agrawal, and Rachidi [4-7], as well as the extension of these methods [8-11]. These methods are based on multi-conductor transmission line (MTL) theory. The voltage source or current source, instead of the incident wave, is placed in an equivalent lumped-circuit model to calculate the terminal response. Numerous automotive wiring harnesses cannot always satisfy the approximate conditions of the above mentioned methods, such as the distance between the conductors must be larger than the wire radius and smaller than the incident wave length. The complex wiring harnesses are handled as a single conductor in [12] and this simple model ignores the electromagnetic characteristic differences due to terminal loads. The Agrawal model was developed according to electromagnetic topology theory, which dealt with the wiring harnesses one by one while establishing the model [13]. However, this modeling process becomes very complex when harnesses are too many. A method simplified cable bundles in [14], which is according to its characteristic impedance and used the method of moments (MoM) to obtain the common-mode current inducted on the conductors by the incident wave. This simplified method

decreases the complexity of modeling. However, the definition of the common-mode characteristic impedance of harness was not presented.

The present paper proposes a method to simplify the wiring harness model. First, the definition of wiring harness equivalent wave impedance is shown and the calculation formula is deduced to clarify the computing method. The wiring harness group method is then described in detail. The induced current generated by the incident wave can be calculated based on the FEM, which is detailed in the paper. The equivalent model is demonstrated by a numerical example and an experiment. The terminal load equivalent method is also verified.

II. THE EQUIVALENT MODEL

A. Equivalence principle

1) Equivalent wave impedance

Figure 1 shows the multi-conductors transmission line system. r_p and r_q are the radii of the conductors p and q , respectively; h_p and h_q are the heights of the conductors p and q above the ground reference, respectively; s_{pq} is the distance between conductors p and q ; $s_{pq'}$ is the distance between conductor p and mirror conductor q' .

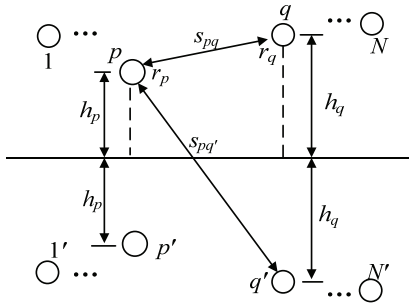


Fig. 1. Multi-conductor transmission line system.

If the electric charge of each per-unit-length (p.u.l) conductor is Q_1, Q_2, \dots, Q_N , then each conductor voltage to ground reference (V_1, V_2, \dots, V_N) can be written as [15],

$$\begin{cases} V_1 = \eta_{11}Q_1 + \eta_{12}Q_2 + \dots + \eta_{1N}Q_N \\ V_2 = \eta_{21}Q_1 + \eta_{22}Q_2 + \dots + \eta_{2N}Q_N \\ \dots \\ V_N = \eta_{N1}Q_1 + \eta_{N2}Q_2 + \dots + \eta_{NN}Q_N \end{cases} \quad (1)$$

where η is potential coefficient, which can be calculated as follows,

$$\begin{cases} \eta_{pp} = \frac{1}{2\pi\epsilon_0} \ln \frac{2h_p}{r_p} \\ \eta_{pq} = \frac{1}{2\pi\epsilon_0} \ln \frac{s_{pq'}}{s_{pq}} = \frac{1}{4\pi\epsilon_0} \ln \left(1 + \frac{4h_p h_q}{s_{pq}^2} \right) \end{cases} \quad (2)$$

where ϵ_0 is the dielectric coefficient of air, $\eta_{pq} = \eta_{qp}$, $p, q = 1, 2, \dots, N, p \neq q$.

When the right side is multiplied by v/v ($v = 1/\sqrt{\mu_0 \epsilon_0}$), equation (1) can be rewritten as follows,

$$\begin{cases} V_1 = \xi_{11}I_1 + \xi_{12}I_2 + \dots + \xi_{1N}I_N \\ V_2 = \xi_{21}I_1 + \xi_{22}I_2 + \dots + \xi_{2N}I_N \\ \dots \\ V_N = \xi_{N1}I_1 + \xi_{N2}I_2 + \dots + \xi_{NN}I_N \end{cases} \quad (3)$$

where ξ is the conductor wave impedance and can be easily obtained,

$$\begin{cases} \xi_{pp} = \frac{\eta_{pp}}{v} = \frac{1}{2\pi} \sqrt{\frac{\mu_0}{\epsilon_0}} \ln \frac{2h_p}{r_p} \\ \xi_{pq} = \frac{\eta_{pq}}{v} = \frac{1}{4\pi} \sqrt{\frac{\mu_0}{\epsilon_0}} \ln \left(1 + \frac{4h_p h_q}{s_{pq}^2} \right) \end{cases} \quad (4)$$

We define the wiring harness equivalent wave impedance as the ratio of the voltage and the sum of the currents on all conductors in the case of the same voltage,

$$\xi_{eq} = \frac{V}{I_1 + I_2 + \dots + I_N} = \frac{1}{\sum_{p=1}^N \sum_{q=1}^N A_{pq} / |\xi|} \quad (5)$$

where A_{pq} is the algebraic of the element ξ_{pq} , and $|\xi|$ is the determinant of the matrix $[\xi]$. The wiring harness equivalent wave impedance contains self- and mutual-wave impedance and depends on the structure of the conductors.

2) Grouping method

The terminal grounded load and equivalent wave impedance determine the electromagnetic characteristics of the transmission line [1]. Thus, the conductors can be grouped as shown in Table I. In Table I, $|Z_{pj}|$ and j ($j=1, 2$) are the terminal grounded load and the terminal number of the conductor p , respectively. If the terminal ground load is the same as the equivalent wave impedance, the conductor achieves matching condition and can be grouped flexibly. For example, if $|Z_{p1}| < \xi_{eq}$ and $|Z_{p2}| = \xi_{eq}$, the conductor can be classified under the first or the second equivalent group. The conductors are physically adjacent to each other in the same group, otherwise, the error of simulation results will increase.

Table I: Conductor classification table.

	End 1 ($j=1$)	End 2 ($j=2$)
First equivalent conductor group (G1)	$ Z_{p1} < \zeta_{eq}$	$ Z_{p2} < \zeta_{eq}$
Second equivalent conductor group (G2)	$ Z_{p1} < \zeta_{eq}$	$ Z_{p2} > \zeta_{eq}$
Third equivalent conductor group (G3)	$ Z_{p1} > \zeta_{eq}$	$ Z_{p2} < \zeta_{eq}$
Fourth equivalent conductor group (G4)	$ Z_{p1} > \zeta_{eq}$	$ Z_{p2} > \zeta_{eq}$

B. Equivalent model

1) P.u.l. capacitance and inductance matrix

By neglecting the resistance and conductance, the transmission line equations become only relevant to the capacitance and inductance [16],

$$\frac{\partial}{\partial z} \begin{bmatrix} I_1 \\ I_2 \\ \vdots \\ I_N \end{bmatrix} = -j\omega \begin{bmatrix} C_{11} & C_{12} & \cdots & C_{1N} \\ C_{21} & C_{22} & \cdots & C_{2N} \\ \vdots & \vdots & \ddots & \vdots \\ C_{N1} & C_{N2} & \cdots & C_{NN} \end{bmatrix} \begin{bmatrix} V_1 \\ V_2 \\ \vdots \\ V_N \end{bmatrix} \quad (6)$$

$$\frac{\partial}{\partial z} \begin{bmatrix} V_1 \\ V_2 \\ \vdots \\ V_N \end{bmatrix} = -j\omega \begin{bmatrix} L_{11} & L_{12} & \cdots & L_{1N} \\ L_{21} & L_{22} & \cdots & L_{2N} \\ \vdots & \vdots & \ddots & \vdots \\ L_{N1} & L_{N2} & \cdots & L_{NN} \end{bmatrix} \begin{bmatrix} I_1 \\ I_2 \\ \vdots \\ I_N \end{bmatrix} \quad (7)$$

The p.u.l. capacitance matrix is calculated using FEM since the condition $d > 5r$ (d is the distance between conductors and r is the conductor radius) is not always satisfied in automotive wiring harnesses [17]. The p.u.l. inductance matrix can be obtained using the analysis method [16]. To obtain the p.u.l. capacitance and inductance matrix of the equivalent groups, three hypotheses are made:

(1) The equivalent group current is equal to the sum of the currents induced on all original conductors in the group. The current flowing along the conductor is equal to the average of the equivalent group current. For example, an equivalent group m contains K conductors, then the group current I_{Gm} and the conductor current I_k ($k=1, 2, \dots, K$) can be written as,

$$\begin{cases} I_{Gm} = I_1 + I_2 + \cdots + I_K \\ I_k = \frac{I_{Gm}}{K} \end{cases} \quad (8)$$

(2) All conductors of the equivalent group have the same electrical potential as compared with the ground reference. Therefore, the group voltage V_{Gm} equals the conductor voltage, which can be written as,

$$V_{Gm} = V_1 = V_2 = \cdots = V_K \quad (9)$$

(3) Compared with the common-mode currents, the differential-mode currents induced by

electromagnetic wave are negligible.

N conductors are assumed present in the wiring harness and can be classified into four groups, as shown in Table I. The equivalent group 1 contains N_1 conductors of $1 \sim \alpha$, the equivalent group 2 contains N_2 conductors of $\alpha+1 \sim \beta$, the equivalent group 3 contains N_3 conductors of $\beta+1 \sim \gamma$, and the equivalent group 4 contains N_4 conductors of $\gamma+1$ to N . Considering the hypotheses, equations (6) and (7) can be simplified as follows,

$$\frac{\partial}{\partial z} \begin{bmatrix} I_{G1} \\ I_{G2} \\ I_{G3} \\ I_{G4} \end{bmatrix} = -j\omega [C]_{eq} \begin{bmatrix} V_{G1} \\ V_{G2} \\ V_{G3} \\ V_{G4} \end{bmatrix} \quad (10)$$

$$\frac{\partial}{\partial z} \begin{bmatrix} V_{G1} \\ V_{G2} \\ V_{G3} \\ V_{G4} \end{bmatrix} = -j\omega [L]_{eq} \begin{bmatrix} I_{G1} \\ I_{G2} \\ I_{G3} \\ I_{G4} \end{bmatrix}, \quad (11)$$

where $[C]_{eq}$ and $[L]_{eq}$ are the p.u.l. capacitance matrix and inductance matrix of equivalent conductor groups, respectively. They can be written as follows,

$$[C]_{eq} = \begin{bmatrix} \sum_{p=1}^{\alpha} \sum_{q=1}^{\alpha} C_{pq} & \sum_{p=1}^{\alpha} \sum_{q=\alpha+1}^{\beta} C_{pq} & \sum_{p=1}^{\alpha} \sum_{q=\beta+1}^{\gamma} C_{pq} & \sum_{p=1}^{\alpha} \sum_{q=\gamma+1}^N C_{pq} \\ \sum_{p=\alpha+1}^{\beta} \sum_{q=1}^{\alpha} C_{pq} & \sum_{p=\alpha+1}^{\beta} \sum_{q=\alpha+1}^{\beta} C_{pq} & \sum_{p=\alpha+1}^{\beta} \sum_{q=\beta+1}^{\gamma} C_{pq} & \sum_{p=\alpha+1}^{\beta} \sum_{q=\gamma+1}^N C_{pq} \\ \sum_{p=\beta+1}^{\gamma} \sum_{q=1}^{\alpha} C_{pq} & \sum_{p=\beta+1}^{\gamma} \sum_{q=\alpha+1}^{\beta} C_{pq} & \sum_{p=\beta+1}^{\gamma} \sum_{q=\beta+1}^{\gamma} C_{pq} & \sum_{p=\beta+1}^{\gamma} \sum_{q=\gamma+1}^N C_{pq} \\ \sum_{p=\gamma+1}^N \sum_{q=1}^{\alpha} C_{pq} & \sum_{p=\gamma+1}^N \sum_{q=\alpha+1}^{\beta} C_{pq} & \sum_{p=\gamma+1}^N \sum_{q=\beta+1}^{\gamma} C_{pq} & \sum_{p=\gamma+1}^N \sum_{q=\gamma+1}^N C_{pq} \end{bmatrix} \quad (12)$$

$$[L]_{eq} = \begin{bmatrix} \frac{\sum_{p=1}^{\alpha} \sum_{q=1}^{\alpha} L_{pq}}{N_1^2} & \frac{\sum_{p=1}^{\alpha} \sum_{q=\alpha+1}^{\beta} L_{pq}}{N_1 \cdot N_2} & \frac{\sum_{p=1}^{\alpha} \sum_{q=\beta+1}^{\gamma} L_{pq}}{N_1 \cdot N_3} & \frac{\sum_{p=1}^{\alpha} \sum_{q=\gamma+1}^N L_{pq}}{N_1 \cdot N_4} \\ \frac{\sum_{p=\alpha+1}^{\beta} \sum_{q=1}^{\alpha} L_{pq}}{N_1 \cdot N_2} & \frac{\sum_{p=\alpha+1}^{\beta} \sum_{q=\alpha+1}^{\beta} L_{pq}}{N_2^2} & \frac{\sum_{p=\alpha+1}^{\beta} \sum_{q=\beta+1}^{\gamma} L_{pq}}{N_2 \cdot N_3} & \frac{\sum_{p=\alpha+1}^{\beta} \sum_{q=\gamma+1}^N L_{pq}}{N_2 \cdot N_4} \\ \frac{\sum_{p=\beta+1}^{\gamma} \sum_{q=1}^{\alpha} L_{pq}}{N_1 \cdot N_3} & \frac{\sum_{p=\beta+1}^{\gamma} \sum_{q=\alpha+1}^{\beta} L_{pq}}{N_2 \cdot N_3} & \frac{\sum_{p=\beta+1}^{\gamma} \sum_{q=\beta+1}^{\gamma} L_{pq}}{N_3^2} & \frac{\sum_{p=\beta+1}^{\gamma} \sum_{q=\gamma+1}^N L_{pq}}{N_3 \cdot N_4} \\ \frac{\sum_{p=\gamma+1}^N \sum_{q=1}^{\alpha} L_{pq}}{N_1 \cdot N_4} & \frac{\sum_{p=\gamma+1}^N \sum_{q=\alpha+1}^{\beta} L_{pq}}{N_2 \cdot N_4} & \frac{\sum_{p=\gamma+1}^N \sum_{q=\beta+1}^{\gamma} L_{pq}}{N_3 \cdot N_4} & \frac{\sum_{p=\gamma+1}^N \sum_{q=\gamma+1}^N L_{pq}}{N_4^2} \end{bmatrix} \quad (13)$$

2) Structural parameters of the equivalent model [12]

(1) Height of equivalent group,

$$h_{Gm} = \frac{h_1 + h_2 + \dots + h_K}{K} \quad (14)$$

where h_1, h_2, \dots, h_K is the height above the ground of each conductor in group m and h_{Gm} is the height of the equivalent conductor group m above the ground reference.

(2) Radius of the equivalent group,

$$r_{Gm} = \frac{2h_{Gm}}{\exp\left(\frac{2\pi \cdot L_{mm_eq}}{\mu_0}\right)} \quad (15)$$

where r_{Gm} is the equivalent radius of the equivalent conductor group m and L_{mm_eq} is the diagonal element of the equivalent inductance matrix $[L]_{eq}$.

(3) Distance between the equivalent groups,

$$d_{Gmn} = \sqrt{\frac{4h_{Gm}h_{Gn}}{\exp\left(\frac{4\pi \cdot L_{mn_eq}}{\mu_0}\right) - 1}} \quad (16)$$

where d_{Gmn} is the distance between the equivalent conductor groups m and n ; h_{Gm} and h_{Gn} are the heights above the ground of the equivalent groups m and n , respectively. L_{mn_eq} is the non-diagonal element of the equivalent inductance matrix $[L]_{eq}$.

(4) Structural parameters adjustment,

Errors may be produced during the equivalent process. For example “ $r_{Gm} + r_{Gn} > d_{mn}$ ” may appear, and the structural parameters must be adjusted. The adjustment process is shown in Fig. 2.

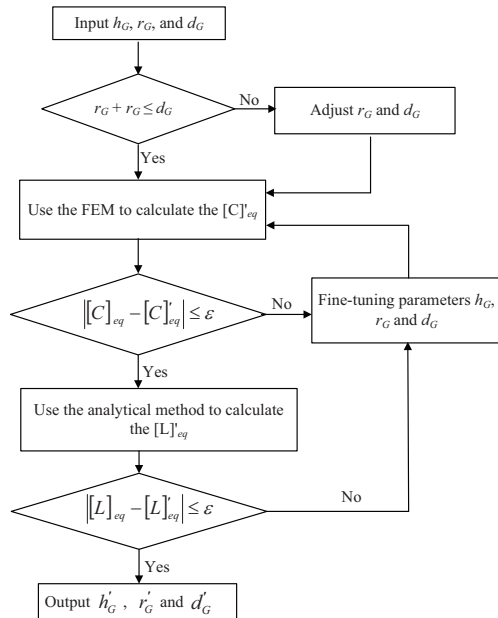


Fig. 2. Flow chart of structural parameters adjustment.

In Fig. 2, $[C]_{eq}$ is calculated based on the structural parameters from FEM, $[L]_{eq}$ is calculated based on the structural parameters by analytical method, and ε is the computational error. Smaller ε corresponds to higher calculation precision. After adjustment, the output structural parameters can establish the equivalent model.

3) Terminal load of the equivalent model [12]

(1) Terminal grounded load,

The terminal grounded load is the load between the conductor and the ground reference. The equivalent grounded load is equal to all the grounded loads in the same equivalent group connected in parallel.

(2) Load between conductors,

If the conductors belong to the same equivalent group, the load between these conductors can be neglected in the equivalent model. However, if the conductors belong to different equivalent groups, load exists between equivalent groups and is equal to the parallel value of all the loads between the conductors.

III. INDUCED CURRENT

An electric current will be induced in any closed circuit when the magnetic flux through a surface bounded by the conductor changes. Therefore, the induced current can be regarded as an evaluation parameter of the electromagnetic radiation (EMR) sensitivity of the wiring harness.

A. Calculation method of the induced current

When a uniform plane wave enters the conductor through the air, the electric and magnetic fields are mutated at the interface for the discontinuousness of the medium, as shown in Fig. 3.

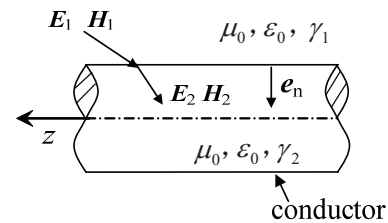


Fig. 3. Uniform plane wave incident on the conductor.

In Fig. 3, E_1 and H_1 are the electric and magnetic field intensities in the air, respectively.

\mathbf{E}_2 and \mathbf{H}_2 are the electric and magnetic field intensities in the conductor, respectively. \mathbf{e}_n is the unit vector normal to the interface pointing from medium 1 to medium 2.

When the electromagnetic wave travels from an ideal medium ($\gamma_1=0$) to an ideal conductor ($\gamma_2 \rightarrow \infty$), the electromagnetic wave will decay to zero quickly. Only a thin layer of the surface current is present on the conductor surface, and the electromagnetic field is almost non-existent in the conductor ($\mathbf{E}_2 \approx 0$, $\mathbf{H}_2 \approx 0$). Using the boundary conditions ($-\mathbf{e}_n \times \mathbf{H}_1 = \mathbf{K}$) and the total fields in the

free space $\mathbf{H}_1 = \mathbf{e}_k \times \frac{\mathbf{E}_i}{Z_0} - \mathbf{e}_k \times \frac{\mathbf{E}_s}{Z_0}$ (Z_0 is the wave impedance of the air space) [16], the induced current along the conductor is given by equation (17), shown at the bottom of the page. In equation (17), $\mathbf{e}_{l\perp}$ is the unit vector of the conductor axis, and l is the closed-loop on the conductor surface.

If the conductor and the reference ground plane are parallel, three coupling modes of the plane wave to the conductor exist, as shown in Fig. 4.

$$\begin{aligned}
 I &= \oint_l (\mathbf{K} \cdot \mathbf{e}_{l\perp}) dl \\
 &= \frac{1}{Z_0} \oint_l [-\mathbf{e}_n \times (\mathbf{e}_k \times \mathbf{E}_i) + \mathbf{e}_n \times (\mathbf{e}_k \times \mathbf{E}_s)] \cdot \mathbf{e}_{l\perp} dl \\
 &= \frac{1}{Z_0} \oint_l \{ [-\mathbf{e}_k (\mathbf{e}_n \cdot \mathbf{E}_i) + \mathbf{E}_i (\mathbf{e}_n \cdot \mathbf{e}_k)] + [\mathbf{e}_k (\mathbf{e}_n \cdot \mathbf{E}_s) - \mathbf{E}_s (\mathbf{e}_n \cdot \mathbf{e}_k)] \} \cdot \mathbf{e}_{l\perp} dl \quad (17) \\
 &= \frac{1}{Z_0} \oint_l \{ (\mathbf{e}_k \cdot \mathbf{e}_{l\perp}) [(\mathbf{e}_n \cdot \mathbf{E}_s) - (\mathbf{e}_n \cdot \mathbf{E}_i)] + (\mathbf{e}_n \cdot \mathbf{e}_k) [(\mathbf{E}_i \cdot \mathbf{e}_{l\perp}) - (\mathbf{E}_s \cdot \mathbf{e}_{l\perp})] \} dl
 \end{aligned}$$

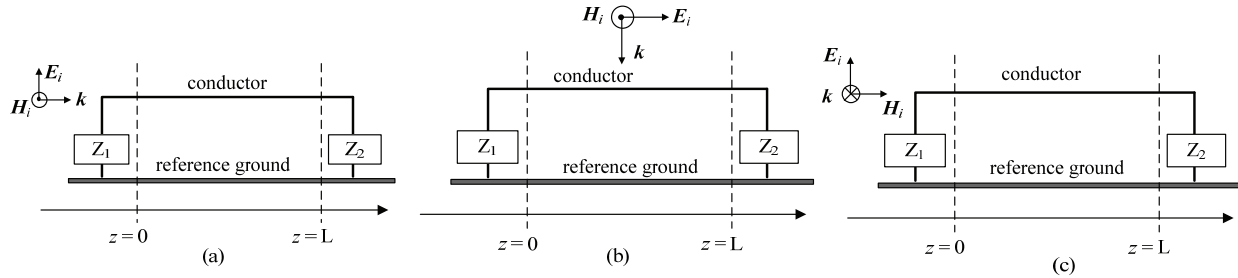


Fig. 4. Three coupling modes of the plane wave to the conductor.

In Fig. 4 (a), the electrical field and the reference ground are orthogonal to each other. The electrical field is named as “vertically polarized wave”. The induced current along the conductor can be obtained using equation (17). Given that $\mathbf{E}_s = f(\mathbf{E}_i)$, the induced current along the conductor can be written as,

$$I = \frac{1}{Z_0} \oint_l (\mathbf{e}_k \cdot \mathbf{e}_{l\perp}) [\mathbf{e}_n \cdot (f(\mathbf{E}_i) - \mathbf{E}_i)] dl \quad (18)$$

In Fig. 4 (b), the electrical field and the reference ground are parallel to each other. The electrical field is termed as “horizontally polarized wave”. Therefore, the induced current can be obtained by using equation (17),

$$I = \frac{2}{Z_0} \oint_l (\mathbf{E}_i \cdot \mathbf{e}_{l\perp}) (\mathbf{e}_n \cdot \mathbf{e}_k) dl \quad (19)$$

In Fig. 4 (c), \mathbf{e}_k and \mathbf{E}_s are all vertical to $\mathbf{e}_{l\perp}$. \mathbf{E}_i and $\mathbf{e}_{l\perp}$ are vertical. Based on equation (17), no induced current exists along the conductor.

B. Effectiveness of the FEM

In the current study, we established a 1 m long uncoated 10-conductor wiring harness model. Figure 5 shows the cross-section geometry. The incident electrical field intensity amplitude is 3 V/m, and the coupling mode is shown in Fig. 6. Table II shows the terminal grounded loads.

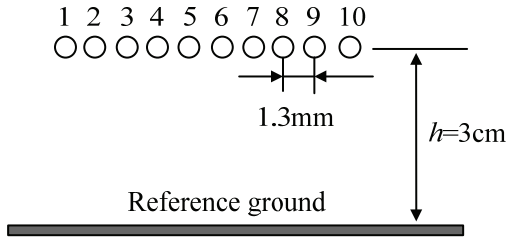


Fig. 5. Cross-section geometry of the wiring harness.

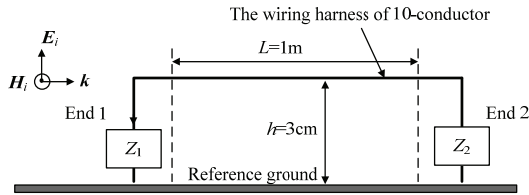


Fig. 6. EMR sensitivity model of the wiring harness.

The induced current calculated at the first end of conductor 4 is simulated based on the FEM and the MTL method, as shown in Fig. 7.

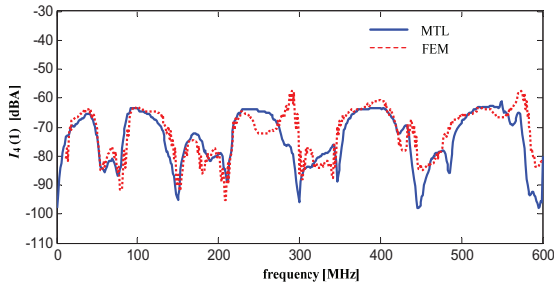


Fig. 7. Current at the first end of conductor 4.

Figure 7 indicates the similarity of the values of the current induced at the first end of the fourth conductor calculated by the FEM and the MTL method. The amplitude differences may have been caused by the differences in the accuracy of the calculation method.

IV. SIMULATION AND ANALYSIS

A. Wiring harness and the equivalent model

To validate the proposed method, we used an 80 cm long nine-conductor wiring harness as an example. The distance between the conductors is 2 mm, and the radius is 0.5 mm. The insulating

medium around the conductor is neglected. Table III shows the grounded terminal loads, while Fig. 8 presents the cross-section.

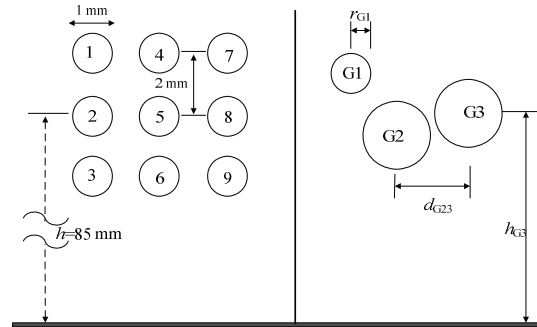


Fig. 8. Cross-section of the original wiring harness (left) and the equivalent model (right).

The wiring harness equivalent wave impedance is 248.6Ω . The nine-conductor wiring harness can be divided into three equivalent groups based on the grouping method (indicated in Table I), as shown below:

- 1) Group 1, G1: conductor 1
- 2) Group 2, G2: conductors 2 to 5
- 3) Group 3, G3: conductors 6 to 9.

The nine-conductor p.u.l. capacitance and inductance matrices can be obtained from the structure parameters, as shown in equations (20) and (21) in the next page. The p.u.l. capacitance and inductance matrices of the equivalent group can be obtained using equations (12) and (13),

$$[C]_{\text{eq}} = \begin{bmatrix} 32.5 & -27.9 & -3.2 \\ & 85.4 & -54.7 \\ & & 62.03 \end{bmatrix} \text{ pF/m} \quad (22)$$

$$[L]_{\text{eq}} = \begin{bmatrix} 11704 & 8389 & 7232 \\ & 9204 & 791.4 \\ & & 9105 \end{bmatrix} \text{ nH/m} \quad (23)$$

After applying the four-phase procedure described in section II-B-2, an equivalent model is obtained, which is composed of three equivalent groups:

$r_{G1} = 0.5 \text{ mm}$, $r_{G2} = r_{G3} = 1.5 \text{ mm}$, $h_{G1} = 86.5 \text{ mm}$, $h_{G2} = 84 \text{ mm}$, $h_{G3} = 84.5 \text{ mm}$, $d_{G1G2} = 2.69 \text{ mm}$, $d_{G1G3} = 4.69 \text{ mm}$, and $d_{G2G3} = 3.28 \text{ mm}$. The terminal grounded loads of the equivalent model are shown in Table IV.

Table II: Terminal grounded loads of the ten-conductor wiring harness.

	1	2	3	4	5	6	7	8	9	10
End 1	50 Ω	110 Ω	50 kΩ	2 Ω	2 kΩ	50 Ω	1 Ω	3 nH	2 pF	500 Ω
End 2	10 kΩ	5 Ω	200 Ω	400 Ω	10 Ω	50 Ω	1 pF	4pF	100 kΩ	10 nH

Table III: Terminal grounded loads of the nine-conductor wiring harness.

	1	2	3	4	5	6	7	8	9
End 1	50 Ω	50 Ω	10 Ω	100 Ω	15 Ω	1 MΩ	150 kΩ	1 kΩ	10 kΩ
End 2	10 Ω	1 MΩ	150 kΩ	15 kΩ	100 kΩ	10 Ω	15 Ω	15 Ω	100 Ω

$$[C]= \begin{bmatrix} 32.5 & -12.1 & -1.84 & -12.1 & -1.91 & -0.39 & -1.84 & -0.39 & -0.61 \\ & 39.2 & -12.1 & -2.19 & -9.03 & -2.19 & -0.39 & -0.18 & -0.39 \\ & & 32.5 & -0.39 & -1.91 & -12.1 & -0.61 & -0.39 & -1.84 \\ & & & 39.2 & -9.03 & -0.18 & -12.1 & -2.19 & -0.39 \\ & & & & 43.8 & -9.03 & -1.91 & -9.03 & -1.91 \\ & & & & & 39.2 & -0.39 & -2.19 & -12.1 \\ & & & & & & 32.5 & -12.1 & -1.84 \\ & & & & & & & 39.2 & -12.1 \\ & & & & & & & & 32.5 \end{bmatrix} \text{ pF/m} \quad (20)$$

$$[L]= \begin{bmatrix} 1170.4 & 890.9 & 749.9 & 893.2 & 821.6 & 727.6 & 754.6 & 729.9 & 680.6 \\ & 1165.8 & 886.2 & 821.6 & 888.5 & 816.9 & 729.9 & 749.9 & 725.3 \\ & & 1161.0 & 727.6 & 816.9 & 883.8 & 680.6 & 725.3 & 745.2 \\ & & & 1170.4 & 890.9 & 749.9 & 893.2 & 821.6 & 727.6 \\ & & & & 1165.8 & 886.2 & 821.6 & 888.5 & 816.9 \\ & & & & & 1161 & 727.6 & 816.9 & 883.9 \\ & & & & & & 1170.4 & 890.9 & 749.9 \\ & & & & & & & 1165.8 & 886.2 \\ & & & & & & & & 1161.0 \end{bmatrix} \text{ nH/m} \quad (21)$$

Table IV: Terminal grounded loads of the equivalent model.

	G1	G2	G3
End 1	50 Ω	5.1 Ω	856 Ω
End 2	10 Ω	11.8 kΩ	4.1 Ω

B. Simulation results and analysis

The amplitude of the plane wave is 1 V/m, and the electric field is normal to the conductor. Figure 9 shows the nine-conductor wiring harness EMR sensitivity model. The EMR sensitivity model configuration of the equivalent group is the same as that in Fig. 9, except that the nine-conductor wiring harness is represented by three equivalent groups. Figure 10 (a) and (b) are the finite element mesh of the original wiring harness and the equivalent model, respectively. To improve the computation speed, subdivision principles are used.

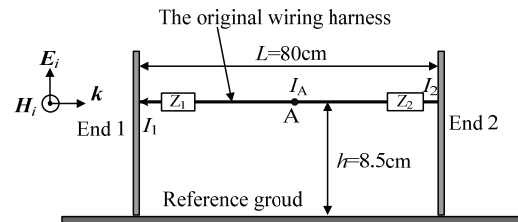
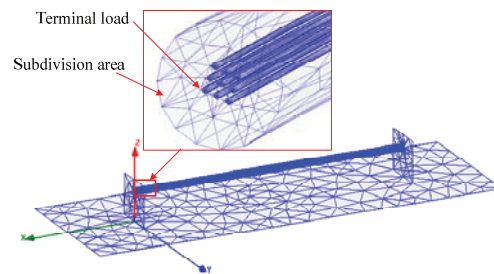
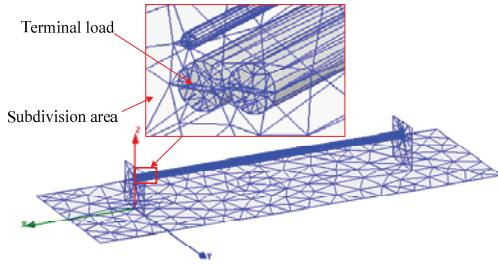


Fig. 9. EMR sensitivity model of the wiring harness.



(a) Finite element mesh of the nine-conductor wiring harness.



(b) Finite element mesh of the equivalent groups.

Fig. 10. Wiring harness finite element mesh.

Figures 11 to 13 show the common-mode current (sum of currents in all conductors) induced at End 1, End 2, and at the center point A of both models.

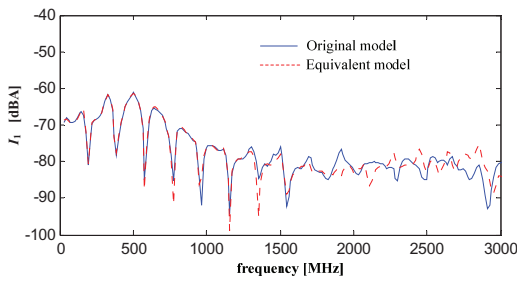


Fig. 11. Common-mode current induced at End 1.

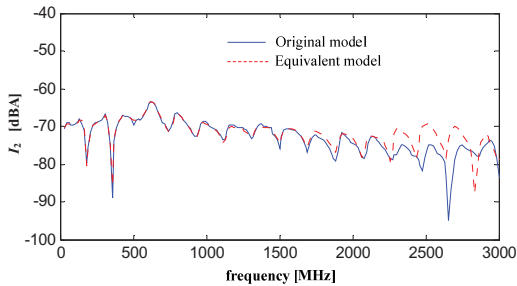


Fig. 12. Common-mode current induced at End 2.

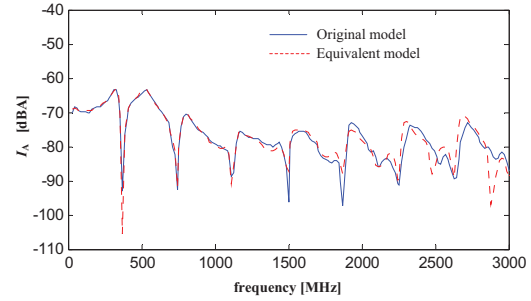


Fig. 13. Common-mode current induced at Point A.

The above three figures show that the common-mode currents induced in the original conductors and the equivalent model follow closely similar trends in the frequency range of 30 MHz to 3 GHz. Almost no discrepancy in amplitude was found from 30 MHz to 1.5 GHz. Meanwhile, the error increased from 1.5 GHz to 3 GHz. This finding indicates that several flaws could occur when circuit theory is used to solve the electromagnetic field problem at high frequency. Given that the automotive EMC standards are always in the frequency range of 30 MHz to 1 GHz, the equivalent model can be used as a simplified method in the EMR sensitivity problem in vehicle wiring harness.

C. Comparison of the simulation resources

In the case of the nine-conductor wiring harness, the simulation resources except for the modeling time are shown in Table V. The simulation was performed under the same conditions [e.g. frequency range (30 MHz to 3 GHz), discrete point numbers (201), calculation frequency and calculation region]. Table V shows that the mesh grid, calculation time, sweep time, computer memory, and disk space decreased. Thus, this method may be useful in modeling numerous automobile wiring harnesses.

Table V: Comparison of simulation resources.

	Equivalent model	Original model	Ratio (%)
Mesh grid quantity	22652	30515	74.23
Calculation time at center frequency	40 s	59 s	67.8
Sweep time	8485 s	12195 s	69.58
Memory	581 MB	796 MB	72.99
Disk space	958 MB	1198.08 MB	79.96

Table VI: Terminal load between conductors (Ω).

	Conductors in same groups			Conductors in different groups		
	G1	G2	G3	G1-G2	G1-G3	G2-G3
End 1	—	$Z_{23}=80$ $Z_{24}=200$ $Z_{35}=50$	$Z_{68}=80$ $Z_{78}=15$	$Z_{12}=50$ $Z_{14}=200$	$Z_{16}=80$	$Z_{26}=500$ $Z_{36}=20$
End 2	—	$Z_{45}=400$	$Z_{69}=5$ $Z_{78}=200$	$Z_{14}=36$ $Z_{15}=100$	$Z_{18}=50$	$Z_{47}=80$ $Z_{48}=400$ $Z_{56}=100$

D. Validation of the equivalent method for the load between conductors

Table VI shows the loads between conductors were added in the example in section III-B by using Z_{pq} representation. For the loads between conductors belonging to the same groups, the common-mode currents at End 2 are calculated as shown in Fig. 14. For the loads between conductors belonging to different groups, the currents at End 2 are obtained as indicated in Fig. 15.

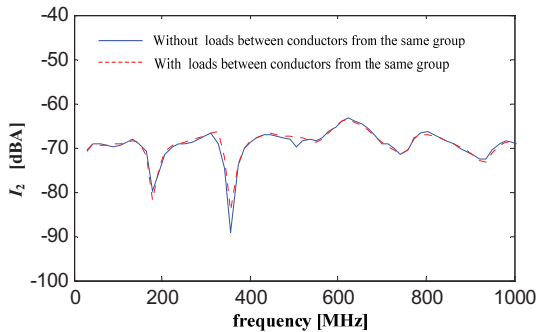


Fig. 14. Current at End 2 with and without the loads between conductors from the same group.

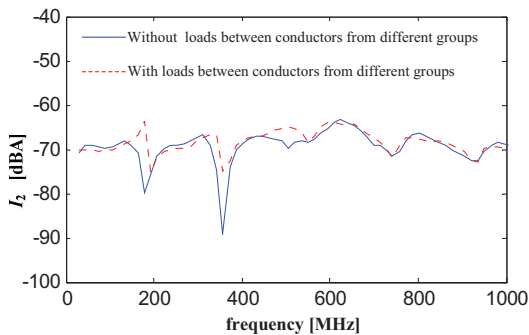


Fig. 15. Current at End 2 with and without the load between conductors from different groups.

Figure 14 illustrates that when conductors belong to the same group, the load between these conductors has no influence on the resonant frequency and amplitude of the current. Figure 15 shows that if the conductors belong to different groups, the load has no influence on the resonant frequency of the induced current, but can affect the amplitude with approximately 15 dB. Therefore, the load between conductors from the same group can be neglected, whereas the load between conductors from different groups needs equivalent processing.

Through the above handling method, the equivalent loads connected between equivalent groups (Z_{Gmn_L}) can be obtained, as shown in Table VII. Afterward, the current at End 2 can be calculated, as shown in Fig. 16.

Table VII: Terminal load between equivalent group conductors (Ω).

	Loads between equivalent groups		
	Z_{G12_L}	Z_{G13_L}	Z_{G23_L}
End 1	40	80	19.2
End 2	26.5	50	40

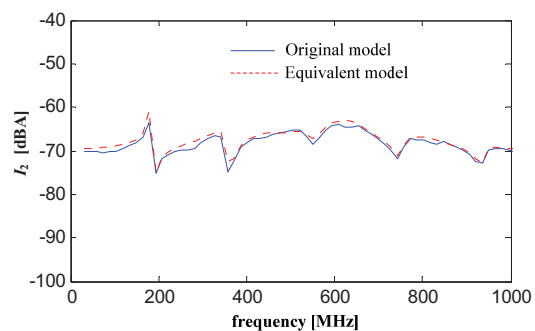


Fig. 16. Current at End 2 before and after the equivalent processing.

Figure 16 shows that after the equivalent processing, the currents were almost coincident with each other, indicating that the load equivalent method is functional.

V. EXPERIMENTAL VALIDATION

A. Experimental arrangement

The experimental validation consisted of an 80 cm long seven-conductor wiring harness. The average height of the conductors is 18 mm above the reference ground. The distance between conductors is 2.6 cm. The radius of the conductors is 0.5 mm, surrounded by a 0.7 mm thick dielectric coating with a relative electric permittivity of 3.5 (neglected in the equivalent processing). Each end

of the wiring harness is supported by a metallic bracket measuring 12 cm high and 12 cm wide. Each end of the conductors is connected to the reference ground through the chip resistors, as shown in Table VIII.

The experimental test is carried out in a semi-anechoic chamber. Figure 17 shows the cross-section structure of the wiring harness and its arrangement. The transmitting antenna is a log-periodic antenna with a frequency range of 80 MHz to 3 GHz. The input power of the antenna is 13 dBm. A broadband current probe (F-65A from FCC Group International Inc., 10 kHz to 1 GHz) measures the common-mode current induced along the conductors. The test arrangement sketch map is described in Fig. 18.

Table VIII: Terminal grounded loads of the seven-conductor wiring harness (Ω).

	1	2	3	4	5	6	7
End 1	50 Ω	50 Ω	50 Ω	50 Ω	50 Ω	50 Ω	50 Ω
End 2	50 Ω	150 Ω	20 Ω	100 Ω	150 k Ω	300 k Ω	100 k Ω

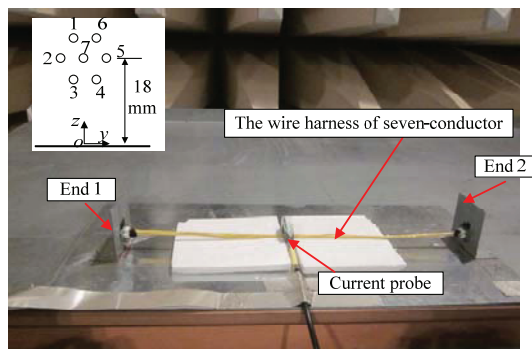


Fig. 17. Cross-section structure of the wiring harness and the wiring harness under test.

B. Simulation model

Using the equivalent method, the wiring harness can be reduced to two equivalent groups. The simulation model is established in HFSS software, as shown in Fig. 19.

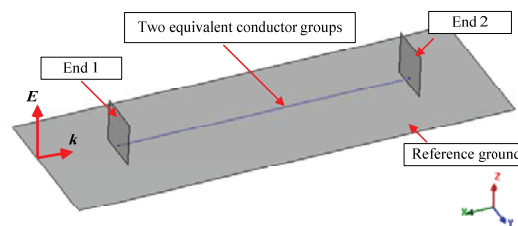


Fig. 19. Simulation model of EMR sensitivity in HFSS software.

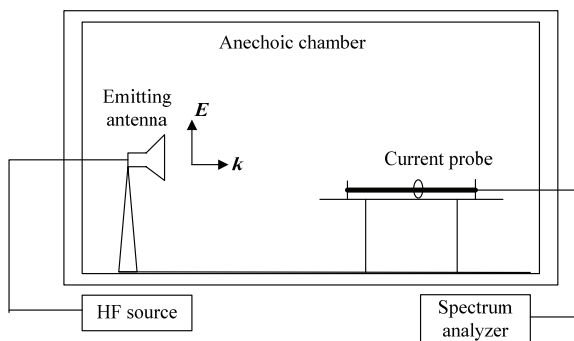


Fig. 18. Test arrangement sketch map.

C. Results and analysis

Figures 20 and 21 present the common-mode induced current measured on the conductors and the simulation results by FEM at End 2 and Point A (at the middle of the conductors), respectively. The two figures above show that the test results are consistent with the simulation results of both the original and the equivalent wiring harness. The results prove that the equivalent model is functional. Meanwhile, the test error increases with increasing frequency, and the error is 6 dB

approximately. Several reasons were identified to explain the degradation of the agreement. We assume that the effects of the parasitic parameters modify the termination loads. Moreover, the arrangement of the conductors is random, which changes the structure parameter, the p.u.l inductance and capacitance matrix. The log-periodic antenna modeling is another reason. However, we know there is an error in the EMC measurement and the error can be received within 6 dB.

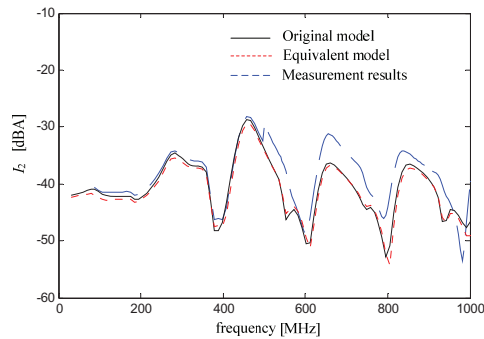


Fig. 20. Induced current at End 2.

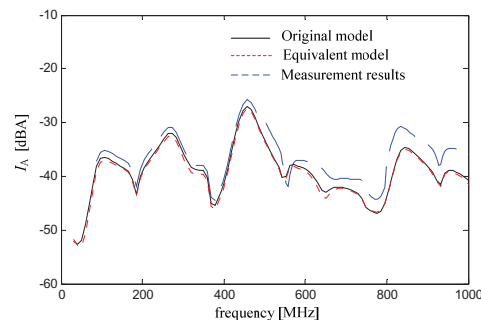


Fig. 21. Induced current at Point A.

VI. CONCLUSIONS

This paper detailed the equivalent wave impedance concept and the induced current along the conductor generated by incident wave. The equivalent method was used for simulating the wiring harness induced current by FEM. The method aims to decrease the complexity of the wiring harness model and the computation time. After the numerical and experimental validation, the method was successfully applied to the wiring harness model physically adjacent to each other in high frequency.

This paper also outlined the wiring harness modeling process by FEM in HFSS. The vehicle model inhomogeneous medium can be easily dealt with in FEM, and thus method can be regarded as

a universal way to research EMC. With the whole automobile structure, wiring harness layout, major interference electromagnetic wave, the induced current along the conductors can be obtained through this efficient method.

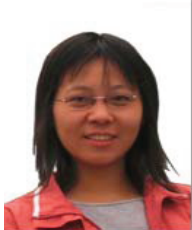
ACKNOWLEDGMENT

This work was supported by the Fundamental Research Funds for the Central Universities (No. CDJZR12110021).

REFERENCES

- [1] C. Paul, *Introduction to Electromagnetic Compatibility (Second Edition)*, John Wiley & Sons, Inc., New York, 2006.
- [2] K. Yang, *Electromagnetic Compatibility Principles and Design Techniques*, Posts & Telecom Press, Beijing, 2004. (In Chinese)
- [3] X. Ma, *Research on the Pre-assessments of Electromagnetic Compatibility in Automobile*, Jilin University, 2008. (In Chinese)
- [4] C. Taylor, R. Satterwhite, and C. Harrison, "The response of a terminated two-wire transmission line excited by a nonuniform electromagnetic field," *IEEE Transactions on Antennas and Propagation*, vol. 13, no. 6, pp. 987-989, 1965.
- [5] A. Agrawal, H. Price, and S. Gurbaxani, "Transient response of multiconductor transmission lines excited by a nonuniform electromagnetic field," *IEEE Transactions on Electromagnetic*, vol. 22, no. 2, pp. 119-129, 1980.
- [6] F. Rachidi, "Formulation of field-to-transmission line coupling equations in terms of magnetic excitation field," *IEEE Transactions on Electromagnetic Compatibility*, vol. 35, no. 3, pp. 404-407, 1993.
- [7] J. Roden, "Coupled-pair transmission line termination revisited: an MTL approach," *Applied Computational Electromagnetics Society (ACES) Journal*, vol. 19, no. 2, pp. 18-23, July 2004.
- [8] M. Omid, Y. Kami, and M. Hayakawa, "Field coupling to nonuniform and uniform transmission lines," *IEEE Transactions on Electromagnetic Compatibility*, vol. 39, no. 3, pp. 210-211, 1997.
- [9] S. Tkatchenko, F. Rachidi, and M. Ianoz, "Electromagnetic field coupling to a line of finite length: theory and fast iterative solutions in the frequency and time domain," *IEEE Transactions on Electromagnetic Compatibility*, vol. 37, no. 4, pp. 509-518, 1995.
- [10] P. Papakanellos and G. Veropoulos, "Load response of terminate transmission lines exposed to external electromagnetic fields," *IET Microwaves, Antennas and Propagation*, vol. 4, no. 7, pp. 917-955, 2010.

- [11] G. Antonini, G. Miscione, and J. Ekman, "PEEC modeling of automotive electromagnetic problems," *Applied Computational Electromagnetics Society (ACES) Journal*, vol. 23, no. 1, pp. 39-50, March 2008.
- [12] S. Frei, R. Jobava, and D. Topchishvili, "Complex approaches for the calculation of EMC problems of large systems," *Electromagnetic Compatibility, 2004 IEEE International Symposium on*, California, no. 3, pp. 826-831, 2004.
- [13] L. Paletta, J. Parmantier, F. Issac, P. Dumas, and J. Alliot, "Susceptibility analysis of wiring in a complex system combining a 3-D solver and a transmission line network simulation," *IEEE Transactions on Electromagnetic Compatibility*, vol. 44, no. 2, pp. 309-317, 2002.
- [14] G. Andrieu, L. Kone, F. Bocquet, B. Demoulin, and J. Parmantier, "Multiconductor reduction technique for modeling common-mode currents on cable bundles at high frequency for automotive applications," *IEEE Transactions on Electromagnetic Compatibility*, vol. 50, no. 1, pp. 175-184, 2008.
- [15] B. Yang, X. Liu, and Y. Dai, *High Voltage Technology*, Chongqing: Chongqing University Press, 2001. (In Chinese)
- [16] F. Tesche, V. Michel, and K. Torbjorn, *EMC Analysis Methods and Computational Models*, John Wiley & Sons, Inc., New York, 1997.
- [17] Y. Peng, J. Ruan, Y. Zhang, and M. Li, "Calculation of very fast transient voltage distribution in pulse transformer," *Proceedings of the CSEE*, vol. 25, no. 11, pp. 140-145, 2005. (In Chinese)



Yali Zheng was born in Henan Province, China in 1982. She received her Ph.D. degree in Electrical Engineering from Chongqing University, Chongqing, China, in 2011. Her research interests include electromagnetic computation, electromagnetic compatibility and transmission-line analysis. Currently, she is a lecturer in the School of Electrical Engineering, Chongqing University.



Quandi Wang was born in Anhui province, China in 1954. She received her Ph.D. degree from the School of Electrical Engineering of Chongqing University, Chongqing, China, in 1998. Currently, she is a Professor in the School of Electrical Engineering, Chongqing University. Her main research interests are simulation

and numerical computation of electromagnetic field.



Guohui Wang was born in Gansu Province, China, in 1984. He received his M.C. degree in Electrical Engineering from Chongqing University, Chongqing, China, in 2009. Now, he works in Chengdu Qingbaijiang Power Supply Company of the State Grid. His current research interest is transmission-line analysis.



Zongyu An was born in Gansu Province, China, in 1986. He received his B.S. degree in Electrical Engineering from Chongqing University, Chongqing, China, in 2009. He is currently working toward the Ph.D. degree in the State Key Laboratory of Power Transmission Equipment & System Security and New Technology, Chongqing, China. His current research interest is vehicle electromagnetic compatibility.



Qingsong Liu was born in Sichuan Province, China, in 1975. He received his M.C. degree in Electrical Engineering from Chongqing University, Chongqing, China, in 2004. Then, he worked in Chongqing Vehicle Test & Research Institute. He is working toward his Ph.D. degree in the School of Electrical Engineering, Chongqing University Chongqing, China. His current research interest is vehicle electromagnetic compatibility.



Xu Li was born in Sichuan Province, China, in 1978. He received his Ph.D. degree in Electrical Engineering from Chongqing University, Chongqing, China, in 2008. He is currently a Senior Engineer in Automotive Engineering Institute of china chang'an Automobile Group. From July 2009 to May 2013 he is also working as a postdoctor in Institute of Electrical Engineering, Chinese Academy of Sciences. His main research interest is vehicle Electromagnetic Compatibility technology.

Effective Analysis of Ridged Circular Waveguides with a Curvilinear Frequency-Domain Finite-Difference Approach

A. Fanti, G. Montisci, G. Mazzarella, and G. A. Casula

Dipartimento di Ingegneria Elettrica ed Elettronica
University of Cagliari, 09123 Cagliari, Italy

alessandro.fanti@diee.unica.it, giorgiom@diee.unica.it, giuseppe.mazzarella@diee.unica.it,
a.casula@diee.unica.it

Abstract — We present a frequency domain finite difference approach in curvilinear coordinates to the computation of the modes of circular ridged waveguides. The use of a polar mesh allows to avoid staircase approximations of the boundary, providing a very effective and accurate procedure. The proposed approach has been assessed, both in terms of accuracy and effectiveness, against general-purpose software, namely CST Microwave Studio and Ansys HFSS, showing a significant reduction of the computational burden.

Index Terms — Finite difference frequency domain, ridged circular waveguides, and waveguide modes.

I. INTRODUCTION

Application of ridged circular waveguides (RCW) [1] can be found in many components like filters, matching networks, orthomode transducers, polarizers, and circulators that are widely used in satellite and terrestrial communication systems [2-6]. Low-cost design, small size, and optimum performance of these components are essential to satisfy today's stringent payload requirements. In the design of these components it is therefore important to characterize accurately the transition between the empty circular waveguide and the RCW section, as well as the interaction between subsequent discontinuities.

The most effective approach to such characterization is the use of the mode-matching (MM) [7], since its computational load is insensitive to the length of the waveguide sections. Moreover, MM accuracy is more or less constant

as the discontinuities spacing becomes smaller. To implement an MM analysis of those components, the knowledge of both eigenvalues and field distribution of waveguides modes are required. For a circular waveguide, the analytic computation of modes is the simplest, and most accurate, approach since the mode distribution can be expressed in terms of Bessel functions [8, 9], and the eigenvalues are the well-known zeroes of these functions.

For RCWs, various numerical techniques have been proposed in the past to compute the modes of single [3], double [1, 10-11], triple [12, 13], and quadruple-ridged [1, 14-16] circular waveguides with ridges of uniform thickness or ridges that are radially cut. All these methods require the ridges to be of equal radial and angular width, and equispaced along the guide circular boundary. The latter requirement cannot be easily relaxed, since those methods use a modal approach, and this limits their flexibility. There is also a technique that allows for the ridges to be of different radial and angular width [17, 18], but this method present one serious disadvantage. Actually, if the total angular width of the ridges becomes larger and larger, the final matrices become more and more ill-conditioned and a suitable adaptive process is required to find a compromise between accuracy and computational efficiency.

Of course, also general purpose EM programs can be used, but, respective of the approach (FDTD, FEM, FIT) they require a very fine mesh to reach the accuracy needed for use in filter design. In principle, frequency-domain finite-difference (FDFD) approach [19], i.e., the direct discretization of the eigenvalue problem, is the

simplest strategy, but, in its standard form, it is a very effective solution only for rectangular waveguides, since the boundary is perfectly fitted to the discretization grid. On the other hand, the standard FDFD requires, for generic curved structures, a staircase approximation of the boundary and its effectiveness (computational burden versus accuracy) is significantly lowered. A further drawback of the standard FDFD approach is the requirement of two different grids for TE and TM modes, justified with the different boundary conditions. This means that TE and TM modes are not known in the same sampling points. However, in many applications, e.g., mode matching or FDTD (using [20]), TE and TM modes needs to be considered together, and in the same points, which prevents standard FDFD results to be easily used.

Aim of this work is to devise an FDFD approach for RCWs, tailored to the structure, but as simple as the standard one in the formulation. Use of a suitable polar grid (which perfectly fits the waveguide boundary) allows to evaluate the RCW modes with the required accuracy using order of magnitude less points than the standard approach. By generalizing a solution already used in [21] for elliptic regular waveguide, and in [22] for rounded-end waveguides, our approach is able also to compute both TE and TM modes on the same set of sampling points. This strategy leads to a very effective computation of the modes eigenvalues, since the matrices resulting from the FDFD procedure are highly sparse. Moreover, the proposed approach is insensitive to the ratio between the area occupied by the ridges and the total cross-sectional area. The presented technique has been validated through comparison with CST Microwave Studio and Ansys HFSS, showing to be significantly more efficient.

II. DESCRIPTION OF THE FDFD PROCEDURE

Let us consider a ridged circular waveguide (see Fig. 1). Both TE and TM modes can be found [23] from a suitable scalar eigenfunction, solution of the Helmholtz equation,

$$\nabla_r^2 \phi + k_r^2 \phi = 0 \quad (1)$$

with the boundary conditions (BC)

$$\begin{aligned} \frac{\partial \phi}{\partial n} &= 0 \quad (TE \text{ modes}) \\ \phi &= 0 \quad (TM \text{ modes}) \end{aligned}, \quad (2)$$

at the boundary of the ridged waveguide. Both equation (1) and the BC (2) can be replaced by a discretized version looking for the eigenfunction values at a suitable set of sampling points, and therefore replacing derivatives with finite approximations. This transforms equation (1) into a matrix eigenvalue problem

$$\underline{A}\underline{\phi} = -k_r^2 \underline{\phi}, \quad (3)$$

whose eigenvectors contain the samples of the potential ϕ at the discretization nodes. The resulting matrix is sparse so a very effective computation is possible [24].

The set of sampling points forms a grid, whose geometry depends on the waveguide section, and which defines a set of cells partitioning the section itself. If the waveguide boundary consists of straight lines, parallel to the coordinate axes, the finite difference method can be applied on a cartesian grid [25, Fig. 28]. This grid defines also a partition of the waveguide surface into rectangular cells, which are rectangular and fill exactly the waveguide section. In this case, grid points are the vertices (or the centers, depending on the implementations) of a partition made of rectangular cells, which exactly fills the section. For every other waveguide, the section cannot be exactly partitioned using rectangular cells. Rather, a cartesian grid can only approximate this section [26, Fig. 3], and this leads to numerical errors (since an eigenvalue problem is quite ill-conditioned [27]).

In order to get an high accuracy, the best approach is to discretize the waveguide surface maintaining also the correct geometry of the boundary. So a discretization scheme based on a non-cartesian grid must be used, which matches exactly the waveguide boundary. Therefore, the discretization nodes must be at the intersections of a suitable framework, in which the waveguide boundary is a coordinate curve. In this way the waveguide section is exactly partitioned into discretization cells. In order to discretize the RCW we use a polar framework with coordinates (r, α) , the same one for both TE and TM modes, with a

regular spacing on the coordinate lines with step Δr , $\Delta\alpha$ (see Fig. 1). We have built this grid in such a way that furthest sampling points are not on the boundary, but at a distance $\Delta r/2$, $\Delta\alpha/2$, and we let $\phi_{nq} = \phi(n\Delta r, q\Delta\alpha)$ as sample values of $\phi(r, \alpha)$, so that the center is a sampling point.

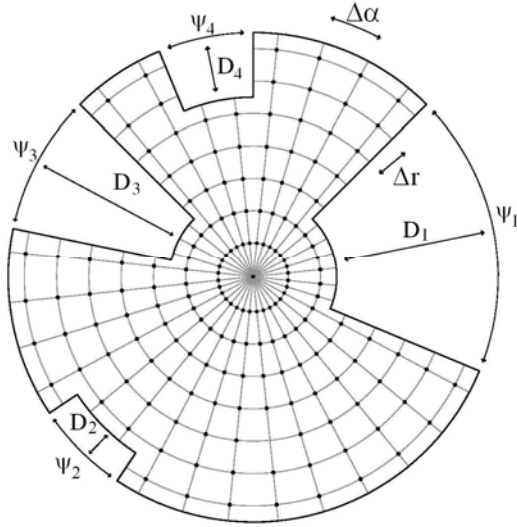


Fig. 1. An example of ridged circular waveguide with the curvilinear discretization grid.

We need a discretized version of equation (1) for each sampling point. For an internal point, such as P in Fig. 2, we start from the Helmholtz equation in polar coordinates,

$$\left[\frac{1}{r_p^2} \cdot \frac{\partial^2 \phi}{\partial \alpha^2} + \frac{1}{r_p} \cdot \frac{\partial \phi}{\partial r} + \frac{\partial^2 \phi}{\partial r^2} \right] = -k_t^2 \phi \quad (4)$$

and express the ϕ around the cell central point P using a second-order Taylor expression as,

$$\phi_D = \phi_P + \frac{\partial \phi}{\partial r} \Big|_P \cdot (\Delta r) + \frac{1}{2} \frac{\partial^2 \phi}{\partial r^2} \Big|_P \cdot (\Delta r)^2 \quad (5)$$

$$\phi_B = \phi_P + \frac{\partial \phi}{\partial r} \Big|_P \cdot (-\Delta r) + \frac{1}{2} \frac{\partial^2 \phi}{\partial r^2} \Big|_P \cdot (-\Delta r)^2. \quad (6)$$

Adding and subtracting equations (5) and (6) we get the derivatives in the r direction,

$$\begin{aligned} \frac{\partial^2 \phi}{\partial r^2} \Big|_P &= \frac{1}{\Delta r^2} \cdot (\phi_B + \phi_D - 2\phi_P) \\ \frac{\partial \phi}{\partial r} \Big|_P &= \frac{1}{2\Delta r} \cdot (\phi_D - \phi_B) \end{aligned} \quad (7)$$

and likely in α direction

$$\frac{\partial^2 \phi}{\partial \alpha^2} \Big|_P = \frac{1}{\Delta \alpha^2} \cdot (\phi_A + \phi_C - 2\phi_P). \quad (8)$$

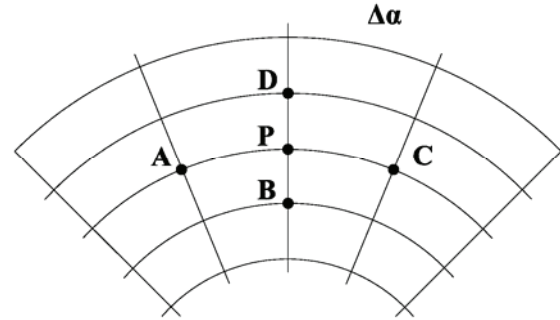


Fig. 2. Internal sampling point.

Now, inserting the derivatives of equations (7) and (8) into equation (4), we get its FD approximation,

$$\begin{aligned} \frac{\phi_A}{r_p^2 \Delta \alpha^2} + \left(\frac{1}{2r_p \Delta r} + \frac{1}{\Delta r^2} \right) \phi_D + \\ + \frac{\phi_C}{r_p^2 \Delta \alpha^2} + \left(\frac{1}{\Delta r^2} - \frac{1}{2r_p \Delta r} \right) \phi_B + \\ - \left(\frac{2}{\Delta r^2} + \frac{2}{r_p^2 \Delta \alpha^2} \right) \phi_P \cong -k_t^2 \phi_P^2 \end{aligned} \quad (9)$$

whose left hand side is the corresponding row of the matrix $\underline{\underline{A}}$ according to equation (3). However, equation (9) cannot be used:

- for the boundary points;
- for the center of the circle, which is a point of singularity for the polar frame;
- for the discretization points in the circle nearest to the center.

Therefore, all the above cases are treated separately in the following subsections.

A. Boundary points

Equation (9) cannot be used for boundary points, where BC of equation (2) must be enforced. In the polar grid used for a RCW, we have two types of boundary points: the radial ones (P in Fig. 3) and the angular ones (P in Fig. 4). The TE boundary condition can be enforced in the same way for both types of boundary points, so we describe it only for a radial one (Fig. 3). The boundary point X in Fig. 3 is not a discretization point. Therefore, the use of Taylor expansion

would require an extrapolation of $\phi(r)$ outside the sampling region, using either ϕ_X or ϕ_Y to enforce the boundary condition $\partial\phi/\partial n = 0$. Actually, we can use two different FD approximations for the normal derivative on the waveguide boundary,

$$\frac{\partial\phi}{\partial n}\Big|_X \simeq \frac{\phi_X - \phi_P}{\Delta r / 2}, \tag{10}$$

or

$$\frac{\partial\phi}{\partial n}\Big|_X \simeq \frac{\phi_Y - \phi_P}{\Delta r}. \tag{11}$$

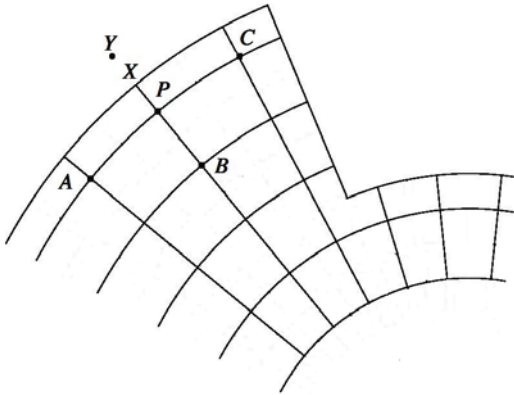


Fig. 3. Geometry pertinent to the first type of boundary point P .

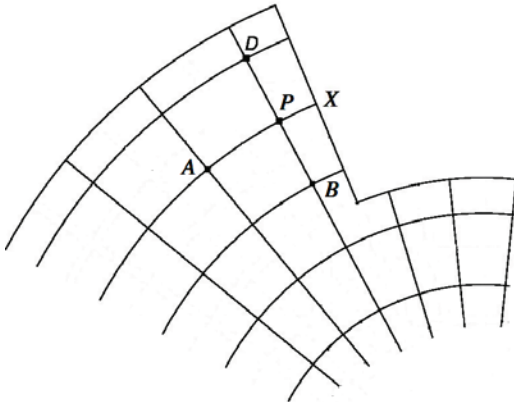


Fig. 4. Geometry pertinent to the second type of boundary point P .

The first one avoids an extrapolation outside the waveguide region, but has an error $O(\Delta r/2)$, whereas the second one is more accurate, with an error $O(\Delta r^2)$, but needs a ϕ value outside the waveguide. So we use the latter, to get $\phi_P = \phi_Y$. As a consequence, equation (7) is replaced by,

$$\begin{aligned} \frac{\partial^2\phi}{\partial r^2}\Big|_P &= \frac{1}{\Delta r^2} \cdot (\phi_B - \phi_P) \\ \frac{\partial\phi}{\partial r}\Big|_P &= -\frac{1}{\Delta r} \cdot (\phi_B - \phi_P) \end{aligned} \tag{12}$$

and equation (9) is replaced by,

$$\begin{aligned} \frac{\phi_A}{r_p^2\Delta\alpha^2} + \frac{\phi_C}{r_p^2\Delta\alpha^2} + \left(\frac{1}{\Delta\alpha^2} - \frac{1}{2r_p\Delta r}\right)\phi_B + \\ - \left(\frac{1}{\Delta r^2} - \frac{1}{2r_p\Delta r} + \frac{2}{r_p^2\Delta\alpha^2}\right)\phi_P \simeq -k_i^2\phi_P^2 \end{aligned} \tag{13}$$

In the same way, for P in Fig. 4 we get,

$$\begin{aligned} \frac{\phi_A}{r_p^2\Delta\alpha^2} + \left(\frac{1}{2r_p\Delta r} + \frac{1}{\Delta r^2}\right)\phi_D + \\ + \left(\frac{1}{\Delta r^2} - \frac{1}{2r_p\Delta r}\right)\phi_B + \\ - \left(\frac{2}{\Delta r^2} + \frac{1}{r_p^2\Delta\alpha^2}\right)\phi_P \simeq -k_i^2\phi_P^2 \end{aligned} \tag{14}$$

For the TM modes, we consider again the radial external point P (Fig. 3). Since, in this case, the BC of equation (2) require $\phi_X = 0$, we can express the potential in B and X using a Taylor approximation,

$$\begin{aligned} \phi_B &= \phi_P + \frac{\partial\phi}{\partial r}\Big|_P \cdot (-\Delta r) + \frac{1}{2} \frac{\partial^2\phi}{\partial r^2}\Big|_P \cdot (-\Delta r)^2 \\ \phi_X &= \phi_P + \frac{\partial\phi}{\partial r}\Big|_P \cdot \left(\frac{\Delta r}{2}\right) + \frac{1}{2} \frac{\partial^2\phi}{\partial r^2}\Big|_P \cdot \left(\frac{\Delta r}{2}\right)^2 \end{aligned} \tag{15}$$

Then, using equation (15) we get

$$\begin{aligned} \phi_B + 2\phi_X &= 3\phi_P + \frac{\partial^2\phi}{\partial r^2}\Big|_P \cdot \frac{3}{4}\Delta r^2 \\ \phi_B - 4\phi_X &= -3\phi_P - \frac{\partial\phi}{\partial r}\Big|_P \cdot 3\Delta r \end{aligned} \tag{16}$$

and, replacing the BC $\phi_X = 0$ in equation (16), we obtain the required derivatives in P ,

$$\begin{aligned} \frac{\partial^2\phi}{\partial r^2}\Big|_P &= \frac{4}{3\Delta r^2} \cdot (\phi_B - 3\phi_P) \\ \frac{\partial\phi}{\partial r}\Big|_P &= -\frac{1}{3\Delta r} \cdot (\phi_B + 3\phi_P) \end{aligned} \tag{17}$$

Finally, after substituting equations (17) and (8) into equation (4) we obtain,

$$\begin{aligned} & \frac{\phi_A}{r_p^2 \Delta \alpha^2} + \frac{\phi_C}{r_p^2 \Delta \alpha^2} + \\ & + \left(\frac{4}{3 \Delta r^2} - \frac{1}{3 r_p \Delta r} \right) \phi_B + \\ & - \left(\frac{4}{\Delta r^2} + \frac{1}{r_p \Delta r} + \frac{2}{r_p^2 \Delta \alpha^2} \right) \phi_P \cong -k_t^2 \phi_P^2 \end{aligned} \quad (18)$$

In the same way, for the point P in Fig. 4, equation (8) becomes,

$$\left. \frac{\partial^2 \phi}{\partial \alpha^2} \right|_P = \frac{4}{3 \Delta \alpha^2} \cdot (\phi_A - 3 \phi_P) \quad (19)$$

and, substituting equations (19) and (7) into equation (4), we get,

$$\begin{aligned} & \frac{4 \phi_A}{3 r_p^2 \Delta \alpha^2} + \left(\frac{1}{2 r_p \Delta r} + \frac{1}{\Delta r^2} \right) \phi_D + \\ & + \left(\frac{1}{\Delta r^2} - \frac{1}{2 r_p \Delta r} \right) \phi_B + \\ & - \left(\frac{2}{\Delta r^2} + \frac{4}{r_p^2 \Delta \alpha^2} \right) \phi_P \cong -k_t^2 \phi_P^2 \end{aligned} \quad (20)$$

B. Center of the circle

The center of the circle (P_0 in Fig. 5) is a point of singularity for the polar frame and no derivatives of ϕ can be computed there. As a consequence, it is not possible to use a Taylor expression using P_0 as initial point. The relevant equation is therefore obtained in a different way, by integrating equation (1) over a circle of radius $\Delta r/4$,

$$\int \nabla_t^2 \phi dS = -k_t^2 \int \phi dS. \quad (21)$$

Then, using the Gauss theorem on equation (21) we obtain,

$$\int_{\Gamma_F} \frac{\partial \phi}{\partial n} \cdot dl = -k_t^2 \int_{S_F} \phi dS \quad (22)$$

where in S_F is the cell surface, and Γ_F is the cell boundary (see Fig. 5).

The left hand side of equation (22) is then computed using the rectangular rule, with $N = 2\pi/\Delta\alpha$ steps. The relevant normal derivatives are computed using a first-order finite difference

approximation. The left hand side of equation (22) is therefore approximated by,

$$\sum_{q=1}^N \frac{(\phi_{A_q} - \phi_{P_0})}{\frac{\Delta r}{2}} \frac{\Delta r \Delta \alpha}{4}. \quad (23)$$

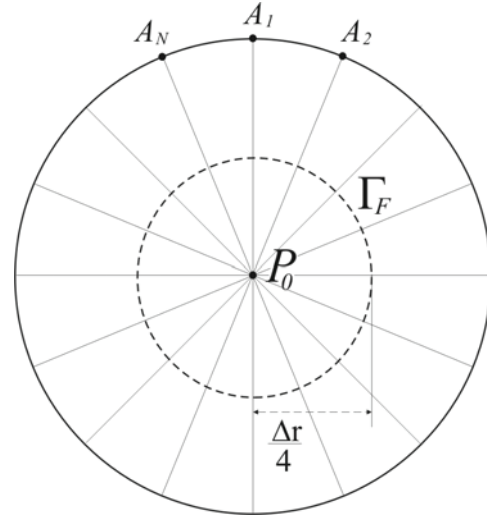


Fig. 5. Central point of the polar framework $|A_1 P_0| = \Delta r/2$.

The right hand side of equation (22) is likely computed as $-k_t^2 \phi_{P_0} \pi (\Delta r/4)^2$ and the discretized form of equation (1) in the center of the circle P_0 is

$$\left(\frac{1}{\pi \left(\frac{\Delta r}{4} \right)^2} \right) \sum_{q=1}^N \frac{(\phi_{A_q} - \phi_{P_0})}{\frac{\Delta r}{2}} \frac{\Delta r \Delta \alpha}{4} = -k_t^2 \phi_{P_0}. \quad (24)$$

C. Points in the circle nearest to the center

Finally, we are left to consider the internal points on the circle at distance $\Delta r/2$ from the center P_0 (see Fig. 6). For these points we can express the potential ϕ using a second order Taylor expression as,

$$\begin{aligned} \phi_D &= \phi_P + \left. \frac{\partial \phi}{\partial r} \right|_P (-\Delta r) + \left. \frac{1}{2} \frac{\partial^2 \phi}{\partial r^2} \right|_P \Delta r^2 \\ \phi_{P_0} &= \phi_P + \left. \frac{\partial \phi}{\partial r} \right|_P \left(\frac{\Delta r}{2} \right) + \left. \frac{1}{2} \frac{\partial^2 \phi}{\partial r^2} \right|_P \left(\frac{\Delta r}{2} \right)^2. \end{aligned} \quad (25)$$

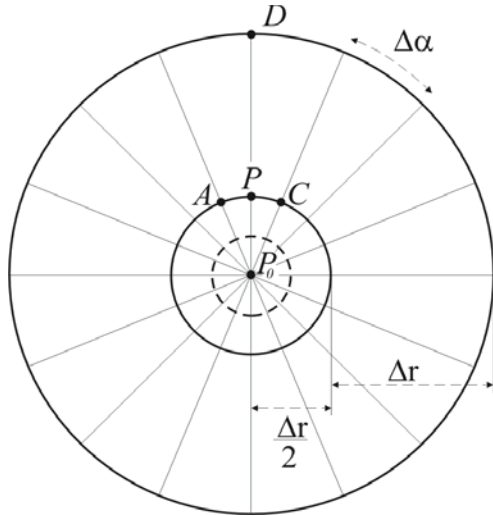


Fig. 6. Internal point P on the circle at distance $\Delta r/2$ from the center P_0 .

Then, we obtain

$$\begin{aligned} \phi_D + 2\phi_{P_0} &= 3\phi_P + \left. \frac{\partial^2 \phi}{\partial r^2} \right|_P \frac{3}{4} \Delta r^2, \\ \phi_D - 4\phi_{P_0} &= -3\phi_P - \left. \frac{\partial \phi}{\partial r} \right|_P 3\Delta r \end{aligned} \quad (26)$$

and the derivative in P is approximated by,

$$\begin{aligned} \left. \frac{\partial^2 \phi}{\partial r^2} \right|_P &= \frac{4}{3\Delta r^2} (\phi_D + 2\phi_{P_0} - 3\phi_P) \\ \left. \frac{\partial \phi}{\partial r} \right|_P &= -\frac{1}{3\Delta r} (\phi_D - 4\phi_{P_0} + 3\phi_P) \end{aligned} \quad (27)$$

After substituting equations (27) and (8) in to equation (4), we obtain

$$\begin{aligned} &\frac{\phi_A}{r_p^2 \Delta \alpha^2} + \left(\frac{4}{3\Delta r^2} - \frac{1}{3r_p \Delta r} \right) \phi_D + \\ &+ \frac{\phi_C}{r_p^2 \Delta \alpha^2} + \left(\frac{8}{3\Delta r^2} + \frac{4}{3r_p \Delta r} \right) \phi_{P_0} + \\ &- \left(\frac{4}{\Delta r^2} + \frac{1}{r_p \Delta r} + \frac{2}{r_p^2 \Delta \alpha^2} \right) \phi_P \cong -k_i^2 \phi_P^2 \end{aligned} \quad (28)$$

III. VALIDATION OF THE FDFD PROCEDURE

Since the cut-off frequencies scale as the inverse of the waveguide size, in all the

simulations presented in this section we will consider all dimensions (and Δr , too) normalized to the radius R of the circular waveguide. The FDFD procedure has been assessed against a commercial FIT software (CST Microwave Studio) and a FEM software (Ansys HFSS) both in terms of accuracy and effectiveness.

Since analytical eigenvalues are not available for RCWs with ridges of arbitrary dimension and position within the cross-sectional area, we have decided to test the accuracy and effectiveness of our procedure using a 270° sectorial waveguide, which is actually a limit case of the RCW described in Fig. 1 with a single ridge of dimension $D_1 = R$, and $\Psi_1 = 90^\circ$. This example has been chosen since it retains the more critical ridge feature, namely the convex wedge, which could affect the accuracy of numerical techniques. Therefore, the eigenvalues of the first five modes, computed either with the FDFD procedure or with CST and HFSS, have been compared with the analytical eigenvalues [28]. Actually, the FDFD procedure is able to reach (with a suitable discretization) a very high accuracy (see Tables I and II), so the true point to assess is its effectiveness. To do this, we have required, for both our FDFD, CST, and HFSS, that the amplitude of the relative error with respect to analytical eigenvalues is less than 0.1% or 0.02%. Then, we have investigated the computational resources needed by these simulations, which are summarized in Tables I and II. It is worth noting that both CST and HFSS require a minimum computational time which, for the computation of the first five eigenvalues, is respectively 48 sec and 14 sec, since the initial mesh is set automatically by these programs (these values are reported in bold characters in Tables I and II). In Figs. 7 and 8 the convergence behavior of the eigenvalue of the first TE mode (TE_1) and of the first TM mode (TM_1) is also show. As apparent from Tables I and II, and Figs. 7 and 8, the computational time required by the FDFD procedure is significantly smaller than the one of CST Microwave Studio and Ansys HFSS (on a PC with 2 CPU Intel(R) Xeon(R) CPU E5504 @ 2.00 GHz, 8 core, Ram 48 GB).

Table I: Computational resources required to achieve a relative error less than 0.1 % with respect to analytical values.

Mode	Analytical Eigenvalue	FDFD			CST		HFSS		
		T [sec]	Sampling Points	Step ($\Delta\alpha$, Δr)	T [sec]	Tetrahedra	T [sec]	Tetrahedra	
TE ₁	1.4012180	0.8	27000	1°, 0.00995	53	10767	22	1465	Fig. 7
TE ₂	2.2577552	0.1	5400	1°, 0.04878	48	6143	14	1206	Not shown
TE ₃	3.0542369	0.1	5400	1°, 0.04878	48	6143	14	1206	Not shown
TM ₁	3.3756107	0.8	27000	1°, 0.00995	48	6143	26	1612	Fig. 8
TE ₄	3.8232239	0.1	5400	1°, 0.04878	48	6143	14	1206	Not shown

Table II: Computational resources required to achieve a relative error less than 0.02 % with respect to analytical values.

Mode	Analytical Eigenvalue	FDFD			CST		HFSS		
		T [sec]	Sampling Points	Step ($\Delta\alpha$, Δr)	T [sec]	Tetrahedra	T [sec]	Tetrahedra	
TE ₁	1.4012180	3.3	94500	1°, 0.00285	65	15584	163	5492	Fig. 7
TE ₂	2.2577552	0.2	9450	1°, 0.02817	48	6143	14	1206	Not shown
TE ₃	3.0542369	0.1	5400	1°, 0.04878	48	6143	14	1206	Not shown
TM ₁	3.3756107	3.8	108000	1°, 0.00250	53	10767	> 1000	> 20000	Fig. 8
TE ₄	3.8232239	0.1	5400	1°, 0.04878	48	6143	14	1206	Not shown

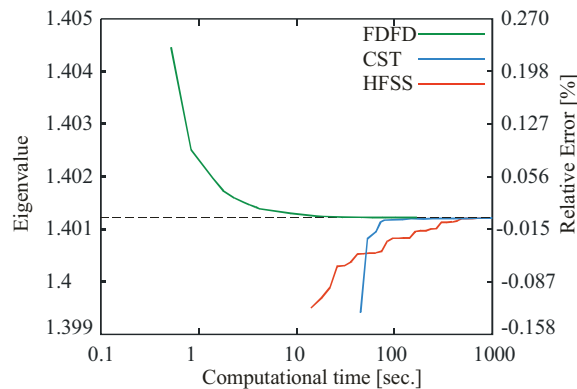


Fig. 7. Convergence behavior of the eigenvalue of the first TE mode. The dashed line represents the analytical value, and the relative error on the right is computed with respect to this value.

A further test to demonstrate the accuracy and effectiveness of the proposed FDFD procedure has been made using a circular waveguide with four ridges (see Fig. 9 and Table III). In this case, both a large ridge and very close and small ridges has been considered in order to assess the robustness of our procedure against a very dense mesh. Analytical results are not available for the structure in Fig. 9, therefore, in this case, our FDFD procedure has been assessed by comparison with the results of CST and HFSS. Due to the

particular geometry and relative position of the ridges #1, #2, and #3 in Fig. 9, a dense mesh is required and, therefore, the angular step of the FDFD grid has been selected equal to $\Delta\alpha = 0.25^\circ$, whereas the radial step Δr of FDFD and the mesh density of CST and HFSS have been varied to study the convergence.

In Fig. 10 the convergence behavior of FDFD compared to CST and HFSS is reported for a number of selected modes. Since all those programs use different discretization strategies, we have set the computational T time as independent variable. As apparent, the FDFD procedure is significantly faster than CST and HFSS, both for lower or higher order modes, either TE or TM. Further comments on Fig. 10 are in order. As a matter of fact, all programs considered have a hardware limit on the discretization size. This limit on CST (and also FDFD) depends on the required number of modes to be computed. For the structure in Fig. 9, we decided to solve the eigenvalue problem for the first 100 modes (61 TE and 39 TM). On the other hand, HFSS does not allow to compute more than 25 modes, so that its limit has been evaluated in this case. Moreover, both CST and HFSS have also a (quite large) minimum computational time since they set automatically the initial mesh. Table IV reports

both the minimum computational times and the computational times at the hardware limit, together with the corresponding meshes.

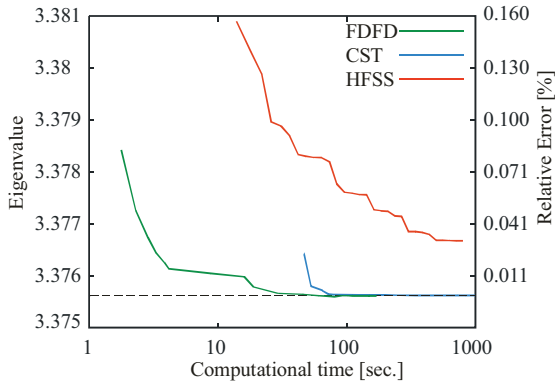


Fig. 8. Convergence behavior of the eigenvalue of the first TM mode. The dashed line represents the analytical value, and the relative error on the right is computed with respect to this value.

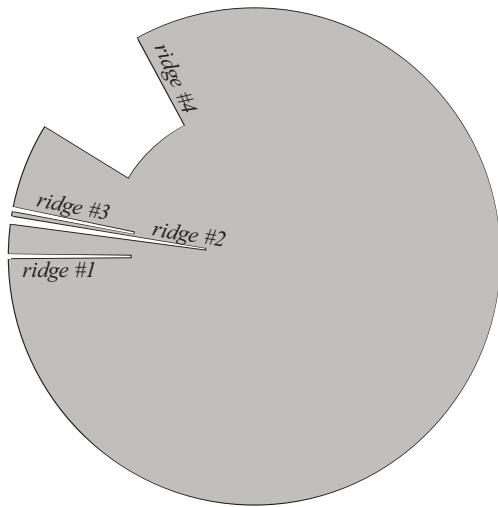


Fig. 9. Circular waveguide with four ridges. The geometry of the ridges is reported in Table III. Waveguide radius $R = 1$ (in normalized units). The angular spacing between ridge #1 and ridge #2 is 7° , between ridge #2 and ridge #3 is 1° , and between ridge #3 and ridge #4 is 20° .

Table III: Geometry of the ridges in Fig. 9.

Ridge	Radial width D_i	Angular width Ψ_i
#1	0.5	1°
#2	0.8	2°
#3	0.5	1°
#4	0.4	30°

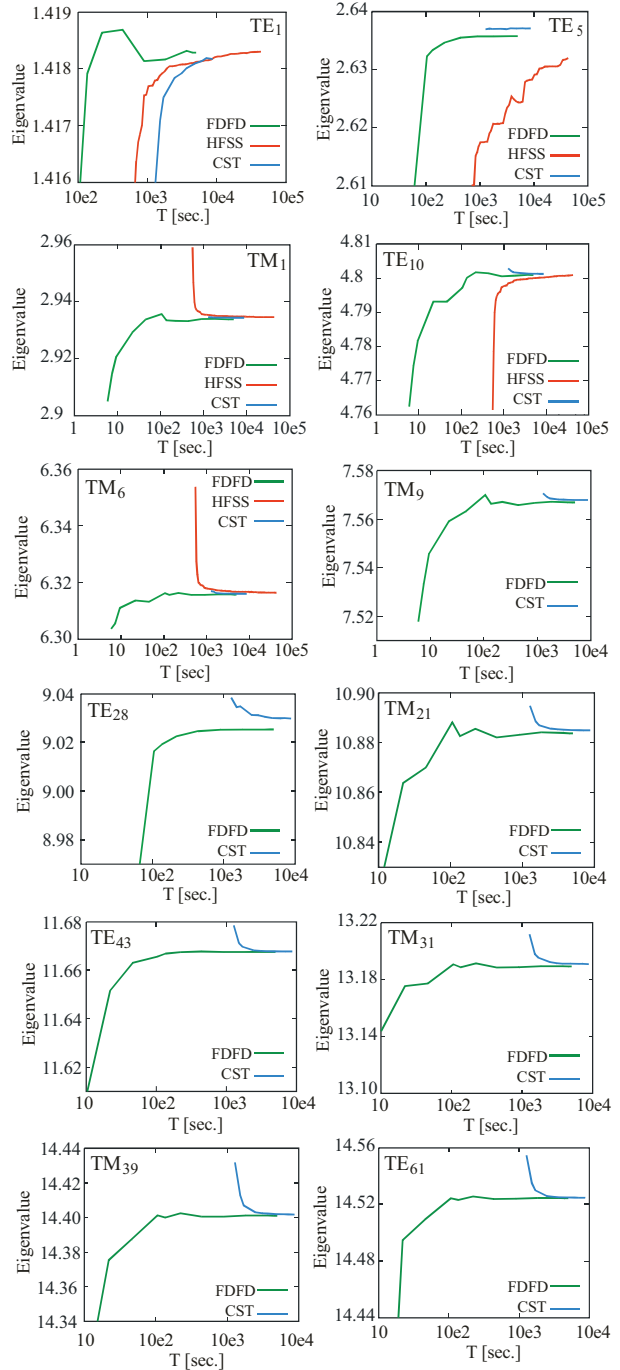


Fig. 10. Convergence behavior of the eigenvalues of selected TE and TM modes. The selected modes are reported with black dots in the curves in Fig. 11.

Table IV: Computational time (T) limits and mesh limits for the computation of the first 100 eigenvalues (either TE or TM) on a PC with 2 CPU Intel(R) Xeon(R) CPU E5504 @ 2.00 GHz, 8 core, Ram 48 GB.

	FDFD	CST	HFSS
Sampling Points at hardware limit	$10.3 \cdot 10^6$	-	-
Tetrahedra at hardware limit	-	501409	894798
T [sec] at hardware limit	5018	8760	43393
Initial mesh (Tetrahedra)	-	17701	9111
Minimum T [sec] (initial mesh)	-	1275	552

In Fig. 11, the relative difference of the eigenvalues computed with CST and HFSS with respect to those computed with the FDFD procedure is shown, using the densest available mesh (the one at the hardware limit, see Table IV). The comparison with HFSS is not complete because this software allows to compute a maximum of 25 modes (in this case 18 TE and 7 TM, since TE and TM are computed together). The results presented in Fig. 11, demonstrate the accuracy of our FDFD procedure both for TE and TM modes. Actually, the difference of the FDFD results with respect to HFSS is lower than 0.14 % (for the first 25 modes), whereas the difference with respect to CST results is lower than 0.05 % (for all the computed 100 modes).

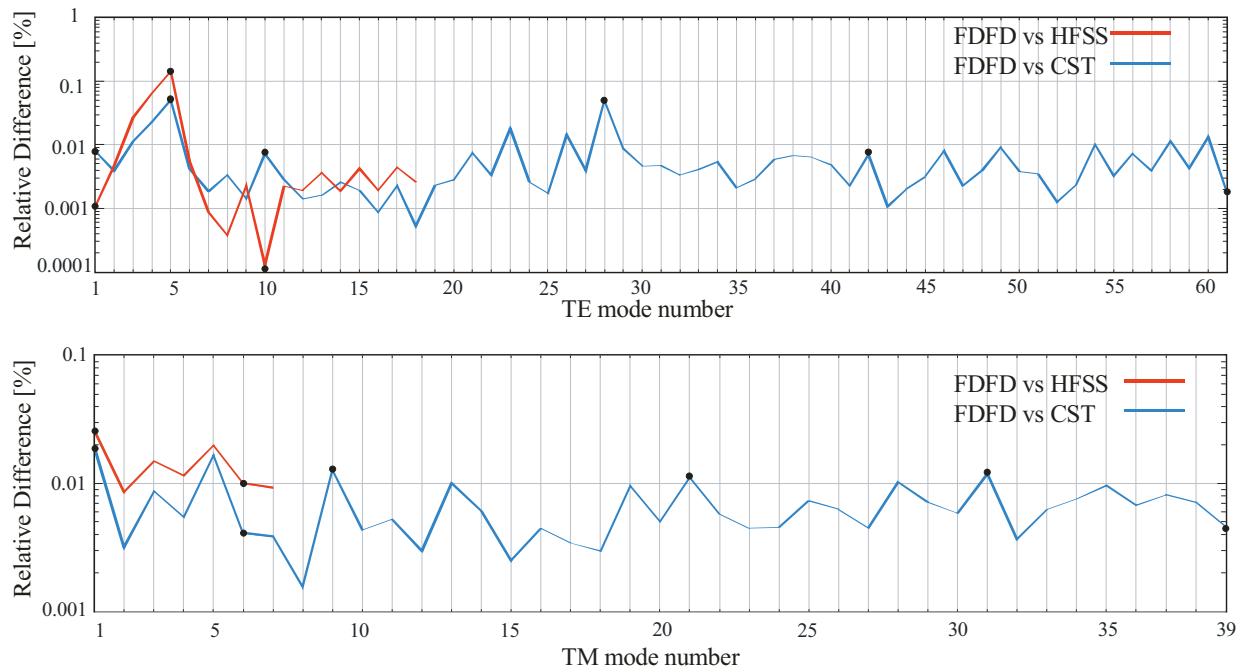


Fig. 11. Relative difference between the eigenvalues computed with the FDFD procedure and those computed with CST or HFSS, computed with the meshes reported in Table IV.

IV. CONCLUSION

We have proposed a finite difference approach to the computation of the modes of circular ridged waveguides. A polar mesh has been used in order to avoid staircase approximations of the boundary. The presented procedure allows to analyze a RCW, with an arbitrary number of ridges of arbitrary dimensions, with a computational burden and accuracy, which is independent both of the total cross-sectional area occupied by the ridges

and of the number of ridges. The proposed approach has been validated by comparison with the results of CST Microwave Studio and Ansys HFSS, showing a significant reduction of the computational time.

ACKNOWLEDGMENT

Alessandro Fanti gratefully acknowledges Sardinia Regional Government for the financial support of her Post Doctoral fellowship (P.O.R.

Sardegna F.S.E. Operational Programme of the Autonomous Region of Sardinia, European Social Fund 2007-2013 - Axis IV Human Resources, Objective 1.3, Line of Activity 1.3.1.).

REFERENCES

- [1] F. Canatan, "Cutoff wavenumbers of ridged circular waveguides via Ritz-Galerkin approach," *Electronic Letters*, vol. 25, pp. 1036-1038, Aug. 1989.
- [2] A. Williams and A. Atia, "Dual-mode canonical waveguide filters," *IEEE Transactions on Microwave Theory and Techniques*, vol. 25, no. 12, pp. 1021-1026, Dec. 1977.
- [3] R. Behe and P. Brachat, "Compact duplexer-polarizer with semicircular waveguide," *IEEE Trans. Antennas Propagat.*, vol. 39, pp. 1222-1224, Aug. 1991.
- [4] B. de la Filolie and R. Vahldieck, "Coaxial and circular waveguide band-pass filters using printed metal inserts," *IEEE MTT-S Int. Microwave Symp. Dig.*, pp. 905-908, 1992.
- [5] J. Huang, R. Vahldieck, and H. Jin, "Computer-aided design of circular ridged waveguide evanescent-mode bandpass filters using the FDTLM method," *IEEE MTT-S Int. Microwave Symp. Dig.*, pp. 459-462, 1993.
- [6] U. Balaji and R. Vahldieck, "Mode matching analysis of circular-ridged waveguide discontinuities," *IEEE Trans. Microwave Theory Tech.*, vol. 46, pp. 191-195, Feb. 1998.
- [7] A. Wexler, "Solution of waveguide discontinuities by modal analysis," *IEEE Trans. Microwave Theory and Techniques*, vol. 15, pp. 508-517, Sep. 1967.
- [8] R. Collin, *Foundations for Microwave Engineering*, 2nd Ed. New York: McGraw-Hill, Sect. 3.18, 1992.
- [9] M. Abramowitz and I. Stegun, *Handbook of Mathematical Functions*, (Applied Mathematics Series 55), Washington, DC: NBS, pp. 32-33, 1964.
- [10] D. Al-Mukhtar and J. Sitch, "Transmission-line matrix method with irregularly graded space," *IEE Proc.*, vol. 128, no. 6, pp. 209-305, Dec. 1981.
- [11] P. Daly, "Polar geometry waveguides by finite element methods," *IEEE Trans. Microwave Theory Tech.*, vol. 22, pp. 202-209, 1974.
- [12] B. Dillon and A. Gibson, "Triple-ridged circular waveguides," *Journal of Electromag. Waves Applicat.*, vol. 9, pp. 145-156, 1995.
- [13] A. Ornar, A. Jostingmeier, C. Rieckmann, and S. Lutgert, "Application of GSD technique to the analysis of slot-coupled waveguides," *IEEE Trans. Microwave Theory Tech.*, vol. 42, pp. 2139-2148, Nov. 1994.
- [14] Y. Tao, Z. Shen, and G. Liu, "Efficient analysis of quadruple corner-cut ridged circular waveguide by hybrid mode-matching boundary element method," *IEEE Trans. Magn.*, vol. 45, pp. 1076-1079, 2009.
- [15] M. Chen, N. Tsandoulas, and F. Willwerth, "Modal characteristics of quadruple-ridged circular and square waveguides," *IEEE Trans. Microwave Theory Tech.*, vol. 22, pp. 801-804, Aug. 1974.
- [16] W. Sun and C. Balanis, "Analysis and design of quadruple ridged waveguides," *IEEE Trans. Microwave Theory Tech.*, vol. 42, pp. 2201-2207, Dec. 1994.
- [17] S. Yu and J. Bornemann, "Classical eigenvalue mode spectrum analysis of multiple ridged rectangular and circular waveguides for the design of narrowband waveguide components," *Int. J. Numer. Model.*, vol. 22, pp. 395-410, April 2009.
- [18] S. Yu and J. Bornemann, "Evanescent-mode filters with arbitrarily positioned ridges in circular waveguide," *IEEE Pacific Rim Conference on Communications, Computers, and Signal Processing*, 2011.
- [19] K. Morton and D. Mayers, *Numerical Solution of Partial Differential Equations: An Introduction*, Cambridge University Press, Chapter 6, 2005.
- [20] F. Alimenti et al. "Efficient analysis of waveguide components by FDTD combined with time domain modal expansion," *IEEE Microw. Guided Wave Lett.*, vol. 5, pp. 351-353, Oct. 1995.
- [21] A. Fanti, G. Mazzarella, G. Montisci, and G. Casula, "Computation of the modes of elliptic waveguides with a curvilinear 2D frequency-domain finite-difference approach," *Progress In Electromagnetics Research M*, vol. 26, pp. 69-84, 2012.
- [22] A. Fanti and G. Mazzarella, "A finite difference polar-cartesian grid approach for mode computation in rounded-end waveguides," *ACES Journal*, vol. 26, no. 9, 2011.
- [23] O. Rübenkönig, *The Finite Difference Method (FDM) - An Introduction*, Albert Ludwigs, University of Freiburg, 2006.
- [24] G. Golub and C. Van Loan, *Matrix Computation*, Johns Hopkins University Press, 1989.
- [25] T. Itoh, *Numerical Techniques for Microwave and Millimeter-wave Passive Structures*, Chapter 2, Section 9.1, Wiley, New York, 1989.
- [26] J. Beggs and R. Luebbers, "Numerical analysis of staircasing effects on cutoff frequencies for FDTD modeling of circular waveguides," *Antennas and Propagation Society International Symposium. AP-S Digest*, pp. 547-549, 1993.

- [27] R. LeVeque, *Finite Difference Methods for Ordinary and Partial Differential Equations*, Philadelphia, PA: SIAM, Chapter 3, 2007.
- [28] R. Harrington, *Time-harmonic Electromagnetic Fields*, IEEE Press, John Wiley Interscience, New York, 2001.



Alessandro Fanti received the Laurea degree in Electronic Engineering and Ph.D. degree in Electronic Engineering and Computer Science from the University of Cagliari, Cagliari, Italy, in 2006 and 2012, respectively. He currently holds a

post-doc scholarship for design of microwave components. His research activity involves the use of numerical techniques for modes computation of guiding structures.



Giorgio Montisci received the Laurea degree (summa cum laude) in Electronic Engineering and Ph.D. degree in Electronic Engineering and Computer Science from the University of Cagliari, Cagliari, Italy, in 1997 and 2000, respectively. Since November

2000, he is Assistant Professor of electromagnetic field at the Dipartimento di Ingegneria Elettrica ed Elettronica, University of Cagliari, teaching courses in electromagnetics and microwave engineering. His research activity is mainly focused on analysis and design of waveguide slot arrays, microwave holographic techniques for the diagnostic of large reflector antennas, numerical methods in electromagnetics, and printed antennas. He is author or coauthor of about 40 papers in international journals and Reviewer for EM Journals.



Giuseppe Mazarella graduated Summa with Laude in Electronic Engineering from the Università "Federico II" of Naples in 1984 and obtained the Ph.D. in Electronic Engineering and Computer Science in 1989. In 1990, he became Assistant Professor at the

Dipartimento di Ingegneria Elettronica at the Università "Federico II" of Naples. Since 1992, he is with the Dipartimento di Ingegneria Elettrica ed Elettronica of the Università di Cagliari, first as Associate Professor and then, since 2000, as full Professor, teaching courses

in Electromagnetics, Microwave, Antennas and Remote Sensing. His research activity has focused mainly on: efficient synthesis of large arrays of slots, power synthesis of array factor, microwave holography techniques for the diagnostic of large reflector antennas, use of evolutionary programming for inverse problems solving. He is author (or co-author) of about 50 papers in international journals, and is a reviewer for many EM journals.



Giovanni Andrea Casula received the Laurea degree (summa cum laude) in Electronic Engineering and Ph.D. degree in Electronic Engineering and Computer Science from the Università di Cagliari, Cagliari, Italy, in 2000 and 2004, respectively. Since March 2006, he

is an Assistant Professor of electromagnetic field and microwave engineering at the Dipartimento di Ingegneria Elettrica ed Elettronica, University of Cagliari. His current research interests are in the field of synthesis, analysis and design of wire, patch, and slot antennas. Dr. Casula serves as reviewer for several international journals and is a member of the Italian Electromagnetic Society (SIEm).

Extended Scheme using Equivalent Dipoles for Characterizing Edge Currents Along a Finite Ground Plane

C. Obiekezie, D. W. Thomas, A. Nothofer, S. Greedy, L. R. Arnaut, and P. Sewell

Electrical Systems and Optics Research Division

University of Nottingham, Nottingham, UK

{eexcso, dave.thomas, angela.nothofer, steve.greedy, luk.arnaut, phil.sewell}@nottingham.ac.uk
chijiokeobiekezie@gmail.com

Abstract — For the assessment of radiated fields, a simplified analytical solution that approximates the effects of the currents induced at the edges of a finite ground plane is presented. These edge currents are induced by the actual current sources on the plane. This method can be used in characterizing the electromagnetic (EM) emission from any practical PCB and avoids the need for using high-frequency techniques in evaluating effects due to diffraction.

Index Terms — Analytical solution, diffraction, edge currents, equivalent dipole model, and multipole expansion.

I. INTRODUCTION

The increasing complexities of electronic circuits and the need for a suitable way of characterizing their electromagnetic (EM) performance has become a major problem in electromagnetic compatibility (EMC). In this work, equivalent infinitesimal dipoles are used for characterizing the EM properties of a PCB. In [1-6] a similar principle was used to characterize emissions from radiating sources above an infinite ground plane. In [7-9], radiations from the edges of the PCB, which are due to the via transitions of high speed signals, have been identified as a significant contributor to the total emissions from the PCB at a given observation point. Also these edge radiations increases as the emission sources are located close to the edges of the PCB. This makes the techniques adopted in [1-6] insufficient in representing all the sources of emissions from a practical PCB of finite size and according to [10]

further deteriorates as the emission sources are located close to the edges. Therefore to develop a model that can fully represent a real life scenario, all the possible sources of the emissions in the PCB need to be taken into consideration. Often, this does not lead to a close form solution. In particular, this greatly increases the mathematical complexities in evaluating the contribution of diffraction to the total emission around a PCB finite ground plane. Though there are classical solutions that offer good approximation for diffraction problems [11, 12], however, they can be complicated analytically and often lead to a complex integral equations. In [13] a hybrid technique that is based on equivalent dipole model and numerical techniques was used to characterize emissions from an enclosure with an aperture.

The uniqueness of our approach is that it offers an analytical solution, based on the equivalent dipole model only, that can approximate the diffraction effects with sufficient degree of accuracy with less than -10dB error. In this approach, equivalent dipoles are aligned on and along the edges of the ground plane to emulate the radiation characteristics of the currents induced at these edges.

II. THEORY

A. Field equivalence principle

This approach is based on the field equivalence principle [14, 15] as introduced by Schelkunoff in 1936 [16] and is equivalent to Huygens' principle [17]. In this method, the actual sources are replaced by fictitious sources placed

on an arbitrary surface surrounding it, producing the same fields outside the bounding surface. The sources are equivalent *inside* a region insofar as they produce the same amount of fields inside that region.

The equivalent sources are now computed through Love's equivalent principle [18] and taking into consideration the boundary conditions for ideal conductor as,

$$\vec{J}_{eq} = \hat{n} \times H_1 \quad (1)$$

$$\vec{M}_{eq} = \hat{n} \times E_1 \quad , \quad (2)$$

where J_{eq} and M_{eq} are the equivalent electric and magnetic sources, respectively. From equations (1) and (2), only the tangential components of the electric, E_t or the magnetic, H_t fields are required in order to compute the equivalent sources (or fictitious currents). Furthermore, in our work, these sources are modeled as infinitesimal dipoles.

B. Multipole expansion of dipole

Through multipole expansion [19] a simple source, D can be approximately modeled by 3 orthogonal electric and (or) magnetic dipole,

$$D = \left(D_x, D_y, D_z \right) \quad (3)$$

where D_x , D_y , and D_z are the 3 orthogonal dipoles along the x , y , and z coordinates. This has been applied in [20] and [21] and the agreement with measurements was good. The solution is further derived as follows:

The magnetic field H_e from an electric dipole is determined from equation (4),

$$H_e = \frac{1}{\mu} \nabla \times \vec{A} \quad (4)$$

and for a magnetic dipole as

$$H_m = -j\omega F - \frac{j}{\omega\mu\epsilon} \nabla \left(\nabla \cdot \vec{F} \right) \quad , \quad (5)$$

where \vec{A} and \vec{F} are the magnetic and electric vector potentials respectively and μ and ϵ the permeability and permittivity of the surrounding media, respectively. For an electric dipole at (x_0, y_0, z_0) oriented along the z -axis, the magnetic (x, y, z) field at a distance r is given by,

$$H_x = -p^z \frac{jke^{-jkr}}{4\pi r^2} \left[1 + \frac{1}{jkr} \right] (y - y_0) \quad (6)$$

$$H_y = -p^z \frac{jke^{-jkr}}{4\pi r^2} \left[1 + \frac{1}{jkr} \right] (x - x_0) \quad , \quad (7)$$

$$H_z = 0. \quad (8)$$

Whereas for a magnetic dipole at (x_0, y_0, z_0) oriented in the z -direction,

$$H_x = M^z \frac{jke^{-jkr}}{4\pi r^4} (x - x_0) \left(z - z_0 \right) \left(jkr + 3 + \frac{3}{jkr} \right) \quad (9)$$

$$H_y = M^z \frac{jke^{-jkr}}{4\pi r^4} (y - y_0) \left(z - z_0 \right) \left(jkr + 3 + \frac{3}{jkr} \right) \quad , \quad (10)$$

$$H_z = M^z \frac{jk^2 e^{-jkr}}{4\pi r} \left[\frac{(z - z_0)^2}{r^2} \left(j + \frac{3}{kr} + \frac{3}{jk^2 r^2} \right) - \left(j + \frac{3}{kr} + \frac{3}{jk^2 r^2} \right) \right] \quad (11)$$

where p^z and M^z are the radiated electric and magnetic dipole moments, respectively. By taking into account the contributions from other dipole coordinates (x and y), we can formulate the relationship between the magnetic field and the dipole moments as,

$$\begin{bmatrix} H_x \\ H_y \\ H_z \end{bmatrix} = \begin{bmatrix} G_x^x G_y^x G_z^x \\ G_y^x G_y^y G_z^y \\ G_x^z G_y^z G_z^z \end{bmatrix} \begin{bmatrix} D_x \\ D_y \\ D_z \end{bmatrix} \quad (12)$$

or, compactly,

$$[H] = [G][D] \quad . \quad (13)$$

In this approach, the field H is extracted from complete circuit through simulation or measurement. Therefore once the matrix G , which is a form of the dyadic Green's function is computed, the moment vector for the dipoles represented by D can then be solved through the solution to the inverse problem. This dipole moment vector can be electric, magnetic, or a combination of both.

C. Solution to inverse problem

In principle, a sufficient number of sampling points are required to properly compute the moments of the dipoles i.e.,

$$N^s \geq N^m,$$

where N^s and N^m are the total number of sampling points and dipoles, respectively. For

$$N^s = N^m,$$

the inverse problem involves a square matrix and basic techniques like Gaussian elimination can be used. But this becomes unfeasible as the size of the problem increases, thereby increasing the computational cost of this solution. In practice,

$$N^s \gg N^m,$$

leading to an over determined solution. Furthermore, as the positions of the infinitesimal dipoles are quite close, their dyadic Greens function with respect to the observation points are highly correlated. This accounts for the increase in the condition number of the matrix i.e.,

$$\text{cond}(A) = \infty.$$

For this reason, a more robust technique is required in solving this ill-posed and near singular inverse problem. So for a linear least square problem [22],

$$\min_x \|Ax - b\|_2, A \in R^{m \times n}, m > n \quad (14)$$

the singular value decomposition (SVD) technique have been demonstrated to offer a unique solution for the inverse problem. The SVD of A is given by,

$$\text{SVD}(A) = U \Sigma V \quad (15)$$

in such a way that they also satisfy,

$$A = U \Sigma V^T \quad (16)$$

where $U(U^T U = I)$ and $V(V^T = V^{-1})$ are matrices with orthonormal columns and Σ is a non-singular diagonal matrix.

In the previous work [1-3] where an infinite ground plane was assumed, only the direct and reflected fields were needed in computing the G matrix. This method achieved a good accuracy in general. However, this accuracy reduces significantly when using the above method to model sources above a finite plane and worsens as the sources are located closer to the edges of the plane. This is due to the scattering at the edges leading to diffractions, whence the image theory (used in approximating the effect of the ground plane) is no longer adequate because of the

additional currents induced at the edges. To simplify this approach, a number of equivalent passive dipoles are placed around the edges of the ground plane to emulate the current induced at these edges due to the active sources on the structure. Therefore, the total field, H_T at any observation point is assumed to be a result of the contributions from the passive, H_{edge} and active dipoles, H_{source} . The set of passive dipoles are combined with the active dipoles (i.e., representing the active sources) to generate the dipole vector required for the model. Their relationship with the total field, H_T is formulated as,

$$H_T = H_{source} + H_{edge} \quad (17)$$

$$[H_T] = [G][D_{source}] + [G][D_{edge}], \quad (18)$$

$$H_T = [G]([D_{source}] + [D_{edge}]). \quad (19)$$

The expression in equation (19) is comparable to equation (13) where D comprises the D_{source} and the D_{edge} . The model for the active dipoles comprises the direct wave and its image while the passive dipoles are modeled in free space. To show the viability of this approach, a simple PCB tract comprising, a simple copper strip (L shape transmission line) is simulated on a dielectric over a finite ground plane. This approach was used to reproduce the fields from the structure at the simulated planes and also predict fields at other planes.

III. SIMULATION PROCEDURE

A. Diffraction effects

In addition to the model used in [1, 2], the finiteness of a ground plane also results to scattering at its edges. These scattering are due to currents induced at the edges of the ground plane by the actual electromagnetic (EM) sources on the device under test (DUT). This is also known as diffraction. This diffraction effects if ignored as in [1-6], degrades the performance of the equivalent dipole modeling (EDM) especially when the EM sources are located closer to the edges. Furthermore, to evince this effect, a rectangular PCB, with a simple L trace of $30\text{mm} \times 70\text{mm}$, was simulated using an MoM-based numerical code [23]. Firstly, the simple L trace was positioned at the centre of a large perfect electric conducting (PEC) ground plane with dimension $100\text{mm} \times$

160mm as shown in Fig. 1 (a). This is then repeated with the L trace positioned close to the bottom-right of the PEC as shown in Fig. 1 (b). A dielectric surface of the same dimension as the PEC ($\epsilon = 4.6$) with a thickness of 1.5 mm was placed in between the trace and the PEC to represent the typical FR4 properties. Figure 1 shows the physical layout of the two cases being considered here.

For uniformity, the same discretisation as shown was used and the trace was excited with 8dBmW signal at the shorter leg while the longer leg was terminated with a 50 Ω load in both cases. The load termination ensured continuous wave propagation in one direction. The transverse magnetic field computation in the xy-plane was carried out over a range of frequencies. For consistency, the same sampling resolution and sampling height of 4 mm and 10 mm, respectively were maintained for both cases.

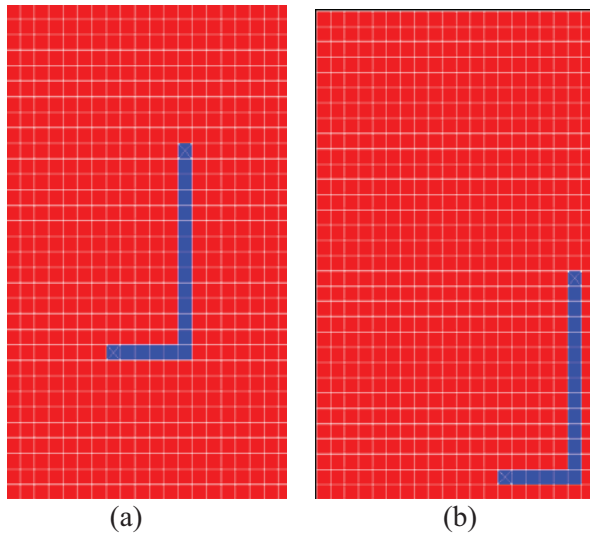


Fig. 1. Physical layout of a simple PCB with an L trace positioned at different locations above its dielectric layer.

This sampling resolution required was deduced from the expression [24],

$$\Delta s = \frac{\lambda}{2\sqrt{1 + \left(\frac{\lambda}{d}\right)^2}}. \quad (20)$$

This was also found to be sufficient for the frequency range considered in this experiment. The transverse fields were then imported into the dipole model and were used to determine the

moment vector for the equivalent dipoles required to reproduce the same fields. Similar to the approach in [1, 2], the emission of the EM sources were characterized using a number of infinitesimal dipoles, with 10 mm uniform separation, whose images accounted for the reflection due to the PEC. For the two cases, the same number of dipoles and dipole resolution were used. This is to enable clear comparison as the error in equivalent dipole modeling tends to reduce with the increase in the number of dipoles.

Figure 2 compares the error in reproducing the transverse magnetic fields using EDM for the two cases shown in Fig. 1. The error significantly increases in case 2 (i.e., Fig. 1 (b)) and has been shown to be consistent for all the frequencies considered in this problem. The error was computed as the average of the r.m.s error, ζ in reproducing the two transverse fields as given in the expression,

$$\zeta = \sqrt{\frac{\sum_{i=1}^N (H_i^s - H_i^m)^2}{\sum_{i=1}^N H_i^s{}^2}} \quad (21)$$

where H_i^s, H_i^m , and N are the magnetic fields from the numerical code, magnetic field reproduced using the EDM and the total number of sampling points, respectively. This increase in error, as the excited trace or the current sources are located close to the edge is often observed in complex PCBs due to diffraction. This error increases as the number of these sources increase in such a way that the image of the active sources are no longer sufficient to accurately characterize all the scattering effects due to the electric conducting ground plane. Edge dipoles are then introduced as passive sources to emulate the behaviors of the currents induced at the edges of the PEC ground plane by the actual sources. Again, to clearly distinguish the contributions of these passive dipoles from active dipoles used to characterize the active sources, another experiment was carried out.

B. Passive dipoles

To understand the influence of the passive dipoles, the same fields as in the two problems in section III were modeled using the EDM. However, unlike in the previous modeling, a number of infinitesimal dipoles were then introduced and positioned at the edges of the PEC

ground plane. Sufficient number is required so as to fully emulate the current excitation at the edges. Here infinitesimal dipoles of 10mm uniform separation was used. This is in addition to the number of infinitesimal dipoles of 10mm uniform separation, used previously to characterize the actual sources.

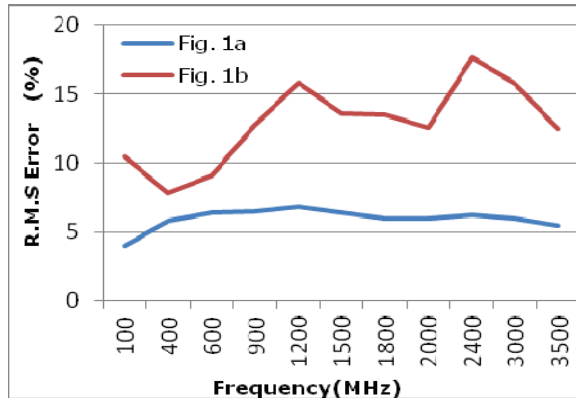


Fig. 2. R.M.S error for the different positions of the L trace.

It is necessary to distinguish the influence of the edge dipoles from just any additional dipole used for characterizing the active sources. It is expected that the increase in the number of dipoles reduces the error. However, it is important to show that the edge dipoles particularly represent the effects due to diffraction hence will only improve cases that are affected by diffraction.

The transverse magnetic fields were computed at the xy-plane for the two cases. These were then reproduced using the EDM with the additional active and passive dipoles. This implies that in addition to the number of active dipoles used in characterizing these problems previously, different dipoles (i.e., 52 passive dipoles, 31, 42, 64 active dipoles) were then added to highlight their contributions.

In case 1, the trace is located at the middle of the large ground plane with a good isolation from the edges. It is assumed that through this, there is minimal current induced at the edges of the ground plane due to the trace. Figure 3 shows the percentage improvement in the predicted transverse fields for 3 different numbers of active dipoles and also the case where passive dipoles are included. It is shown that addition of passive dipoles does not have much effect as compared

with the addition of active dipoles. This is because the greater proportion of the sources of the EM emissions are located on the surface of the PCB,

$$improvement = \frac{r.m.s_1 - r.m.s_2}{r.m.s_1} \times 100\%$$

where $r.m.s_1$ and $r.m.s_2$ are the error without and with additional dipoles, respectively.

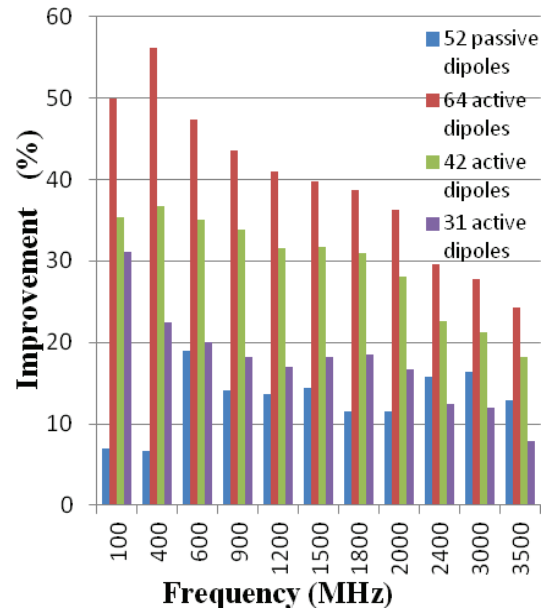


Fig. 3. R.M.S improvement in reproducing case 1 by the addition of more dipoles (passive or active).

Conversely, Fig. 4 shows the results for case 2. A significant improvement is observed for the addition of passive dipoles. Unlike case 1, there is a significant amount of current induced at the edges of the ground plane. This was as a result of moving the L trace close to the right right-angular edge of the ground plane as shown in Fig. 1 (b). Hence, we can deduce from this that these edge dipoles can sufficiently emulate the induced currents at the edges. However, for case 2 additional active dipoles only had quite small an effect. This is because the active dipoles, which are positioned in such a way to characterize the actual sources of the emissions, cannot sufficiently emulate the behaviors of the additional currents induced at the edges of the ground plane. It has been shown that whilst the active dipoles can sufficiently characterize sources isolated from the edges of a ground plane, their performance declines as the sources are located closer to the

edge of the ground plane. The active sources with their images are used to characterize the direct radiation of EM sources including the scattering by PEC ground plane leading to reflection. This is sufficient for an infinite ground plane problem and can also give good results for problems with the EM sources well isolated from the edges of the ground plane. However, for a more realistic scenario in complex PCB designs, passive dipoles are introduced along the edges of the ground plane. This is to emulate the effects of edge currents leading to diffraction due to the finiteness of practical PCBs.

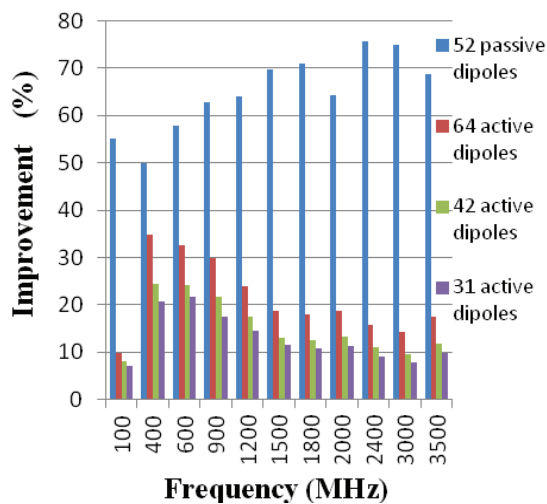


Fig. 4. R.M.S improvement in reproducing case 2 by the addition of more dipoles (passive or active).

C. Practical PCB

To further show the viability of this approach, a long metallic strip over a finite ground plane (160mm \times 100mm) with similar EM performance as a practical PCB was simulated using MoM code [13]. Figure 5 (a) shows the physical design with 5mm mesh size and Fig. 1 (b) the current path along the L strip. The strip is excited with 8dBmW power at the tip of the shorter leg while the longer leg is terminated with a 50 Ω load. This simulation was carried out at 900 MHz and field results were extracted 10 mm above the planes. As given in equations (1) and (2), only the transverse fields are required in order to compute the equivalent currents. Unlike the problem treated earlier, the transverse fields on all the planes surrounding the PCB are required in the model. This is to provide sufficient information required to compute the

moments of the passive dipoles, which have been shown to contribute most to the diffracted fields. Samples taken from the xy-plane as used in sections III A) and III B) were sufficient because of the size of the trace and fewer edge current excitation is expected. However, for a larger trace located close to the edge, significantly more edge current excitation is expected and to properly characterize these edge currents, sufficient sampling around the PCB is required. The extracted complex-valued field are then imported into the equivalent dipole model of equation (13). The LHS of equation (13) comprises all the transverse fields extracted at each of the planes surrounding the structure. The first term on the RHS, which includes the direct, reflected, and diffracted field components, is then computed using equations (6) to (8) or equations (9) to (11) for electric or magnetic dipoles, respectively. The dipole moment vector is then calculated through the solution for the inverse problem.

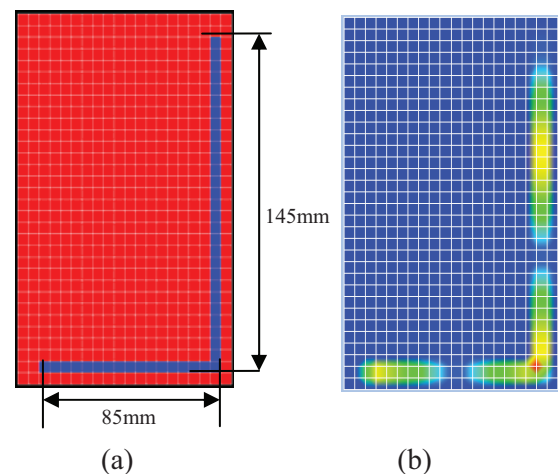


Fig. 5. (a) Physical design and (b) current path on the L-shape strip.

As described in section II C), the singular value decomposition technique was used. Following from the multipole expansion as also mentioned in section II B), 6 dipoles comprising 3 electric D_x^E, D_y^E, D_z^E and 3 magnetic D_x^M, D_y^M, D_z^M were first used to model each dipole point. This is computationally expensive and requires about 25 mins to run on an Intel core i7 3 GHz processor and 6 GB RAM PC. By trying different combination of dipoles and reducing the individual dipole moment redundancies, 3 orthogonal electric

dipoles were found to be sufficient in modeling the actual sources (active sources) while a combination of electric and magnetic dipoles were required for modeling the currents at the edges of the ground plane (passive sources). This is summarized as,

$$D_{active} = \begin{bmatrix} D_x^E \\ D_y^E \\ D_z^E \end{bmatrix} \quad (22)$$

$$D_{passive} = \begin{bmatrix} D_x^E \\ D_y^E \\ D_z^M \end{bmatrix}. \quad (23)$$

Though, any of the 3 orthogonal magnetic dipoles can equally be used in modeling the active sources with good accuracy, only the vertical magnetic dipoles can be used at the edges as the polarization of the horizontal magnetic dipole cannot generate currents in the direction of the actual currents induced at the edges. Initially, 468 dipoles were used, which takes approximately 5 minutes run time using the same PC. Figures 6 and 7 show the fields computed in the principal planes of the structure.

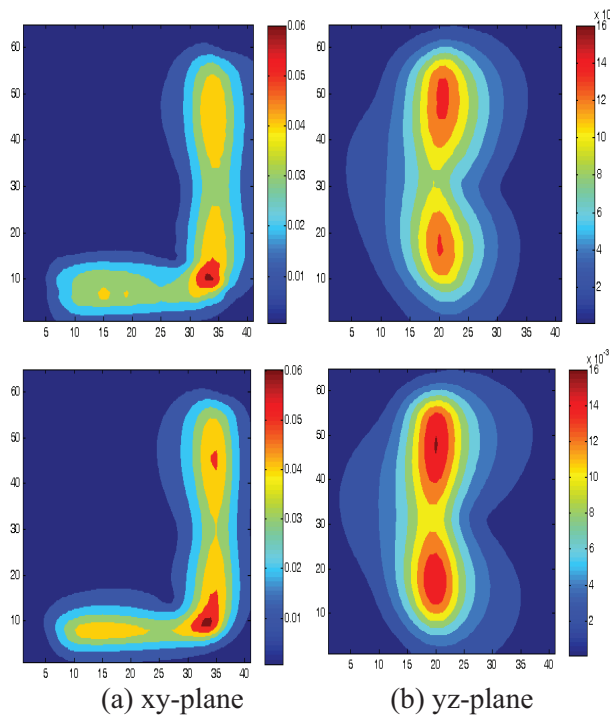


Fig. 6. Equivalent dipole model (1st row) and simulation (2nd row) of total magnetic field H_T , at 10 mm.

$H_T = \sqrt{H_x^2 + H_y^2 + H_z^2}$, also predictions were made at far-field distances from the structure using equivalent dipole model and results were compared with those from concept-II. These also show good agreement between the fields predicted with the equivalent dipole model and those computed using the MoM based concept-II software as shown in Fig. 8. Furthermore, by retaining only the dipole moments with significant contributions, D_0 (i.e. $D_0 \geq p \times D_{mMax}$), to the

total field observed at any given point, the total number of dipoles required for this model was reduced from 468 to 102, where D_{mMax} is the maximum dipole moment in the initial dipole moment vector and p is given proportion. Here we used a p value of 10 %. Figure 9 Shows the initial dipole and optimized final dipole positions on the surface of the structure. In Fig. 9 (b) the dipoles were found to be aligned along the current path as expected according to Fig. 5 (b). The moments of these optimized dipoles were then calculated according to equation (13) and used to predict these fields.

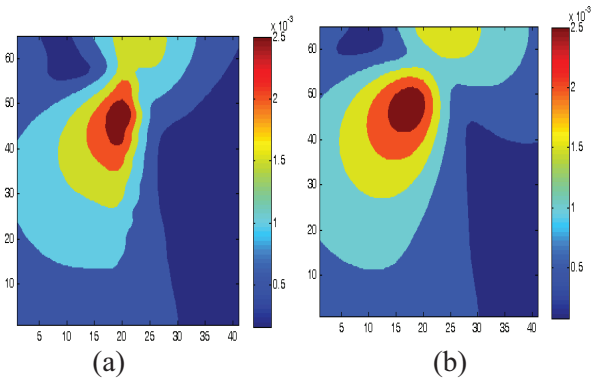


Fig. 7. (a) Equivalent dipole model and (b) simulation results of the total magnetic field H_T , at 10 mm for xz -plane.

The maximum difference between the two models is found for the top plane, because sufficient number of dipoles are required to accurately model the fields parallel to the surface of the large structure. Far-fields results for the different models were also computed. As shown in Fig. 8 (a) and (b), inclusion of the edge dipoles in the equivalent dipole model can closely predict radiations from finite structures in different EMC

environments. Dipole moments computed from the information obtained only from the top plane of the structure (i.e., xy-plane) results to higher error. This is represented by the magenta line. By including the field information from all planes surrounding the structure to compute the dipole moment, a more accurate prediction is observed as represented in green.

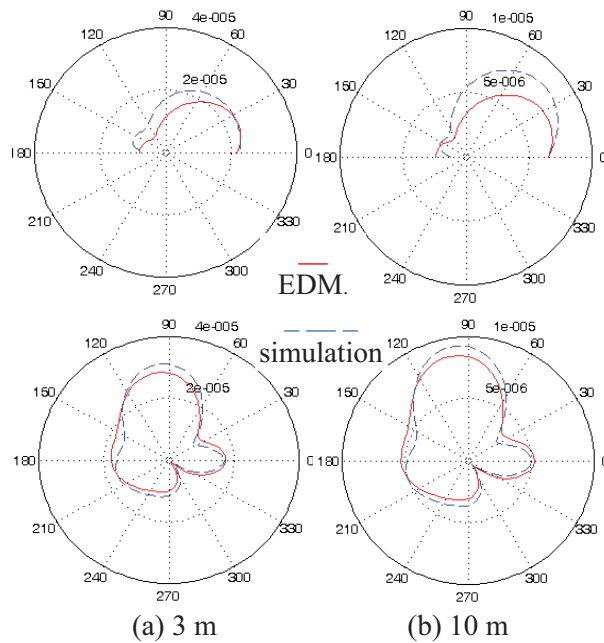


Fig. 8. H_θ (1st row) and H_ϕ (2nd row).

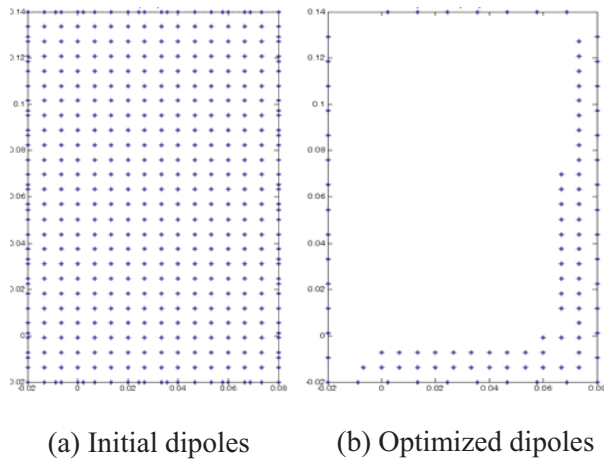


Fig. 9. Dipoles positions on the plane.

This is quite similar to the results for 468 dipoles in Fig. 10, while the blue dash represents the simulated results in both cases. The maximum

fields at far-field regions 3 m and 10 m between 468 dipoles, 102 dipoles and numerical simulation also show a good agreement. Thus for this model, the specified degree of accuracy determines the number of dipoles to be used.

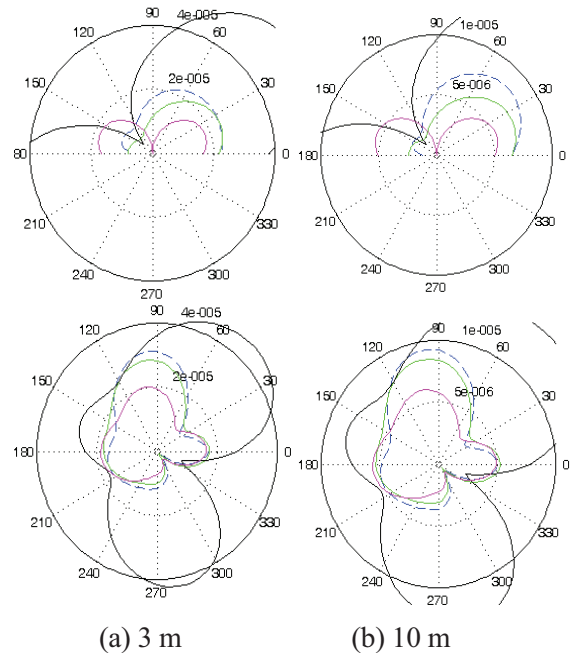


Fig. 10. H_θ (1st row) and H_ϕ (2nd row), { blue dash, green, magenta, and black }- {Simulation, 102 dipole model, dipole model with only top plane, dipole model without edge dipoles}.

IV. CONCLUSION

A scheme using equivalent dipoles to model radiated fields from complex radiators has been extended by including additional dipoles to represent diffraction effects. It is shown that a number of equivalent dipoles distributed along the edge of a finite ground can approximate the effects of the induced currents at its edges that leads to diffraction. The accuracy of this approach depends on the number of dipoles used. As this number increases, the time needed to evaluate the inverse problem increases correspondingly and can lead to ill-conditioning. However, techniques exist for solving ill-conditioned inverse problems. This approach will be used in the future work for predicting the coupling between different EM sources and their environments.

ACKNOWLEDGMENT

The authors are with the George Green Institute for Electromagnetics Research at the University of Nottingham, UK and the project is funded by the EPSRC, Grant No: EP/H 05138/1.

REFERENCES

- [1] C. Obiekezie, D. Thomas, A. Nothofer, S. Greedy, and P. Sewell, "Electromagnetic characterization of 3D radiators," *EuroEM Conf.*, Toulouse, France, July 2012.
- [2] X. Tong, D. Thomas, A. Nothofer, P. Sewell, and C. Christopoulos, "Modelling electromagnetic emissions from printed circuit boards in closed environments using equivalent dipoles," *IEEE Trans. Electromagn. Compat.*, vol. 52, no. 2, pp. 462-470, 2010.
- [3] Y. Vives-Gilabert, C. Arcambal, A. Louis, F. de Daran, P. Eudeline, and B. Mazari, "Modeling magnetic radiations of electronic circuits using near-field scanning method," *IEEE Trans. Electromagn. Compat.*, vol. 49, no. 2, pp. 391-400, May 2007.
- [4] L. Beghou, B. Liu, L. Pichon, and F. Costa, "Synthesis of equivalent 3-D models from near field measurements - Application to the EMC of power printed circuit boards," *IEEE Transactions on Magnetics*, vol. 45, no. 3, pp. 1650-1653, 2009.
- [5] J.-R. Regué, M. Ribó, J.-M. Garrell, and A. Martín, "A genetic algorithm based method for source identification and far-field radiated emissions prediction from near-field measurements for PCB characterization," *IEEE Trans. Electromagn. Compat.*, vol. 43, no. 4, pp. 520-530, Nov. 2001.
- [6] X. Tong, D. Thomas, A. Nothofer, P. Sewell, and C. Christopolous, "A genetic algorithm based method for modeling equivalent emission sources of printed circuits from near-field measurements," *Asia-Pacific International Symposium on Electromagn. Compat.*, Beijing, China, April 2010.
- [7] J. Pak, H. Kim, J. Lee, and J. Kim, "Modeling and measurement of radiated field emission from a power/ground plane cavity edge excited by a through-hole signal via based on a balanced TLM and via coupling model," *IEEE Trans. on Adv. Packag.*, vol. 30, pp. 73-85, Feb. 2007.
- [8] W. Cui, X. Ye, B. Archambeault, D. White, M. Li, and J. Drewniak, "EMI resulting from signal via transitions through the DC power bus," *IEEE International Symposium on Electromagnetic Compatibility*, pp. 821-826, 2000.
- [9] H. Park, H. Jang, and H. Park, "Simulation and design of a PCB-chassis system for reducing radiated emissions," *Applied Computational Electromagnetics Society (ACES) Journal*, vol. 26, no. 8, pp. 679-687, August 2011.
- [10] C. Obiekezie, D. Thomas, A. Nothofer, S. Greedy, L. Arnaut, and P. Sewell, "Optimization of equivalent dipole model to include edge effect," *ICEAA Conf.*, Torino, Italy, Sep. 2013.
- [11] J. Keller, "Geometrical theory of diffraction," *J. Opt. Soc. Amer.*, vol. 52, no. 2, pp. 116-130, Feb. 1962.
- [12] P. Ufimtsev, "Approximate computation of the diffraction of plane electromagnetic waves at certain metal bodies, Part I: Diffraction patterns at a wedge and a ribbon," *Soviet Phys.-Technical Phys.*, vol. 2, no. 8, pp. 1708-1718, Aug. 1957.
- [13] C. Obiekezie, D. Thomas, A. Nothofer, S. Greedy, P. Sewell, and C. Christopoulos, "Prediction of emission from a source placed inside a metallic enclosure over a finite ground plane," *EMC Europe Conf.*, Rome, Italy, Sept. 2012.
- [14] C. Balanis, *Advanced Engineering Electromagnetic*, Wiley, New York, 1989.
- [15] C. Balanis, *Antenna Theory, Analysis and Design*, 3rd ed., Wiley, New Jersey, 2005.
- [16] S. Schelkunoff, "Some equivalence theorems of electromagnetics and their application to radiation problems," *Bell Syst. Tech. J.*, vol. 15, pp. 92-112, 1936.
- [17] C. Huygens, *Traite de la Lumiere*, S. P. Thompson, London, 1912.
- [18] A. Love, "The integration of the equation of propagation of electric waves," *Phil. Trans. Roy. Soc. London, Ser. A*, vol. 197, pp. 1-45, 1901.
- [19] J. Wikswo and K. Swinney, "Scalar multipole expansions and their dipole equivalents," *J. Appl. Phys.*, vol. 57, pp. 4301, 1985.
- [20] P. Wilson, "On correlating TEM cell and OATS emission measurements," *IEEE Trans. Electromagn. Compat.*, vol. 37, no. 1, pp. 1-16, Feb. 1995.
- [21] D. Geselowitz, "Multipole representations for an equivalent cardiac generator," *Proc. IRE*, vol. 48, pp. 75-79, Jan. 1960.
- [22] P. Hansen, "Regularization tools: A Matlab package for analysis and solution of discrete ill-posed problems," *Numer. Algo.*, vol. 46, pp. 189-194, March 2008.
- [23] Concept - II homepage, <http://www.tet.tu-harburg.de/concept/index.en.html>, 2012.
- [24] E. Joy and D. Paris, "Spatial sampling and filtering in near-field measurements," *IEEE Trans. Antennas Propagat.*, vol. 20, pp. 253-261, May 1972.



Chijioke S. Obiekezie received the B.Eng. and M.Sc. degrees in Electrical and Electronic Engineering from the Federal University of Technology Owerri, Nigeria and Queen Mary University of London, U.K., in 2006 and 2009, respectively. He is currently working towards a Ph.D. degree in electrical and electronic engineering from the University of Nottingham, U.K.



David W. P. Thomas received the B.Sc. degree in physics from Imperial College of Science and Technology, London, U.K., the M.Phil. degree in space physics from Sheffield University, Sheffield, U.K., and the Ph.D. degree in Electrical Engineering from Nottingham University, Nottingham, U.K., in 1981, 1987, and 1990, respectively.

In 1990, he joined the Department of Electrical and Electronic Engineering, University of Nottingham, Nottingham, as a Lecturer, where he is currently a Professor of electromagnetic applications. His research interests include power system transients, power system protection, electromagnetic compatibility, and electromagnetic simulation.

Prof. Thomas is a member of International Council on Large Electric Systems and a Convenor for JWG 4.207.



Angela Nothofer was born in Uelzen, Germany, in 1967. She received the Dipl.-Ing. degree in Electrical Engineering from the University of Hannover, Hannover, Germany, in 1995, and the D.Phil. degree in Electronics from the University of York, York, U.K., in 2001.

In 2000, she joined the National Physical Laboratory, London, U.K., as a Member of the RF and Microwave Team, where she was engaged in developing standards and methods for measuring electromagnetic field strength. In 2005, she joined the George Green Institute for Electromagnetics Research, University of Nottingham, Nottingham, U.K., as a Lecturer in electromagnetic applications. Her current research interests include electromagnetic compatibility, and RF and microwave measurements using TEM waveguides, fully anechoic rooms, and reverberation chambers.



Stephen Greedy was born in Cardiff, U.K. in 1966. He received the M.Eng. and Ph.D. degrees in Electrical and Electronic Engineering from the University of Nottingham, UK, in 1998 and 2002, respectively. The subject of his Ph.D. dissertation was the development and application of tools for the design of photonic integrated circuits and was titled "Advances in the Spectral Index Method for Optoelectronic design.". He was sponsored by DERA for the duration of his Ph.D. Following his Ph.D. he spent two years working as a research fellow on projects supported by Qinetiq and the Mobile telecommunications and health Research Programme.

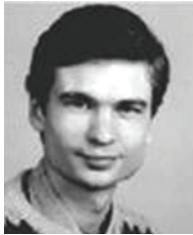
He is a lecturer in the Department of Electrical and Electronic Engineering, University of Nottingham, UK. Research interests are in the area of computational electromagnetics, specifically the implementation of numerical algorithms on a variety of computational platforms and the simulation of systems for electromagnetic compatibility and signal integrity studies.



Luk R. Arnaut received the B.Sc. and M.Sc. degrees in Electrical and Electronic Engineering from the University of Ghent, Ghent, Belgium, in 1989, and the M.Sc. and Ph.D. degrees in Communication Engineering and Digital Electronics from the University of Manchester Institute of Science and Technology (UMIST), Manchester, U.K., in 1991 and 1994, respectively. From 1993 to 1994, he was a Research Associate at UMIST. During 1994, he was a Postdoctoral Research Scientist at the Defence Research Agency (now QinetiQ plc), Farnborough, U.K., where he was engaged in modeling, fabrication, and measurement of synthetic chiral composites. During 1995, he was a Visiting Scientist at the Naval Research Laboratory, Washington, DC. During 1995–1996, he was a Consultant at the Operations Division, British Aerospace plc (now BAE Systems), Bristol, U.K. From 1996 to 2010, he was a Senior Research Scientist at the National Physical Laboratory, Teddington, U.K., where he was a Key Scientific Advisor on mathematical modeling and the Lead Scientist of the Wireless Communications Science and Technology Group, within the Time, Quantum and Electromagnetics Division. Since 2008, he has been a Visiting Professor at the Imperial College of Science, Technology and Medicine, London, U.K. Since 2012, he has been a Research Fellow at the George Green

Institute for Electromagnetics Research at the University of Nottingham, U.K., where he is working on stochastic methods for analysis of circuits and complex sources. He is author or coauthor of more than 100 refereed publications, and holds two patents. His current research interests include electromagnetic interaction effects, statistical electromagnetics, complex media for radio-frequency and photonic applications (plasmonics), and multiple-input-multiple-output (MIMO) wireless communication systems.

Dr. Arnaut is the Convenor of the Joint Task Force on Reverberation chambers (JWG REV) between SC77B and CISPR/A of the International Electrotechnical Commissions, Geneva, Switzerland. He is a member of various past and present national and international networks, institutions, and steering groups. He is a Fellow of the Institution of Engineering and Technology. He is listed in *Who's Who in Science and Engineering*, *Who's Who in the World*, and *International Biographical Centre's Cambridge Blue Book*.



Phillip Sewell received the B.Sc. (Hons.) degree in Electrical and Electronic Engineering and the Ph.D. degree from the University of Bath, Bath, U.K., in 1988 and 1991, respectively. From 1991 to 1993, he was a Postdoctoral Fellow with the University of Ancona, Ancona, Italy. In 1993, he was a Lecturer in the School of Electrical and Electronic Engineering, University of Nottingham, Nottingham, U.K., where he became a Reader and a Professor of electromagnetic, in 2001 and 2005.

Issues in Antenna Optimization - A Monopole Case Study

Richard A. Formato

Consulting Engineer and Registered Patent Attorney
P. O. Box 1714, Harwich, MA 02645 USA
rf2@ieee.org

Abstract — A typical antenna design optimization problem is presented, and various issues involved in the design process are discussed. Defining a suitable objective function is a central question, as is the type of optimization algorithm that should be used, stochastic versus deterministic. These questions are addressed by way of an example. A single-resistor loaded broadband HF monopole design is considered in detail, and the resulting antenna compared to published results for similar continuously loaded and discrete resistor loaded designs.

Index Terms — Algorithm, bandwidth, broadband, central force optimization, CFO, HF, impedance loading, monopole, numerical methods, optimization, and wire antenna.

I. INTRODUCTION

“Good against remotes is one thing. Good against the living, that’s something else”. Han Solo thus cautioned Luke Skywalker as he practiced lightsaber skills in the classic 1977 film **Star Wars**. This note echoes a similar sentiment when it comes to designing antennas with optimization algorithms, *“Good against benchmarks is one thing. Good against ‘real world’ antennas, that’s something else”*. This admonition is examined by way of an example, designing an optimized resistively-loaded broadband high-frequency (HF) base-fed monopole. The antenna and its ground plane are perfectly electrically conducting (PEC), so that decreased radiation efficiency results solely from i^2R losses in the resistor. This example highlights the importance of, and the difficulties in, choosing an appropriate objective function and the

advantages of using a deterministic optimizer in doing so.

Optimization algorithms typically are evaluated against benchmarks with known extrema (fitnesses and locations). How well an algorithm works is measured by its accuracy and efficiency, referring respectively to how close it gets to the extrema and how much computational effort is expended in the process (usually the number of function evaluations). An algorithm’s performance often depends on user-specified setup parameters, and it may change dramatically with different values. Additional complications are introduced by inherently stochastic optimizers, such as particle swarm or ant colony optimization, because this type of algorithm returns a different answer on successive runs, relying as they do on true random variables computed from a probability distribution. Even before an antenna problem has been precisely stated, the designer must choose suitable run parameters for a stochastic optimizer and somehow guess how well it will work on the antenna problem at hand, neither of which is a simple matter.

The picture is further complicated because real world antenna problems introduce yet another level of complexity, defining a suitable objective function. If an optimization algorithm’s performance is sensitive to its setup parameters, and if its results vary from one run to the next, then the added problem of having to define a “good” objective function can be daunting. Of course, this question does not come up in benchmark testing because the benchmark itself is the objective function. But, as the results reported here show, this question is central in optimizing even a simple antenna.

II. DESIGN GOALS

The first step in antenna optimization is defining a clear set of performance goals. There are many measures to consider, such as directivity, radiation pattern, bandwidth, efficiency, and physical size, among others. Goals for all parameters must be articulated in order to define an objective function that effectively measures how well they are met. There are two main objectives for the monopole example described here: (1) as flat as possible an impedance bandwidth from 5 MHz to 30 MHz and (2) maximum gain. The PEC metallic monopole element is 10.7 meters high with 0.005 meter radius (dimensions chosen for comparison to other designs) fed against a PEC ground plane.

III. THE OBJECTIVE FUNCTION

The next step is defining an objective function that measures how well a particular antenna design meets the performance goals. For purposes of illustration, the monopole's decision space, Π , is chosen to be two-dimensional (2-D) because the objective function's topology ("landscape") can be visualized. The decision variables are (1) the value of the loading resistor, R (Ω) and (2) its placement along the monopole, H (m), as shown in Fig. 1. The decision space is defined as $\Pi : \{(R, H) \mid 0 \leq R \leq 1000 \Omega, 0.05 \leq H \leq 10.65 \text{ m}\}$. Real world antenna problems, of course, usually contain many more than two variables, often far more, which considerably complicates the definition of a good objective function because then the landscape cannot be visualized.

The antenna parameters considered for inclusion in the objective function in this example are: minimum radiation efficiency, $Min(\varepsilon)$; minimum value of the maximum gain, $Min(G_{max})$; the voltage standing wave ratio $VSWR/Z_0$ computed relative to a purely resistive feed system characteristic impedance Z_0 ; and monopole input impedance $Z_{in} = R_{in} + jX_n$. Each parameter is evaluated as a function of frequency, and G_{max} at a given frequency is the maximum gain over the polar angle θ in Fig. 1.

Needless to say, there are myriad ways these parameters can be combined, and the question is, which combination is best? Unfortunately, there is no answer to this query, other than trying different possibilities and evaluating each one's

performance. A deterministic optimizer can make a big difference in this regard. Because stochastic algorithms return different results for every run, there is no (good) way of determining whether or not better designs are the result of a more suitable objective function or the inherent variability of the algorithm itself. By contrast, a deterministic optimizer always returns the same results for given setup parameters, so that any improvement in the antenna performance is attributable to changes in the objective function. These considerations are illustrated below using three different objective functions for the loaded monopole.

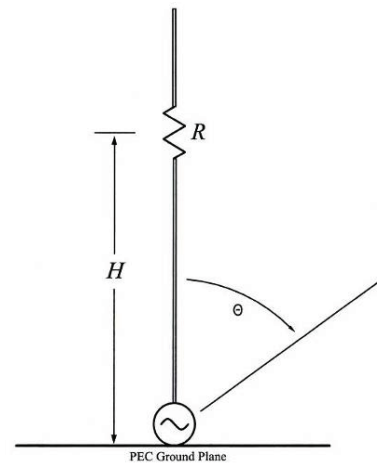


Fig. 1. Base-fed monopole geometry.

IV. FUNCTION $f_1(R, H, Z_0)$

The first monopole objective function (to be maximized) combines the minimum radiation efficiency and maximum gain with the maximum VSWR excursion in a simple formula,

$$f_1(R, H, Z_0) = \frac{Min(\varepsilon) + Min(G_{max})}{\Delta VSWR(Z_0)} \quad (1)$$

where $\Delta VSWR(Z_0)$ is the difference between maximum and minimum standing wave ratios over the 5 MHz-30 MHz HF band relative to Z_0 . The fitness increases with increasing efficiency and minimum gain and decreasing VSWR difference. f_1 's landscape with $Z_0 = 50 \Omega$ appears in Fig. 2 (a)-(b), which show, respectively, perspective and plan views and projections onto the $R - Z$ and $H - Z$ planes. f_1 is smoothly varying and unimodal with a maximum fitness of 2.3764... at the point $(R, H) = (5.025126 \Omega, 1.621357 \text{ m})$. The global

maximum was located by computing $f_1(R, H, 50)$ over the decision space Π using a grid of 200×200 points and searching for the maximum. This procedure is used for each of the 2-D landscapes discussed here.

The monopole was modeled using numerical electromagnetics code (NEC), version 2, double precision [1, 2]. The 10.7 meter tall element was divided into 107 segments with the resistor placed at the segment's midpoint using NEC's "LD" loading cards. Because the antenna is loaded by segment number, not by distance above the ground plane, the height coordinate H was converted to the loading segment number as $n = [0.5 + H/\Delta]$ where $\Delta = 0.1$ m is the segment length. A typical NEC input file appears in Fig. 3.

While f_1 's functional form may seem quite reasonable for measuring the monopole's performance, an examination of its topology reveals two potential concerns: (1) maximum fitness occurs close to Π 's lower resistance boundary and (2) it varies very little with height. The first characteristic may impede an optimization algorithm's ability to search Π while the second may impede convergence (exploration versus exploitation). In a higher dimensionality decision space these characteristics cannot be ascertained by inspection, which is a further complication in defining a useful 'real world' objective function.

Apart from the question of how "searchable" Π is for f_1 's maxima, perhaps the more important question is how well f_1 actually reflects a good monopole design, that is, one that performs well against the stated performance objectives. In this example, because f_1 's maximum can be visualized and located, the resulting "best" monopole design can be evaluated by computing its performance using the known maximum's coordinates. A feed system characteristic impedance of $Z_0 = 50 \Omega$ is assumed because typical HF transmitters are designed for 50Ω systems, and the results appear in Fig. 4. In the plots, calculated data points are shown as symbols (5 MHz-30 MHz every 1 MHz), and the solid curves are interpolated using a natural cubic spline. Total power gain was computed every 10° for $0^\circ \leq \theta \leq 90^\circ$ where θ is the polar angle in NEC's standard right-handed spherical polar coordinate system (see Fig. 1).

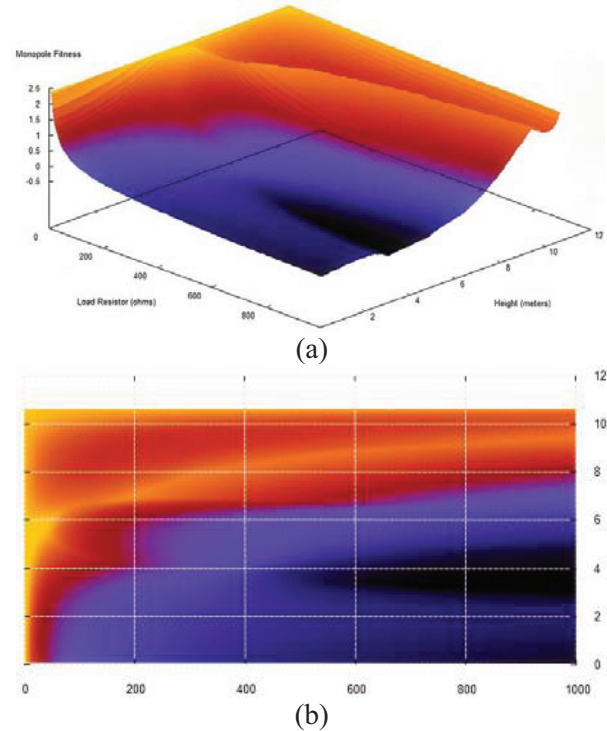


Fig. 2. Landscape for objective function $f_1(R, H, 50)$.

The radiation efficiency and maximum gain numbers are quite good. Minimum efficiency is just below 80 %, and for most part the efficiency exceeds 95 % above 10 MHz. Of course, this result is not altogether unexpected in view of the very light loading, $R \approx 5 \Omega$. The maximum power gain figures also are quite good, with minimum $G_{max} \approx 4$ dBi. This result also is expected in view of the light loading. But in stark contrast, the VSWR performance is very poor. The goal of flattening VSWR as much as possible was missed completely. VSWR varies from 1.61 to nearly 37 with pronounced fluctuations. The impedance bandwidth of this design, typically specified as $VSWR \leq 2:1$ (return loss ≤ -10 dB), is extremely small. Perhaps somewhat surprisingly, even though $f_1(R, H, 50)$'s functional form appeared to be a reasonable measure of how well the loaded monopole meets the design goals, the fact is, it is not. The best that a perfectly accurate optimization algorithm could do is to discover the design in Figs. 3 and 4, and that design happens to be quite poor. This example shows how important it is to choose an appropriate objective function.

```

CM File: DES1.NEC
CM NEC2D run using R,Z values
CM from DESIGN #1 DS plot
CM R=5.025126 ohms, Z=1.621357 m
CM seg # = INT(0.5+Z/SegLen) = 16
CM Z0=50 ohms
CE
GW1,107,0.,0.,0.,0.,10.7,.005
GE1
LD0,1,16,16,5.025126,0.,0.
GN1
FR 0,26,0,0,5.,1.
EX 0,1,1,1,1.,0.
RP 0,10,1,1001,0.,0.,10.,0.,100000.
EN
    
```

Fig. 3. Typical monopole NEC input file.

V. FUNCTION $f_2(R, H, Z_0)$

$f_1(R, H, Z_0)$'s disappointing results make it clear that another, hopefully better, objective function must be defined. f_1 's major failing was its inability to flatten the VSWR curve, which suggests that a more aggressive approach is required. Dealing directly with $Z_{in} = R_{in} + j X_{in}$, for example, might work better than trying to minimize VSWR variability. To that end, a quite different objective function will be considered next,

$$f_2(R, H, Z_0) = \frac{Min(\epsilon)}{|Z_0 - Max(R_{in})| \cdot |Max(X_{in})|}. \quad (2)$$

As before, this functional form is simple and ostensibly serves to achieve the design goals. As will be seen below, it does perform better than $f_1(R, H, Z_0)$ with respect to VSWR, but its topology is such that many optimization algorithms will have considerable difficulty locating maxima. $f_2(R, H, Z_0)$'s global maximum of 0.11117... at the point $(R, H) = (819.095477, 2.953015)$. The loading resistance $R \approx 819 \Omega$ is much heavier than before, which will reduce efficiency and maximum gain but hopefully will tame the VSWR. This reflects the inevitable trade-off in using impedance loading for improving antenna bandwidth, which increases with heavier loading at the expense of the radiation efficiency and gain.

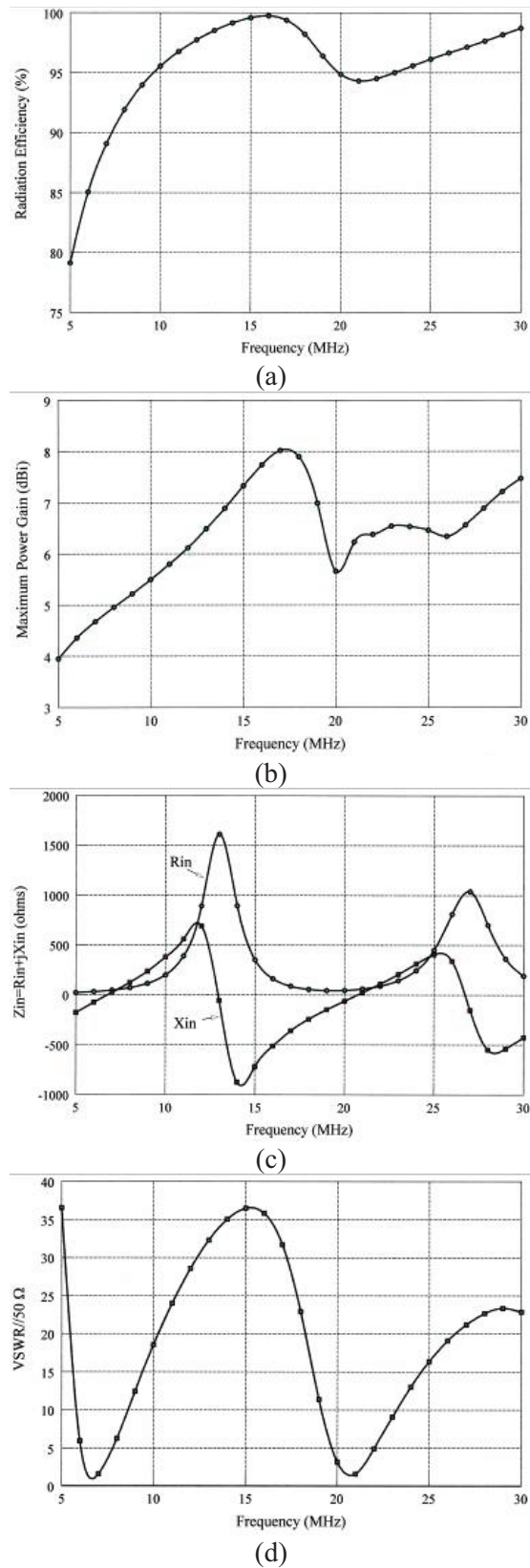
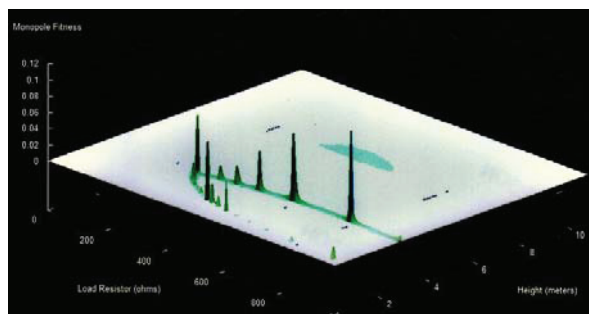


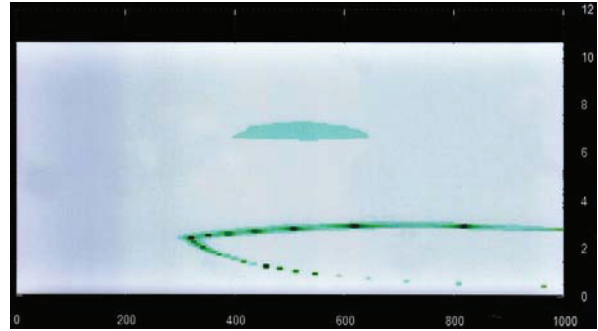
Fig. 4. Performance of monopole design #1, $f_1(5.025, 1.62, 50)$.

Figure 5 shows f_2 's landscape. It comprises a series of spikes along a bullet-shaped curve in the (R, H) -plane, and the peaks are quite sharp. For example, changing H slightly from 2.8731... to 2.8198... with $R = 819.0954...$ results in nearly three orders of magnitude decrease in fitness. Topologies like this usually are described as "pathological" because many optimization algorithms have difficulty dealing with them. Thus, even though objective function f_2 may be better than f_1 for achieving the design goals, its pathological landscape may impede an optimization algorithm to such a degree that better designs are not discovered.

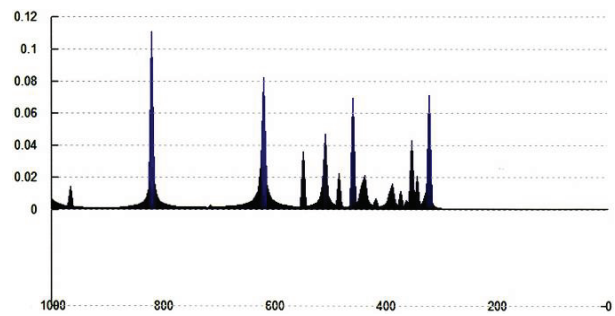
NEC-2D again was used to model the monopole with $f_2(R, H, 50)$'s best fitness, and the results appear in Fig. 6. As expected, the radiation efficiency is much lower, especially at low frequencies. Below 15 MHz it ranges from about 5 % to 25 %. The efficiency does increase substantially mid-band, reaching a peak near 80 % at 19 MHz and falling thereafter. The power gain more or less tracks the efficiency, but it is quite low at low frequencies. Above 15 MHz, however, the gain is moderate to good. The heavier loading in this case considerably reduced the input impedance variation resulting in a fairly smooth variation in R_{in} and to a lesser degree in X_{in} as well. As a result VSWR variability is less than in the previous design, but still quite substantial. The VSWR is well-behaved and moderate, $\leq 5:1$, above 20 MHz, but it is very high at lower frequencies with a peak $\approx 21:1$ at 18 MHz. Thus, while f_2 is an improvement over f_1 in terms of meeting the design goals, it still falls far short of yielding a good monopole design. In addition, its pathological landscape may defeat the effectiveness of many optimization algorithms. Further refinement of the objective function is required.



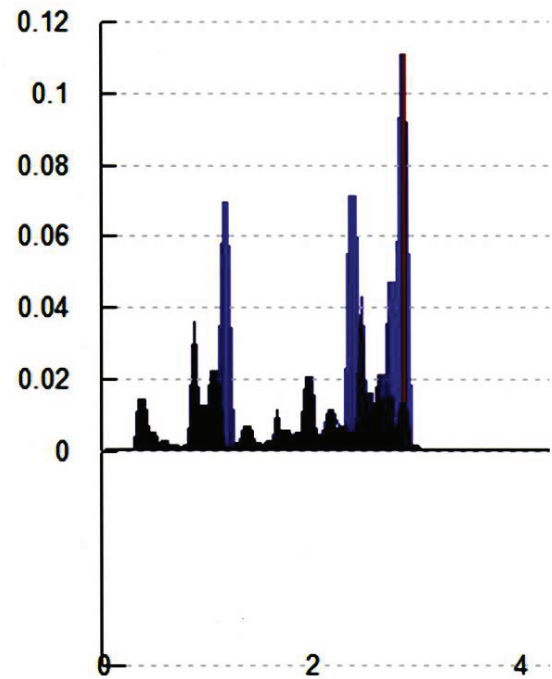
(a)



(b)



(c)



FoM_8: View #4

(d)

Fig. 5. Landscape for objective function $f_2(R, H, 50)$.

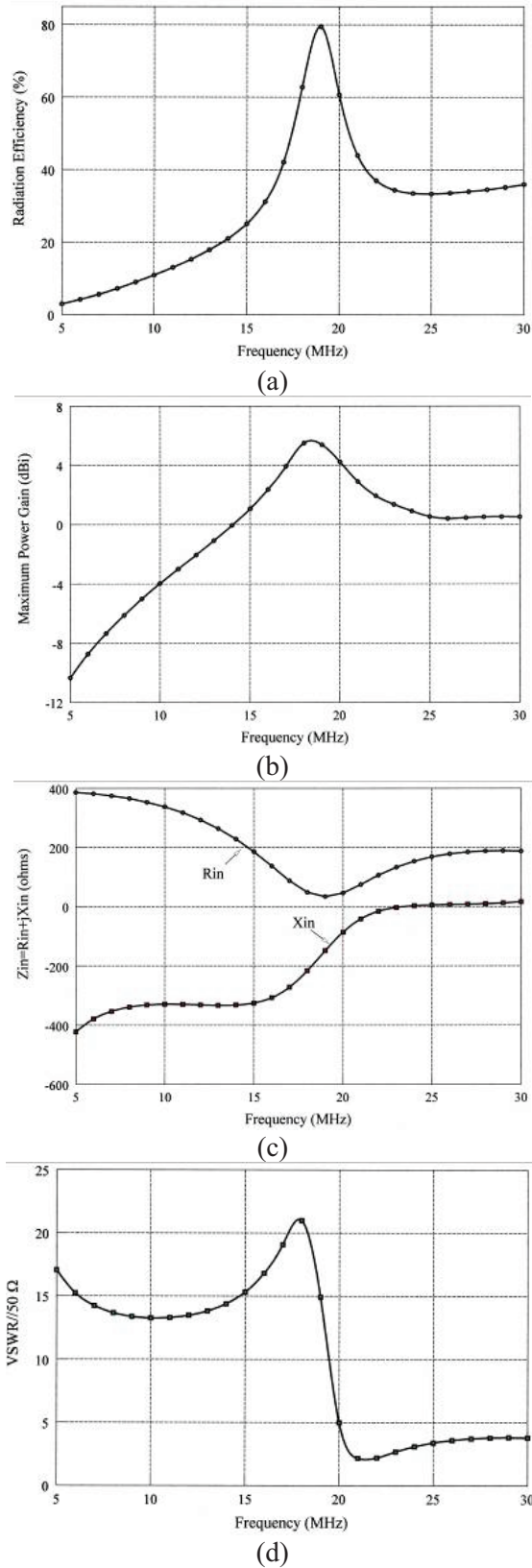


Fig. 6. Performance of monopole design # 2, $f_2(819,1,2.95,50)$.

VI. FUNCTION $f_3(R, H, Z_0)$

Because VSWR variability is the biggest problem with the first two objective functions, an even more aggressive approach will be taken with the third function defined as,

$$f_3(R, H, Z_0) = \frac{Min(\epsilon)}{|Z_0 - Max(R_{in})| \cdot \Delta VSWR(Z_0) \cdot [Max(Xin) - Min(Xin)]} \quad (3)$$

The gain does not appear in the numerator because it tracks fairly well with efficiency. The denominator comprises three factors that minimize VSWR in different ways. The first drives the real part of the input impedance toward the feed system characteristic impedance. The second minimizes the VSWR variability across the band, while the third attempts to flatten the input reactance.

Because this functional form is determined empirically, other forms probably merit consideration as well. For example, the objective function $f_3(R, H, Z_0)$ could be written as

$$f_3(R, H, Z_0) = \frac{Min(\epsilon)^{\eta_1}}{|Z_0 - Max(R_{in})|^{\eta_2} \cdot \Delta VSWR(Z_0)^{\eta_3} \cdot [Max(Xin) - Min(Xin)]^{\eta_4}} \quad (4)$$

where the exponents η_i are constants or functions of frequency. The terms in f_3 could be combined differently, say, by addition with weighting coefficients. Other functions, such as logarithms or trigonometric functions, might be useful in combining the antenna's performance measures. And, of course, other performance measures might be included as well. All of these considerations are involved in defining suitable objective functions. As the results for f_1 and f_2 show, presumably good ones can turn out to be quite poor. It consequently is imperative to investigate how the objective function's form influences the resulting antenna design.

$f_3(R, H, 50)$ is unimodal with a smoothly varying topology and a maximum fitness of $1.4624 \dots \times 10^{-5}$ at $(R, H) = (502.512563, 7.2143215)$. Its landscape is plotted in Fig. 7. This objective function results in the design whose performance is shown in Fig. 8. The radiation efficiency increases more or less monotonically from just over 15 % at 5 MHz to nearly 40 % at 27 MHz and about 38 % at 30 MHz. Maximum power gain ranges from a low near -3.1 dBi to a maximum of

2 dBi. The input impedance is well behaved across the HF band, and the resulting VSWR is much flatter than in the previous cases. Maximum VSWR is just below 13:1 at 5 MHz, and it falls very quickly to just above 3:1 at 7.5 MHz. The VSWR increases to $\sim 8:1$ at 13 MHz and remains fairly flat thereafter. A comparison of these data to the curves in Figs. 4 (d) and 6 (d) clearly shows that $f_3(R,H,50)$ is the best objective function of the three. Its monopole design is superior to the others, and its topology lends itself well to being searched by an optimization algorithm.

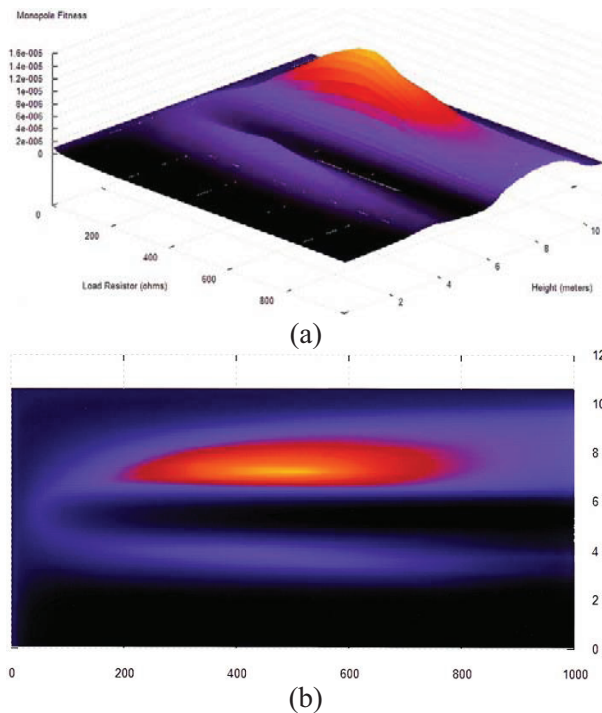


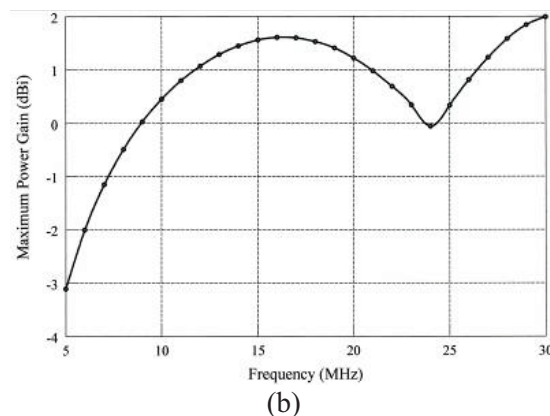
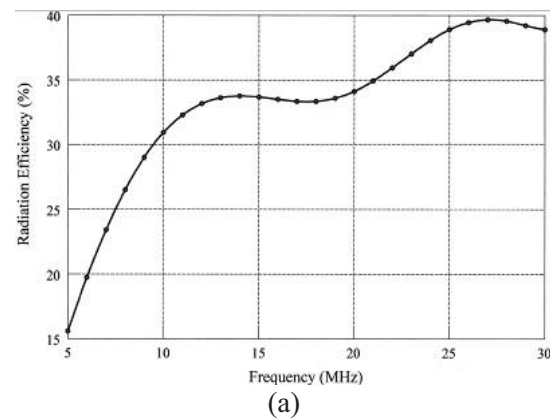
Fig. 7. Landscape for objective function $f_3(R, H, 50)$.

VII. OPTIMIZATION ALGORITHMS

The previous sections discussed some of the issues in defining suitable objective functions for the broadband HF monopole design problem. Three functions were considered, and the results varied considerably from one to the next, with the last one being the best. Each of these objective functions has a known global maximum that can be visualized because the monopole decision space is 2-D. Unfortunately, this cannot be done in higher dimensionality spaces, so that their topologies are unknown. The problem faced by the antenna designer therefore is defining an effective

objective function that can be searched accurately and efficiently in the n -D decision space. The type of optimization algorithm can be an important factor in aiding or inhibiting the process of defining a suitable objective function.

Because stochastic optimization algorithms return different results on successive runs, it is difficult to assess the effects of changing the objective function on their accuracy and efficiency. For example, if particle swarm optimization is applied to the monopole problem, the antenna designer cannot know why successive runs using, say, $f_2(R,H,Z_0)$ and $f_3(R,H,Z_0)$, yield different results. It may be a consequence of the different objective functions (for example, pathological versus well-behaved), or it may be the algorithm's inherent randomness. Which of these it is can be ascertained only by doing a statistical analysis that probably requires tens or hundreds, possibly thousands, of runs. This dilemma is avoided by using a deterministic optimizer, one that yields the same answer for every run with the same setup.



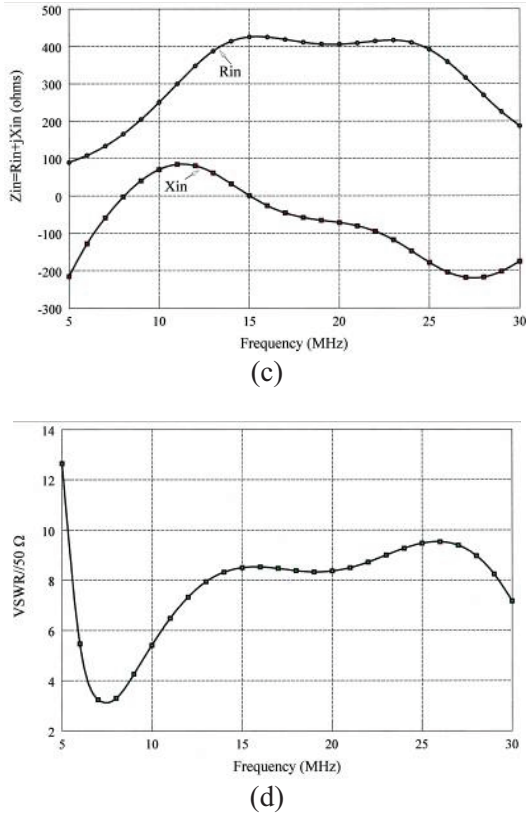


Fig. 8. Performance of monopole design # 3, $f_3(502.5,7.214,50)$.

Central force optimization (CFO) is a deterministic nature-inspired search and optimization metaheuristic for an evolutionary algorithm (EA) based on gravitational kinematics [4-6]. Proofs of convergence for CFO and an extended version have been developed [7, 8], and the algorithm has been implemented on a GPU using various topologies [9-11]. The algorithm has been successfully applied to a variety of problems, among them: training neural networks [12]; drinking water distribution networks [13]; solving nonlinear circuits [14]; array synthesis [15, 16]; microstrip patch antenna design [17]; multiband slotted bowtie design [18]; rectangular microstrip patch design [19]; microwave broadband absorber design [20]; antenna optimization generally [21]; notched ultra wideband E-shape antenna design [22]; and increasing impedance bandwidth [23, 24].

CFO therefore was used to search the decision spaces for each of the three monopole objective functions. A “parameter free” implementation was employed as described in [5, 6] without directional

information in errant probe repositioning. CFO pseudocode appears in Fig. 9. Hardwired parameter values were $N_d = 2$, $F_{rep}^{init} = 0.5$, $\Delta F_{rep} = 0.1$, $F_{rep}^{min} = 0.05$, $\gamma_{start} = 0$, $\gamma_{stop} = 1$, $\Delta\gamma = 0.3333$, $(N_p/N_d)_{max} = 6$, $N_t = 200$ with an early termination criterion of fitness variation $\leq 10^{-6}$ for 25 consecutive steps starting at step #35.

Table 1 summarizes the CFO results. It shows that the algorithm performed well against objective functions f_1 and f_3 by discovering maxima close to the known values. The results for f_1 are consistent with its topology in which the global maximum is near Π 's lower boundary in R and not particularly sensitive to variations in H . CFO essentially recovered f_3 's global maximum, but clearly it had a problem with f_2 's pathological landscape. As expected, NEC-2D's computed performance for the antenna design using CFO's (R,H) coordinates for the best objective function, f_3 , is essentially the same as that shown in Fig. 8.

Table 1. CFO optimization results.

Objective Function	Known Max Fitness / Coords	CFO Max Fitness / Coords
$f_1(R,H,50)$	2.376 / (5.025,1.621)	2.371 / (8.179,5.361)
$f_2(R,H,50)$	0.1112 / (819.1,2.953)	0.0684 / (322.2,2.366)
$f_3(R,H,50)$	1.462×10^{-5} / (502.5,7.241)	1.401×10^{-5} / (499.6,7.302)

CFO's performance probably would be better still if a more stringent early termination criterion were employed, or if none were used in a much longer run. The purpose of this note, however, is to discuss real-world design issues, and one of those is having to make the engineering decision of when the design is “good enough” relative to the resources expended. In this case, CFO achieved an acceptable design very close to the known best design using f_3 and a total of 4,636 function evaluations. This meets the “good enough” test.

This simple monopole example demonstrates that how well an “optimized” antenna performs

can be highly dependent upon both the objective function against, which it is optimized and how accurately and efficiently the optimization program performs against that function's landscape. Because CFO is deterministic, it allows the antenna designer to investigate the effects of changing the objective function's form and parameters that determine its landscape. It is evident that defining an effective function is much easier when the optimizer returns the same results every time instead of different ones. In the author's opinion this is an important consideration in addressing real-world antenna problems, or, for that matter, any problem in which definition of the objective function is an issue.

VIII. OTHER MONOPOLE DESIGNS

The monopole example was inspired by the HF monopole designed and tested by Rama Rao and Debroux [25, 26]. They employed analytically computed continuous resistive loading and achieved $VSWR \leq 2:1$ from 5 MHz-30 MHz with the use of a matching network. Radiation efficiency, gain, and pattern were reasonable and well-behaved for typical HF links. A CFO-designed discrete-resistance loading profile for the same antenna provided even better performance [23], and it is instructive to compare that CFO design, which utilized fourteen discrete resistors, to the $f_3(499.6, 7.302, 50)$ design utilizing only one resistor.

Figure 10 shows the NEC input file for the 14-segment, CFO-optimized monopole. Note that $Z_0 = 300 \Omega$ instead of $Z_0 = 50 \Omega$ because the 300 Ω reference was used in [25, 26]. Each segment is loaded at its center with a discrete resistor whose value ranges from about 7.2 Ω to 82.7 Ω ("LD" cards). The NEC-computed radiation efficiency ranges from about 8 % to 45 %, with maximum gain increasing from ~ -5.5 dBi at 5 MHz to ~ 3 dBi at 28 MHz with a pronounced mid-band dip. $VSWR/300\Omega$ is quite good, $\leq 2.25:1$ at all frequencies and $\leq 2:1$ above about 5.5 MHz. The $VSWR \leq 2:1$ goal is met essentially across the entire HF band with no matching network. The only additional element needed to feed this antenna from a 50 Ω system is a low-loss, broadband 6:1 unun, which is readily available.

The VSWR results for the 14-segment monopole suggest that a better feed system

impedance for the $f_3(499.6, 7.302, 50)$ design might be $\approx 300 \Omega$, a conjecture that was investigated by recalculating this design's VSWR parametrically in Z_0 from 225 Ω to 350 Ω . Figure 11 plots the results. The best overall performance indeed does occur with $Z_0 \approx 300 \Omega$ ($\leq 2:1$ from ~ 7.5 MHz through ~ 28 MHz). Above 28 MHz VSWR remains fairly low, below 2.5:1, but at the low end of the band it increases quickly with decreasing frequency. The maximum is $\sim 5.5:1$ at 5 MHz, but even this value is quite acceptable because it is high only in a fairly narrow band (values $\leq 10:1$ are readily matched).

At this point it is apparent that the PEC metallic monopole loaded by a single correctly placed resistor may perform nearly as well as one employing fourteen resistors, and probably better than the designs in [25, 26] employing continuous loading. Because the objective function's landscape changes with Z_0 , even if only slightly, and because the $Z_0 = 50 \Omega$ CFO-optimized antenna exhibits better VSWR when Z_0 is increased to 300 Ω , it is instructive to tweak the previous design by making another CFO run against f_3 's landscape with $Z_0 = 300 \Omega$, that is, with $f_3(R, H, 300)$ as the objective function. CFO's best fitness in this case is 9.66379×10^{-5} at the point $(R, H) = (501.78982, 7.107012)$ using 5,016 function evaluations.

This single-resistor monopole outperforms the 14-segment antenna by every measure except VSWR. Radiation efficiency increases nearly monotonically from a minimum of 15%, compared to the 14-segment's that starts off near 8% and exhibits considerable fluctuation with increasing frequency. The tweaked design's gain increases from ≈ -3.25 dBi at 5 MHz to ≈ 2.25 dBi at 30 MHz with a dip to 0 dBi at 24 MHz. The 14-segment design has a similar behavior, but a lower gain at 5 MHz (~ -5.6 dBi) and a very slightly higher gain at 28 MHz (~ 3.1 dBi).

VSWR for the tweaked antenna is somewhat worse, but nonetheless quite good, $\leq 2:1$ from 7.5 MHz-26 MHz and only slightly above that through 30 MHz where it reaches 2.5:1. Below 7.5 MHz VSWR increases quickly with decreasing frequency, reaching just over 5:1 at 5 MHz, a degree of variability easily handled by a simple matching network. It therefore is reasonable to

expect a VSWR below 2:1 across the entire 5 MHz-30 MHz band, possibly well below 2:1.

Another important measure of the tweaked monopole's effectiveness is its radiation pattern compared to the 14-segment's. The tweaked design generally exhibits higher power gain at all polar angles, especially in the range of interest for moderate to long HF links, $60^\circ \leq \theta \leq 80^\circ$. The single-resistor $f_3(R,H,300)$ loaded design actually provides better overall performance than the 14-segment monopole. Moreover, it is simpler to fabricate and maintain, and arguably substantially better than the continuously loaded designs in [25, 26].

```

Procedure CFO [ $f(\vec{x}), N_d, \Pi$ ]
Internals:  $N_p, F_{rep}^{min}, \Delta F_{rep}, F_{rep}^{max}, \left(\frac{N_p}{N_d}\right)_{MAX}, \gamma_{start}, \gamma_{stop}, \Delta\gamma$ 
Initialize  $f_{max}^{global}(\vec{x})$  = very large negative number, say,  $-10^{4200}$ .
For  $N_p/N_d = 2$  to  $\left(\frac{N_p}{N_d}\right)_{MAX}$  by 2:
(a.0) Total number of probes:  $N_p = N_d \cdot \left(\frac{N_p}{N_d}\right)$ 
For  $\gamma = \gamma_{start}$  to  $\gamma_{stop}$  by  $\Delta\gamma$ :
(a.1) Re-initialize data structures for position/
acceleration vectors & fitness matrix.
(a.2) Compute IPD (see [4]).
(a.3) Compute initial fitness matrix,  $M_p^0, 1 \leq p \leq N_p$ .
(a.4) Initialize  $F_{rep} = F_{rep}^{min}$ .
For  $j = 0$  to  $N_j$  (or earlier termination - see [4]):
(b) Compute position vectors,  $\vec{R}_p^j, 1 \leq p \leq N_p$  (eq. (2) in [4])
(c) Retrieve errant probes ( $1 \leq p \leq N_p$ ):
If  $\vec{R}_p^j \cdot \hat{e}_i < x_i^{min} \therefore \vec{R}_p^j \cdot \hat{e}_i = \max\{x_i^{min} + F_{rep}(\vec{R}_{p-1}^j \cdot \hat{e}_i - x_i^{min}), x_i^{min}\}$ .
If  $\vec{R}_p^j \cdot \hat{e}_i > x_i^{max} \therefore \vec{R}_p^j \cdot \hat{e}_i = \min\{x_i^{max} - F_{rep}(x_i^{max} - \vec{R}_{p-1}^j \cdot \hat{e}_i), x_i^{max}\}$ .
(d) Compute fitness matrix for current probe
distribution,  $M_p^j, 1 \leq p \leq N_p$ .
(e) Compute accelerations using current probe
distribution and fitnesses (eq. (1) in [4]).
(f) Increment  $F_{rep} : F_{rep} = F_{rep} + \Delta F_{rep}$ ; If  $F_{rep} > 1 \therefore F_{rep} = F_{rep}^{min}$ .
(g) If  $j \geq 20$  and  $j \text{ MOD } 10 = 0$  :
(i) Shrink  $\Omega$  around  $\vec{R}_{best}$  (see [4]).
(ii) Retrieve errant probes [procedure Step (c)].
Next  $j$ 
(h) Reset  $\Omega$  boundaries [values before shrinking].
(i) If  $f_{max}(\vec{x}) \geq f_{max}^{global}(\vec{x}) \therefore f_{max}^{global}(\vec{x}) = f_{max}(\vec{x})$ .
Next  $\gamma$ 
Next  $N_p/N_d$ 
    
```

Fig. 9. CFO pseudocode.

IX. CONCLUSION

This paper discussed an example antenna optimization problem using a single-resistor loaded HF monopole. It addressed issues in defining an objective function that effectively measures antenna performance, and the suitability of stochastic and deterministic optimization algorithms. Assessing how well a particular objective function will achieve design goals is a difficult question because the landscape of functions beyond 2-D cannot be visualized (note that CFO's tendency to distribute probes may be useful in this regard; see §9 in [4]). Three different objective functions and their landscapes were considered.

Deterministic central force optimization was applied to each objective function's topology and the results compared. The best objective function then was used to develop a final tweaked design that was compared to a similar, previously CFO-optimized design utilizing fourteen discrete loading resistors. The single-resistor monopole performs as well or better than the fourteen resistor version and better than other continuously loaded antennas reported in the literature.

```

CM File: LD_MONO.NEC
CM Run ID 02-16-2011 10:43:46
CM Nd= 14, p= 2, j= 120
CM Zo=300 ohms
CE
GW1,14,0.,0.,0.,0.,0.,10.668,0254
GE1
LD0,1,1,1,82.7045,0.,0.
LD0,1,2,2,29.31145,0.,0.
LD0,1,3,3,9.2825,0.,0.
LD0,1,4,4,7.154042,0.,0.
LD0,1,5,5,7.397769,0.,0.
LD0,1,6,6,7.310225,0.,0.
LD0,1,7,7,27.58697,0.,0.
LD0,1,8,8,26.55749,0.,0.
LD0,1,9,9,24.70102,0.,0.
LD0,1,10,10,22.80148,0.,0.
LD0,1,11,11,20.82445,0.,0.
LD0,1,12,12,16.44918,0.,0.
LD0,1,13,13,11.4537,0.,0.
LD0,1,14,14,9.471994,0.,0.
GN1
FR 0,26,0,0,5.,1.
EX 0,1,1,1,1.,0.
RP 0,10,1,1001,0.,0.,10.,0.,100000.
EN
    
```

Fig. 10. NEC file for CFO-optimized 14-segment loaded monopole.

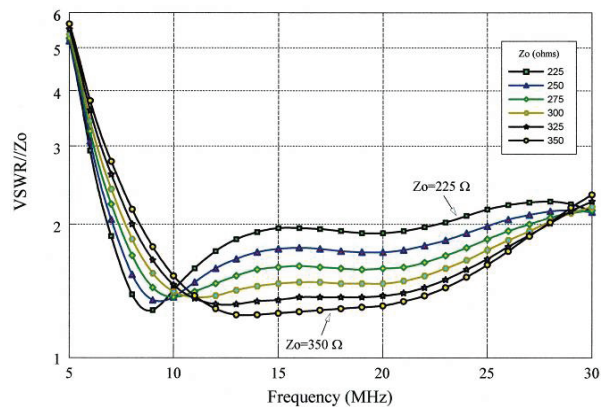


Fig. 11. VSWR for CFO design $f_3(499.6,7.302,Z_0)$ parametric in Z_0 .

REFERENCES

- [1] (i) 4nec2 Antenna Modeling Freeware by A. Voors, online <http://home.ict.nl/~arivoors/>.
(ii) Unofficial Numerical Electromagnetic Code Archives, online at <http://www.silist.net/swindex.html>
- [2] G. Burke and A. Poggio, *Numerical Electromagnetics Code (NEC) – Method of Moments, Parts I, II and III*, January 1981, UCID-19934, Lawrence Livermore National Laboratory, Livermore, California, USA
- [3] G. Burke, *Numerical Electromagnetics Code – NEC-4, Method of Moments, Part I: User's Manual and Part II: Program Description – Theory*, January 1992, UCRL-MA-109338, Lawrence Livermore National Laboratory, Livermore, California, USA
- [4] R. Formato, "Central force optimization: a new metaheuristic with applications in applied electromagnetics," *Prog. Electromagnetics Research*, vol. 77, pp. 425-491, 2007.
- [5] R. Formato, "Parameter-free deterministic global search with simplified central force optimization," *Advanced Intelligent Computing Theories and Applications (ICIC2010)*, Lecture Notes in Computer Science (LNCS 6215). Springer-Verlag Berlin Heidelberg; 2010.
- [6] R. Formato, "Central force optimization with variable initial probes and adaptive decision space," *App. Math. Comp.*, vol. 217, no. 21, pp. 8866-8872, 2011.
- [7] D. Ding, X. Luo, J. Chen, X. Wang, P. Du, and Y. Guo, "A convergence proof and parameter analysis of central force optimization algorithm," *Jour. Convergence Information Technology (JCIT)*, vol. 6, no. 10, pp. 16-23, 2011.
- [8] D. Ding, X. Qi, X. Luo, J. Chen, X. Wang, and P. Du, "Convergence analysis and performance of an extended central force optimization algorithm," *App. Math. Comp.*, vol. 219, no. 4, pp. 2246-2259, 2012.
- [9] R. Green, L. Wang, M. Alam, and R. Formato, "Central force optimization on a GPU: A case study in high performance metaheuristics using multiple topologies," *Jour. Supercomputing*, vol. 62, no. 1, pp. 378-398, 2012.
- [10] R. Green, L. Wang, and M. Alam, "Evaluating the impact of multiple neighborhood topologies on central force optimization," www.parallelcoding.com.
- [11] R. Green, L. Wang, M. Alam, and R. Formato, "Central force optimization on a GPU: A case study in high performance metaheuristics using multiple topologies," *IEEE Cong. Evol. Comp.*, New Orleans, Los Angeles, pp. 550-557, June 2011.
- [12] R. Green, L. Wang, and M. Alam, "Training neural networks using central force optimization and particle swarm optimization: insights and comparisons," *Expert Systems with Applications*, vol. 39, pp. 555-563, 2012.
- [13] A. Haghghi and H. Ramos, "Detection of leakage freshwater and friction factor calibration in drinking networks using central force optimization," *Water Resource Management*, vol. 26, pp. 2347-2363, 2012.
- [14] O. Roa, I. Amaya, F. Ramírez, and R. Correa, "Solution of nonlinear circuits with the central force optimization algorithm," *2012 IEEE 4th Colombian Workshop on Circuits and Systems (CWCAS)*, pp. 1-6, 1-2 Nov. 2012.
- [15] G. Mohammad and N. Dib, "Synthesis of antenna arrays using central force optimization," *Mosharaka International Conf. Communications, Computers and Applications, MIC-CPE 2009*.
- [16] G. Qubati, R. Formato, and N. Dib, "Antenna benchmark performance and array synthesis using central force optimization," *IET Microwaves, Antennas and Propagation*, vol. 4, no. 5, pp. 583-592, 2010.
- [17] G. Qubati and N. Dib, "Microstrip patch antenna optimization using modified central force optimization," *Prog. Electromagnetics Research B*, vol. 21, pp. 281-298, 2010.
- [18] A. Montaser, K. Mahmoud, and H. Elmikati, "Tri-band slotted bow-tie antenna design for RFID reader using hybrid CFO-NM algorithm," *29th National Radio Science Conference (NRSC 2012)*, April 10-12, 2012.
- [19] K. Mahmoud, "Central force optimization: Nelder-Mead hybrid algorithm for rectangular microstrip antenna design," *Electromagnetics*, vol. 31, no. 8, pp. 578-592, 2011.
- [20] M. Asi and N. Dib, "Design of multilayer microwave broadband absorbers using central force optimization," *Prog. Electromagnetics Research B*, vol. 26, pp. 101-113, 2010.
- [21] R. Formato, "Improved CFO algorithm for antenna optimization," *Prog. Electro-magnetics Research B*, vol. 19, pp. 405-425, 2010.
- [22] A. Montaser, K. Mahmoud, A. Abdel-Rahman, and H. Elmikati, "Design bluetooth and notched-UWB E-shape antenna using optimization techniques," *Prog. Electromagnetics Research B*, vol. 47, pp. 279-295, 2013.
- [23] R. Formato, "New techniques for increasing antenna bandwidth with impedance loading," *Prog. Electromagnetics Research B*, vol. 29, pp. 269-288, 2011.
- [24] R. Formato, "Improving bandwidth of Yagi-Uda arrays," *Wireless Engin. Tech.* vol. 3, no. 1, pp. 18-24, 2012.

- [25] B. Rao and P. Debroux, "Wideband HF monopole antennas with tapered resistivity loading," *IEEE Military Comm. Conf. (MILCOM '90)*, Monterey, CA, September 30 - October 3, 1990.
- [26] B. Rao, "Optimized tapered resistivity profiles for wideband HF monopole antenna," *IEEE Ant. and Prop. Soc. Symp.*, London, Ontario, Canada, 1991.



Richard A. Formato is a Consulting Engineer and Registered Patent Attorney. He received his JD from Suffolk University Law School, PhD and MS degrees from the University of Connecticut, and MSEE and BS (Physics) degrees from Worcester

Polytechnic Institute. In the early 1990s, he began applying genetic algorithms to antenna design problems and developed YGO3 freeware (Yagi Genetic Optimizer). His interest in optimization algorithms led to the development of Central Force Optimization and Dynamic Threshold Optimization. He also invented the proprietary Variable Z_0 antenna technology that treats an antenna's feed system impedance as a true optimization variable, not a fixed parameter.

2013 INSTITUTIONAL MEMBERS

DTIC-OCP LIBRARY
8725 John J. Kingman Rd, Ste 0944
Fort Belvoir, VA 22060-6218

AUSTRALIAN DEFENCE LIBRARY
Northcott Drive
Canberra, A.C.T. 2600 Australia

BEIJING BOOK CO, INC
701 E Linden Avenue
Linden, NJ 07036-2495

DARTMOUTH COLLEGE
6025 Baker/Berry Library
Hanover, NH 03755-3560

DSTO EDINBURGH
AU/33851-AP, PO Box 830470
Birmingham, AL 35283

SIMEON J. EARL – BAE SYSTEMS
W432A, Warton Aerodome
Preston, Lancs., UK PR4 1AX

ENERGY KEN LIBRARY
PO Box 300613
Jamaica, NY, 11430

ENGINEERING INFORMATION, INC
PO Box 543
Amsterdam, Netherlands 1000 Am

ETSE TELECOMUNICACION
Biblioteca, Campus Lagoas
Vigo, 36200 Spain

GA INSTITUTE OF TECHNOLOGY
EBS-Lib Mail code 0900
74 Cherry Street
Atlanta, GA 30332

TIMOTHY HOLZHEIMER
Raytheon
PO Box 1044
Rockwall, TX 75087

HRL LABS, RESEARCH LIBRARY
3011 Malibu Canyon
Malibu, CA 90265

IEE INSPEC
Michael Faraday House
6 Hills Way
Stevenage, Herts UK SG1 2AY

INSTITUTE FOR SCIENTIFIC INFO.
Publication Processing Dept.
3501 Market St. Philadelphia, PA
19104-3302

LIBRARY – DRDC OTTAWA
3701 Carling Avenue
Ottawa, Ontario, Canada K1A OZ4

LIBRARY of CONGRESS
Reg. Of Copyrights
Washington DC, 20559

LINDA HALL LIBRARY
5109 Cherry Street
Kansas City, MO 64110-2498

MISSOURI S&T
400 W 14th Street
Rolla, MO 56409

MIT LINCOLN LABORATORY
244 Wood Street
Lexington, MA 02420

NATIONAL CHI NAN UNIVERSITY
Lily Journal & Book Co, Ltd
20920 Glenbrook Drive
Walnut, CA 91789-3809

JOHN NORGARD
UCCS
20340 Pine Shadow Drive
Colorado Springs, CO 80908

OSAMA MOHAMMED
Florida International University
10555 W Flagler Street
Miami, FL 33174

NAVAL POSTGRADUATE SCHOOL
Attn:J. Rozdal/411 Dyer Rd./ Rm 111
Monterey, CA 93943-5101

NDL KAGAKU
C/0 KWE-ACCESS
PO Box 300613 (JFK A/P)
Jamaica, NY 11430-0613

OVIEDO LIBRARY
PO BOX 830679
Birmingham, AL 35283

DAVID PAULSEN
E3Compliance
1523 North Joe Wilson Road
Cedr Hill, TX 75104-1437

PENN STATE UNIVERSITY
126 Paterno Library
University Park, PA 16802-1808

DAVID J. PINION
1122 E Pike Street #1217
SEATTLE, WA 98122

KATHERINE SIAKAVARA
Gymnasiou 8
Thessaloniki, Greece 55236

SWETS INFORMATION SERVICES
160 Ninth Avenue, Suite A
Runnemede, NJ 08078

YUTAKA TANGE
Maizuru Natl College of Technology
Maizuru, Kyoto, Japan 625-8511

TIB & UNIV. BIB. HANNOVER
Welfengarten 1B
Hannover, Germany 30167

UEKAE
PO Box 830470
Birmingham, AL 35283

UNIV OF CENTRAL FLORIDA
4000 Central Florida Boulevard
Orlando, FL 32816-8005

UNIVERSITY OF COLORADO
1720 Pleasant Street, 184 UCB
Boulder, CO 80309-0184

UNIVERSITY OF KANSAS –
WATSON
1425 Jayhawk Blvd 210S
Lawrence, KS 66045-7594

UNIVERSITY OF MISSISSIPPI
JD Williams Library
University, MS 38677-1848

UNIVERSITY LIBRARY/HKUST
Clear Water Bay Road
Kowloon, Honk Kong

CHUAN CHENG WANG
8F, No. 31, Lane 546
MingCheng 2nd Road, Zuoying Dist
Kaoshiung City, Taiwan 813

THOMAS WEILAND
TU Darmstadt
Schlossgartenstrasse 8
Darmstadt, Hessen, Germany 64289

STEVEN WEISS
US Army Research Lab
2800 Powder Mill Road
Adelphi, MD 20783

YOSHIHIDE YAMADA
NATIONAL DEFENSE ACADEMY
1-10-20 Hashirimizu
Yokosuka, Kanagawa,
Japan 239-8686

INFORMATION FOR AUTHORS

PUBLICATION CRITERIA

Each paper is required to manifest some relation to applied computational electromagnetics. **Papers may address general issues in applied computational electromagnetics, or they may focus on specific applications, techniques, codes, or computational issues.** While the following list is not exhaustive, each paper will generally relate to at least one of these areas:

1. **Code validation.** This is done using internal checks or experimental, analytical or other computational data. Measured data of potential utility to code validation efforts will also be considered for publication.
2. **Code performance analysis.** This usually involves identification of numerical accuracy or other limitations, solution convergence, numerical and physical modeling error, and parameter tradeoffs. However, it is also permissible to address issues such as ease-of-use, set-up time, run time, special outputs, or other special features.
3. **Computational studies of basic physics.** This involves using a code, algorithm, or computational technique to simulate reality in such a way that better, or new physical insight or understanding, is achieved.
4. **New computational techniques** or new applications for existing computational techniques or codes.
5. **“Tricks of the trade”** in selecting and applying codes and techniques.
6. **New codes, algorithms, code enhancement, and code fixes.** This category is self-explanatory, but includes significant changes to existing codes, such as applicability extensions, algorithm optimization, problem correction, limitation removal, or other performance improvement. **Note: Code (or algorithm) capability descriptions are not acceptable, unless they contain sufficient technical material to justify consideration.**
7. **Code input/output issues.** This normally involves innovations in input (such as input geometry standardization, automatic mesh generation, or computer-aided design) or in output (whether it be tabular, graphical, statistical, Fourier-transformed, or otherwise signal-processed). Material dealing with input/output database management, output interpretation, or other input/output issues will also be considered for publication.
8. **Computer hardware issues.** This is the category for analysis of hardware capabilities and limitations of various types of electromagnetics computational requirements. Vector and parallel computational techniques and implementation are of particular interest. Applications of interest include, but are not limited to,

antennas (and their electromagnetic environments), networks, static fields, radar cross section, inverse scattering, shielding, radiation hazards, biological effects, biomedical applications, electromagnetic pulse (EMP), electromagnetic interference (EMI), electromagnetic compatibility (EMC), power transmission, charge transport, dielectric, magnetic and nonlinear materials, microwave components, MEMS, RFID, and MMIC technologies, remote sensing and geometrical and physical optics, radar and communications systems, sensors, fiber optics, plasmas, particle accelerators, generators and motors, electromagnetic wave propagation, non-destructive evaluation, eddy currents, and inverse scattering.

Techniques of interest include but not limited to frequency-domain and time-domain techniques, integral equation and differential equation techniques, diffraction theories, physical and geometrical optics, method of moments, finite differences and finite element techniques, transmission line method, modal expansions, perturbation methods, and hybrid methods.

Where possible and appropriate, authors are required to provide statements of quantitative accuracy for measured and/or computed data. This issue is discussed in “Accuracy & Publication: Requiring quantitative accuracy statements to accompany data,” by E. K. Miller, *ACES Newsletter*, Vol. 9, No. 3, pp. 23-29, 1994, ISBN 1056-9170.

SUBMITTAL PROCEDURE

All submissions should be uploaded to ACES server through ACES web site (<http://www.aces-society.org>) by using the upload button, journal section. Only pdf files are accepted for submission. The file size should not be larger than 10MB, otherwise permission from the Editor-in-Chief should be obtained first. Automated acknowledgment of the electronic submission, after the upload process is successfully completed, will be sent to the corresponding author only. It is the responsibility of the corresponding author to keep the remaining authors, if applicable, informed. Email submission is not accepted and will not be processed.

EDITORIAL REVIEW

In order to ensure an appropriate level of quality control, papers are peer reviewed. They are reviewed both for technical correctness and for adherence to the listed guidelines regarding information content and format.

PAPER FORMAT

Only camera-ready electronic files are accepted for publication. The term **“camera-ready”** means that the material is neat, legible, reproducible, and in accordance with the final version format listed below.

The following requirements are in effect for the final version of an ACES Journal paper:

1. The paper title should not be placed on a separate page.

The title, author(s), abstract, and (space permitting) beginning of the paper itself should all be on the first page. The title, author(s), and author affiliations should be centered (center-justified) on the first page. The title should be of font size 16 and bolded, the author names should be of font size 12 and bolded, and the author affiliation should be of font size 12 (regular font, neither italic nor bolded).

2. An abstract is required. The abstract should be a brief summary of the work described in the paper. It should state the computer codes, computational techniques, and applications discussed in the paper (as applicable) and should otherwise be usable by technical abstracting and indexing services. The word "Abstract" has to be placed at the left margin of the paper, and should be bolded and italic. It also should be followed by a hyphen (–) with the main text of the abstract starting on the same line.
3. All section titles have to be centered and all the title letters should be written in caps. The section titles need to be numbered using roman numbering (I. II.)
4. Either British English or American English spellings may be used, provided that each word is spelled consistently throughout the paper.
5. Internal consistency of references format should be maintained. As a guideline for authors, we recommend that references be given using numerical numbering in the body of the paper (with numerical listing of all references at the end of the paper). The first letter of the authors' first name should be listed followed by a period, which in turn, followed by the authors' complete last name. Use a comma (,) to separate between the authors' names. Titles of papers or articles should be in quotation marks (" "), followed by the title of journal, which should be in italic font. The journal volume (vol.), issue number (no.), page numbering (pp.), month and year of publication should come after the journal title in the sequence listed here.
6. Internal consistency shall also be maintained for other elements of style, such as equation numbering. Equation numbers should be placed in parentheses at the right column margin. All symbols in any equation have to be defined before the equation appears or right immediately following the equation.
7. The use of SI units is strongly encouraged. English units may be used as secondary units (in parentheses).
8. Figures and tables should be formatted appropriately (centered within the column, side-by-side, etc.) on the page such that the presented data appears close to and after it is being referenced in the text. When including figures and tables, all care should be taken so that they will appear appropriately when printed in black and white. For better visibility of paper on computer screen, it is good to make color figures with different line styles for figures with multiple curves. Colors should also be tested to insure their ability to be distinguished after

black and white printing. Avoid the use of large symbols with curves in a figure. It is always better to use different line styles such as solid, dotted, dashed, etc.

9. A figure caption should be located directly beneath the corresponding figure, and should be fully justified.
10. The intent and meaning of all text must be clear. For authors who are not masters of the English language, the ACES Editorial Staff will provide assistance with grammar (subject to clarity of intent and meaning). However, this may delay the scheduled publication date.
11. Unused space should be minimized. Sections and subsections should not normally begin on a new page.

ACES reserves the right to edit any uploaded material, however, this is not generally done. It is the author(s) responsibility to provide acceptable camera-ready files in pdf and MSWord formats. Incompatible or incomplete files will not be processed for publication, and authors will be requested to re-upload a revised acceptable version.

COPYRIGHTS AND RELEASES

Each primary author must execute the online copyright form and obtain a release from his/her organization vesting the copyright with ACES. Both the author(s) and affiliated organization(s) are allowed to use the copyrighted material freely for their own private purposes.

Permission is granted to quote short passages and reproduce figures and tables from and ACES Journal issue provided the source is cited. Copies of ACES Journal articles may be made in accordance with usage permitted by Sections 107 or 108 of the U.S. Copyright Law. This consent does not extend to other kinds of copying, such as for general distribution, for advertising or promotional purposes, for creating new collective works, or for resale. The reproduction of multiple copies and the use of articles or extracts for commercial purposes require the consent of the author and specific permission from ACES. Institutional members are allowed to copy any ACES Journal issue for their internal distribution only.

PUBLICATION CHARGES

All authors are allowed for 8 printed pages per paper without charge. Mandatory page charges of \$50 a page apply to all pages in excess of 8 printed pages. Authors are entitled to a total of two, free of charge, copies of the printed journal issue in which their paper was published. These two copies will be mailed to the corresponding author. Additional reprints are available for \$50. Requests for additional re-prints should be submitted to the managing editor or ACES Secretary.

Corresponding author is required to complete the online form for the over page charge payment right after the initial acceptance of the paper.

ACES Journal is abstracted in INSPEC, in Engineering Index, DTIC, Science Citation Index Expanded, the Research Alert, and to Current Contents/Engineering, Computing & Technology.